STEEL AND GFRP BEAMS/HEAVY-DUTY VEHICLE LEAF SPRINGS UNDER CYCLIC LOADING

A dissertation

Submitted by

Roselita Fragoudakis

In partial fulfillment of the requirements
for the degree of

Doctor of Philosophy

in

Mechanical Engineering

TUFTS UNIVERSITY

February 2012

Adviser: Dr. Anil Saigal
Co-Adviser: Dr. Douglas Matson

To my grandfather

Abstract

Technological advances in many areas of the industry require of lighter and stronger materials. Especially in the automotive industry, composites have replaced many metallic components. The scope of this analysis is to determine how appropriate composite materials are for cyclic loading applications such as in the case of leaf springs.

AISI 4130, AISI 6150, E glass fiber/epoxy and S2 glass fiber/epoxy were examined to determine their fatigue life and failure behavior. Experimental results, theoretical calculations and finite element analysis were performed in order to examine the important parameters that affect the fatigue life of these materials, and determine the material that will have longer life. Induction of a compressive residual stress field in a steel component, as a result of surface and heat treatment of the material, enhances the fatigue life of the material and its performance. Different ply stacking sequences of a laminate result in structures of different strength and fatigue life.

Among the materials examined AISI 6150 and S2 glass fiber/epoxy have longer lives, and the steel showed longer lives than the composite at higher applied stresses. Hybrid structures were constructed from AISI 6150 and S2 glass fiber/epoxy, and examined through experimental testing and theoretical calculations, in order to determine their applicability as leaf spring structures.

Comparison of the steel, composite and hybrid structures, together with an economic analysis of the manufacturing process for steel and composite leaf springs, showed that composites provide the lightest, stronger and more economical option for leaf spring material.

Acknowledgements

First and foremost I offer my sincere gratitude to my advisor, Professor Anil Saigal, who guided me during the majority of my years as a student at Tufts University. His advice, knowledge and encouragement, helped me achieve the level of my Ph.D degree, and evolve from the stage of a college student to a researcher.

I would like to thank Professor Douglas Matson for his encouragement during various stages of my work. For a researcher and a graduate student, financial support is one of the major aspects that may influence their research. Partial funding for this work was provided by NASA grant NNX08AL21G.

I would also like to thank Professor Michael Zimmerman for his valuable support and offer to my research, Professor Georgios Savaidis who helped me complete a significant part of my experimental research at his laboratory in the Aristotle University of Thessaloniki, and Professor Gary Leisk, for his insight and interesting ideas on my research subject.

Mr. Jim Hoffman, the machine shop coordinator at Bray Laboratories at Tufts University, and Mr. Vincent Miraglia, coordinator of the Bray Laboratory, helped me prepare and carry out an important set of fatigue experiments, and I am grateful for their help.

It is a pleasure to thank the Aristotle University of Thessaloniki, and especially Mr. M. Malikoutsakis, Mr. S. Karditsas, Mr. G. Pappas and Mr. I. Bazios, for their help in

running fatigue tests on steel leaf springs, and Professor Nikolaos Michailidis, for offering me access to Physical Metallurgy Laboratory.

Finally, my greatest thank goes to my friends and family, for standing by my side during every step of the way to the completion of this thesis. I am forever indebted to my dear friend Dr. Nicolaos Prevelakis for his unconditional help, support, encouragement and advice during the difficult and easy moments of my work. This thesis would not have been possible if it weren't for the everyday support and encouragement of my mother, Giolanda Vadokas, and my sister, Mirka Fragoudakis. Although they were back home in Greece, they shared all my anxiety, troubles and successes, and made me feel they were with me all the way.

Contents

INTRODUCTION..1

I. STEEL

I.1 Leaf Spring Manufacturing Process 15
I.1.1 Heat Treatments..20
I.1.2 The Role of Carbon Content and Alloying Elements..............................28
I.1.3 Residual Stresses and Residual Stress Relaxation....................................30
I.1.4 Surface Treatments 36
I.2 Fatigue and Fatigue Life of Steel 41
I.2.1 Stress-Life Approach..47
I.2.2 Mean Stress Effects 50
I.2.3 Strain-Life Approach..56
I.2.4 Predicting the Fatigue Life of Steel Using the Stress-Life Approach
    I.2.4.1 Power Relationship of S-N Curve 60
    I.2.4.2 Power Relationship of S-N Curve Using Hardness as a Function of Carbon Content 62
    I.2.4.3 Damage Prediction Models 63
I.2.5 Factors Affecting the S-N Curve 68
I.3 Results and Discussion 72
I.3.1 Experimental Results
    I.3.1.1 Surface Treatment Effects on the Fatigue Life of AISI 4130 CF..............74
    I.3.1.2 Fatigue Life of AISI 6150 Leaf Springs..86
    I.3.1.3 Fatigue Life of AISI 6150 under Fully Reversed Loading.........................93
    I.3.1.4 Failure Analysis of AISI 6150..97
I.3.2 Calculations
    I.3.2.1 Prediction of Fatigue Life of 4130 CF using the Power Relationship......106
    I.3.2.2 Prediction of Fatigue Using Damage Prediction Models 114
I.3.3 Finite Element Analysis...122
I.4 Repairs of Steel Leaf Springs 162

I.5 Conclusions 167

II. COMPOSITES

II.1 Composite Materials 170
II.2 Manufacturing of Composite Leaf Springs 178
II.3 Classical Lamination Theory (CLT) 183
II.4 Lamina Failure Prediction Using Failure Theories 189
II.5 Results and Discussion 196
II.5.1 First Ply Failure of GFRP Laminates 198
II.5.2 Finite Element Analysis 206
II.5.3 Prediction of Fatigue Life Using Damage Prediction Models 232
II.5.4 Experimental Results 241
II.6 Repairs of Composite Leaf Springs 247
II.7 Conclusions 248

III. HYBRID STRUCTURES

III.1 Hybrid Laminates 251
III.2 Hybrid Leaf Springs 254
III.3 Results and Discussion 257
III.3.1 Finite Element Analysis 257
III.3.2 Hybrid Laminate Failure Using Failure Theories 265
III.3.3 Experimental Results 270
III.4 Conclusions 271

IV. ECONOMIC ANALYSIS

IV.1 Introduction 273
IV.2 Non-recurring Costs 276
IV.2.1 Tooling and Equipment 276
IV.2.2 Plant Facilities 279
IV.2.3 Conclusion on Non-recurring Costs 280
IV.3 Manufacturing Costs 281

IV.4 Economic Analysis 286
IV.5 Conclusions...288

V. COMPARISON OF MATERIALS

V.1 Comparison of Materials Based on Damage Prediction Models 292
V.2 Comparison of Materials Based on Fatigue Life 295
V.1.1 Life Estimation Using fe-safe^{TM} 295
V.2.2 Life Estimation from Experimental Results...297
V.3 Material Selection 298

VI. CONCLUSIONS...300

RFERENCES 305

APPENDIX A A1

APPENDIX B B1

List of Tables

I. STEEL

1: The Role of Alloying Elements and Impurities in Steel 29
2: Values of Surface Treating Factors 85
3: Stress Measurements at the Tension Surface 90
4: Maximum Displacements and Spring Rates 92
5: Effect of Decarburization on the Fatigue Limit of High Strength Steel 100
6: Rockwell-C Macro-hardness Measurements and Corresponding Tensile Strength 104
7: Power Law Relationship and Parameters 107
8: BHN Hardness for Fine Pearlite and Martensite Steels at 0.3wt% and 0.9wt% C Concentrations 111
9: Shape and Scale Parameters of AISI 4130 CF and AISI 6150 for all Damage Models 115
10: Average Cumulative Distribution of Damage for AISI 4130 CF and AISI 6150 118
11: Average Fatigue Life of AISI 4130 CF and AISI 6150 121
12: Stress Intensity Factor Coefficients 130
13: Material Properties for Fatigue Life Estimation 141
14: Stress Concentration Factor and Fatigue Limit for Cracked Specimens 150

II. COMPOSITES

15: Mid-surface Strains and Curvatures 199
16: Minimum Moment to Cause First-ply failure in Laminates 203
17: Beam Deflections for Different Materials and Different Fiber Orientations 208
18: Symmetric and Anti-symmetric Beam Deflections 211
19: Deflection of 22 Layer Beams 213
20: MCT average quantities symbols 222
21: Shape and Scale Parameters of Composites for all Damage Models 233
22: Average Cumulative Distribution of Damage for S2 glass fiber/epoxy composite and for E glass fiber/epoxy composite 236
23: Average Fatigue Life for S2 glass fiber/epoxy composite and E glass fiber/epoxy

composite 240

III. HYBRID STRUCTURES

24: Maximum Displacement and Volume of Hybrid Beams..257
25: Mid-surface Strains and Curvatures 266

IV. ECONOMIC ANALYSIS

26: Non-recurring costs for steel material leaf springs..277
27: Non-recurring costs for composite material leaf springs..278
28: Plant Facilities Costs...279
29: Non-recurring Costs for the two Production Lines..280
30: Direct Labor Costs...281
31: Unit Cost for Steel Leaf Spring Raw Materials...282
32: Unit Cost for Composite Leaf Spring Raw Materials...282
33: Total Prime Costs for Each Production Line in One Week.......................................288
34: Total Non-recurring Costs for Each Production Line in One Week.........................288

V. COMPARISON OF MATERIALS

35: Fatigue Life of Structures 297
36: Deflection and Weight of Structures 298

List of Figures

I. STEEL

1: Types of Spring Suspension Systems 2

2: Multi-leaf spring with helper leaves 4

3: Various Spring Eyes and Ends...6

4: Load-Deflection Diagram: (a) stiff, high rate spring with small deflection, (b) flexible, low rate spring with large deflection 7

5: Steps of Steel Leaf Spring Manufacturing...16

6: Cambering station with leaf spring ready for quenching..................................17

7: Stress patterns due to shot peening, stress peening and presetting in the absence of carburizing 19

8: Iron-carbide phase diagram 23

9: BCC and FCC crystal structures of iron 24

10: BCT crystal structures of iron..24

11: Effect of Tempering on stress-strain relationship..27

12: Residual Stresses in unotched beam under bending 30

13: Residual Stress Relaxation of shot peened, stress peened and warm peened under torsional loading...34

14: Stress Relaxation of notched components under R=-1...................................35

15: Vickers micro-hardness patterns for AISI 8620 steels carburized at different case depths 37

16: S-N Curves for shot peened EN45A steel at different Almen intensities..........40

17: Initiation and Propagation Lives..45

18: S-N curve for AISI 1045 steel 48

19: S-N probability curves for the fatigue life of 7075 aluminum, loaded at *R*=-1...........49

20: Stress Parameters affecting Fatigue Life 51

21: Effect of Mean Stress magnitude (a) and direction (b) on fatigue life 52

22: Effect of Load Ratio to Fatigue Life..52

23: Haigh Diagram: (a) Lines of constant life, (b) Lines of Mean Stress Equations (a. Soderberg, b. Goodman, c. Gerber, d. Morrow)...53

24: Goodman estimate for notched component on Haigh Diagram 55
25: S-N curves for different wrought steels...60
26: Hardness as a function of carbon concentration 62
27: Stress gradient in different size components 69
28: R.R. Moore Rotating Beam Apparatus...75
29: Fatigue Specimen for the R.R. Moore Rotating Beam Apparatus...............................76
30: Carburizing process; Temperature versus Time 77
31: Experimental Results of AISI 4130 CF steel under fully reversed loading.................79
32: Fractured AISI 4130 Fatigue Specimens: (a) non-treated (b) carburized....................81
33: Ductile (left) and brittle (right) tensile fractures...82
34: Second Leaf of parabolic rear suspension for Mercedes ACTROS series 87
35: Leaf Spring sketch for ABAQUS/CAE modeling...87
36: Fatigue Test Rig at Aristotle University of Thessaloniki 89
37: Positions of strain measurements...90
38: Stress Measurements at the Tension Surface...90
39: Experimental Results of Leaf Spring Fatigue Tests 91
40: Maximum Stress vs. Applied Load for all Specimens...92
41: AISI 6150 Fatigue Specimen, dimensions in mm 94
42: AISI 6150 Fatigue Specimen..94
43: Rotating Beam Apparatus in Aristotle University of Thessaloniki 94
44: AISI 6150 Fatigue Life under fully reversed loading..95
45: Fatigue life for AISI 6150 Steel at R=-1 and R=0.25..96
46: Fractured Surfaces of Leaf Spring...97
47: Fractured Surface of Fatigue Specimen...98
48: Automated press (a) and Specimen mounted in Bakelite Amber mold (b).................99
49: Core microstructure of the leaf spring (left) and fatigue (right) specimens 100
50: Lath Martensite 101
51: Surface microstructure of the leaf spring (left) and fatigue (right) specimens..........101
52: Vickers pyramidal impressions on surface of the leaf spring (left) and fatigue (right) specimens..102
53: Micro-hardness profiles of the core and surface of the two types of AISI 6150

specimens 103

54: Roughness measurements on the tension (a) and compression (b) surfaces of the leaf spring specimen 105

55: S-N Curves of AISI 4130 CF Steel from Power Law Relationships........................108

56: S-N curve of AISI 4130 CF Fatigue Specimens, based on surface Carbon content 112

57: Cumulative Distribution of Damage for AISI 4130 CF (a) and AISI 6150 (b).........117

58: Mean Stress vs. Cycles to Failure for AISI 4130 CF (a) and AISI 6150 (b)............120

59: 3D Sketch of Fatigue Specimen for ABAQUS/CAE modeling (all dimensions are in cm) 123

60: 3D meshed Fatigue Specimen for ABAQUS/CAE Modeling..................................123

61: Maximum Bending Stress vs. Applied Bending Moment 124

62: 3D Fatigue Specimen, Visualization of Bending in ABAQUS/CAE 126

63: 2D sketch of Fatigue Specimen for ABAQUS/CAE modeling (Dimensions in cm)...127

64: 2D Fatigue Specimens with cracks 128

65: The three basic modes of fracture: (a) Mode I (tensile opening), (b) Mode II (in-plane sliding), (c) Mode III (anti-plane shear) 129

66: Edge-notched Beam under Bending 130

67: KI vs. Applied Load...131

68: JI vs. Applied Load..132

69: Bending Stress Profiles in the center of 2D cracked Specimens 133

70: Contour Plots of Stress Profiles at crack Region 134

71: Normal and Shear Stresses along surface planes for Fatigue Life Estimation using the Brown Miller Algorithm 138

72: Effect of Morrow Mean Stress on the Fatigue Life of AISI 4130 CF steel, estimated using fe-safe^{TM} 140

73: Surface Finish Factor vs., Surface Roughness and Strength for Steel Component ...142
74: Effect of Surface Finish Factors on the Fatigue Limit of Steels 142
75: Effect of Surface Concentration Factor on Fatigue Life 144
76: AISI 4130 CF Fatigue lives; Comparison of fe-safe^{TM} estimates and experimental results 145
77: Fatigue Life estimates at Ks=1 and different compressive residual stress levels 147
78: Fatigue Life estimates at Ks=1.5 and different compressive residual stress levels 147
79: Estimated Fatigue Life of cracked AISI 4130 CF Specimens 149
80: ABAQUS/CAE straight beam models with center hole (left) and without (right) (Dimensions in mm). Loading and supports are also shown (left) 152
81: Bending Stress vs. Applied Load in AISI 6150 Beam ABAQUS/CAE models 152
82: ABAQUS/CAE visualization of stresses in straight beam models with center hole (a) and without (b) and leaf spring (c)... 154-155
83: fe-safe^{TM} Fatigue Life estimates for 995 MPa Ultimate Strength 157
84: fe-safe^{TM} Fatigue Life estimates for 1630 MPa Ultimate Strength 157
85: Effect of Ultimate Tensile Strength on Fatigue Life if AISI 6150 Steel 158
86: fe-safe^{TM} Fatigue Life estimates for 995 MPa Ultimate Strength with residual stresses at Ks=1.5 160
87: fe-safe^{TM} Fatigue Life estimates for 1630 MPa Ultimate Strength with residual stresses at Ks=1.5 161
88: Flow Lines and Concentration of Stress 164
89: Stress Concentration Regions (circled areas) for welds 165
90: S-N curves for Weldment Fatigue Design (BS 7608 Standard) 166

II. COMPOSITES

91: Laminated Composite 173

92: Unbonded views of anti-symmetric (a) and symmetric (b) cross-ply laminates 173

93: Representation of an angle lamina with the local and principal directions 174

94: Orientation of the fibers of a unidirectional composite along x1 direction 175

95: Analysis Levels of Laminated Structures 177

96: Filament Winding Process 180

97: Compression Molding Process 181

98: Cutting of Leaf Springs..182

99: CLT Plate Geometry 183

100: Nomenclature of Laminae Stacking 185

101: Positive Sign Convention for CLT of Forces (a) and Moment (b)..........................186

102: Maximum normal tensile stress in the x-direction as a function of lamina angle, θ, using maximum stress (a) and maximum strain (b), Tsai-Hill (c) and Tsai-Wu (d) failure theories 193-194

103: Analysis of Laminate Strength 195

104: Dimensioned Sketch of Composite Laminate with Span Length Markings, Dimensions in mm 198

105: Maximum Applied Moment per layer that will cause Failure, for the different stacking sequences and materials examined 200-202

106: Maximum Applied Moment per layer that will cause Failure, for symmetric and anti-symmetric angle-ply, E glass fiber/epoxy laminates 205

107: Sketch of Composite Lamina Plate with Hole, Dimensions in mm 207

108: Detail of Bending Stress Contour Plot around Hole Area 210

109: Maximum Bending Stress per Ply of Symmetric and Anti-symmetric Composite Beams...212

110: General Stacking Sequence: Ply Stack Plot with Ply Fiber Orientation 213

111: Maximum Bending Stress per Lamina of Anti-symmetric 22 Layer General Stacking S2 glass fiber/epoxy Beam..214

112: Principal Stress per Lamina of Anti-symmetric 22 Layer Angle Ply (a), Cross Ply

(b), and General Stacking (c) S2 glass fiber/epoxy Beam 215-216
113: Bending stress profile of AISI 6150 steel and S2 glass fiber/epoxy Beams............217
114: Fatigue Failure Prediction Process Helius: Fatigue and fe-safe^{TM}/composites 221
115: Energy barrier and activation energy required to move from State 1 to State 2......225
116: fe-safe^{TM}/Composites life estimate for S2 glass fiber/epoxy anti-symmetric 2-layerd laminate..229
117: fe-safe^{TM}/Composites life estimate for S2 glass fiber/epoxy symmetric 3-layerd laminate..230
118: fe-safe^{TM}/Composites life estimate for E glass fiber/epoxy anti-symmetric 2-layerd laminate..231
119: Cumulative Distribution of Damage vs. Mean Stress in S2 glass fiber/epoxy (a) and E glass fiber/epoxy (b) 234
120: Mean Stress vs. Life to Failure for S2 glass fiber/epoxy (a), E glass fiber/epoxy (b) 238
121: Experimental Fatigue Test Set-up of Composite Tests Beams................................241
122: Plain Weave Representation 243
123: Development of Damage in Woven Fabric Composites, when Loaded under Quasi-static Tension: (a) Before Loading and (b and c) After Loading.........................245
124: Carbon/epoxy Composite Fatigue Life Curves for Tension-Compression Loading 246

III. HYBRID STRUCTURES

125: Laminar and Interlaminar Hybrid Laminates 252
126: Hybrid Leaf Spring with two separate leaves...255
127: Manufacturing of hybrid leaf spring in compression mold 256
128: ABAQUS Hybrid Beam: Straight Beam (a) Straight Beam with Bent Edges 258
129: Contour Plot of Bending Stress in Hybrid Beam with Bent Edges 259
130: Contour Plot of Bending Stress in Ply 22 of Hybrid Beam with Straight Edges 259

131: Macromechanic Bending Stress in Hybrid Beams 261
132: Micromechanic Bending Stress in Hybrid Beams; Straight edges (a), Bent Edges (b) 263
133: Longitudinal Stress Profiles in Hybrid Beam..267
134: Minimum Applied Moment per layer that will cause Failure 268
135: Experimental Fatigue Test Set-up of Hybrid Tests Beams......................................270

V. COMPARISON OF MATERIALS

136: Cumulative Distribution of Damage of AISI 6150 Steel and S2 glass fiber/epoxy 292
137: Mean Stress vs. Cycles to Failure of AISI 6150 Steel and S2 glass fiber/epoxy 294
138: Fatigue Life of AISI 6150 Steel and S2 glass fiber/epoxy using fe-safe^{TM}.............296

INTRODUCTION

The choice of buying a new vehicle is always based on a variety of factors that emerge from the buyer's everyday needs and reasons for the purchase. As a result the size, horsepower, torque, acceleration, engine capacity, together with aesthetics and design of the vehicle are some of the main topics discussed and researched before the purchase. Safety and comfort also preoccupy the buyer who wants to have full control of his/her vehicle when on the road, and a comfortable ride despite the shape and conditions of the road surface. The latter conditions are based on car suspension, which few perspective buyers care to investigate, but always expect to be of top quality.

The carriage of the car may be the main part of the vehicle that to one's eyes is the major characteristic that distinguishes it among other vehicles, and the engine may be another important vehicle characteristic to those who indulge a little further in the car facts manuals and magazines. However, the chassis is one of the most important parts of a vehicle as it incorporates all vehicle aspects that connect the driver to the road. The chassis, being the bottom part of a car, includes the tires and wheels that let the vehicle move on a surface by maintaining the right amount of friction to keep it on that surface, the steering system that gives the driver control of the vehicle by enabling him/her to drive the vehicle to the desired direction, the frame of the vehicle that gives shape and holds together the vehicle structure while supporting the carriage and engine loads, and finally the suspension system which also works as a load support of the car parts as well as the components that facilitate tire contact with the road surface [1].

Vehicle suspension, therefore, is defined as the system of springs and shock absorbers that support and protect the vehicle against road conditions. The springs compress and extend in order to support the car at every upward and downward movement respectively, while the shock absorbers minimize the unpleasant effects of these movements [1-2]. Depending on the area of the vehicle the set of springs and shock absorbers is found, suspensions are characterized as front or rear. There are various spring types used in suspension depending on the car type, weight and function. The springs belong to one of the following categories (Fig. 1):

- Coil Springs
- Torsion Bars
- Air Springs
- Leaf Springs

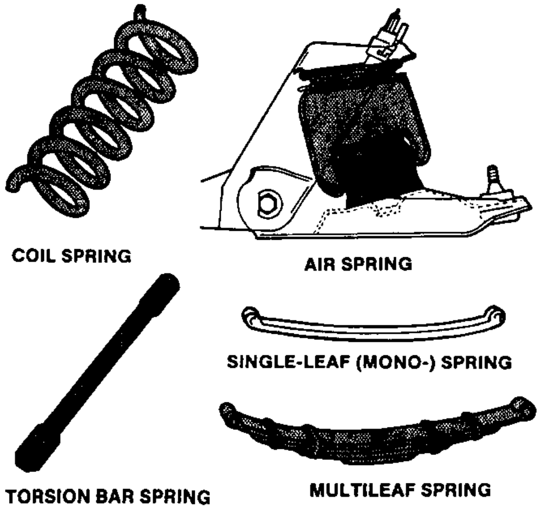

Figure 1: Types of Spring Suspension Systems [1]

Coil Springs are the most widely known and used type of springs. Suspension coil springs have a helical shape, which through their compression and extension absorb the shocks and maintain equilibrium between the tires and the road. A coil springs suspension system is used in most passenger cars nowadays [1].

Torsion Bars are mainly used as front suspension in late pick up truck and SUV models. They differ from the above spring type on the way they absorb, store and release energy. Torsion bars do not compress or extend, instead they twist and straighten in order to absorb road shocks. Similar to coil and leaf springs, torsion bars are made of heat-treated alloy steel [1].

Air Springs (also referred to as air suspensions) are also used in the same manner and sometimes in place of coil springs. Made of a reinforced rubber bag containing pressurized air, air springs compress and extend due to changes in the air volume they contain. Air springs provide the most comfortable rides to the driver, mainly because of them having a variable spring rate [1].

From the 19th century carriages to the 1970s cars, leaf springs were the main suspension system used [3]. Today leaf springs are used in heavy-duty vehicles, railroad carriages and many SUVs, while with the introduction of front wheel drive cars [4], leaf springs in passenger cars have been replaced by coil suspension [1]. Leaf springs are beams of high deflection [4] that can be used individually as a single leaf, or in stacked assemblies of up to twenty leaves, as multi-leaf [1,5], depending on the type of the vehicle to be used on. Multi-leaf assemblies are more common than a mono-leaf (a single leaf spring), especially in cases where the vehicle load is very high. The multi-leaf assembly is composed of different length leaf springs tied together either at the center, the ends, or both, depending on the type of vehicle they are designed for, with different types of fasteners. The main, or first leaf is the longest and is positioned at the bottom of the assembly, followed by progressively shorter leaves on top [1,5]. Some multi-leaf assemblies have a smaller "extra", multi-leaf assembly, the helper leaves (Fig. 2) in order to provide a larger spring rate [5]. Leaf springs are shaped in the form of an arc, and therefore many times are referred to as semi-elliptical springs [1,4-5]. They are of rectangular cross-section and although originally manufactured at constant thickness, sometimes varying width, a more advanced modification is the parabolic leaf spring, which still has a rectangular cross-section but while width is in most cases kept constant, thickness varies. In the first type of springs the maximum width occurs in the middle of the beam, while this is the case for the maximum thickness in the parabolic design [5].

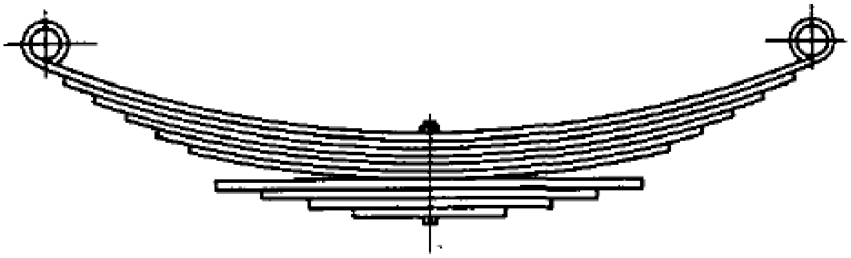

Figure 2: Multi-leaf spring with helper leaves [5]

As mentioned above, suspension systems employ the basic characteristic of springs to absorb, store and release energy. As the spring goes through these stages the stresses in the spring do not remain constant. As the leaf spring is loaded it bends in a manner resembling part of the arc of a circle. The surfaces of the leaf spring will, therefore, change in length and the outer/top surface will be longer than the inner/bottom surface. The outer surface is said to be in tension while the inner in compression, therefore a stress is induced in the beam [4-5]. If this stress overcomes a maximum value dictated by the material and geometry of the spring, failure of the structure will result. Therefore, each spring is designed with a maximum stress capacity it can store [5].

Leaf springs are manufactured in such a way so as not only to be employed as springs but they have all the appropriate parts to be positioned and attached to the chassis for a proper suspension system. As a result, many leaf springs have their ends curled in a round shape, called the “spring eye” (Fig. 3), which enables the leaf spring, or multi-leaf spring, to be attached to the chassis. The eyes, fasteners, bolts, and other components that enable anchorage of the leaf spring to the vehicle, are the “inactive” parts of the leaf spring as they do not perform as an energy absorbing, storing and releasing device themselves. The rest of the spring assembly is the actual spring, and is termed the “active” part of the leaf spring [5]. As a result, the total mass of the leaf spring is not fully utilized as a spring, which puts leaf springs in a more disadvantageous situation when compared to other types of springs, especially coil springs, because the former are heavier limiting the amount of energy stored in the spring at a maximum stress level. On the other hand this disadvantage is overcome by the design of leaf spring assemblies to incorporate in their shape the appropriate mounting parts, and the fact that they can be used in applications different than those of suspension systems, such as attaching linkages or structural members [5]. For that reason, engineers and leaf spring designers have tried to design leaf springs in such a way so as to minimize their weight and make full use of their advantages. For this reason, multi-leaf suspensions have leaves of progressively shorter lengths in order to make the assembly lighter. A modification to leaf springs, leading to weight economy, is parabolic leaf springs having a varying thickness throughout the leaves. Parabolic leaf springs are more commonly used today, especially in vehicles where total vehicle weight minimizing is essential [4-5].

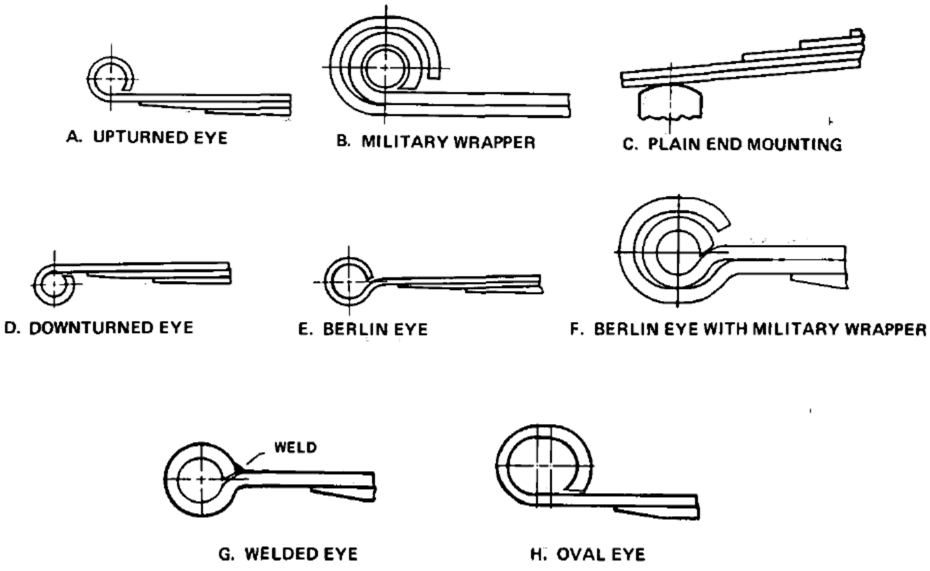
A. UPTURNED EYE
B. MILITARY WRAPPER
C. PLAIN END MOUNTING
D. DOWNTURNED EYE
E. BERLIN EYE
F. BERLIN EYE WITH MILITARY WRAPPER
G. WELDED EYE
H. OVAL EYE

Figure 3: Various Spring Eyes and Ends [5]

The spring rate and static deflection of a spring are of the most determining characteristics of suspension springs [5]. The spring rate is the change in load per unit of deflection, and static deflection is the distance the spring deflects under the static load, and is calculated when the static load is divided by the spring rate at this load [2,5]. The area under the load-deflection diagram (Fig. 4) is the energy stored in a spring at a maximum stress, but also represents the required mass of the spring. Therefore, there is a connection between the maximum allowable stress in the spring and its mass, which declares mass and energy stored as inversely proportional to that stress. Consequently, the energy stored in a heavy leaf spring at a certain maximum stress is less than that stored in a lighter spring at the same stress [5].

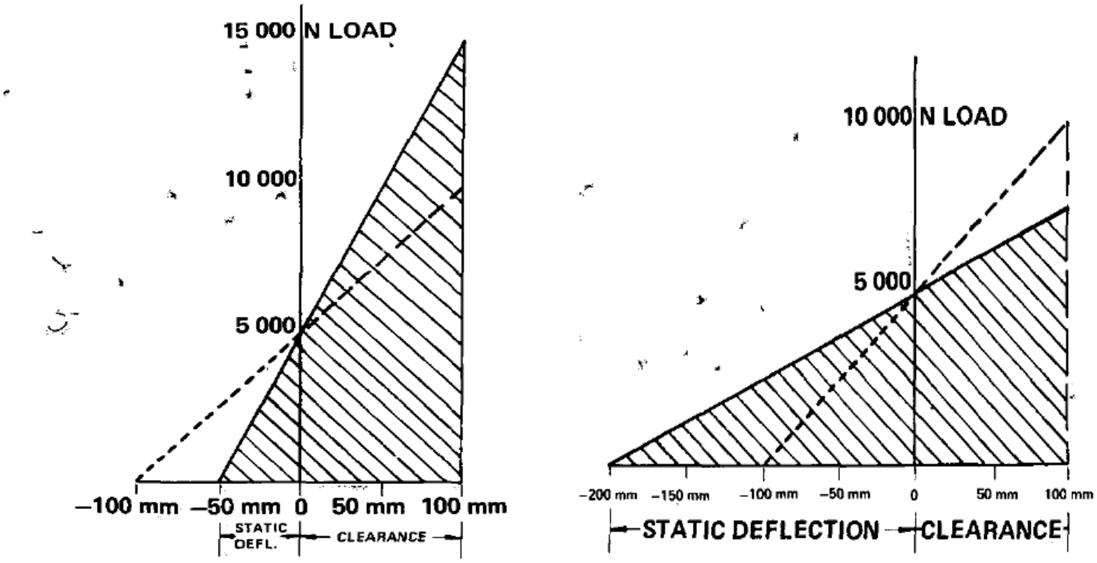

(a) **(b)**

Figure 4: Load-Deflection Diagram: (a) stiff, high rate spring with small deflection, (b) flexible, low rate spring with large deflection [5]

Springs, as many structures destined for loading applications, are designed to operate at a load level that will cause stresses below a maximum stress level, which may result in failure of the spring. The maximum amount of load the leaf spring can sustain is called the *design load* [5]. When the leaf spring is mounted on a vehicle, depending on the road conditions, the spring will support a load and according to this load will deflect a certain distance. The maximum possible of this distance, if the leaf spring is properly designed, will occur below the *design load*. The difference between this distance and the spring's deflection at the condition when the maximum stress is reached is called *clearance* [5]. When the load-deflection diagram for a spring is created, the deflection axis may be separated into two regions; on the left side of the origin is the *static deflection* region, and on the right hand side is the *clearance* region (Fig. 4).

Stiffness, as the mechanical property measuring the resistance of an elastic component to deformation, is a parameter that needs to be considered when discussing springs. Since spring rate relates the leaf's deflection to the applied load, it should also be influenced by the material's stiffness. A stiff spring will have a high spring rate, as more load should be applied to deflect the spring. By the same token, a flexible, less stiff spring, will have a lower spring rate (Fig. 4) [5].

The traditional and contemporary mainstream leaf spring material is steel. Many different grades of steels are used in the manufacturing of leaf springs, differing in the carbon content and alloying elements. The weight percent content of carbon or other elements, depends on the type of leaf spring manufactured, whether it is of constant thickness or parabolic, the vehicle type, the manufacturing process and many times the price of raw materials. Chromium and Silica are some of the most common alloy elements in the raw steel material, while medium carbon steel (0.30-0.60%C) is usually utilized [4]. Since stiffness variation, as measured by the Young's Modulus, is negligible among different steel grades, the desired stiffness and consequently spring rate of the leaf spring is determined by the design of the spring. Parabolic leaf springs are lighter and more flexible than multi-leaf springs of constant thickness [4-5].

In the automotive world there is constant research for the improvement of various aspects of a vehicle. Minimizing the weight of the vehicle and enhancing passenger safety and comfort are some major areas that concern car manufacturers. Improving leaf spring design and choice of materials for these leaves, can greatly affect these concerns. In the early 1980s the British automotive company GKN [6] started developing a composite leaf spring, aiming for a lighter yet stronger alternative to the conventional steel leaf springs. Similar developments were realized for racing and sports cars, such as in the case of Chevrolet who was among the first car manufacturers to incorporate composite leaf springs in passenger cars. The Corvette sports model has composite suspensions that render the vehicle much lighter [7]. Comfort is also maximized especially in sports car where the passengers are in closer contact to the road surface [1].

The composite materials used in the manufacturing of composite leaf springs, as suspension systems are known as Glass Fiber Reinforced Plastics (GFRP) [1,6-7]. A GFRP, many times referred to as fiberglass, is a composite material of two constituents, a polymer matrix reinforced by glass fibers [8]. Although glass fibers may come as long strands in a roving, or in the form of woven cloth, the composite leaf spring manufacturers prefer the long strands that they then impregnate in a polyethylene matrix [9-10]. Depending on the manufacturing process, filament winding or compression molding, unidirectional pre-impregnated fibers in polyethylene epoxy may be used [9]. Composites weigh less than metals and have high strength and stiffness [8,11], and as a result, they become a good alternative to steel for the manufacturing of leaf spring suspension systems, as they help in minimizing the total weight of the vehicle [1,7], which may also have an effect in the comfort of the ride, fuel economy and emissions. Past research has shown that fiber reinforced plastics (FRP) used to manufacture leaf springs have given satisfactory results while minimizing the weight of the leaf up to 85% [12-14]. Commercially, composite leaf springs are used in vehicles where a low weight carriage is crucial, as well as comfort of the passengers, for example in sports cars [1,7]. If a leaf spring can combine the desirable design properties of stiffness and low weight, while maintaining good strength, it is worth looking into the reasons why composite leaf springs have not yet conquered the suspensions aftermarkets.

As mentioned above, it is always desirable to minimize the vehicle's weight, and consequently that of its suspension. Since mass, as well as energy stored, is inversely proportional to the stress induced in the spring, if the leaf spring operates under a high stress, the mass of the spring will be low. This mass can be minimized as the stress is increased, but care should always be taken for this stress not to be destructive for the spring. Based on the *SAE manual on design and application of leaf springs* [5], there are three factors that limit this stress: the settling under the applied load, which usually occurs during the first few cycles of the cyclic loading operation of the spring at high stresses, the fatigue life of the spring, and finally the quality and processing of the material used for manufacturing the leaf spring. From the three factors mentioned above, which affect the operational stress of the leaf spring, this research will discuss that of fatigue life.

The fatigue life of four different materials will be discussed in the following pages. The fatigue lives of AISI 4130 CF and AISI 6150 steels will be compared to S2 and E glass fiber/epoxy composites, in order to determine whether a GFRP is suitable for operation as a leaf spring in a vehicle suspension system. To arrive to the results of this comparison, the effects of steel grade and processing during leaf spring manufacturing on the fatigue life of a leaf spring will be presented. In addition the difference between the failure mechanisms of the two types of materials, the steel and the composites, will also be discussed.

In more detail, in Part I the first section will discuss the manufacturing process of steel leaf springs paying close attention to the heat treating and surface finish stages of the process. Section I.2 will present different approaches to estimating the fatigue life of metals. The effect of the processes, presented in section I.1, on the fatigue life of the leaf spring will be presented in section I.3 through experimental results. A cumulative damage analysis based on three damage models as developed by Palmgren and Miner, Broutman and Sahu, and Hashin and Rotem, will show how damage accumulates in the two steel materials per loading cycle, and how the fatigue life of the material can be approximated using these models (section I.3.2). Section I.3.3 will discuss finite element analysis results using ABAQUS/CAE and fe-safe^{TM}. The part on steel will be concluded by a brief discussion of the available methods of repairing leaf springs, and their effectiveness (section I.4), and primary conclusions (section I.5).

The second part of this thesis will discuss the two GFRPs, E glass fiber/epoxy and S2 glass/fiber epoxy. Section II.1 will discuss the concept of composite materials, their advantages and disadvantages. In section II.2 the two main manufacturing processes for composite leaf springs will be introduced. Due to the anisotropic and inhomogeneous nature of composites there is a need to develop new theories that will help evaluate different composite properties. The Classical Lamination Theory (CLT) will be presented in section II.3 to introduce a computational analysis of composite laminate failure (section II.4). Section II.5.1 will discuss three different stacking sequences for the leaf spring laminates, and using failure analysis will decide upon the optimum sequence. Due to the laminar nature of the composites that preoccupy this research, an analysis of the composite as a structure, as well as an assembly of smaller structures is important in order to understand how composite material components behave under loading and failure. Simulations of the fatigue life of both composites will be carried out using fe-safe^{TM} in section II.5.1. Furthermore, using the three damage models mentioned above, and experimental data from literature, a discussion of how damage accumulates in each of the two composites will be presented, and the fatigue life of each of them will be theoretically calculated and compared to experimental data in section II.5.3. The above analysis will be accompanied with experimental data on composite beams in section II.5.4. The way laminated composite leaf springs may be repaired will follow (section II.6), and conclusions on Part II will be given in section II.7.

Part III of this research will discuss a combination of composite and steel materials for the construction of hybrid structures, which is also a new alternative to steel leaf springs in the automotive industry. An introduction to hybrid laminates and hybrid leaf springs will be given in the first two sections of this part, followed by failure prediction using failure theories and life prediction through experimental results (section III.3).

Concerning the case study of leaf springs, and the reasons for which composite materials would be a good alternative for the manufacturing of these products, an economic analysis will be given in the fourth part. A comparison of the costs of the two different production lines, for composite and steel leaf springs, will be presented.

Finally, based on the information gathered from the first four parts of this thesis, an attempt to select the ultimate materials and/or structure for applications similar or identical to suspension requirements will be made in the fifth part.

I. STEEL

I.1 Leaf Spring Manufacturing Process

Whether the suspension system requires a single semi-elliptical spring or a multi-leaf assembly, each leaf spring is produced individually. The raw material of the steel alloy is purchased in the form of long flat plates. A first step in the manufacturing process of leaf springs is to cut these plates into the desired length of the leaf spring. Cutting of the flat plates is the first step of the manufacturing process and is done with cutting equipment, the saw. Depending on how the leaf spring will be mounted on the vehicle, and whether it is going to be part of a multi-leaf assembly, a center hole will be punched into the center of the flat plate, which may be of circular or elliptical circumference, depending on the spring model. The center hole punching is done at a punching machine, which drives a hot die through the center of the plate creating the hole. Again based on the type of suspension, the ends of the leaf spring will be processed on the next step. The ends may be trimmed, tapered, cut in width or formed in a curled shape called the eye. Other suspension systems require bent ends of the leaf spring, or punched holes at the end for assembly mounting purposes. The above end formations may require hot or cold processing and are part of the end-forming step, the third step of the manufacturing process of a leaf spring [15].

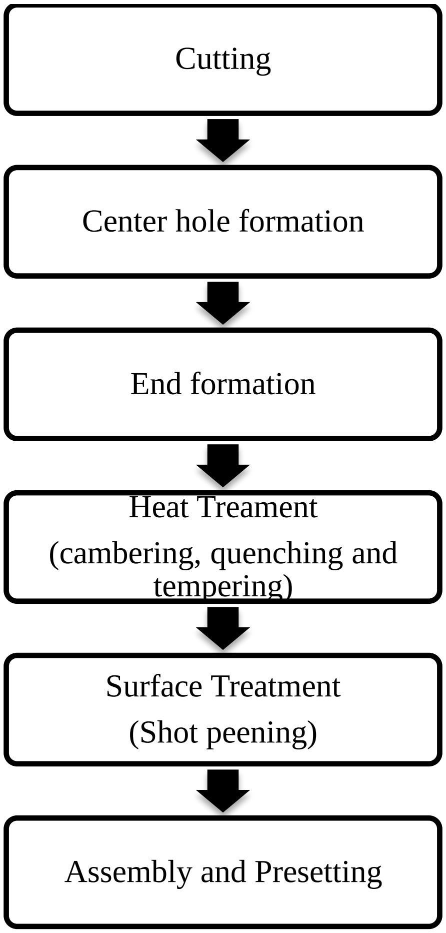
Cutting
Center hole formation
End formation
Heat Treament
(cambering, quenching and tempering)
Surface Treatment
(Shot peening)
Assembly and Presetting

Figure 5: Steps of Steel Leaf Spring Manufacturing

The next two steps (Fig. 5) in the manufacturing process are the most important in the production line of leaf spring manufacturing, as they have a direct effect in the fatigue life and strength of the end product. The first of these two steps is the heat treatment process. During heat treating the leaf spring will first be given one of its characteristic aspects of its shape, its arc shape called the camber. The process of cambering, involves heating the leaf spring to a very high temperature, which varies among the steel grades of the raw materials, but is usually close to 950°C [15]. Depending on the thickness and length of the leaf spring, as well as the properties of the raw material, the leaf will be placed in an oven for a certain amount of time until it becomes red in color and ductile enough to be bend to a desired shape. The red-hot leaf will then be placed in a cambering chamber (Fig. 6), which will clamp it and bend it to the desired arc radius. Depending on the leaf spring type to be manufactured, cambering stations will vary in arc radii. The leaves of a multi-leaf assembly do not always have the same camber [4-5,15]; as a result the cambering station should have a variety of chambers to cover the desired cambering arcs for manufacturing a range of products, or these chambers should have the possibility of adjusting to the required dimensions for a full range production. The leaf spring securely positioned in the cambering chamber is immersed in an oil bath at room temperature and undergoes quenching. It is then tempered in an oven under a certain temperature (750-850°C depending on the steel grade and leaf dimensions) and for a certain time considering the properties that the end product should have [15-16].

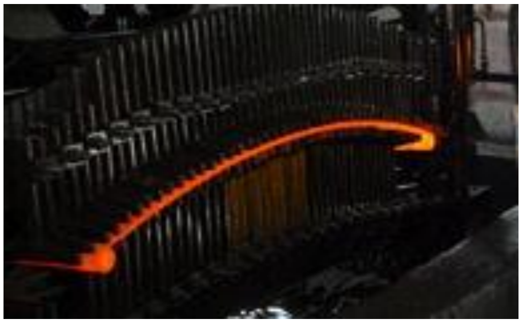

Figure 6: Cambering station with leaf spring ready for quenching [17]

Surface treatment follows heat treatment. The surface of the leaf spring is conditioned using a peening treatment and painting [5,15]. The peening treatment can be either *shot peening* or *stress peening*. During the peening process, which in steel leaf spring manufacturing is a cold work process, a metal surface is bombarded with a metal spherical medium, the shot, in order to improve the material properties of the metal’s surface by inducing compressive residual stresses to that surface [5,16,18]. The difference between shot peening and stress peening is that during the second process the leaf spring is loaded, most often in the tensile direction or the direction of the subsequent loading application, while it is being shot peened [5,19]. Stress peening is a more recent procedure, which gives better results, while however, increasing the cost of the end product. Although, both procedures are used in the manufacturing world, shot peening, for economic and time reasons, is still more widely used in the industry world [10]. Fig. 6 shows the effects of the two peening procedures for the induction of compressive residual stresses on a leaf spring [5]. Shot and stress peening, apart for the induction of residual stresses, also clean the leaf spring surface from any quenching oil residues and prepare the leaf for painting [20]. Painting, usually carried out in a spray-painting chamber, gives an aesthetically pleasing finish to the spring, enables for the leaf spring model and manufacturer’s logo to be stamped on the leaf, but above all protects the metal from corrosion and similar environmental effects [5,15].

Following the surface finish step is the process of eye bushing preparation and the assembly step. In the former process, if the leaf spring has an eye end, the appropriate bushings will be placed in the eye to enable mounting of the leaf spring on the vehicle, as well as any required processing of the eye or bushing such as reaming and boring. The assembly step, is the final step of the manufacturing process, during which the multi-leaf springs are assembled and fastened together, any presetting and loading tests are carried, and finally any touch up painting, if required, such as company logo placement, will be done. Finishing this step the leaf springs are practically ready for the aftermarket [15].

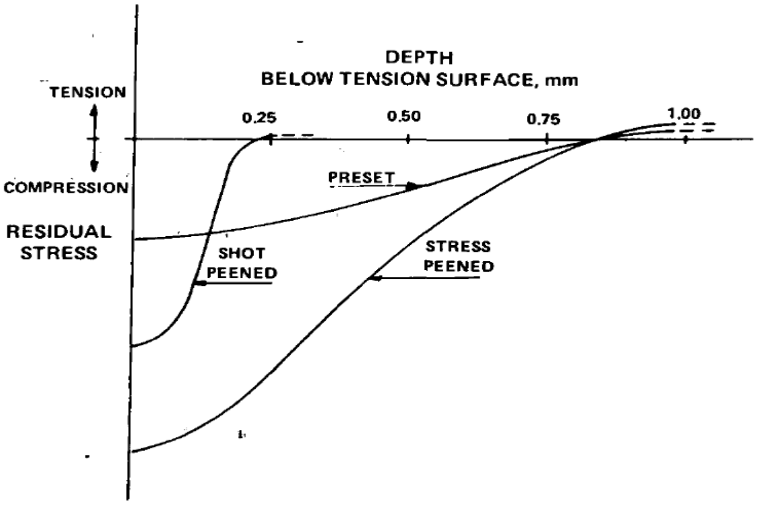

Figure 7: Stress patterns due to shot peening, stress peening and presetting in the absence of carburizing [5]

The leaf spring assemblies will face one more process that will affect their fatigue life, and this is presetting. The leaf spring assemblies are preset under a certain load, in order for the leaves to take the appropriate form and direction appropriate to the final application. Presetting induces compressive residual stresses to the tension surface of the leaves, and tensile residual stresses to the opposite surface, the compression surface of the leaves. Presetting will also alter the curvature of the leaf spring. Despite the tensile residual stresses, presetting has a positive effect on the fatigue life of the leaf spring assembly (Fig. 7) [5, 21].

I.1.1 Heat Treatments

As the name heat-treating implies, and as described in the previous section, this step involves heating the metal piece at very high temperatures and then quenching it rapidly in an oil bath at a much lower temperature, followed by raising the temperature to a high level and keeping it constant for a certain length of time during the tempering stage of the treatment. The three stages of the heat-treating step have as the ultimate goal to improve the hardenability of the steel material, by creating a martensitic layer below the surface of the steel leaf spring [22-23].

Martensite is an iron alloy phase, due to which steel can demonstrate very high levels of strength. Martensite does not exist in the steel alloy from the beginning, as it is a non-equilibrium iron alloy phase [24]. As a result, for martensite to exist in the microstructure of steel, some processing of the steel is required.

The steel grades used as raw material by leaf spring manufacturers have in the majority of cases a carbon content between 0.5-0.68%C [5]. Looking at an iron-iron carbide phase diagram (Fig. 8, it can be seen that the leaf spring steels, also referred to as spring steels, have a carbon composition below the eutectoid point, and therefore are called hypoeutectoid steels [16]. At temperatures below the eutectoid temperature of 725°C, the phases present in the microstructure of these steels are two: ferrite (α) and cementite (Fe_3C) (Fig. 8). The most common microstructure of steels formed below the eutectoid temperature is pearlite [24]. Ferrite is a product of the solid solution of carbon in BCC α-Fe, and cementite is an orthorhombic unit cell containing 12 Fe and 4C atoms. Pearlite is composed of both ferrite and cementite in a lamellar structure [23-24]. At the range between 725°C to 912°C, referred to as the upper critical temperature [16], and after the pearlite structure has lost all traces of cementite and ferrite, the sole phase of the steel microstructure is austenite. Austenite is an interstitial product of solid solution of carbon in FCC γ-Fe, where carbon atoms occupy the interstitial sites of the FCC unit cell of the γ-Fe atoms [24]. The process of heating steel to a high enough temperature, is called austenization [16], and is the first stage of the heat treatment step of the manufacturing process of leaf springs during which the leaf is heated to a red-hot color. The austenization temperature of steels depends on the carbon content of the steel grade used, and from the diagram of Fig. 8 for 0.5-0.68%C the austenization temperature is approximately 850°C. The austenization temperature also depends on the content of the steel in alloying elements [16].

As mentioned before, the microstructure of steel at room temperature contains the two phases of ferrite and cementite, mostly in the form of pearlite in hypoeutectoid steels. Ferrite and cementite will, therefore, have a certain content of the carbon and other alloying elements, which may not be the same in the two phases [16]. As these two phases transform to austenite when steel is raised to the austenization temperature, the content of carbon and alloying elements is not uniform in the austenite formed. As a result, it becomes important to homogenize the content of these elements in austenite before proceeding with the rest of the heat treatment steps. The process of homogenization becomes therefore, a sub-process of austenization during which a homogenized content of carbon and alloying elements in austenite is attained. The process of homogenization is a diffusive process based on temperature and time. Grain growth is affected by the austenization temperature, therefore, great care should be taken in choosing the right temperature and duration for homogenization, in order to avoid rapid grain growth, which may have a negative effect on the toughness of the material [16]. As a result, homogenization and grain growth should be taken into account in order to choose the appropriate austenization temperature, as well as the steel's carbon and alloying elements content. The *Heat Treater's Guide: Practices and Procedures for Iron and Steels* suggests as typical normalizing temperatures for AISI 4130 steel 900°C and 870°C for AISI 6150 steel [25].

When the steel microstructure has been fully austenized and is composed of a homogeneous content of carbon and the rest of the alloying elements, the next step of the heat-treating stage of manufacturing follows. This is the step where austenite is cooled to create martensite.

In the manufacturing process of leaf springs the step that follows heating the leaf to a high temperature, is oil quenching. Cooling the austenitic steel to an oil bath at room temperature dictates a very rapid cooling rate, i.e. the temperature of the austenized steel drops by hundreds of degrees per second [25]. Following a phase diagram, as the one of Fig. 8, cooling austenized steel should change the steel's microstructure back to pearlite. However, if the cooling rate is very fast, the austenite will become unstable as the temperature drops, and due to rapid cooling the typical diffusion-controlled transformation to pearlite will not occur. Instead a diffusionless transformation will take place, during which the crystal structure of austenite changes, and martensite is formed [16].

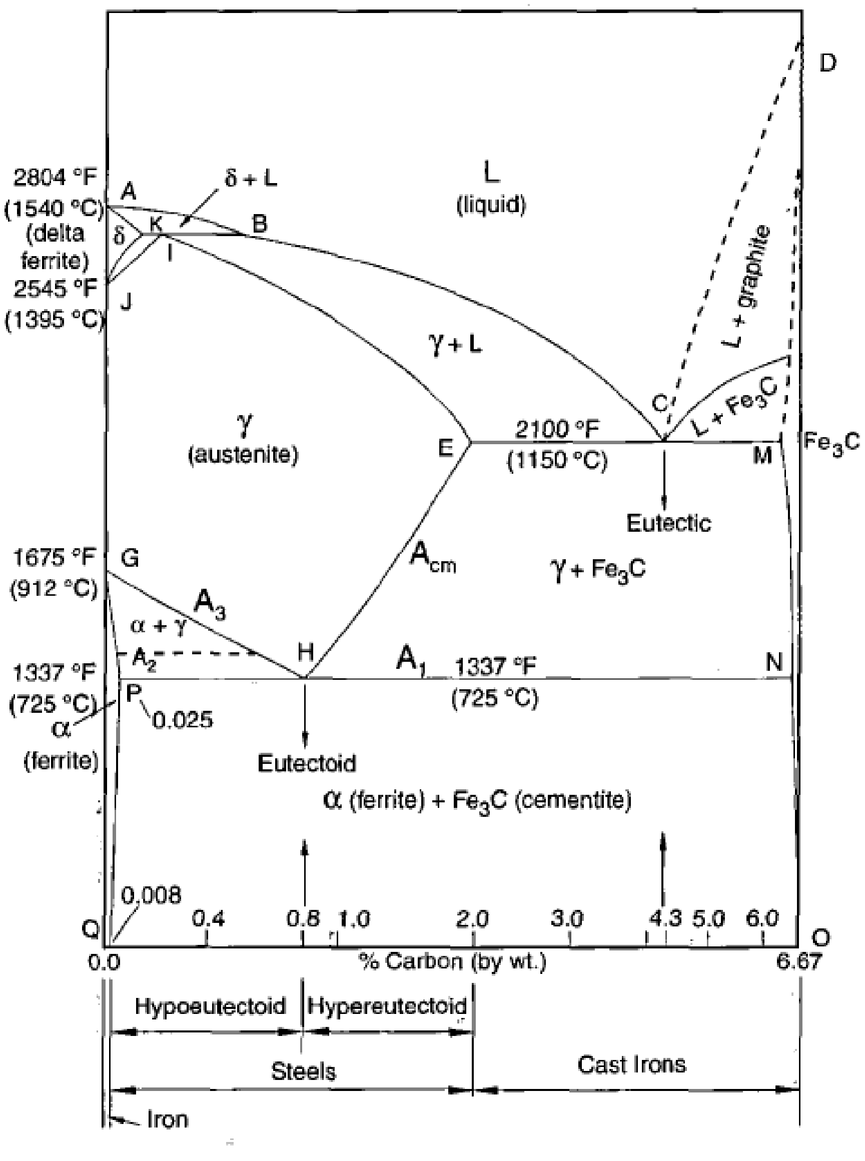
D
2804 °F
(1540 °C)
A
δ + L
L
(liquid)
(delta
ferrite)
δ
K
B
I
2545 °F
(1395 °C)
J
L + graphite
γ + L
L + Fe₃C
C
γ
(austenite)
E
2100 °F
(1150 °C)
M
Fe₃C
Eutectic
1675 °F
(912 °C)
G
A_cm
γ + Fe₃C
A₃
α + γ
A₂
H
A₁
1337 °F
N
1337 °F
(725 °C)
P
0.025
(725 °C)
α
(ferrite)
Eutectoid
α (ferrite) + Fe₃C (cementite)
0.008
Q
0.4
0.8
1.0
2.0
3.0
4.3
5.0
6.0
O
0.0
% Carbon (by wt.)
6.67
Hypoeutectoid
Hypereutectoid
Steels
Cast Irons
Iron

Figure 8: Iron-carbide phase diagram [16]

As mentioned above, martensite is a non-equilibrium alloy phase and this is why it does not exist on the phase diagram of iron carbide (Fig. 8). Such phases are called *metastable*, as an example bainite is another one of these phases [16]. Martensite forms because the FCC structure of austenite cannot transform into a BCC ferrite structure (Fig. 9). The reasons obstinating this transformation depend on the high carbon content of the austenitic steel, which is much higher than the allowable amount of carbon content that can dissolve in ferrite. The resulting structure, martensite, has a body-centered structure that is tetragonal (BCT) (Fig. 10) instead of cubic (BCC). The extent to which the crystal structure distorts is dependent on the carbon content of the steel [23-24].

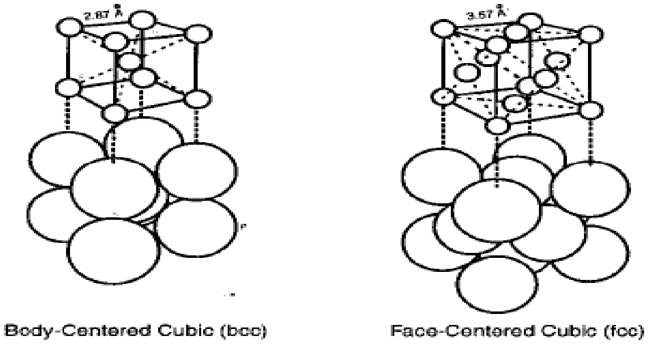

Body-Centered Cubic (bcc)

Face-Centered Cubic (fcc)

Figure 9: BCC and FCC crystal structures of iron [16]

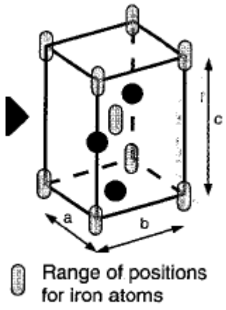

Figure 10: BCT crystal structure of iron [16]

During the quenching process, the cooling rate of the steel component is not uniform throughout the component's cross-section. The cooling rate is proportional to the thickness of the leaf [16]. The first part of the leaf spring to cool during quenching is the outer surface of the leaf. The inner layer towards the core cools due to conduction. As a result, the thicker the leaf the lower the cooling rate of the core, and the higher that of the surface. This difference in cooling rates, results in different microstructures of the surface and the core, and as a result different properties of these parts of the leaf [16,26]. This variety of microstructures and the thermal contractions, are responsible for the induction of residual stresses in the leaf, which can affect the performance of the leaf spring [16-18,27-28].

The residual stresses induced in the steel because of the quenching process, and the distortion of the crystal structure of martensite, are the reasons why quenched steels have very high hardness and strength, while on the other hand demonstrate poor ductility and low toughness [16]. The hardness of the martensitic steel is dependent on the microstructure of the steel, its carbon content and presence of alloying elements [16].

Depending on the carbon and alloying elements' content in the steel the temperature that triggers the transformation of austenite to martensite may vary. The same applies to the temperature at which all austenite has been completely transformed to martensite [16]. These two temperatures are the martensite start (M_s) and martensite finish (M_f) temperatures, respectively [16,29]. A general rule is that the carbon content is inversely proportional to M_s and M_f, and alloying elements, with the exception of Cobalt (Co), decrease these two temperatures [16,23]. As austenite transforms to martensite, during quenching, there is always the risk of the generation of cracks or distortion of the material. These undesirable effects are due to the large temperature gradients that develop in the steel component during the cooling process. To avoid such detrimental for the component effects, the cooling rate between the start and finish martensite temperatures should be low. However, a high rate is required above the M_s temperature to make sure that all austenite will transform to martensite. To regulate these rates, and avoid the undesirable cracking and distortions, the quenching medium should be chosen with care, and detailed examination of Continuous Transformation (CT) curves for the materials, and the cooling curves of the quenching mediums should take place. Oil quenchants are preferable and currently used in the quenching stage of leaf spring manufacturing.

Due to its BCT structure and the compressive residual stresses induced in the martensitic leaf spring, the leaf is brittle and has low toughness [16]. As a result, although the structure has a high strength and hardness, it is prone to brittle failure. Consequently, further processing is required to render the material appropriate for load carrying, cyclic applications. Heating the leaf to a relative low temperature, and keeping it at that temperature for a defined time interval will further alter the microstructure of the leaf spring metal. In the beginning of this process the strains produced during the martensite phase formation are relieved [27] followed by the diffusion of carbon in the BCT martensite. This results in the formation of small carbides in the martensite [16]. In the case that the quenched steel microstructure contains traces of retained austenite, tempering will allow their decomposition into carbide and ferrite. The carbides first formed in the steel are metastable and as heating is extended to a higher temperature, these non-equilibrium carbides transform to cementite, which is a stable phase [16]. During this heating stage the distortion of martensite is reduced, and the release of the internal strains reduces the induced stresses in the material's microstructure. This results in a more ductile and tougher leaf spring, although some of the hardness, strength and wear resistance characteristics of the leaf spring are sacrificed [16]. This last step of improving hardenability is tempering. This is also the third stage of the heat-treating step in the leaf spring manufacturing process. Tempering times and temperatures can be regulated in order to achieve the desired mechanical properties of the component in question [16]. The effect of tempering steel on the stress strain relationship of steel is shown in comparison to quenched steel in Fig. 11.

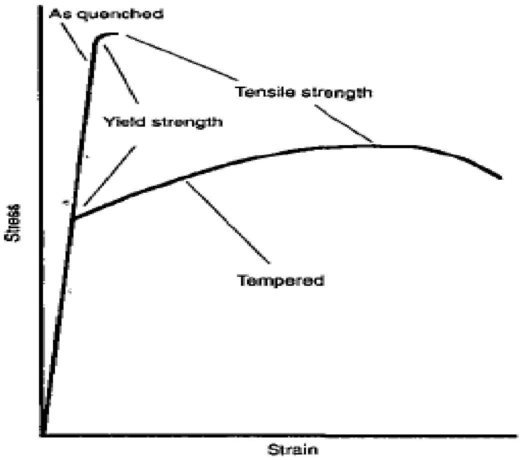

Figure 11: Effect of Tempering on stress-strain relationship [30]

I.1.2 The Role of Carbon Content and Alloying Elements

Steel grades used as raw materials by leaf spring manufacturers have different carbon contents, ranging between 0.5-0.68%C [5] as previously discussed, but also different alloying elements at different concentrations.

Carbon is the main element in steel. It is the element that enables the heat-treating processes to start and be completed due to the fact that carbon is more soluble in austenite than ferrite. It is responsible for the metals' strength, hardenability, ductility, toughness and other mechanical properties that define how easily the steel can be machined and processed. The carbon content of steel is proportional to the properties of strength and hardenability, and inversely proportional to ductility, toughness, workability, and other properties determining processing of the material [16].

The choice of the rest of the alloying elements in steel depends on the desired microstructure and properties, as well as processing of the alloy metal, as in heat treatments, especially tempering [16]. As mentioned above, alloying elements may lower the start and finish martensite temperatures, but will also affect the tempering rate of martensite by affecting the type of carbides formed [23]. Alloying elements, such as chromium (Cr) and cobalt (Co), increase hardenability, as they influence the carbon diffusion, lowering it due to their atom interactions with the carbon atoms. This way, there is more time for the formation of ferrite and pearlite. Alloying elements can therefore be chosen in such contents so as to regulate the properties of the metal and result in steel of high hardenability and good strength and toughness

[16]. Table 1 is a summary of the most common alloying elements and impurities in leaf springs steels, and their role in the steel alloy [31].

Table 1: The role of Alloying Elements and Impurities in Steel

Alloying Elements	
Chromium (Cr)	Provides solution strengthening to ferrite, increases hardenability in medium carbon steels, and is responsible for the strength and oxidation resistance of steels at high temperatures. At high concentration above 11.5% its reaction with oxygen, protects the steel from corrosion and oxidation, and becomes the basis of stainless steels.
Manganese (Mn)	Present in the majority of commercial steels to prevent sulfur embrittlement due to the sulfur impurity presence. Responsible for the strength of steel, as it solution strengthens ferrite and refines pearlite. Increases hardenability. For contents above 2% increases steel embrittlement.
Molybdenum (Mo)	Solution strengthens ferrite, and enables carbide formation. Usually present in steel together with chromium and nickel. Improves hardenability, especially in high carbon steels. Operates as a barrier to temper embrittlement, induces secondary hardening during tempering of quenched steels.
Nickel (Ni)	Increases hardenability, especially in medium carbon steels. Responsible for the increase in notch toughness. Usually used in combination with chromium in steels to obtain high hardenability, impact strength and fatigue resistance.
Vanadium (V)	A strong carbide former, better than Cr and Mo. Affects positively grain refinement and secondary tempering during tempering. Responsible for the strength and toughness of the alloy, forms carbides that provide wear resistance and high temperature strength to the steel.
Impurity Elements	
Aluminum (Al)	Helps control grain size, especially that of austenite in reheated steel.
Phosphorus (P)	Has similar detrimental effects as S, and its combination with iron to form iron phosphide reduces steel toughness. During heat treatment, it segregates and becomes responsible for temper embrittlement. On the other hand, it may work as an iron hardener.
Silicon (Si)	Similar to Al, Si works as a deoxidizer. Its combination with oxygen enables the formation of silicates, which in turn prevent porosity of steel.
Sulfur (S)	A dangerous impurity present in steels. Its combination with iron towards the formation of iron sulfides is responsible for steel cracking in cold and hot working processes.

I.1.3 Residual Stresses and Residual Stress Relaxation

In the preceding discussion the term “induced residual stress” has been mentioned in relation to heat-treating (quenching) and shot peening processes. As a metallurgical term defined in CASTI Metals Black Book, a residual stress is *a stress present in a body that is free of external forces or thermal gradients* [16]. Residual stresses may be either compressive or tensile, and depending on the material and its applications may have a beneficial or detrimental effect on the component’s performance [16,32].

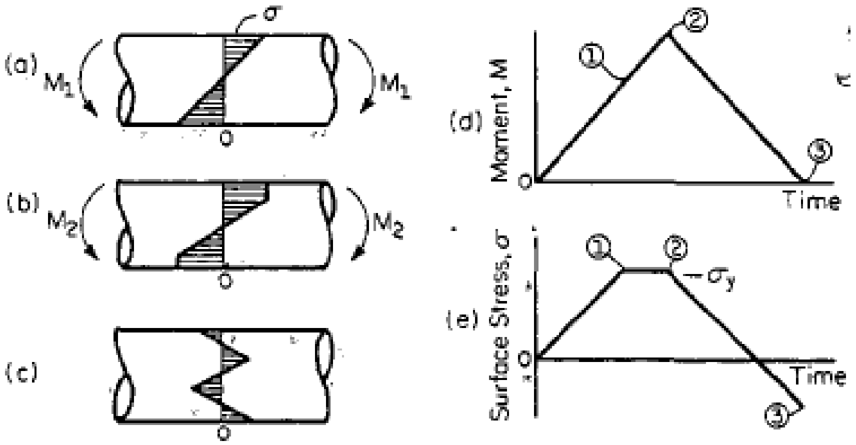

Figure 12: Residual Stresses in unotched beam under bending [21]

Fig. 12 shows an unotched beam of circular cross-section made of an elastic-perfectly plastic material, and subjected to a bending moment of varying magnitude [21]. The stress profile at two different moments is shown in diagrams (a) and (b). From the moment versus time graph (diagram (d)), it is obvious that the first bending moment is of lower magnitude than the second, while the beam is completely unloaded at point 3 on the graph. Diagram (a) shows that the stress profile in the beam is linear.

As the moment is increased the surface of the beam starts to yield, and this is obvious from the stress profile in the beam as shown in diagram (b) of Fig. 12. As the moment is reduced to zero magnitude, there is still a stress distribution in the beam (diagram (c)) that of the residual stress. Diagram (e) of the same figure, is a graphical representation of the beam's surface stress versus time. The stresses due to moments 1 and 2 are equal to the yield stress of the material, meaning that the surface of the beam has undergone yielding and elongated. When the bending moment 2 has been released, and the beam is not loaded at all, the stresses and strains should return to equilibrium. To counterbalance for the stresses due to tension yielding, the beam is now in compression despite the fact that it is not loaded at all. It is said that the beam is in residual compression and the stress profile in diagram (c) and point 3 in diagram (e) show the compressive nature of these residual stresses [21,33-34].

Residual stresses are therefore, the outcome of non-uniform plastic deformations on regions of a component. They may also be the result of volume changes during phase transformations [35]. Depending on whether they are tensile or compressive, they can be detrimental or beneficial, respectively, to the component's behavior, especially in regards to failure and fatigue [28,32].

Processes that induce residual stresses may be mechanical or heat processes. In both cases non-uniform, permanent deformations affect the component in question [32]. As discussed in the previous section during a thermal process, as in heat-treating of steel leaf springs, the steel is heated, clamped in the cambering chamber and cooled rapidly in the oil bath. The process involving restrained expansion and contraction of the leaf spring, causes permanent deformation locations in the material, and therefore induces residual stresses. Residual stresses due to a mechanical process, as will be shown in the following section (I.1.4), are also the result of non-uniform plastic deformations [32].

In regards to the fatigue behavior, residual stresses are more effective during the initiation life (which correlates with Low cycle Fatigue Life (LCF) [21,32]), since failure begins, in most cases, on the surface of a component due to stressing under tensile loads. As a result, compressive residual stress field (CRSF) may reduce the effects of the applied tension [32,35]. In general, residual stresses have a similar effect on the fatigue behavior of components, and are of the same magnitude, as mechanically imposed static stresses [35].

Residual stresses are very important in the leaf spring manufacturing technology, and apart from heat treatment there are other treatments to induce them in the leaf spring surface, such as surface treatments. However, although compressive stresses have a very positive effect on the leaf spring’s performance, their induction is not permanent, and there exist a variety of factors that may cause their relaxation. Such factors include heating or operation at high temperatures, overloading and cyclic loading [21,28].

Farahhi et al. tested 60SC7 spring steel specimens in torsion and observed, with the help of an X-Ray diffraction-meter, that the residual stress field on the surface of the specimens tested reduces during the fatigue life of the steel. Observations lead to the conclusion that a decrease in the compressive residual stress field begins after the first few cycles of the component's life, and continues throughout the cycling application. However, when the loading was higher the compressive residual stress field decrease was faster [36].

Menig et al., in their study of quenched and tempered AISI 4140 steel rods, also tested under torsion at $R=0$, observed a quasi-static reduction in the residual stress field of the shot-peened components, and an even greater reduction in the stress peened ones (Fig. 13) [37].

A progressive decrease in residual stresses of fully reversed cycled steel was also observed in the study by Capello et al., who noticed a decrease in residual stresses from the first cycles and a stabilization of the relaxation past 10^5 cycles [38]. Similar results were given by Torres and Voorwald, who noticed a 50% relaxation in the stresses of rotating bent quenched and tempered AISI 4340 steel between 10^3 and 10^4 cycles [39]. Iwata et al. studying the effect of shot peening on the fatigue fracture of as quenched martensitic steel also detected relaxation of residual stresses at lower lives [40].

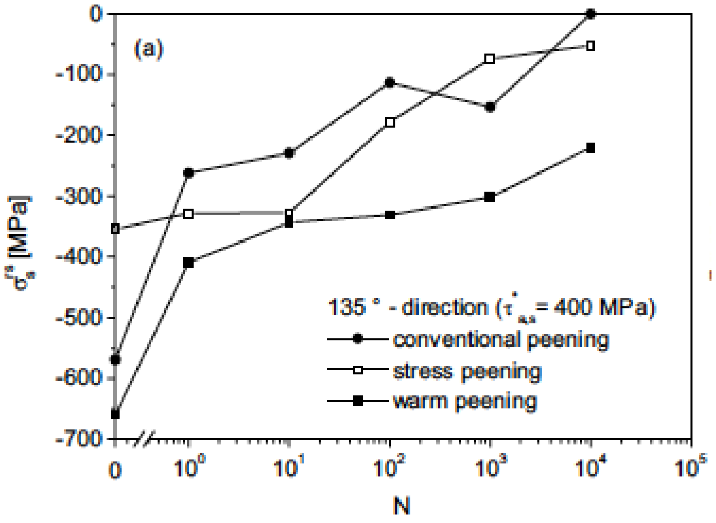

Figure 13: Residual Stress Relaxation of shot peened, stress peened and warm peened under torsional loading [37]

The reason behind stress relaxation is based on the fact of superposition of the residual stress and the applied stress exceeding the yield strength of the component tested [33,38,41]. Bergström et al. compared specimens under *R*=-1 and *R*=0, concluding that relaxation is indeed present from the early cycles under *R*=-1 (Fig. 14), especially in the axial direction, but only present just before failure at *R*=0. As a result, they drew a final conclusion that relaxation in axial direction occurs during compressive loads and depends on the loading range, while in the tangential direction relaxation exists but is smaller [41].

As a result shot peening, and many other surface treatments inducing residual stresses, have a shortcoming; that of stress relaxation during cyclic. Therefore, when designing a component that will be surface treated by a peening process the appropriate peening intensity should be chosen with care, and knowledge of the possible stress relaxation should be considered. Relaxation of residual stresses may also exist in other treatments involving reduction of residual stresses, such as carburizing. However, in the case of the experiments carried out on carburized components for this research relaxation of residual stresses was not obvious from the results.

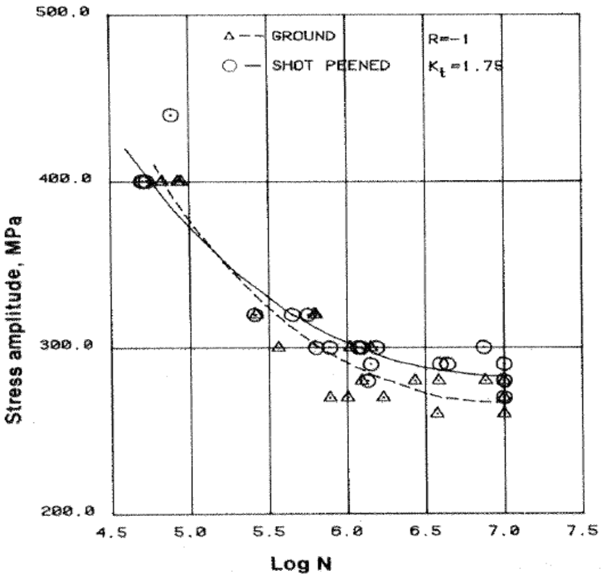

Figure 14: Stress Relaxation of notched components under R=-1 [41]

I.1.4 Surface Treatments

As the term suggests, a surface treatment is the condition of the steel's surface in order to improve the properties, or appearance of the steel's surface. Surface treatments may be chemical, such as nitriding, mechanical, such as shot and stress peening, or thermal, such as carburizing [42-43]. In the automotive industry, shot peening and carburizing are of the most commonly used surface treatments.

Carburizing is a thermal process during which the austenite of low carbon steels interacts with a high carbon atmosphere, when heated below the melting point of the alloy. Through a diffusive mechanism the steel surface absorbs carbon, thus increasing the concentration of this element in the alloy [16,44-45]. As the carbon content on the steel surface increases, the hardness of that surface increases, without affecting the hardness of the core. Depending on the application of the steel component being carburized, the depth of the carburized surface may be up to 6.4 mm. This layer of the metal surface whose carbon content and mechanical properties change due to the surface treatment is called *case depth*. During carburization the amount by which the carbon content of the steel surface is increased depends on the temperature at which the process takes place, as well as its duration. Temperature and duration also have an effect on the size of the case depth. Longer times and higher temperatures result in higher carbon contents and deepper case depths (Fig. 15) [44-46].

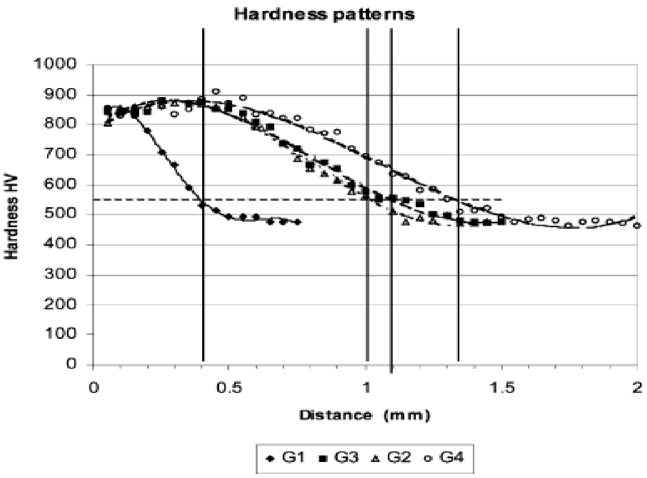

Different specimen groups used in the experiments

Group	Hard layer thickness (mm)
G1	0.4
G2	1.0
G3	1.1
G4	1.35

Figure 15: Vickers micro-hardness patterns for AISI 8620 steels carburized at different case depths [46]

Shot peening, as explained previously, is a mechanical surface treatment during which the surface of steel is plastically deformed by its continuous bombardment of small, most often steel, shots. Depending on the effect of the shot peening, and the material being treated, the diameter of the shots varies. The intensity of shot peening is also variable, and is measured using the Almen scale. The duration of the shot peening processs determines the coverage of the peening, meaning the area fraction impacted by the shots [47].

Shot peening coverage is most often assessed optically [48], and may exceed 100%, many times reaching even 1000% [49]. As the coverage increases, and the process of shot peening takes longer to complete, the uniformity of a compressive residual field on the surface of the component under treatment becomes better. It is believed that 100% coverage provides the appropriate uniformity of surface compression needed to improve fatigue life [47].

As the shots hit the metallic surface during the peening process, they create indentations at the region of impact, due to the fact that they plastically deform that region. Upon unloading of the impact from the shots, the indented regions tend to expand. However, their expansion is restrained by the non-plastically deformed metal layers below, in the subsurface of the component. This restraining is compressive. As the shot frees the indented area, only a partial amount of that surface’s strains are recovered. As a result only elastic strains recover, and plastic strains still remain due to the plastic deformation. In an effort to attain the stress and strain equilibrium existing before the shot peening process, and its results, a layer of compressive stresses is left on the subsurface, and a tensile stress layer below it [50].

The intensity of shot peening is measured in the Almen scale. The Almen intensity does not provide information on the residual stress field profile, which is important in fatigue [49,51-52]. There are three different Almen scales, A, N and C [53], depending on the way the measurements are taken. Almen intensity increases with increasing shot size, but high Almen intensity does not mean necessarily higher residual stress values [36,42].

There are a variety of shot sizes and materials that will impact differently the surface under treatment, and as a result a different residual stress field will be created on the surface of the component. The degree of shot peening a component has suffered is measured by the shot peening intensity in the Almen scale. Shot peening is a surface treatment process, and consequently only affects the surface of the component and not its core. M. L. Aggarwal et al. [42] show in their research that the beneficial effect of shot peening on the fatigue life of steel, is not always increasing with increasing shot peening intensity. In the corresponding study, Aggarwal et al. show that for the EN45A spring steel, increasing the shot peening intensity has a positive effect on the fatigue life of the steel up to an intensity of 17 A. As the intensity is further increased, the fatigue life of the steel becomes shorter. Fig. 16 shows the S-N graph from the Aggarwal et al. study, giving proof that at 22 A the fatigue life is shorter than at 17 A. Farrahi et al. [36] in their research of residual stresses, show that there exists a correlation between the fatigue strength of a component and the area under the curve showing the distribution of residual stresses in the component. It is argued in their paper that fatigue life improvements are based on the maximum residual stress and the depth of the plastically deformed layer [36]. The danger of overpeening to the fatigue life is an eminent one, and the appropriate shot peening intensity and residual stress depth can only be defined empirically through knowledge of the material and its applications [52].

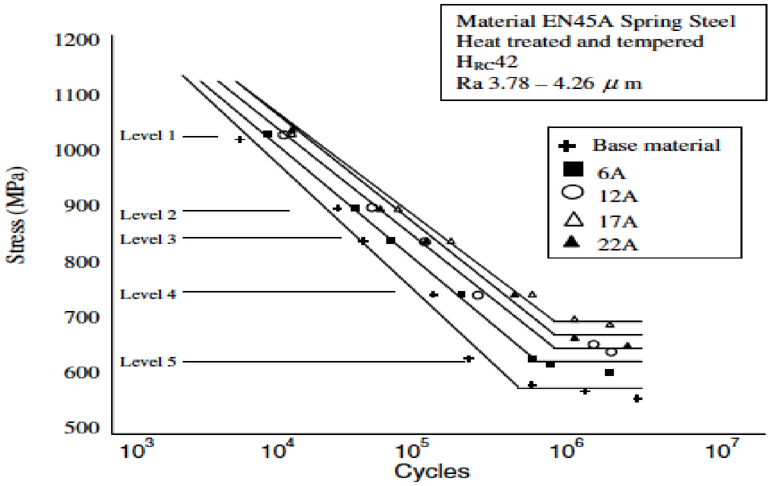

Fig. 3. *S/N* comparative curves.

Figure 16: S-N Curves for shot peened EN45A steel at different Almen intensities [42]

Both carburizing and shot peening will induce compressive residual stresses in the treated surface layer of steel [28,32,46]. Due to the increase of carbon content in the carburized surface, the steel ceases to have a homogenized microstructure, especially if carburizing is done after a heat-treating process. The volumetric changes occurring in the steel due to the carburizing process result in compressive residual stresses [16,35]. On the other hand, during shot peening the surface is being plastically deformed by the fast impact of the steel shots and is subjected to residual tension while the core is in residual compression. This residual compressive layer is about 1 mm in depth and has a value of up to half the yield strength of the material [21]. In the case peening coverage is extended too far into the material by extended peening time, and stress intensity increases to a critical value, depending on the material and geometry under peening, the tensile residual stress region extends too much causing fatigue failure [42, 50].

I.2 Fatigue and Fatigue Life of Steel

In 1964 The International Organization for Standardization in Geneva, published the definition of fatigue in the report *General Principles for Fatigue Testing of Metals*, as follows [28]:

> *"(Fatigue is the term that) applies to changes in properties which can occur in a metallic material due to the repeated application of stresses or strains, although usually this term applies specially to those changes which lead to cracking or failure"*

All structures will fail at some point during their application. Depending on the material, geometry and application of the structure, failure may occur at or below the maximum tensile strength of the material. The concept of fatigue refers to failure, as demonstrated through fracture, when a structure is subjected to repeated or fluctuating stresses, failing below its maximum tensile strength [16,21].

There exist different types of fatigue depending on the environment as well as the way the cyclic loading is performed. As a result, there exists *creep-fatigue* when the cyclic application is associated with high temperatures, *thermomechanical fatigue* occurring in situations when apart from the cyclic loading, temperature fluctuates as well, *corrosion-fatigue* where the environment of the cyclic application may chemically affect the component or cause its embrittlement, *rolling contact fatigue* where apart from the repeated loading the components exhibit rolling contact between their materials, and *fretting fatigue*, a very common problem in multi-leaf spring suspension systems, which is due to cyclic stresses occurring together with an oscillatory motion and frictional sliding between surfaces of the component being cycled [28]. However, the simplest type of fatigue, which will preoccupy this thesis, is *mechanical fatigue* and is the result of fluctuating stresses or strains applied externally to a component [28].

The concept of fatigue can give great insight to mechanics and engineers on how and why cyclic loaded structures fail, and how they can be properly designed to avoid or delay their failure. It is only reasonable therefore, that since the early 19th century engineers and scientists of the time working on metals, started experimenting on and studying the concept of fatigue. Carriages and trains were of the major means of transportation of the time, and although carriage suspension had troubled the mechanics of the time, railway accidents made imperative the improvement of railroad axles, bridges and train suspensions. It was the railways therefore, that drew more and more the attention of scientists and engineers to study the fatigue of metal structures and especially those made of steel [28,33]. Among the major contributors to the study of fatigue worth mentioning are Wöhler, Gerber, Goodman, Bauschinger, Palmgren, Miner, Coffin and Manson.

August Wöhler, in 1860, was the first to carry a systematic study of railroad axles' fatigue failure and to observe that the static strength of these steel axles was much higher than their strength under cyclic loading. Wöhler's investigations led to one of the primary fatigue analysis methods used today, meaning the stress-life approach (S-N curves), as well as the concept of *endurance limit* [28,33]. In 1874 Gerber developed the methodology for fatigue design, and calculation of the fatigue life under different levels of cyclic mean stresses, also studied by Goodman in 1899. The concept of fatigue was further investigated and developed, to include the damage accumulated in the material leading to catastrophic failure, and this work is attributed to Palmgren (1924) and Miner (1945), while further work discussing the effect of plastic strains in cyclic damage was initiated by Coffin (1954) and Manson (1954) [28]. Engineers are still studying the concept of fatigue, as it is one of the most common reasons of failure of structures operating under cyclic loading. Since the 1970s the concept of fatigue of composite materials has also been preoccupying engineers [8].

Metal components fail though initiation and propagation of a crack. The degradation of the properties of a component under cyclic loading leading to failure, is characterized as fatigue damage, and is demonstrated in the following order [28]:

1. Changes in the substructure and microstructure of the metal component lead to nucleation of defects, and as a result a damage of a more permanent nature.
2. Cracks are created in the microscopic level.
3. Microcracks start growing and propagation of these cracks begin.
4. Macrocracks propagate.
5. The component becomes unstable or fails through fracture.

These stages are influenced by the environment or the loading application, the microstructure of the component, as well as mechanical factors such as loading [28]. The fourth step in the order in which fatigue damage is demonstrated, discusses the fine line that exists between the initiation and propagation of a crack [28,32]. Unless otherwise mentioned, the fatigue of materials is investigated on the pretext that no prior damage, flaws or defects exist in the material. As a result, the fatigue life of a component is the number of cycles a component can withstand without failing [5]. The fatigue life of the component concludes when the component fails, usually through fracture. The fatigue life of a component therefore, includes two phases: the number of cycles required to cycle the component until the initiation of a crack, and the number of cycles the component is further cycled until this crack is propagated to a critical size that leads to fracture [28,32]. The former phase is termed the *initiation life*, and the latter the *propagation life* (Fig. 17) [21,32]. Distinction of the threshold life cycles between the *initiation* and *propagation lives* is a cumbersome task to complete, and it is beyond the scope of this thesis. The current study will not be based on distinguishing between the two phases of fatigue life. All structures examined will be assumed as flawless, unless otherwise specified, and failure will be understood as the catastrophic failure of the component due to fracture.

There exist three primary methods to discuss and evaluate the fatigue life of metal components: the *stress-life*, *strain-life* and *fracture mechanics approach* [21]. The *stress-life* approach is the first method developed to examine and evaluate metal fatigue, and is based on S-N diagrams developed by Wöhler [33]. The *stress-life* approach uses the stresses applied cyclically on the component in question and defines the number of life cycles the component performs without failure under these stresses. The *strain–life* method on the other hand, introduced approximately one hundred years after Wöhler’s studies, in the 1960s [33], uses the strain response of the component. The *stress* and *strain-life* approaches are also referred to together as *total-life* approaches [28]. Depending on the number of cycles that are needed to lead a steel component to failure, the fatigue life of a component is divided between low cycle fatigue (LCF), for components that survive between 10 and 10^3 cycles, and high cycle fatigue (HCF), for components that survive an amount of life cycles above 10^3 [32]. The upper limit of LCF may be large, but depends on the material of the component examined [21].

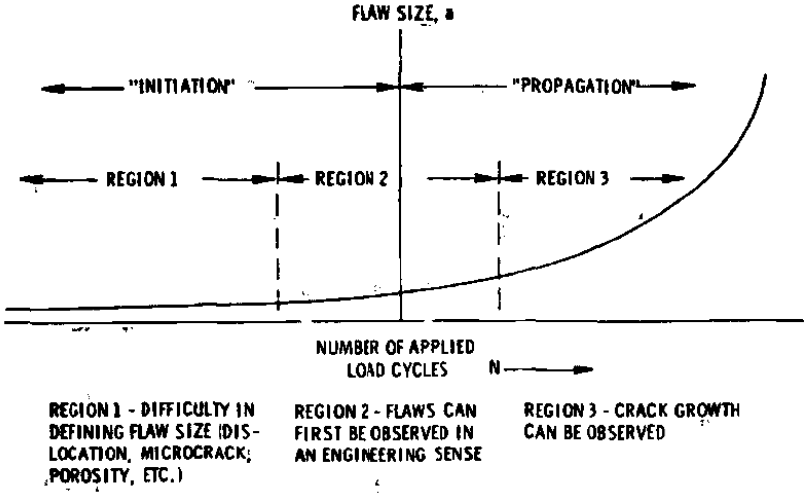
FLAW SIZE, a
"INITIATION"
"PROPAGATION"
REGION 1
REGION 2
REGION 3
NUMBER OF APPLIED LOAD CYCLES
N
REGION 1 - DIFFICULTY IN DEFINING FLAW SIZE (DISLOCATION, MICROCRACK, POROSITY, ETC.)
REGION 2 - FLAWS CAN FIRST BE OBSERVED IN AN ENGINEERING SENSE
REGION 3 - CRACK GROWTH CAN BE OBSERVED

Figure 17: Initiation and Propagation Lives [32]

Stress and *strain-life* approaches have some differences between them and therefore the one cannot be used instead of the other in all applications. The *stress-life* approach assumes that all strains in the component are elastic, and as a result, fails to interpret the true stress-strain behavior of the material considered. Therefore, the *stress-life* approach is more appropriate for situations where fatigue of the component is due to low stresses that deform the material mainly elastically. Such situations have fatigue lives lying in the HCF region [21,28]. On the other hand, the *strain-life* approach is used in situations where the response of the component under cyclic loading is due to strains or deformation [21,33]. There are cases however, when the load applied is low enough, so that the stresses and strains are related to each other through a linear relation, as a result, both *stress* and *strain-life* approaches may be used equivalently [21]. A material that fails too soon in the area of LCF is subjected to high stresses that may cause plastic deformation to the material, before it fractures. Such situations should be evaluated using the *strain-life* approach [21,28]. Notched components are also better evaluated using the *strain-life* approach, as plastic strains are developed in the vicinity of the notch due to stress concentrations [21].

The *fracture mechanics* approach is used to estimate the propagation life of a component. Knowledge of an initial crack size is required when using this approach; otherwise a good assumption of the initial crack size should be made. If the component is considered flawless at the beginning of testing, the fracture *mechanics* approach is used to evaluate the propagation life, and *strain-life* approach will evaluate the initiation life, once the propagation life is subtracted from the total life of the component, as evaluated using the *strain-life* approach [21].

I.2.1 Stress-life Approach

The stress-life approach is represented with the aid of S-N diagrams, commonly referred to in Europe as Wöhler curves. The S-N diagrams plot the alternating stress, S, versus the cycles leading to failure, N (Fig. 18) [21]. Not all components under certain cyclic loads have exactly the same fatigue life. When similar specimens are tested under the same conditions, scattering of data will be observed in most of the cases. This scattering does not necessarily indicate errors in testing procedures, but is mainly a characteristic among metallic components [35]. The amount of scattering is often measured using the standard deviation of the data, and is observed that this scattering is related to stress and appears larger at stresses just above the fatigue limit, an important parameter in the characterization of fatigue life that will be discussed in later sections, and smallest at high stresses [35]. For this reason, many trials should be made to measure the fatigue life under one loading condition, in order to collect enough data points to acquire a representative mean value of the fatigue life [35]. Depending on the complexity of the loading, environmental conditions and geometry of the component, the number of repetitions of the tests will vary. However, it is common to use three to five data points to determine the mean value of a fatigue life at a single stress level [35]. These mean data points are then plotted on an S-log N plot, and compose a straight-line representation of the fatigue life of the material [21]. Although traditionally, the alternating stress, S, is plotted on the vertical axis of an S-N curve, maximum applied stress (S_{max}), or other combinations of stresses applied, strengths, or the linearization of the applied stress are sometimes plotted on the vertical axis of the S-N diagram [35].

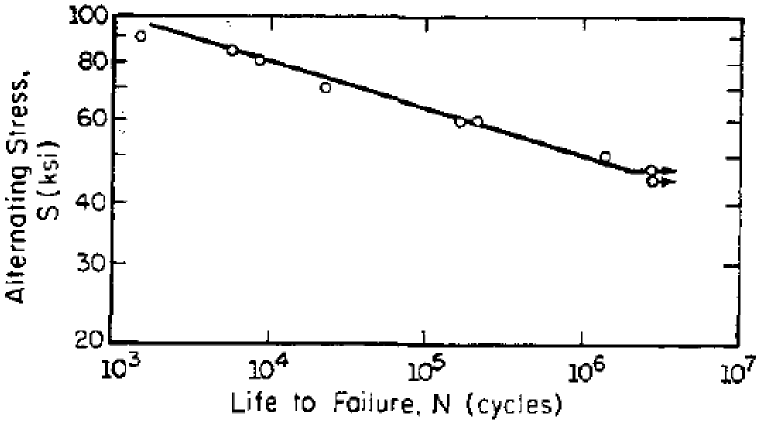

Figure 18: S-N curve for AISI 1045 steel [21]

The S-N diagrams are not the same for all types materials. A special case of S-N diagrams is that of BCC steels. As shown in Fig. 18, the S-N curve of the steel has a descending slope, showing that at lower alternating stresses the number of cycles to failure is larger. As the curve enters the HCF region, above 10^6 cycles, the curve becomes horizontal, showing that at the current stress level the life of the steel component tends to approach infinity. The stress level where this “infinite” fatigue life occurs is common in BCC steels and is termed the *endurance* or *fatigue limit* (S_e) [21]. For convenience, it is common to consider the fatigue limit to equal the stresses level at 10^6 cycles [21], unless experimental data shows otherwise. However, based on the scattering of data points, it is hard to conclude one value for the fatigue limit. It is often the case, that instead of a mean value S-N curve, a plot of a family of curves is used to represent the fatigue life of a component, where each S-N curve indicates a probability of failure. The curve representing longer lives is that of the highest failure probability (Fig. 19) [35].

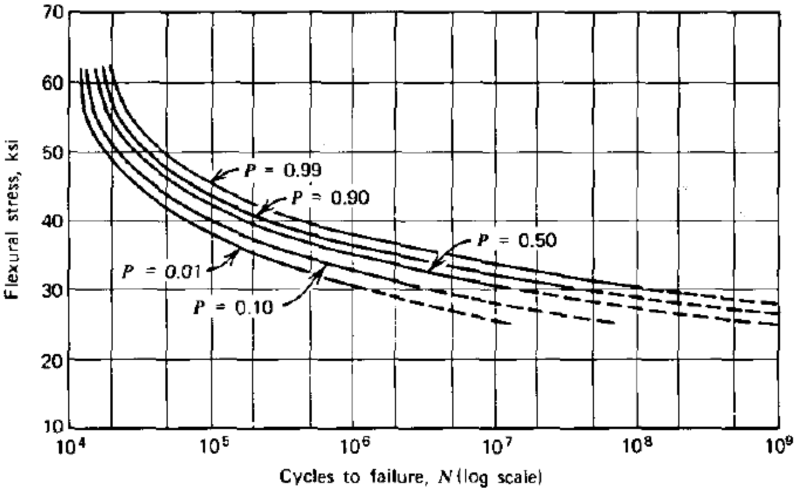

Figure 19: S-N probability curves for the fatigue life of 7075 aluminum, loaded at *R*=-1 [35]

The existence of the fatigue limit depends on dislocation sites in the microstructure of the steel. When carbon or nitrogen occupy interstitial sites in the iron atom, these dislocations are pinned, and formation of microcracks is prevented as the slip mechanism is not set in motion. Consequently, the fatigue limit depends on factors that may affect or prevent the pinning of these dislocations, such as a corrosive environment, high temperatures, or periodic overloads [21].

I.2.2 Mean Stress Effects

While discussing the stress-life approach the concept of *alternating stress* was mentioned. When a component undergoes cyclic loading it is subjected to two different loads, whether they are equal in magnitude and opposite in direction, or imposed along the same direction and they differ in magnitude. These loads produce corresponding stresses that are responsible for the way the material will fatigue. The *stress amplitude* (σ_α) therefore, is the one half the difference the two different stresses as shown in Eq. 1. As seen from Eq. 1 the stress amplitude depends on another parameter, the *stress range* ($\Delta\sigma$), which is the difference between the *maximum* and *minimum stress* applied to the component being cycled. While the stress amplitude shows the average value of the stress range where the component is cycled, there is another important parameter when discussing fatigue. This parameter is the *mean stress* (σ_m), which as will be shown later, has a significant effect on the fatigue life of the component. The mean stress is expressed as one half of the sum of the *maximum* (σ_{max}) and *minimum* (σ_{min}) *stresses* applied (Eq. 2). The mean stress affects the fatigue life of a component depending on the way the component is cycled, which is defined based on the relationship between the maximum and minimum stresses [21,28,33]. The relationship between these stresses is expressed with the *load ratio* (R) (Eq. 3). R is negative when the loading is characterized as *reversed*, where maximum stress and minimum stress have opposite values. R is positive when the maximum and minimum stresses are both tensile. When the load ratio equals 1 the loading is monotonic, with no stress variation. At R=0 the component's fatigue is characterized by zero tension. Finally at R=-1, fully reversed loading occurs, where the maximum stress is tensile and the minimum stress compressive [21,28,33,54]. Another ratio often related to mean stress is the *amplitude ratio* (*A*) relating stress amplitude and mean stress [21] (Eq. 4).

$$\sigma_a = \frac{\Delta_\sigma}{2} = \frac{\sigma_{max} - \sigma_{min}}{2} \tag{1}$$

$$\sigma_m = \frac{\sigma_{max} + \sigma_{min}}{2} \tag{2}$$

$$\mathrm{R} = \frac{\sigma_{min}}{\sigma_{max}} \tag{3}$$

$$\mathrm{A} = \frac{\sigma_a}{\sigma_m} \tag{4}$$

Judging from the above equations and these parameters as expressed in Fig. 20, it can be concluded that at fully reversed loading (*R*=-1), where minimum and maximum stresses are equal and opposite, the mean stress is zero.

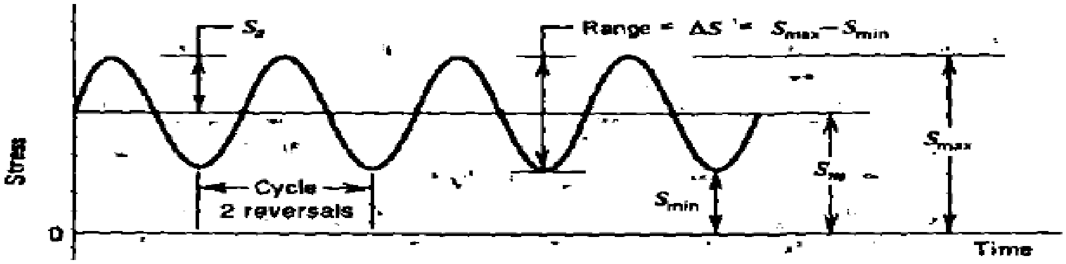

S_a
Range = ΔS = $S_{max} - S_{min}$
Stress
S_{max}
S_m
S_{min}
Cycle
2 reversals
0
Time

Figure 20: Stress Parameters affecting Fatigue Life [33]

The effect on the fatigue life of a component of an increasing tensile mean stresses, is negative [28,33]. Especially in the case of uniaxial loading, the fatigue life of a component decreases as the tensile mean stress increases. Fig. 21, represents the *mean stress* effect on the fatigue life. The effect of a decreasing *R* is also negative (Fig. 22) [54].

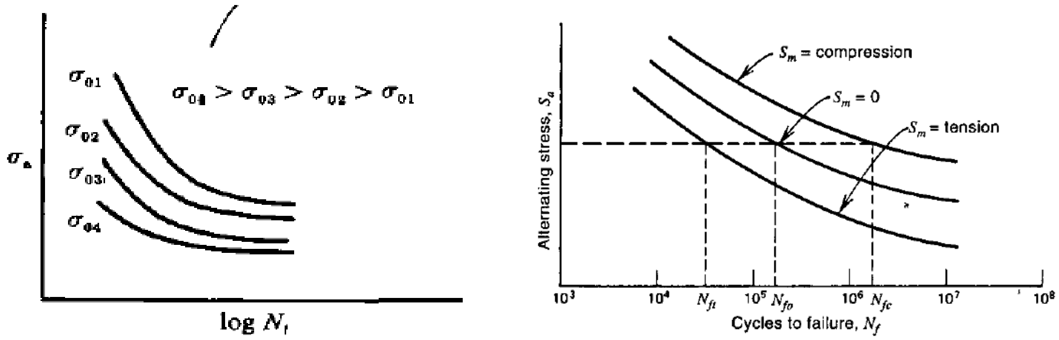

(a) **(b)**

Figure 21: Effect of Mean Stress magnitude (a) and direction (b) on fatigue life [28,33]

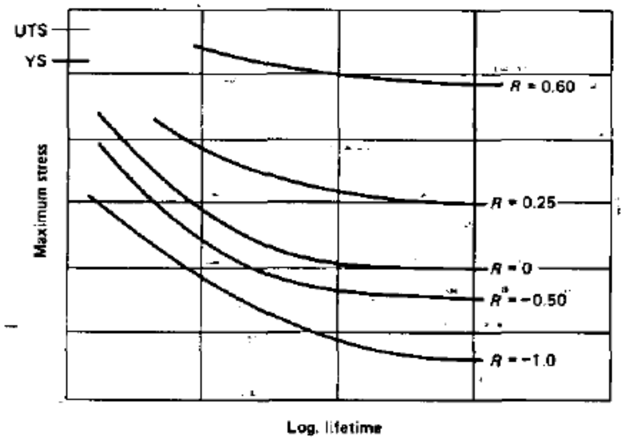

Figure 22: Effect of Load Ratio to Fatigue Life [54]

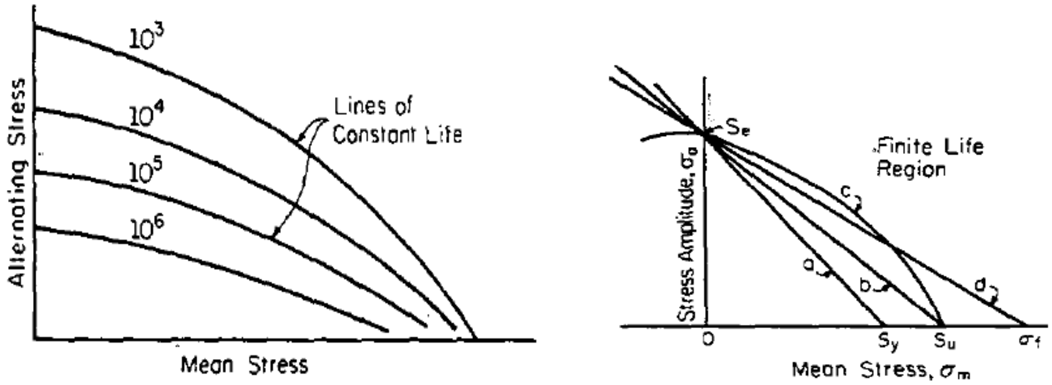

(a) (b)

Figure 23: Haigh Diagram: (a) Lines of constant life, (b) Lines of Mean Stress Equations (a. Soderberg, b. Goodman, c. Gerber, d. Morrow) [21]

The effect of mean stress on fatigue life, is also depicted on a Haigh diagram, representing the relationship of alternating stress to mean stress though curves of constant life (Fig. 23). As the derivation of Haigh diagrams requires multiple tests, which in the majority of cases are time consuming and very costly, empirical relationships have been developed to generate constant life diagrams, relating the stress amplitude (σ_a) and mean stress (σ_m) using the fatigue or endurance limit (S_e), as the stress range that when applied to a material will not cause failure, and ultimate tensile strength (S_u) or yield strength (S_y), or true fracture stress (σ_f) . The most common of these relationships are attributed to Gerber (1874), Goodman (1899), Soderberg (1930) and Morrow (1960) [21,33].

Gerber: $$\frac{\sigma_\alpha}{S_e} + \left(\frac{\sigma_m}{S_u}\right)^2 = 1 \qquad (5)$$

$$\text{Goodman:} \quad \frac{\sigma_a}{S_e} + \frac{\sigma_m}{S_u} = 1 \tag{6}$$

$$\text{Soderberg:} \quad \frac{\sigma_a}{S_e} + \frac{\sigma_m}{S_y} = 1 \tag{7}$$

$$\text{Morrow:} \quad \frac{\sigma_a}{S_e} + \frac{\sigma_m}{\sigma_f} = 1 \tag{8}$$

When the mean stresses in question are tensile the Soderberg method is judged conservative, and for that reason is rarely used. Experimental data tends to be between the predictions of the Gerber and Goodman curves. A further observation is useful, depending on the steel's hardness. Steels of high hardness, which are brittle, having an ultimate tensile strength close in value to their true fracture stress, tend to have Morrow and Goodman curves that coincide. On the other hand, ductile steels, of true fracture stress below their ultimate tensile stress show less influence by mean stresses, when the Morrow relationship is used, while the Goodman relationships stands very conservative in such cases. Finally, for situations of loading where R<1, the above empirical relationships tend to give similar predictions for the mean stress influence on the fatigue life of the component. As the load ratio approaches unity (monotonic loading) it is preferable to use the yield stress of the material as a limiting parameter to design [21].

The above observations are limited to the case of tensile mean stresses. Similar to the case of residual stresses, when compressive mean stresses are considered, the fatigue life is benefited by these stresses [33]. However, when the component in consideration is notched, compressive mean stresses have no effect on its fatigue life, as shown on the Haigh diagram Fig. 23 [21].

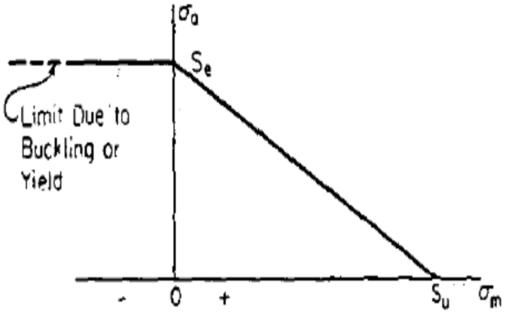
σ_a
S_e
Limit Due to Buckling or Yield
-
0
+
S_u
σ_m

Figure 24: Goodman estimate for notched component on Haigh Diagram [21]

I.2.3 Strain-life Approach

As mentioned earlier, when the response of a critical site of a component, as is a notch, depends on strain or deformation, the strain-life approach is more appropriate in estimating the fatigue of the material. Due to this response of the components, based on strain and deformations, the strain-life approach evaluates plastic strains and/or deformation and describes better LCF. The strain-life method tends to ignore the propagation stage of crack growth, and instead evaluates the initiation life of the component. This approach may be combined with information regarding the stress-strain history at critical sites of the components, such as notches, mean stress effects, as well as damage accumulation models as the Plamgren-Miner model.

When the component is loaded in tension, the strain recovered upon unloading is the linear elastic strain. The portion of strain not recovered is the plastic strain.

$$\varepsilon_t = \varepsilon_e + \varepsilon_p \tag{9}$$

For cyclic loading the power law function, relates true stress to plastic strain as

$$\sigma = K'\left(\varepsilon_p\right)^{n'} \tag{10}$$

The plastic strain and total strain relationships for cyclic loading can be expressed in terms of the *cyclic strain-hardening exponent* (n') and the *cyclic strength coefficient* (K'):

$$\varepsilon_p = \left(\frac{\sigma}{K\prime}\right)^{1/n'} \tag{11}$$

$$\varepsilon_t = \frac{\sigma}{E} + \left(\frac{\sigma}{K\prime}\right)^{1/n'} \tag{12}$$

Using the above equations and the concept of stress and strain ranges, the total strain range can be represented by the following equation [20]

$$\Delta\varepsilon = \frac{\Delta\sigma}{E} + 2\left(\frac{\Delta\sigma}{2K'}\right)^{1/n'} \tag{13}$$

The equation of total strain can be expressed in life terms as

$$\frac{\Delta\varepsilon}{2} = \frac{\sigma\prime_f}{E}\left(2N_f\right)^b + \varepsilon'_f\left(2N_f\right)^c \tag{14}$$

to form the strain-life relation, where σ'_f is the *fatigue strength coefficient*, which is approximately equal to the fracture strength (σ_f), $2N_f$ represents the cycle reversals needed to achieve failure of the component, where one reversal is half of one cycle, ε'_f is the *fatigue ductility coefficient*, which is approximately equal to true fracture ductility (ε_f), b is the *fatigue strength exponent*, also known as the Basquin exponent ranging between -0.05 and -0.12, and finally c is the *fatigue ductility exponent* or Coffin-Manson exponent taking values between -0.5 and -0.7 [21].

Earlier the concept of mean stress effects was mentioned. Properties of the fatigue of a material are most often obtained by cycling the components under completely reversed loading, while keeping the strains at constant amplitude. Cyclic loading of components is very rarely carried out in this manner; as a result, mean stress effects are important to be considered as they may alter significantly the fatigue life of a component. The effect of mean stresses on the fatigue life of a component may either be beneficial and increase the fatigue life of the component due to a nominal compressive load, or detrimental and due to tensile loading decrease the fatigue life of the component (Fig. 21b) [33]. Mean stress effects are demonstrated mostly at longer lives. However, there is always the chance that means stresses will relax and become insignificant, when plastic strains become significant at high strain amplitudes [21].

Many scientists have proposed modifications to the strain-life relationship (Eq. 14), to account for the effect of mean stresses. They have developed different forms of the strain-life relationship including mean stress effects, either including the effects in the elastic component, or plastic or both of the strain-life equation. The following equations show two different strain-life equations with mean stress effects [21,28]:

Smith-Watson-Topper: $$\frac{\Delta\varepsilon}{2}\sigma_{max} = \frac{\left(\sigma'_f\right)^2}{E}\left(2N_f\right)^{2b} + \sigma'_f\varepsilon'_f\left(2N_f\right)^{b+c} \qquad (15)$$

Morrow: $$\frac{\Delta\varepsilon}{2} = \frac{(\sigma'_f - \sigma_m)}{E}\left(2N_f\right)^b + \varepsilon'_f\left(2N_f\right)^c \tag{16}$$

However, between the above equations the one suggested by Morrow (Eq. 16) will be the one considered in this thesis.

I.2.4 Predicting the Fatigue Life of Steel Using the Stress-Life Approach

I.2.4.1 Power Relationship of S-N curve

The S-N curves for various steels tend to coincide, as observed when the non-dimensional form of the *fatigue ratio* is plotted on the vertical axis of the S-N diagram (Fig. 25). The *fatigue ratio* is the ratio of the fatigue limit to the ultimate strength of the steel in question. This ratio ranges between 0.35 and 0.6 for steels whose ultimate strength is below 1,400 MPa [21,33]. The choice of 1,400 MPa as an upper limit of ultimate strength to steels, whose fatigue limit falls within the above values, is based on the microstructure of steel. Steels with ultimate strengths above 1,400 MPa, are prone to cracks due to their microstructure, and therefore have a lower fatigue limit [21].

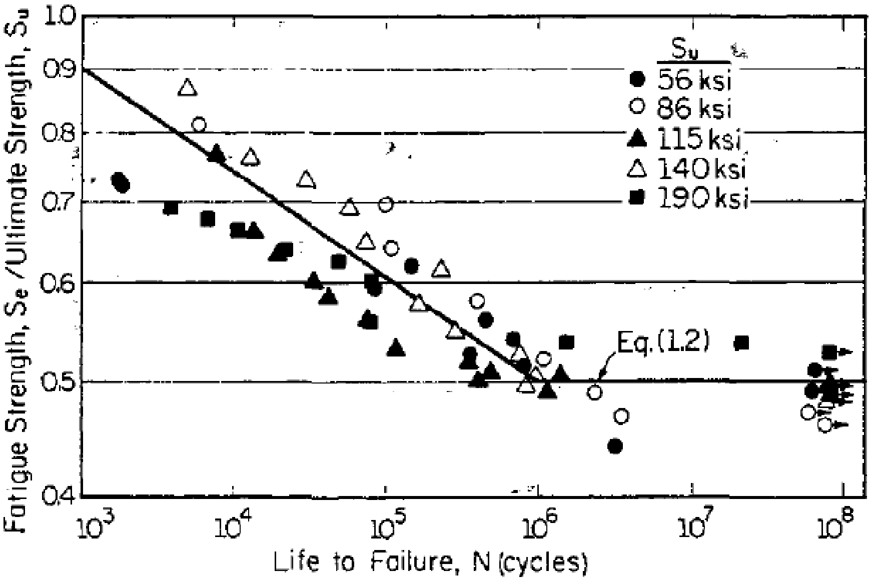

Figure 25: S-N curves for different wrought steels [21]

The ultimate strength (S_u) and fatigue limit (S_e) are related to the materials hardness, (in the Brinnell scale), by the following relations.

$$S_u = 3.45 \times BHN \ \ for\ MPa\ units\ and\ S_u = 0.5 \times BHN\ for\ ksi\ units \tag{17}$$

$$S_e = 1.725 \times BHN\ for\ MPa\ units\ and\ S_e = 0.25 \times BHN\ for\ ksi\ units$$
$$when\ BHN \leq 400 \tag{18a}$$

$$S_e \approx 700\ MPa\ \ for\ BHN > 400 \tag{18b}$$

These relationships can be combined to relate the ultimate strength to fatigue limit [33].

$$S_e = 0.5 \times S_u\ \ for\ \ S_u \leq 1{,}400\ MPa \tag{19a}$$

$$S_e \approx 700\ MPa\ for\ S_u > 1{,}400\ MPa \tag{19b}$$

Using these parameters, and the corresponding stress of the material at a fatigue life of 1000 cycles (S_{1000}) a power relationship can be formed to estimate the fatigue life of steels for lives between 10^3 and 10^6 cycles [21].

$$S = 10^C N^b \ \ for\ \ 10^3 < N < 10^6 \tag{20}$$

where $$C = \log_{10}\frac{(S_{1000})^2}{S_e}\ \ and\ \ b = -\frac{1}{3}\log_{10}\frac{S_{1000}}{S_e} \tag{21a and b}$$

I.2.4.2 Power Relationship of S-N Curve using Hardness as a Function of Carbon Content

The fatigue limit and ultimate strength in the power relationship discussed in the previous section is calculated based on knowledge of the hardness of the steel component, provided the hardness is measured in the Brinell scale. The hardness of a material, as mentioned earlier, depends on the microstructure and carbon content of the metal. As a result using the appropriate graph (Fig. 26), information on the hardness of a component can be gathered, if carbon content is known. Therefore, using information on hardness from Fig. 26, the S-N curve of steel at various carbon concentrations can be produced.

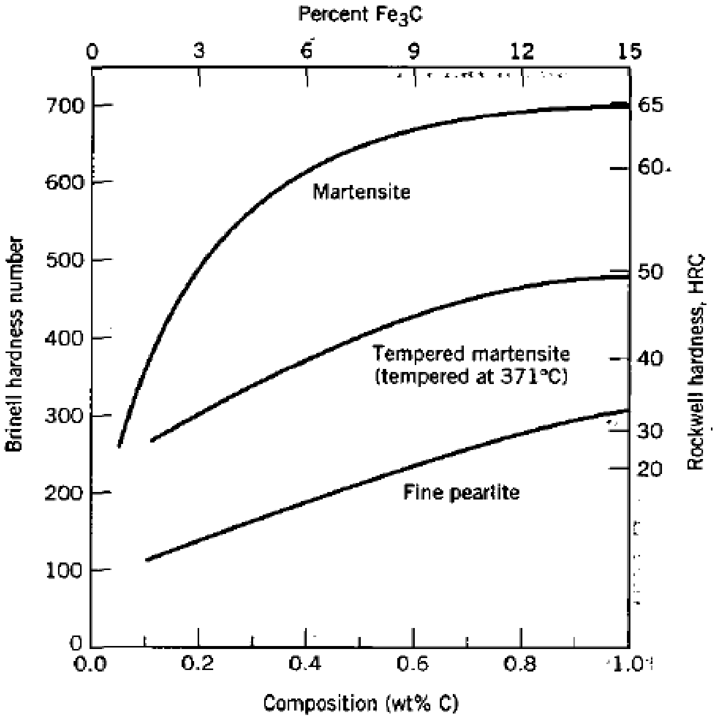

Figure 26: Hardness as a function of carbon concentration [55]

I.2.4.3 Damage Prediction Models

Cumulative Damage theory is the ensemble of attempts to calculate the damage caused by cycling, as well as its accumulation when cycling includes more than one stress amplitudes [56]. There are two ways to discuss the concept of cumulative damage: residual strength, being the instantaneous static strength that the material can still maintain after being loaded to stress levels causing damage, and the estimation of cumulative damage through damage models, such as the ones discussed in this study [57].

In the case of homogeneous isotropic materials, such as metals, failure is characterized by the initiation and propagation of a crack. In metals the strength of the material changes little or not at all during fatigue cycling [58], and is the crack propagation that defines fatigue damage at low stresses. As a result, these stresses become critical in the design of a metal structure [59]. The damage generated in a material under loading can be predicted using damage models even when minimum information on the fatigue of the material is known.

The three damage models to be discussed in this thesis are the following:

Palmgren-Miner [60-61]:

$$\left(\sum_{i=1}^{n} \frac{n_i}{N_i}\right) \mathrm{K} = 1 \tag{22}$$

Broutman-Sahu [61-62]:

$$\left(\sum_{i=1}^{n}\frac{(\sigma_{Ultimate}-\sigma_i)}{(\sigma_{Ultimate}-\sigma_{i+1})}\frac{n_i}{N_i}\right)\mathrm{K}=1 \tag{23}$$

and Hashin-Rotem [56,61]:

$$\left(\sum_{k=1}^{i-1}\left(\frac{n_{(k-1)}}{N_{(k-1)}}\right)^{\frac{(1-S_k)}{\left(1-S_{(k-1)}\right)}}+\frac{n_i}{N_i}\right)\mathrm{K}=1 \tag{24}$$

$$S_k=\frac{\sigma_k}{\sigma_{Ultimate}} \tag{25a}$$

$$S_{(k-1)}=\frac{\sigma_{k-1}}{\sigma_{Ultimate}} \tag{25b}$$

where n_i is the number of cycles under the applied stress, N_i the cycles to failure under this same stress, σ_i and σ_k are the stresses applied, $\sigma_{Ultimate}$ is the ultimate strength, and K is the number of repetitions of the loading cycle. When each of these equations equals 1, the damage accumulated leads to failure. However, damage is still being caused even if the right hand side of the above equations is less than 1 [63].

A specimen may be subjected to one or more stress levels and undergo cycling. When there are two stress levels, where σ_1 and σ_2 are imposed on the specimen for an amount of n_1 and n_2 cycles, respectively, n_2 is the number of cycles that will lead the specimen to failure. The amount of cycles of n_2 is called the *residual lifetime*. Residual lifetime can be predicted by all three of the above models, when their mathematical expression equals 1, i.e. at failure. The couples σ_i and n_i are the stress and respective number of cycles, used to create a damage curve. The S-N curve is the damage curve that presents the ultimate damage caused to the specimen, when its residual life is zero. Each point on a damage curve, defined by (σ, n), shows the damage caused to a specimen after n cycles under a load of σ. It can therefore be concluded, that damage is a way to describe the life of the specimen that is spent when it is loaded at σ. The ratio $\frac{n_i}{N_i}$ $represents$ a life fraction for the specimen, which is loaded at σ_i [56]. The Palmgren-Miner model defines damage in the material, in the form of life fractions, the sum of which when 1 defines failure of the material, when no more residual life remains to be expended. The other two models also define damage in the form of life fractions, but in these two cases the models account for the loading sequence, which is not accounted for in Palmgren-Miner.

The Palmgren-Miner damage rule, sometimes referred to as Miner’s sum, (the concept of fatigue damage first introduced by Palmgren in 1924, and later represented in mathematical form in 1945 by Miner [34]), expresses damage in terms of cycles applied at a stress level, divided by the number of cycles that lead to failure at this stress level. Each such ratio represents a percentage of life consumed [28,56,62]. When the summation of all these ratios equals 1, Eq. 22, failure has occurred. The order in which the stresses are applied has no effect in the fatigue life [28].

When a metal specimen is undergoing a two-stress level loading, damage, according to Palmgren-Miner rule, is greater when the first stress is higher than the second stress (the sum in Eq. 22 is close or higher than 1), and less damage occurs when the loading sequence is a low to high stress (the sum in Eq. 22 is less than 1) [28,62]. To account for this discrepancy from unity in the Miner's sum, Broutman and Sahu presented in 1972 a modified Miner's sum. Broutman and Sahu used the linear strength reduction curves, together with the assumption that the residual strength is a linear function of the fractional life spent when the specimen is loaded at a given stress level, in order to more accurately predict the fatigue behavior in GFRP, especially at higher stress levels [62].

In 1978 Hashin and Rotem used the concept of damage curve families to represent residual lifetimes for two-stress level loading, as well as the fact that equivalent residual lives are expended by specimens that undergo different loading schemes[1]. They developed a cumulative damage model to predict damage in two-stress level loading, which can be expanded for use in multi-stress level loadings [56].

The Palmgren-Miner rule has been shown not to account for loading sequences, as the sum can be calculated irrespective of the loading order. As a result for a high-low stress test the predicted cumulative damage by this model is greater than 1, and for a sequence of low-high stress the sum is less than 1 [27,57,63]. The other two models take into account the order of loading, thus giving more accurate results. Palmgren-Miner and Hashin-Rotem rules have been initially designed and tested on metals, although later used in GFRP damage predictions. Broutman-Sahu rule was developed and tested on GFRP.

---

[1] This is referred to as the *equivalent loading postulate* that states: " *cyclic loadings which are equivalent for one stress level are equivalent for all stress levels* [56]."

Damage models can be classified according to the parameters required for their calculation as well as their linearity or non-linearity [64]. Consequently, Palmgren-Miner is a linear stress independent model, Broutman-Sahu is a linear stress-dependent model and Hashin-Rotem is a non-linear stress-dependent model. Other models have been developed for the prediction of damage accumulation, mostly in metals, but also in composites. Most of these models are attempts to modify existing damage accumulation theories in order to cover for existing inaccuracies, and develop models dependent on the stress level (Marco and Starkey model in 1945) [34]. Other models accounted for the damage due to crack initiation and propagation through parameters estimating a life fraction factor for the initiation of the crack (Manson model 1966) [34]. In 2007 Christensen derived a general cumulative damage model using the Paris Law expression. His model can be applied to predict damage in the case of creep leading to failure and cyclic fatigue leading to failure. The models chosen to be discussed in the present study represent the three classes of damage accumulation, as mentioned above, do not require calculation of parameters other than stresses and number of cycles, and have been used in predicting fatigue both in metals and GFRPs.

I.2.5 Factors Affecting the S-N Curve

While discussing the manufacturing process of leaf springs, it was mentioned that there are various treatments involved in leaf spring production to improve the fatigue life of the spring. When designing a steel component to operate under cyclic loading applications it is usually desirable to aim for that component to endure many cycles of operation, and not to fail unexpectedly. Knowledge of the fatigue limit, which is the stress at which the component will have an “infinite” life, becomes a useful design parameter.

As there exist factors that determine the type of fatigue of a component, and treatments that will improve the fatigue life of the component, there also exist similar factors that influence the fatigue limit. It is important to consider them while designing the component. The most important of these factors are the size of the component, the type of loading it will be subjected to, its surface finish, the surface treatment it will be submitted to, and the temperature and environment it will operate under [21,42].

The appropriate fatigue limit will account for all factors that will affect and thus determine the fatigue life of the component. In estimating the appropriate fatigue limit based on the conditions for which the component is being designed, the fatigue limit of a smooth component with a diameter of less than 8 mm loaded under fully reversed bending, acts as the base fatigue limit (S'_e), which will be multiplied by the appropriate coefficients describing the factors affecting the fatigue life of the component [21,42]. Eq. 26 gives an example of how to calculate the modified fatigue limit (S_e).

$$S_e = \left(C_{size} C_{load} C_{surf.finish} C_{surf.treat} C_{temp} C_{envir}\right) S'_e \qquad (26)$$

Empirical quantities have been determined over the years of research to define different situations of the above factors, in order to estimate a modified fatigue limit. This modified fatigue limit should approximate the fatigue limit of the component as tested under the conditions described by these factors. Generally, these factors are of greater importance at HCF levels, as they have little influence at short lives. When loading ceases to be fluctuating and is monotonic, these factors approach 1 [21]. Modifying factors include:

Size: The stress gradient in a large component will be less steep, and as a result a larger volume of that component will be subjected to the maximum stress (Fig. 27).

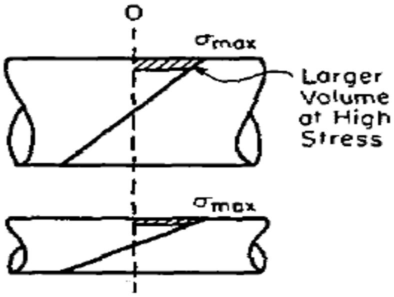

Figure 27: Stress gradient in different size components [21]

Loading: The fatigue limit for a material loaded axially or in torsion may be related to that of a material in bending through

$$S_e\,(\text{axial}) \approx 0.6 \text{ to } 0.9 S_e\,(\text{bending}) \tag{27}$$

$$\tau_e(\text{torsion}) \approx 0.5 \text{ to } 0.6 S_e\,(\text{bending}) \tag{28}$$

Surface Finish: Stress concentrators may be added to the surface of a component by various ways, such as scratches or machining. As the surface roughness is increased, the performance of the component is decreased. Care should also be taken on the type of residual stresses the surface finish may induce in the material. The effects of tensile residual stresses are detrimental, while compressive residual stressed will improve the fatigue life of the component.

Surface Treatment: The majority of cracks initiate on the surface of the component. As a result, the surface treatments play a significant role in the fatigue life of the component. When the conditioning of the surface induces compressive residual stresses and/or increases the carbon content of the material’s surface then the effect is positive and the fatigue limit is improved.

Temperature: High temperatures enable the mobilization of dislocations, may initiate creep, or cause annealing. As a result, the fatigue limit decreases or even disappears as the steel hardness is affected. Lower temperatures have a positive effect on the endurance limit.

Environment: The medium in which the component undergoes cyclic loading may determine the fatigue type that will lead it to failure. Corrosive environments are particularly detrimental leading to corrosive fatigue, and greatly decrease the fatigue limit.

I.3 Results and Discussion

Sections I.1 to I.2.5 of this first part discussed the manufacturing process of steel leaf springs, as well as the theory behind estimating the fatigue life of a component. In more detail, in sections I.1 to I.1.4 the manufacturing process of steel leaf springs was discussed paying extra attention to the heat and surface treatment steps, as well as the effect of these steps on the life and strength of the material. The fatigue life of steel and the different approaches to its estimation were presented in sections I.2 to I.2.4, while section I.2.5 presented the factors that affect fatigue life and how to account for them.

Using the above sections as theoretical background, section I.3 discusses the fatigue life of two different steels, AISI 4130 CF and AISI 6150, through experimental results, finite element analysis and calculations.

The Chromium Molybdenum steel, AISI 4130 CF, of 0.3% carbon content was tested under rotating bending (R=-1). Results of shot peened, carburized and carburized then shot peened specimens cycled till failure will be given in section I.3.1.1, showing the effects of surface treating, residual stresses and carbon content on the fatigue life of steel. Predictions of the fatigue life of AISI 4130 CF, as discussed in theory in section I.2.4, will be given in sections I.3.2.1 and I.3.2.2. Finally, section I.3.3 shows how finite element analysis (FEA) is useful in predicting the fatigue life of steel by introducing a new finite element software that estimates the fatigue life of different materials, fe-safe^{TM}.

The second steel, AISI 6150, is a Chromium Vanadium steel which was fatigue tested at two different load rates. One set of tests was completed at an average loading ratio of *R*=0.25 on heavy-duty vehicle leaf springs, and a second set at *R*=-1 (section I.3.1.2), on specimens appropriate for rotating bending. Based on these results a discussion on the effect of load ratio on the fatigue life of the particular steel (I. 3.1.3), and a failure analysis of AISI 6150 steel specimens based on surfaces of fracture, microstructure, micro and macro-hardness, as well as roughness of these surfaces (section I.3.1.4) is included. As in the case of AISI 4130 CF, the fatigue life of AISI 6150 components is estimated in section I.3.2.2 using Damage Prediction models, and sections I.3.3.1 and I.3.3.2, using FEA.

Both steel grades are common in the automotive industry. However, AISI 6150 is stronger and is more appropriate in leaf spring manufacturing. It is actually one of the most common steels used by leaf spring manufacturers.

The chemical compositions and mechanical properties for the two steels are given in Appendix A.

I.3.1 Experimental Results

I.3.1.1 Surface Treatment Effects on the Fatigue Life of AISI 4130 CF

Rotating bending fatigue experiments of AISI 4130 CF were completed on an R.R. Moore Rotating Beam apparatus (Fig. 28), in order to determine the effects of three different surface treatment methods on the fatigue life of steel specimens. The three surface treatments examined are: shot peening, carburizing, and carburizing followed by shot peening. Smooth, completely untreated, specimens were also cycled until they failed by fracture and were compared to the surface treated ones.

The rotating bending tests are fully reversed loading tests at R=-1. As a result, the minimum and maximum loads, and therefore stresses, applied to the specimens are equal and opposite. In the rotating beam apparatus the specimen is a simple beam that is loaded symmetrically at two points. The beam is rotated around its neutral axis. When the beam is first loaded and cycling has not yet begun, the part of the beam below the neutral axis is stressed in tension. After half a revolution is completed, this part of the beam is now under compression, and when the revolution has completed one full cycle, these stresses are back to their tensile state. As a result, each cycle of rotating bending subjects the specimen through a complete cycle of flexural stress (from tension to compression and back to tension).

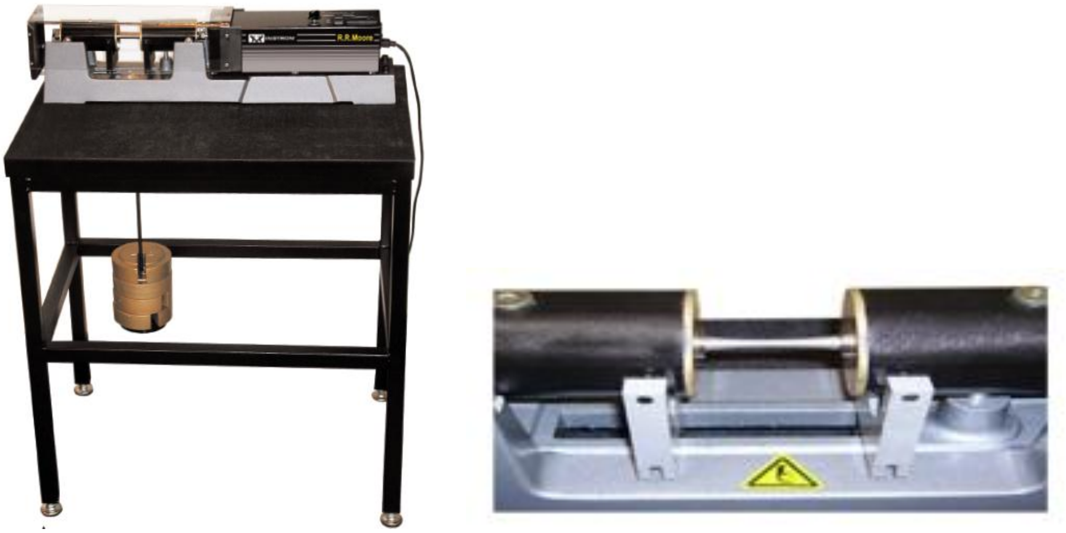

Figure 28: R.R. Moore Rotating Beam Apparatus [66]

The specimens of AISI 4130 CF for the R.R. Moore Rotating Beam tests have an hourglass shape [67] (Fig. 28) with a diameter of 0.95 cm on the sides and a center diameter of 0.48 cm. The total length of the specimen is 7.62 cm. The specimens are fixed on the apparatus with the aid of collets that embrace the right and left sides of the specimen. The specimen is loaded symmetrically at two points, on the right and left of the middle of the beam, while the load can be varied by choosing the desired loading weights, at increments between 0.05 kg to 5 kg. The bending moment capacity of the apparatus ranges between 25 kgcm to 230 kgcm, while a 5kg minimum effective weight should always be accounted for in calculations. Finally the machine has a rotational speed capacity of 500 to 10,000 rpm, and records the number of completed cycles electronically [66].

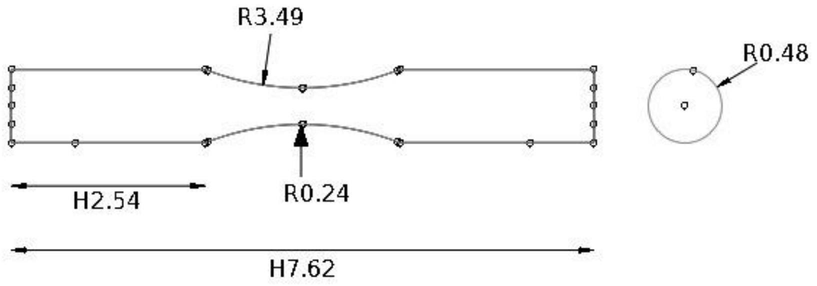

Figure 29: Fatigue Specimen for the R.R. Moore Rotating Beam Apparatus (Dimensions in cm)

The tests on the fatigue life of AISI 4130 CF steel were all completed at a speed of 1,800 rpm (30Hz). The loading varied between 1.6 kg to 18.2 Kg[2], and the tests were completed at maximum stresses varying between 292 MPa and 1081 MPa, depending on the surface treatment. Three specimens were tested at each stress level, in each of the cases of a different treatment.

Fifteen smooth, untreated, AISI 4130 CF hourglass shaped specimens were tested under rotating bending conditions at loads varying from 1.6 kg to 5.45 kg in increments of approximately 0.9 kg. The corresponding stresses range between 292 MPa and 476 MPa, respectively. The specimens were cycled until they failed by fracture. In the HCF region when the specimens have completed a life of approximately 10^7 cycles, assuming that the fatigue limit has been reached at approximately one million cycles, the acceptable life range for steel [21], the tests were interrupted and the current cycle value was recorded.

---

[2] These values do not include the minimum effective weight of 5 kg. This weight was accounted for in the calculation of stresses.

In addition to the above smooth specimens, fifteen AISI 4130 CF hourglass shaped specimens were carburized to a 0.762 mm case depth (typical case depths for the automotive industry range between 0.8 and 1.4 mm [44]), in order to increase the carbon content in the steel. For the carburizing process the specimens, at originally 0.3wt% carbon, were first heated in an endothermic atmosphere to 927°C for four hours. This resulted in a 0.9wt% carbon potential. The temperature was then reset to 829°C for another hour maintaining the 0.90wt% carbon content in the steel. Finally, the specimens were quenched in oil, and then tempered at 216°C for two hours and air cooled at room temperature. The carburizing process is shown in Fig. 30 as temperature versus time in hours.

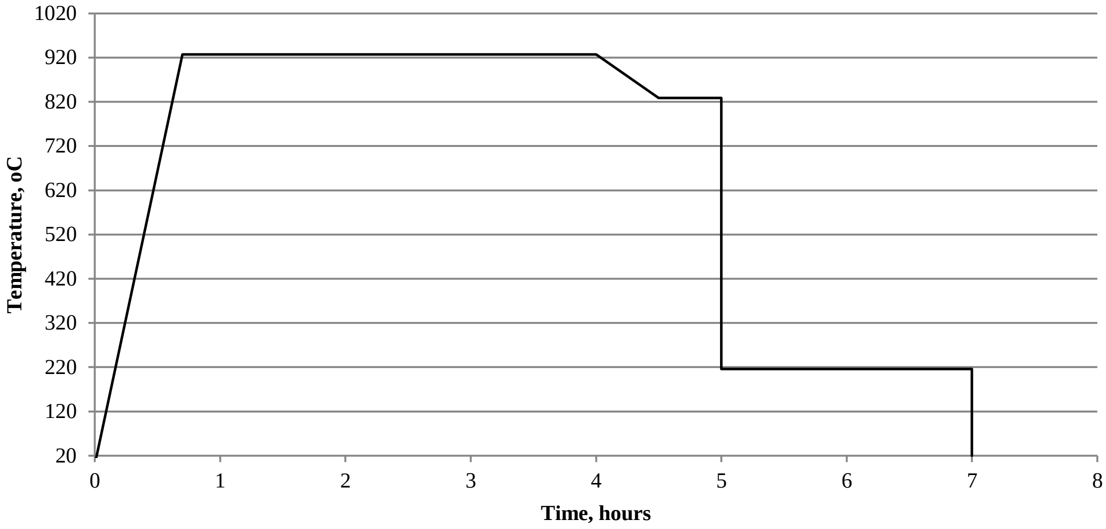

Figure 30: Carburizing process; Temperature versus Time

Apart from the 0.6% increase in the carbon content of the specimens, the surface hardness of the specimens was increased as well. The non-treated AISI 4130 CF specimens have a surface hardness of approximately 201 BHN, while the hardness of the carburized specimens is 615 BHN.

The specimens were tested at seven maximum stress levels between 292 MPa and 1081 MPa. As in the case of the non-treated specimens tests, the maximum stress is equal to the stress amplitude of the tests.

Fifteen AISI 4130 CF hourglass shaped specimens were tested under rotating bending conditions after being shot peened at an intensity of 17 A at a 100% coverage. The shot peening process was completed using a shot of ASH-330 size, which is a steel spherical shot of nominal diameter of 0.84 mm. The process increased the surface hardness of the steel fatigue specimens to 345 BHN, from the hardness of the non-treated specimens of 201 BHN.

The effect on the fatigue life in the case when both of the above surface treatments, carburizing and shot peening, have been applied on the surface of the component was also examined. This double treatment is often used to improve the fatigue strength of high performance gearing [21].

Testing of these double treated components was completed under the same conditions as the ones of the previous three cases of tests. Nine specimens were treated and tested in this case. Tests were carried out at three different maximum stress levels, 562, 865 and 1081 MPa. The results are plotted on an S-N plot in Fig. 31.

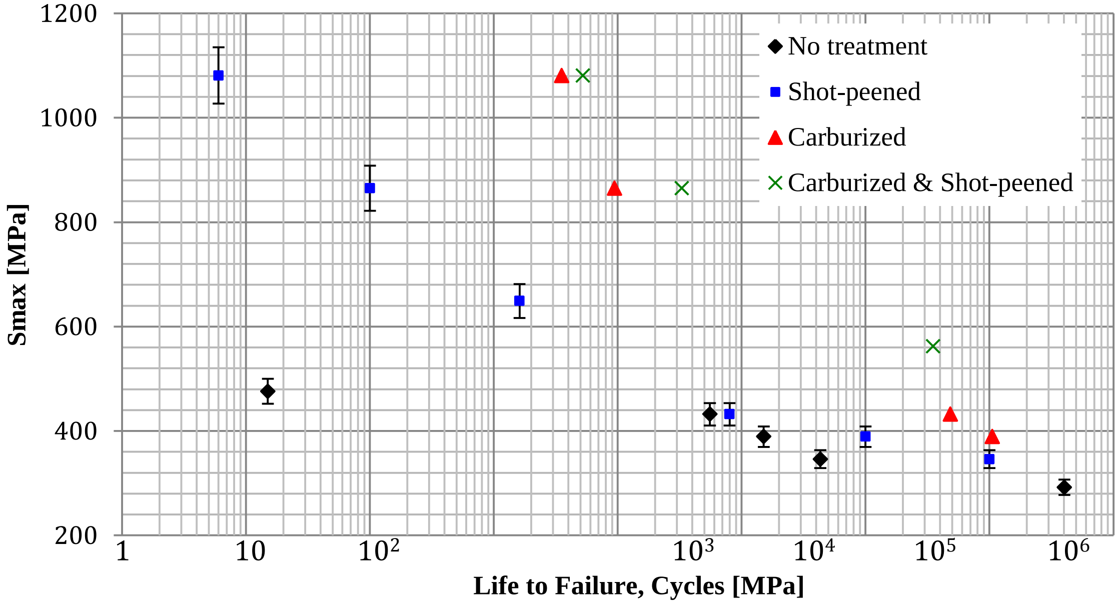

Figure 31: Experimental Results of AISI 4130 CF steel under fully reversed loading

For each stress level of testing three repetitions (trials) of testing were completed and an average fatigue life for the each respective stress level was evaluated. As mentioned earlier the S-N diagrams are plots of stress amplitude (S_a) versus the life to failure of the component, in cycles (N). In the case of rotating bending tests, where loading is fully reversed and R=-1, the stress amplitude equals the maximum stress. The data points of Fig. 31 show the fatigue life of AISI 4130 CF specimens at different stress levels. Each corresponds to a set of data points representing the fatigue life of specimen with different surface treatments. Although three trials were repeated at each stress level, the S-N curves of Fig. 31 represent 50% probability of life [33,35].

For the smooth specimens the life range is between 4×10^7 cycles, at the HCF region, and an average of approximately 20 cycles at the LCF region. At stresses at and above 476 MPa failure was almost instantaneous at loading, and the specimen cycled for at most 46 cycles. This value is below the ultimate tensile strength (UTS) of 676 MPa, as specified by the specimen manufacturer (Appendix A). Machining of the raw material of UTS at 676 MPa, to the hourglass shape appropriate for the rotating bending fatigue tests, has therefore an effect on the fatigue life of the specimen. It is often the case that machining affects the fatigue life of a specimen even when static properties are not affected [21,68]. Taking the fatigue limit of steel to occur at approximately one million cycles and above [21], from the plot of Fig. 31 the fatigue limit of the particular smooth specimens can be approximated to 319 MPa.

Regarding the carburized components it can be observed that for most of the stress levels at which the specimens were tested fatigue lives are in the HCF region. For stresses between 292 and 562 MPa, the fatigue lives of the specimens are much longer than those of the non-treated specimens, and all have magnitudes above 10^6 cycles. The last two stresses examined are at 865 and 1081 MPa, maximum stress values. Fatigue life for these stresses falls in the LCF region, although the specimens still do not fail below 1,000 cycles. The fatigue limit at fatigue lives above 10^6 for the AISI 4130 CF carburized specimens, can be determined from Fig. 31 at a value of approximately 362 MPa, which is 43 MPa larger than that for the non-treated specimens. The surface treatment of carburizing has indeed a positive effect on the fatigue life of the material with an increase of approximately 13% in the fatigue limit.

The fatigue life has thus benefited from carburizing, as presented in the works of Asi and Matloc [45-46,69].

However, carburizing also has a drawback, which demonstrates itself when examining the way the component fails through fracture. Carburizing while increasing the hardness of the component's surface, at the same time renders it more brittle. Fig. 32 shows a non-carburized, (a), and a carburized specimen, (b), that failed under rotating bending. Observing the fractured tips, it is obvious that the non-carburized specimen underwent some deformation before fracture, while the carburized specimen did not deform at all before fracture. Comparing specimens to the photo of Fig. 33, of the two specimens under tensile fracture [31], the carburized steel surface is therefore, more brittle compared to the non-carburized one, as a result of the carburizing process. A change in the color of the steel's surface due to carburizing is also obvious from Fig. 32.

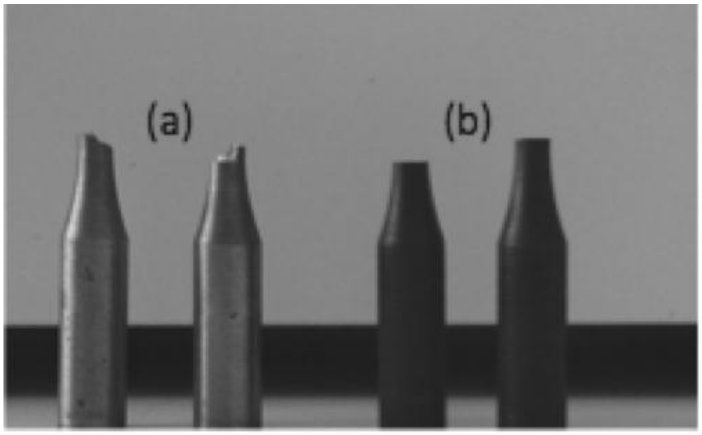

Figure 32: Fractured AISI 4130 Fatigue Specimens: (a) non-treated (b) carburized

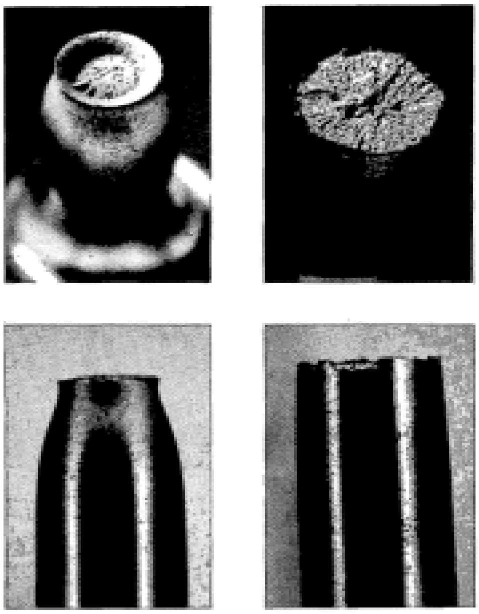

Figure 33: Ductile (left) and brittle (right) tensile fractures [31]

The maximum stress range for the tests on the shot peened components varies between 389 MPa and 1081 MPa, and similarly to the previous two cases of rotating bending tests, this maximum stress range is the same as the stress amplitude range. Again, the specimens were cycled until they failed through fracture, except for the case when their fatigue life extended further than 10^7 cycles. The shot peened specimens survived stresses larger than the ultimate tensile strength of 676 MPa of the untreated material. Almost instantaneous failure upon loading occurs at the maximum stress of 1081 MPa, where the component, if strong enough to be cycled, has a life less than 10 cycles. On the other hand, shot peened specimens survive lives of the HCF region when loaded below 432 MPa.

The fatigue limit for the shot peened components can be set at approximately 341 MPa, at fatigue lives above one million cycles. The fatigue limit of the shot peened components in conjunction with the S-N data shows that shot peening, and consequently induction of compressive residual stresses on the surface of the specimen, favor the fatigue life of the specimen. The fatigue limit of the shot peened component is 22 MPa larger than that of the non-treated components, and 21 MPa lower than that of the carburized components. However, although carburizing seems as a more optimum surface treatment than shot peening, one should always take into consideration the brittle fracture of carburized specimens.

Testing of the double treated components was completed under the same conditions as the ones of the previous three cases of tests. Nine specimens were treated and tested in this case. Tests were carried out at three different maximum stress levels, 562, 865 and 1081 MPa. The lower stress level of 562 MPa, is survived by the components at lives in the HCF region, while 865 and 1081 MPa are sustained by the component for 1.5×10^3 to approximately 4×10^4 cycles.

This double surface treatment of the AISI 4130 CF components gives the best results among the three cases of surface treatments, or no treatment, examined, as far as fatigue life of the specimens is concerned. The fatigue limit in the case of the double surface treatment is 562 MPa, 200 MPa higher than in the case of the carburized specimens, and the surface hardness measured at 562 BHN. However this treatment is not only time consuming, but very costly too.

A closer look at the fatigue lives in the vicinity of 10^5 cycles, shows that the cycles the shot peened component can survive at 432 MPa is within the same magnitude range as those survived by the non-treated specimen. However, below and above 432 MPa the lives of the shot peened component are longer than those of the non-treated one. The question thus arises: what happens in the transition from LCF to HCF region when cycling a shot peened component under fully reversed loading?

The answer to the above question is explained by the concept of residual stress relaxation. As Aggarwal et al. discuss in their study on the effect of shot peening on fatigue life [42], relaxation of residual stresses depends both on the stress level the component is cycled as well as the duration of the cycling process. It seems therefore, that shot peening in the case of AISI 4130 CF specimens is effective above 432 MPa, and has no impact on the fatigue life of the components below that stress. This may be an indication that peening influences flaw nucleation behavior at elevated stresses, but is not as effective at lower stresses.

The factors that have an effect on the fatigue life of a component were mentioned in detail in Section I.2.5. Among these factors size, surface treatments and type of loading were discussed. For the case of the AISI 4130 CF specimens tested under fully reversed loading the surface finish factor can be estimated for the three different surface treatments examined. Table 2 gives these values.

Table 2: Values of Surface Treating Factors

Surface Treatment	**S_e [MPa]**	**S'_e [MPa]**	**$C_{surf.treat}$**
No treatment	319	319	1
Shot Peening	341	319	1.069
Carburizing	362	319	1.135
Carburizing & Shot Peening	562	319	1.762

I.3.1.2 Fatigue Life of AISI 6150 Leaf Springs

AISI 4130 CF is a medium carbon steel utilized in the automotive industry for the manufacturing of different auto parts, but not leaf springs. A more appropriate steel for manufacturing leaf springs, is the previously introduced AISI 6150. AISI 6150 is widely used in the manufacturing of parabolic leaf springs, and it has a composition (Appendix A) high in carbon, manganese and chromium. Contrary to AISI 4130 CF, the spring steel does not contain chromium but the alloying element Vanadium, responsible for the wear resistance of the material, as well as secondary tempering during the tempering procedure of the material.

The leaf springs tested were part of a parabolic multi-leaf assembly, serving as rear suspension in heavy-duty vehicles of the Mercedes ACTROS series. The second leaf of the assembly was used as the specimen for the fatigue tests of AISI 6150 steel (Fig. 34). The geometry of the leaf is shown in Fig. 35. The leaf spring is 1480 mm long and has a varying width of 100 mm at the center and 72 mm at the ends[3]. The characteristic of parabolic leaf springs is their varying thickness lowering the leaf spring's weight, and providing more efficient flexibility, and thus improving ride comfort [5]. As is always the case in parabolic leaf springs, the maximum thickness of the leaf is at its center. In the particular model tested, maximum thickness measures 37 mm, gradually decreasing to 14 mm at the sides. The leaf springs tested have some geometry features that enable the leaf to be assembled with the rest of the leaves of the multi-leaf spring assembly. A center hole of 19 mm diameter allows a bolt to pass through and keep all leaves of the assembly together. The fillet indentations (50 mm in radius) at the ends allow passage for the clamps and U-bolts that hold the assembly together at the sides. The cambering arc varies among the leaves of the assembly. For the second leaf, the one used as specimen for the current fatigue tests, the cambering arc is approximately 23 mm.

---

[3] A detailed engineering drawing of the leaf spring is not displayed due to a non-disclosure agreement signed with the manufacturing company Aysan.

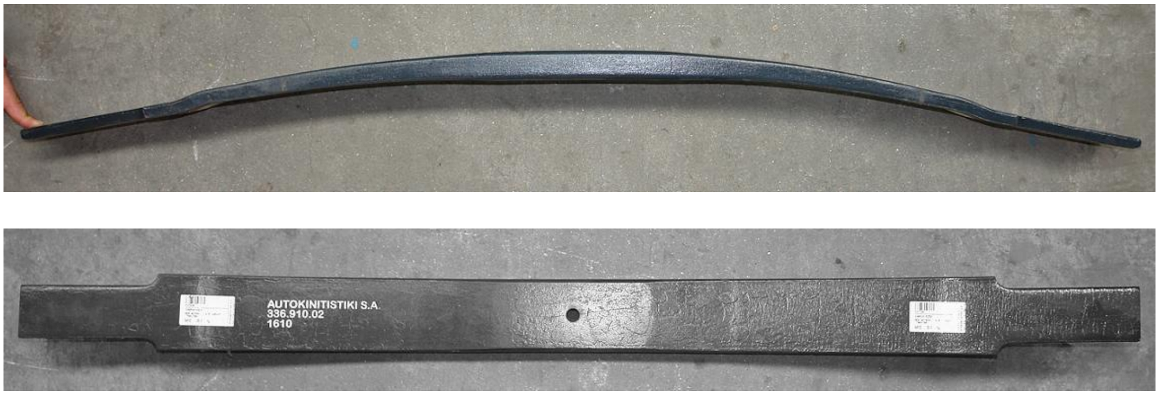

Figure 34: Second Leaf of parabolic rear suspension for Mercedes ACTROS series

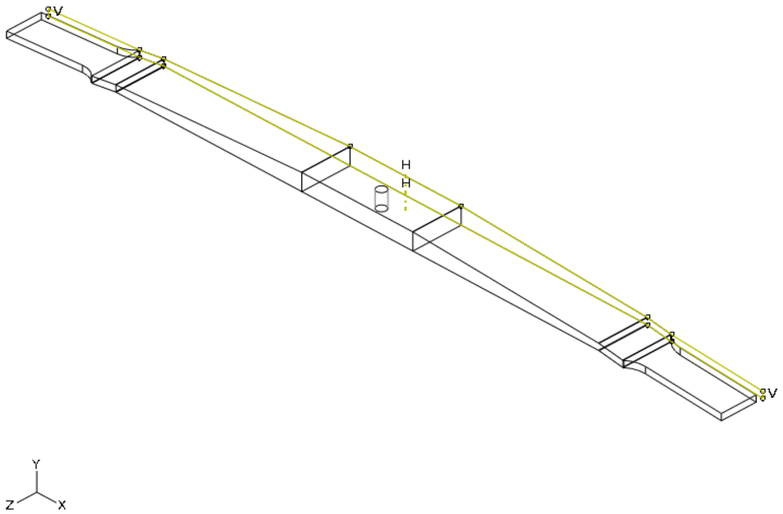

Figure 35: Leaf Spring sketch for ABAQUS/CAE modeling

The manufacturing process for this leaf spring, did not vary from the one presented earlier in this study, apart from an extra stage where the steel leaf is pressed in such a way, so that a variable thickness is achieved. The heat treatment and surface treatment steps of the process were followed, as presented earlier, and as a result the microstrucure of the raw material has been altered, as will be shown later in the discussion of the experiments. The surface of the tempered steel was shot-peened at Almen C intensity between 0.25-0.35, based on the manufacturers specifications.

Eleven full-scale parabolic leaf springs were tested on a servohydraulic fatigue rig (Fig. 36) in the Laboratory Facilities of the Department of Mechanical Engineering at the Aristotle University of Thessaloniki, in Greece. The tests were conducted at three different frequencies: 0.5 Hz at amplitudes of 1,100 MPa, 1.5 Hz, for tests of stress amplitude of 900 MPa, and at 2.1 Hz for stress amplitudes of 500 MPa. The maximum stresses for the tests ranged between 500 and 1,100 MPa, and minimum stresses from 7 to 26 MPa, establishing a test load ratio ranging from 0.1 to 0.3. The load was administered to the center of the leaf spring, which was supported by two simple bearing supports at both sides, at 500 mm from the center of the leaf spring. The leaf springs were cycled until total failure was demonstrated through fracture.

As mentioned earlier, it is at the tension surface of the leaf spring where failure will be initiated [5]. Based on the way the leaf spring is mounted on the test rig (Fig. 36) the tension surface of the leaf during loading is the bottom one. At this surface strain gages were positioned in order to take static measurements of the stress distribution over the length of the leaf spring (Fig. 37).

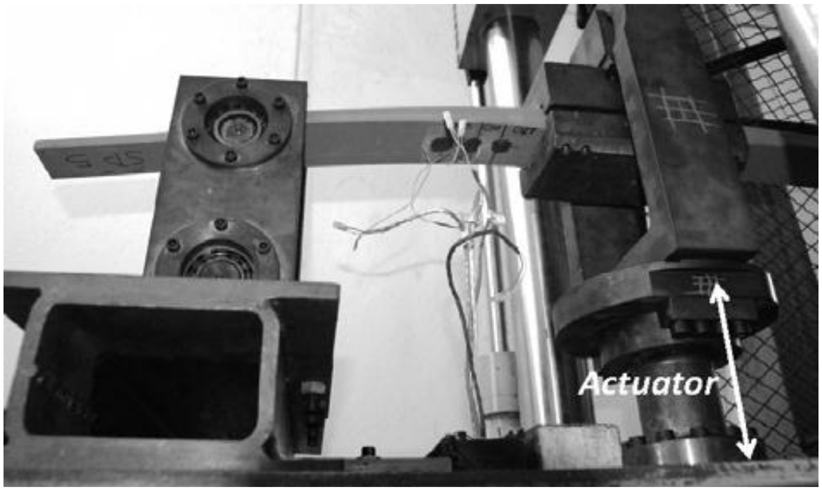

Figure 36: Fatigue Test Rig at Aristotle University of Thessaloniki [26]

The gauge length of the gages was 3 mm, and the gages were positioned at five different distances from the center of the leaf spring, on both sides of the leaf. The leaf spring was loaded monotonically and strain measurements were taken. The corresponding static stresses were calculated using the AISI 6150 Young’s Modulus of 210 GPa. Table 3 and Fig. 38 show the five positions (distance in mm form the center of the leaf) of the strain gages, and the respective stress measurements. The maximum force applied during the monotonic loading of the leaf spring was 103.3 kN. Measurements taken closer to the center of the leaf are of the same order of magnitude, therefore for a distance between 160 and 250 mm the stresses are between 1,030 and 1,100 MPa. However, as measurements are taken further from the center of the leaf the stress magnitude drops an order of magnitude, to 784 MPa at 370 mm, the furthest point tested. The maximum stress occurs at a distance of 250 mm from the center of the leaf, and the magnitude of this stress is 1,100 MPa. Based on this stress profile the leaf spring is expected to fail in the area between the center and loading point of the leaf spring up to approximately 250 mm away. Since the leaf spring is symmetrical on both its sides, and loaded at its center, the same failure prediction sites hold for both sides of the leaf. The 1,100 MPa become therefore, the maximum permissible applied stress and 103.3 kN the maximum allowable load, to be considered on the leaf spring tension surface [26].

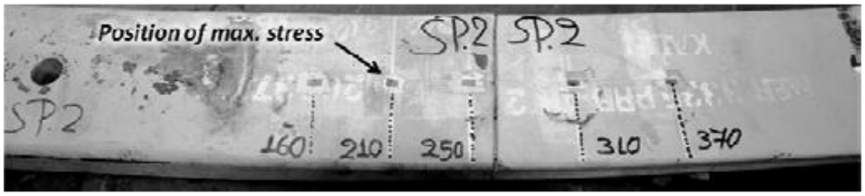

Figure 37: Positions of strain measurements [26]

Table 3: Stress Measurements at the Tension Surface

Position of Strain Gage [mm]	160	210	250	310	370	**Force [kN]**
Stress [MPa]	1030	1100	1082	965	784	103.3

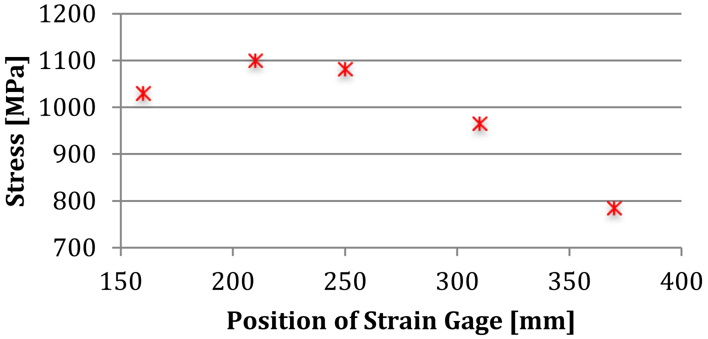

Figure 38: Stress Measurements at the Tension Surface

The fatigue life of the leaf spring is shown in Fig. 39 on a S-N diagram. For the maximum stresses applied, the fatigue life of the component spans between 30,000 cycles and approximately 700,000 cycles. Typical leaf spring applications for heavy-duty vehicles have a design load in the range of 350 and 550 MPa [5]. For these values the current leaf spring tested survives HCF lives above 400,000 cycles. A satisfactory design of leaf spring survives for an average life of 100,000 cycles [5]. Of course, the survival of the leaf spring depends on the road conditions and the loading amplitude the suspension is subjected to. Lower amplitudes, in the proximity of the design load, will survive more cycles than larger amplitudes, when the maximum stress and strain range are increased [5].

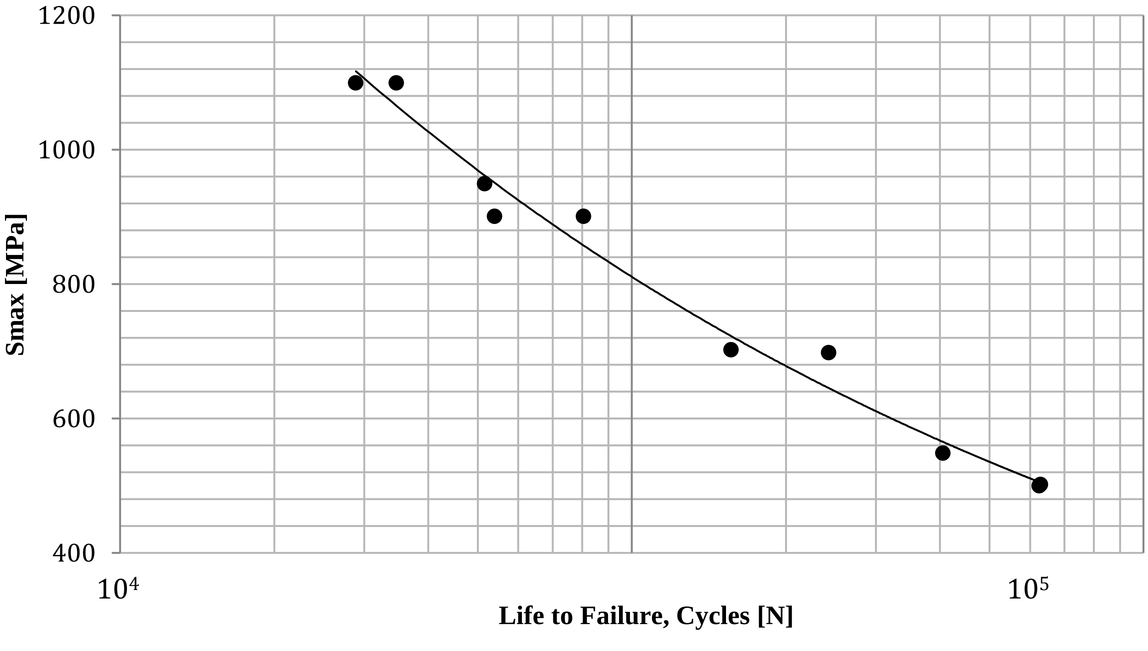

Figure 39: Experimental Results of Leaf Spring Fatigue Tests

The predicted failure location and fracture points, for each specimen are shown in Table 3 and Fig. 38. It is observed that actual failure location is always within the predicted distance between the center and 250 mm from the center.

For each specimen tested the maximum displacement at each cycle was measured, and is shown in Table 4. This displacement and the maximum applied load were used to calculate the spring rate for each specimen. The average spring rate for this leaf spring type is approximately 3 kN/mm.

Table 4: Maximum Displacements and Spring Rates

Max. Displacement [mm]	27.1	22.5	16.6	15.7	31.6	20.2	21.6	28.9	26.9	25.5
Spring rate, k [kN/mm]	3.12	2.83	3.10	2.93	2.27	3.19	3.21	3.20	3.23	3.27

Finally, a linear relationship was observed between the maximum measured stress from the strain gages and the applied load on the leaf. Fig. 40 shows this relationship for all specimens tested.

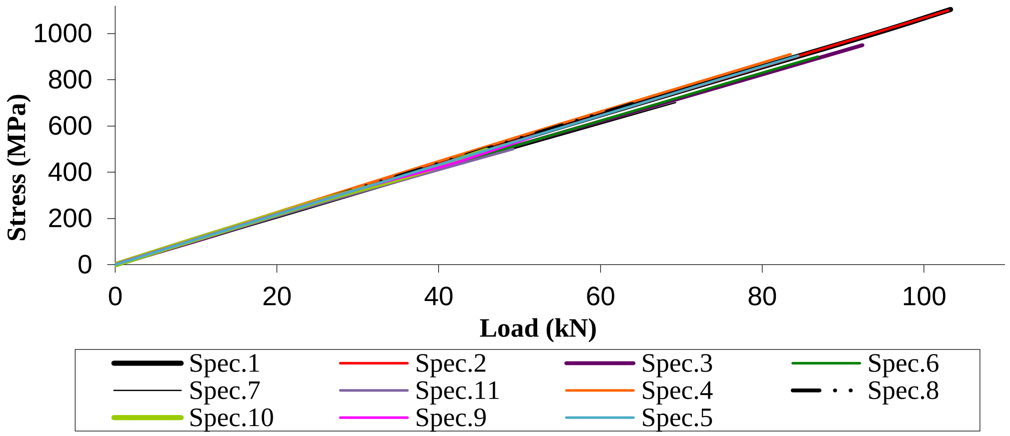

Figure 40: Maximum Stress vs. Applied Load for all Specimens

I.3.1.3 Fatigue Life of AISI 6150 Under Fully Reverse Loading

The same type of leaf springs used as specimens in the previous section’s tests, were used to prepare hourglass shaped fatigue specimens for rotating bending fatigue tests. The specimens were similar in shape to those made of AISI 4130 CF, discussed in the fatigue tests presented in section I.3.1.1, but of different dimensions appropriate for the rotating beam apparatus. Fig. 41 shows a dimensioned drawing of the 9 mm in nominal diameter specimens, and a picture of a mirror polished specimen ready for testing is shown in Fig. 42. The tests were completed on a rotating beam apparatus in the Laboratory Facilities of the Department of Mechanical Engineering at the Aristotle University of Thessaloniki, in Greece (Fig. 43). The specimens were fixed symmetrically on each of their sides on the testing apparatus via mechanical clamps, and two equal masses were positioned on the left and right side of the apparatus, to provide the appropriate loading for the tests. The specimens were rotated with the help of an electric motor at a speed of approximately 100 Hz (6,000 rpm). The tests were completed for stress amplitudes between 450 and 850 MPa. Specimens were rotated until failure was detected through fracture, or until the specimens survived at least one million cycles.

Similarly to the leaf spring fatigue tests, static stress measurements were taken before cycling of each specimen. A single strain gage was positioned in the middle of the specimen (Fig. 43), were failure has occurred in the AISI 4130 CF rotating bend tests, and the specimen was loaded and cycled one full revolution manually.

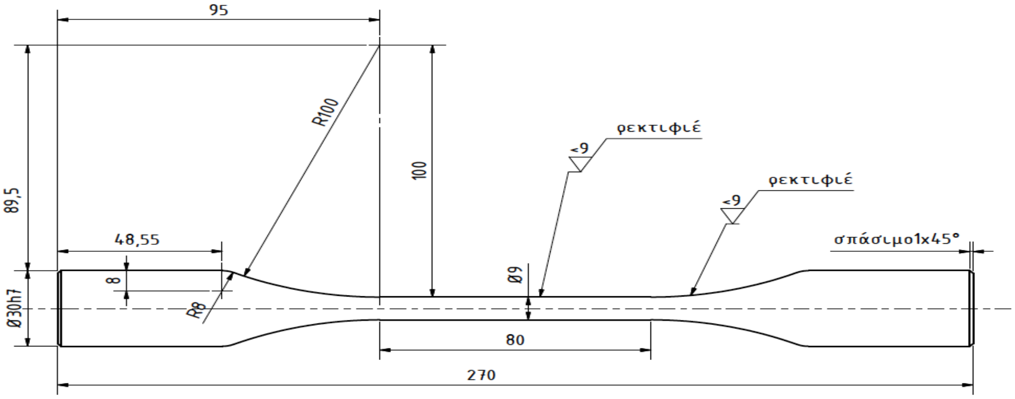
95
R100
100
89,5
48,55
8
R8
Ø9
ρεκτιφιέ
<9
ρεκτιφιέ
<9
σπάσιμο1x45°
Ø30h7
80
270

Figure 41: AISI 6150 Fatigue Specimen, dimensions in mm

Figure 42: AISI 6150 Fatigue Specimen

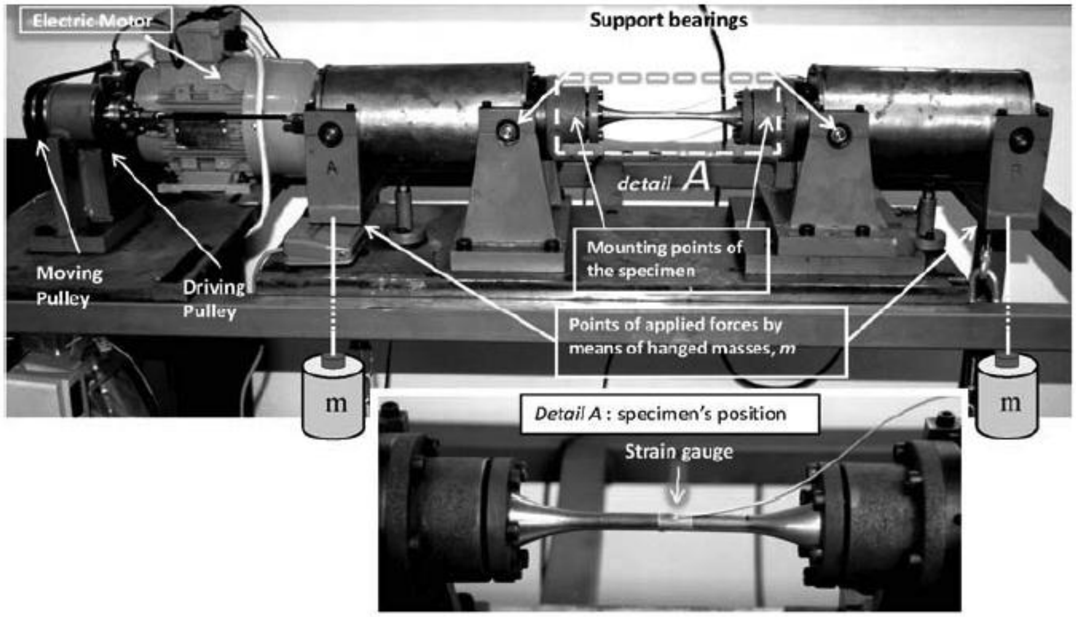
Electric Motor
Support bearings
A
detail A
B
Mounting points of the specimen
Moving Pulley
Driving Pulley
Points of applied forces by means of hanged masses, m
m
m
Detail A : specimen's position
Strain gauge

Figure 43: Rotating Beam Apparatus in Aristotle University of Thessaloniki

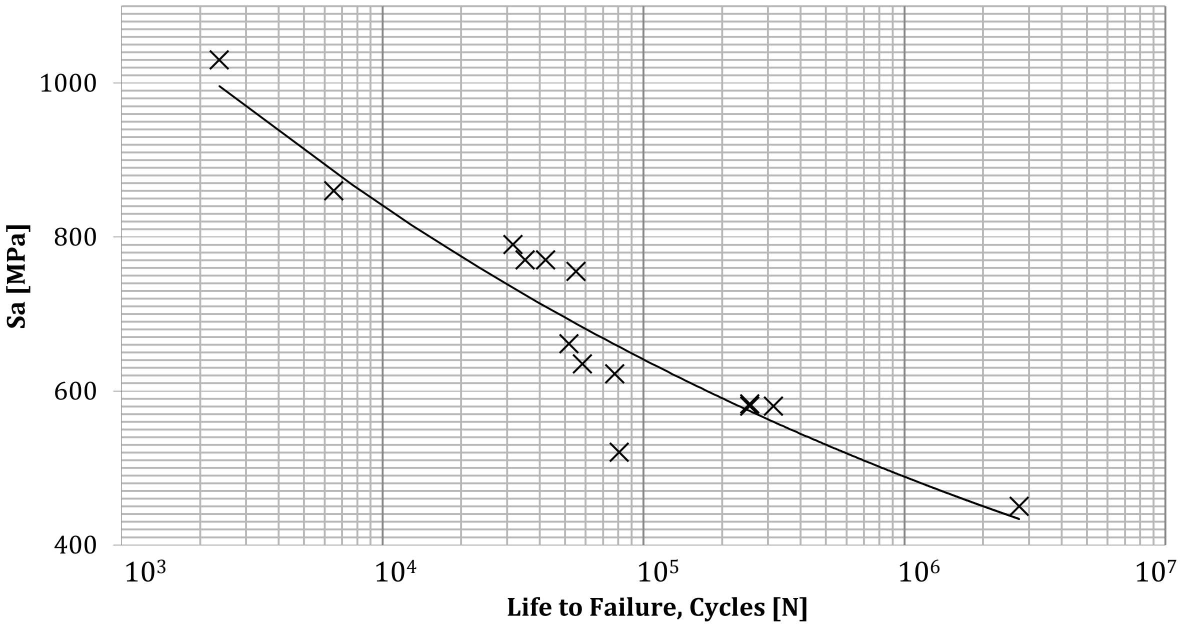

Figure 44: AISI 6150 Fatigue Life under fully reversed loading

It was previously mentioned that the fatigue life of a component is longer at applications of larger loading ratios [21,28,32-33,54]. On the other hand, the ultimate strength of a material also plays a significant role in determining the fatigue life of a component. A comparison between the leaf spring fatigue tests at an average load ratio of 0.25, and the rotating bend tests under fully reverse loading (R=-1), shows that the rotating bend fatigue data, at the smallest load ratio, survives larger lives. As shown in Fig. 45, where the applied stress amplitude, linearized to the ratio of the ultimate strengths of the surface and the core, is plotted versus life to failure, specimens under R=-1 loading fail slower despite the low loading ratio. In the case of the tests compared here the ultimate strength and microstructure of the core of the leaf spring present better performance than the microstructure and ultimate strength of the surface of the leaf spring.

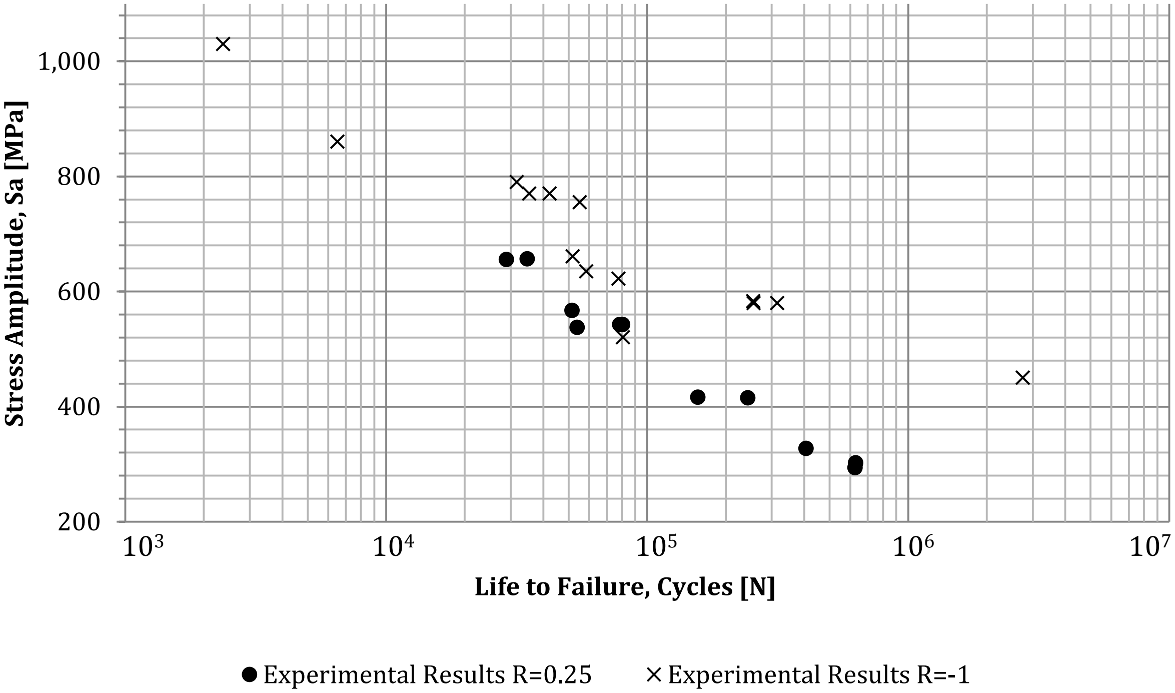

Figure 45: Fatigue life for AISI 6150 Steel at R=-1 and R=0.25

I.3.1.4 Failure Analysis of AISI 6150

Surfaces of Fracture

As mentioned previously, failure in leaf springs generally starts in the tension surface of the leaf [5]. This was also shown during failure of the tested leaf spring in section I.3.1.2. Failure occurred in the predicted region of maximum stress on the tension surface of the leaf spring specimens, and the fatigue cracks were either initiated at a corner or the surface of the leaf spring (Fig. 46). In the case of the rotating bend specimens, pictures of the fractured surface were taken under a stereo-microscope (Fig. 47). From the two figures of the fractured surfaces, in each of the two cases of AISI 6150 specimens, the initiation point is visible, as expected under cyclic fatigue conditions [70], the crack propagation striations, along which the crack grew until it reached a critical length leading the leaf spring to failure. The propagation duration and crack length depend on the applied load magnitude.

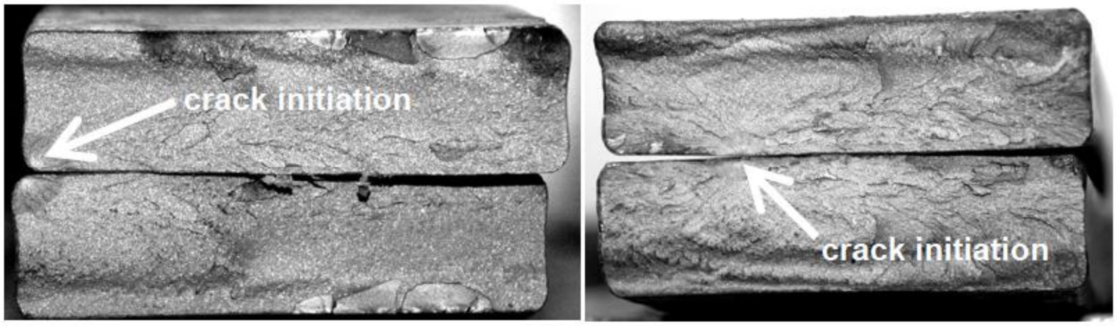

Figure 46: Fractured Surfaces of Leaf Spring [26]

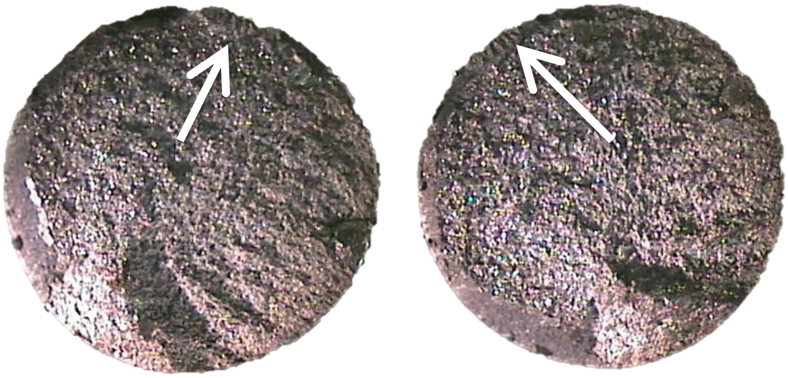

Figure 47: Fractured Surface of Fatigue Specimen

Microstructure of Surfaces of Fracture

A macroscopic observation of the fractured surfaces may give information on the initiation point and propagation path of a crack, but an analysis of the microstructure of these surfaces can give greater insight of the surface properties of the components.

Samples from the vicinity of fracture were cut after the fatigue tests on AISI 6150 steel were completed. The samples were mounted on a Bakelite amber mold using an automatic press, similar to the one in Fig. 48(a) [31]. When the Bakelite powder had consolidated, the sample (Fig. 48(b)) was then removed form the press to be ground. Grinding paper of grit ranging from 120 to 1200 was used for coarse to fine grinding. The specimens were then coarsely polished to 3-μm roughness. Polishing was completed using an Alumina abrasive (Al_2O_3), and a synthetic suede cloth. Before observing the microstructure of the steel samples under an optic microscope, the samples surfaces were etched with 4 % Nital.

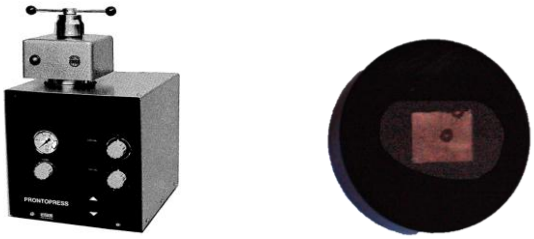

(a) **(b)**

Figure 48: Automated press (a)[31], Specimen mounted in Bakelite Amber mold (b)

Samples of both the core and surface of the specimens were examined. The core specimens display a martensitic microstructure, as is expected for a steel that has undergone quenching and tempering [5,16], as the steel undergoing a leaf spring manufacturing process. Both the leaf spring and rotating bent specimens exhibit a tempered martensitic microstructure shown in Fig. 49, as compared to Fig. 50. On the other hand, when comparing the surface microstructures of the leaf spring and the rotating bend AISI 6150 specimens, it can be observed from Fig. 51, that only the rotating bend specimen maintains the same tempered martensitic microstructure. This is based on the fact that the rotating bend specimens are machined from the very core of a leaf spring, where the microstructure is uniform. The surface structure of the leaf spring specimen (Fig. 51) shows a recrystallized zone, with denser grain structure than that of the surface microstructure of the rotating bend specimen. The color of the leaf spring surface microstructure, is lighter than that of the rotating bend specimen due to decarburization of the leaf spring surface during the tempering process of its manufacturing. Decarburization works in the opposite direction than carburization. It is the loss of carbon from the surface of a ferrous metal, when the later is heated in a medium that may initiate a reaction with carbon [5,16]. The effects of the loss of surface carbon have a negative effect on the fatigue life, and as a result fatigue limit of the component in question [21,35]. Table 5 shows the effects of decarburization on some high strength steels, of lower carbon content than the one examined in this study [35]. The fatigue limit of these steels reduces up to approximately 80% in a decarburized component.

Table 5: Effect of Decarburization on the Fatigue Limit of High Strength Steel [35]

			Fatigue Limit [MPa]	
Steel	**Core Hardness, Rc**	**Tensile Strength [MPa]**	**Undecarburized**	**Decarburized**
AISI 4140 bars	48	1,634	717	214
	28	965	503	221
AISI 5140 bars	48	1758	862	200
	28	972	538	241

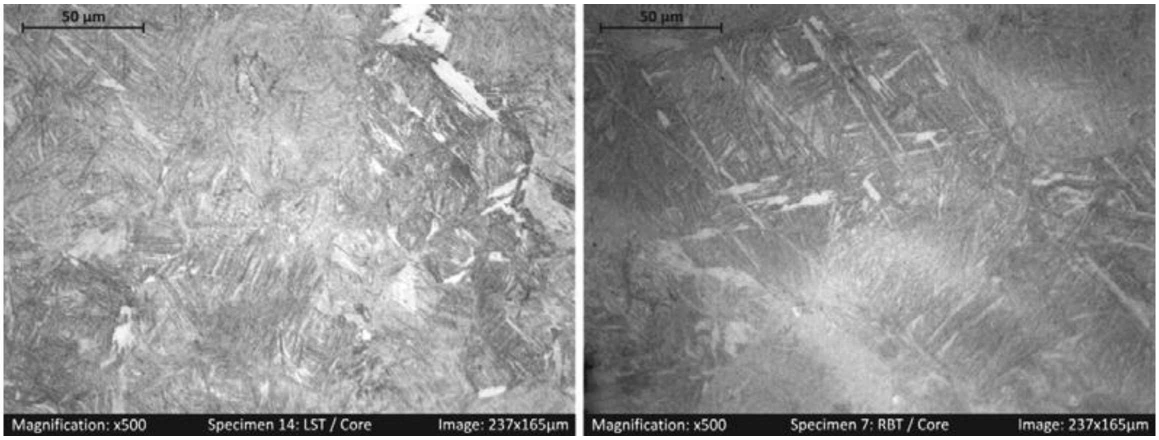
50 µm
Magnification: x500
Specimen 14: LST / Core
Image: 237x165µm
50 µm
Magnification: x500
Specimen 7: RBT / Core
Image: 237x165µm

Figure 49: Core microstructure of the leaf spring (left) and fatigue (right) specimens [26]

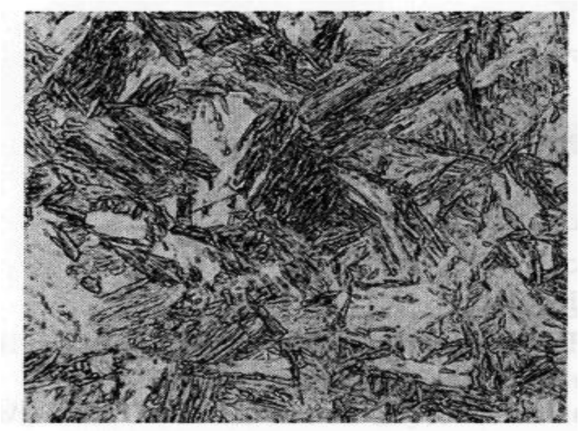

Figure 50: Lath Martensite [71]

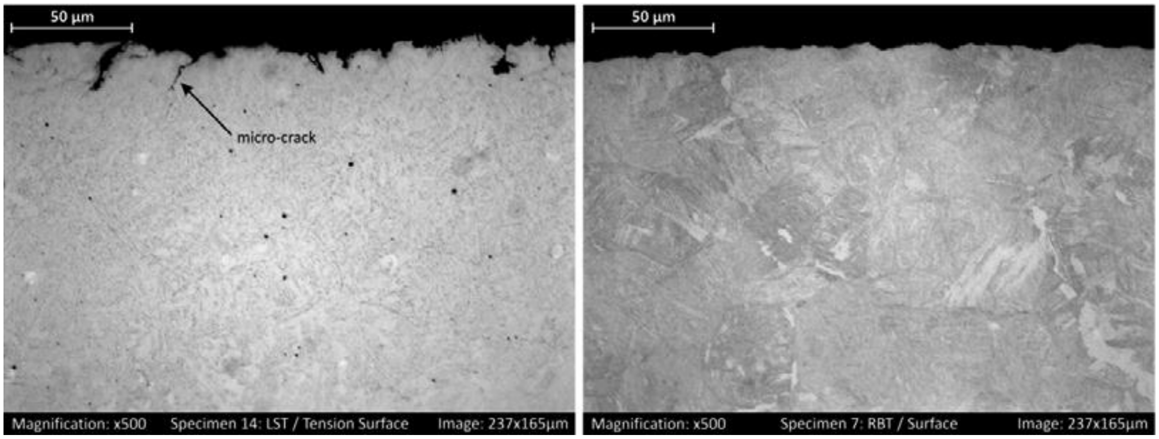
50 µm
micro-crack
Magnification: x500
Specimen 14: LST / Tension Surface
Image: 237x165µm
50 µm
Magnification: x500
Specimen 7: RBT / Surface
Image: 237x165µm

Figure 51: Surface microstructure of the leaf spring (left) and fatigue (right) specimens [26]

Micro-hardness of Surfaces Fracture

Following the microstructure observations, micro-hardness measurements were taken on samples from both the leaf spring and the rotating bend specimens. The measurements were made on the Vickers scale (HV10), and Vickers pyramid impressions were taken stepwise, on the surface and to a depth of approximately 400 μm form the surface (Fig. 52). Measurements were also taken along the surface of the samples, thus giving comprehensive hardness profiles of the core, tension and compression surfaces. The micro-hardness profiles are shown in Fig. 53 as a function of distance form the surface of the sample. It is obvious from the graph that for the leaf spring specimens the micro-hardness of the tension and compression surfaces is lower closer to the surface than closer to the core. It was mentioned earlier, when discussing the heat treatment processes, that carburizing increases the hardness of a steel component [5,16], as was also the case of the carburized AISI 4130 CF rotating bend specimen. Decarburizing has the opposite effect, and this is why the surface hardness of the leaf springs is lower at and near the surface. The fact that the heat treatment the steel is subject to, during the leaf spring manufacturing process, is the reason of the lower micro-hardness values, can be understood if the leaf spring measurements are compared to those made on the rotating bend specimen. The measurements on the rotating bend specimens, machined form the core of the leaf spring, being the steel part the least affected by the tempering process, present an almost constant profile of micro-hardness as measurements are taken from the surface to the center of the component. These measurements are close to the micro-hardness measurements taken close to the core of the leaf spring.

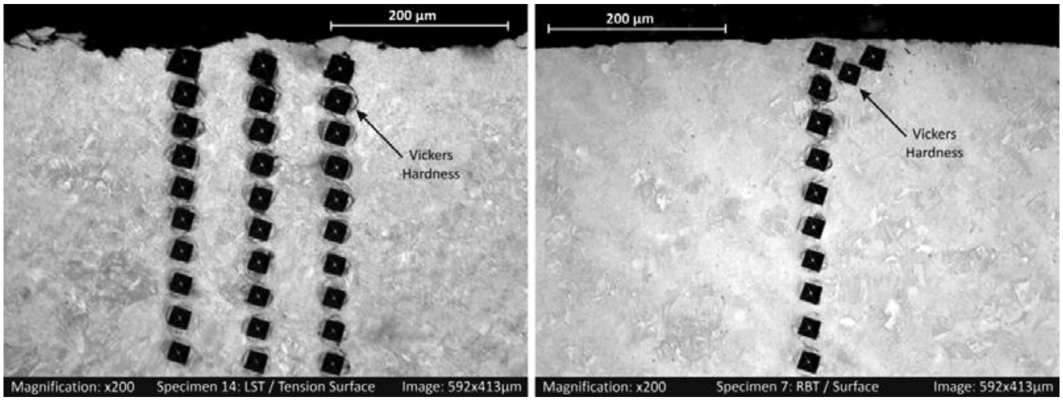
200 µm
Vickers Hardness
Magnification: x200
Specimen 14: LST / Tension Surface
Image: 592x413µm
200 µm
Vickers Hardness
Magnification: x200
Specimen 7: RBT / Surface
Image: 592x413µm

Figure 52: Vickers pyramidal impressions on surface of the leaf spring (left) and fatigue (right) specimens [26]

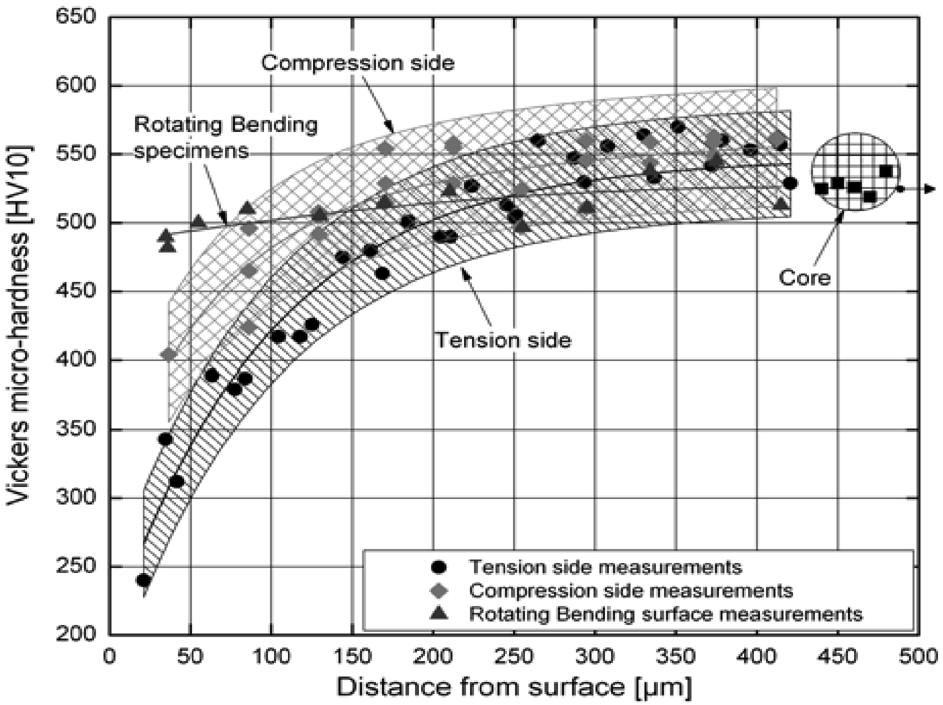

Figure 53: Micro-hardness profiles of the core and surface of the two types of AISI 6150 specimens [26]

Macro-hardness of Surfaces of Fracture

To investigate the effect the change in hardness has on the steel properties, macro-hardness measurements were also taken at the tension and compression surfaces, as well as the core of the leaf spring specimens. The measurements were made in the Rockwell C scale (HRC) and the corresponding tensile strength was calculated [70,72]. Table 6 shows the macro-hardness measurements, as they decrease from the core to the tension and compression surfaces. Both surfaces exhibit the same hardness, as they were both exposed to the same heat-treating environment during the manufacturing process. A decrease of approximately one order of magnitude is observed in the tensile strength, as the macro-hardness decreases from the core to the surface, giving a reason why a crack will initiate on the surface. These values also explain why the specimens under fully reversed loading perform at longer lives than the leaf springs.

Table 6: Rockwell-C Macro-hardness Measurements and Corresponding Tensile Strength

Core		Surface			
		Tension		Compression	
Mean HRC	R_m [MPa]	Mean HRC	R_m [MPa]	Mean HRC	R_m [MPa]
49.1	1630	31	995	31	995

Roughness of Surfaces of Fracture

Earlier it was mentioned that the critical surface of a leaf spring is the surface that will operate under tension, during the cyclic loading of the leaf [5]. Consequently, between the tension and compression surfaces, the former is the one whose fatigue life needs to be enhanced. For reasons concerning manufacturing time and economics, the shot peening step of the manufacturing process is not performed on both surfaces of the leaf. The leaf is inserted in the shot peening chamber with the tension surface exposed to the shots, and when the peening is over, instead of repeating the process on the other surface, the leaf is sent to the painting chamber. A measurement of the surface roughness of the AISI 6150 leaf spring specimen shows that only the tension surface was shot peened in the case of the specimens tested, having a mean roughness value of 30 μm on the tension surface [26], twice the value of roughness measured on the compression surface (Fig. 54).

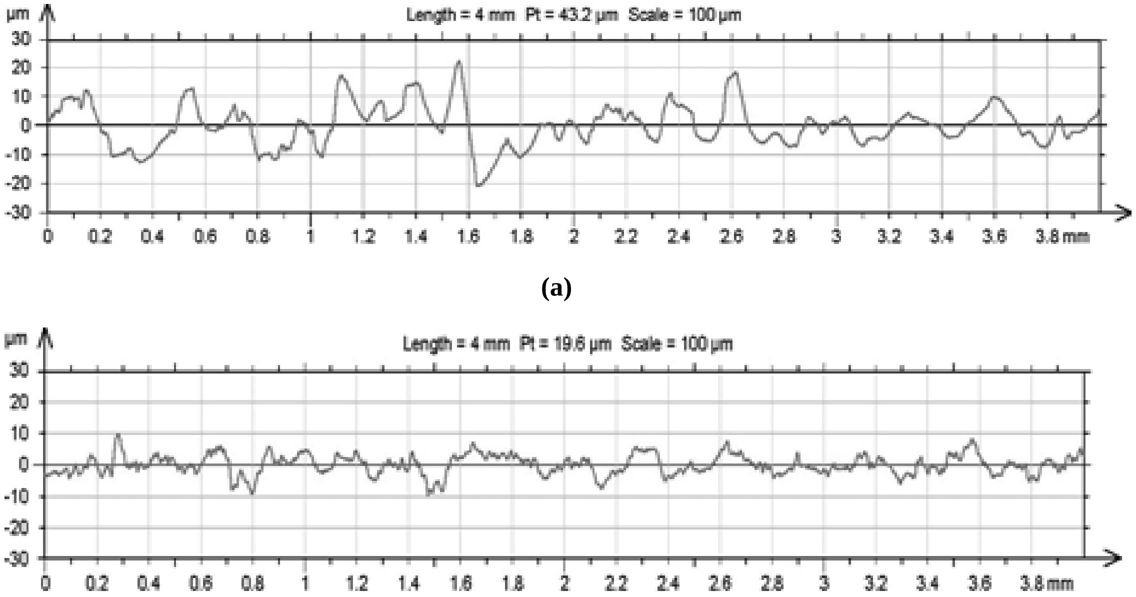

(a)

(b)

Figure 54: Roughness measurements on the tension (a) and compression (b) surfaces of the leaf spring specimen [26]

I.3.2 Calculations

I.3.2.1 Prediction of Fatigue Life of AISI 4130 CF using the Power Relationship

Earlier in this discussion a power law relationship was presented as the estimate of the S-N curve for steel components, (Eq. 20). The power law relationship will estimate the S-N curve for lives between 10^3 and 10^6 cycles [21].

The exponents, C and b, in the relationship of Eq. 20 are estimated based on the fatigue limit (S_e) and the alternating stress at which the component survives 1,000 cycles (S_{1000}).

In the aforementioned discussion it was shown that the fatigue limit (S_e) similar to the ultimate strength (S_u), could be calculated if information on the hardness of the component is known.

The power law relationship parameters of Eq. 21a and 21b require information on the stress level that is survived at approximately 1,000 cycles. This life is the smallest life for which the power relationship gives an estimated prediction for the S-N curve. If there is no information on the alternating stress corresponding to 1,000 cycles to failure (S_{1000}), this stress can also be estimated using the ultimate strength (S_u) [21]

$$S_{1000} = 0.9 \times S_u \tag{29}$$

The power relationship for each of the above cases of surface treated AISI 4130 CF components are shown in Table 7. Since the fatigue limit (S_e) can be estimated based on Eq. 18b and 19b for hardness of no more than 400 BHN, and above this hardness value the fatigue limit will always be equal to 700 MPa, predictions for the carburized and double treated components will be identical.

Table 7: Power Law Relationship and Parameters

Hardness [BHN]	Treatment	S_u [MPa]	S_e [MPa]	S_{1000} [MPa]	$S=10^C N^b$
201	No treatment	693	347	624	$S=10^{3.05}N^{-0.085}$
345	Shot peened	1190	595	1071	$S=10^{3.29}N^{-0.085}$
555	Carburized	1400	700	1260	$S=10^{3.36}N^{-0.085}$
615	Carburized &Shot peened	1400	700	1260	$S=10^{3.36}N^{-0.085}$

Fig. 55 shows the curves of Table 7 in comparison to the experimental results from the previous sections. The S-N curves for experimental results are those of the average value of all trials. A closer look helps draw a first observation regarding the shot peened component. The estimated fatigue life using the power law relationship is much longer than the experimental results. This discrepancy between the two curves is based on the fact that the theoretical model does not account for the relaxation of residual stresses, which affects the fatigue life of a component, as shown in the previous section.

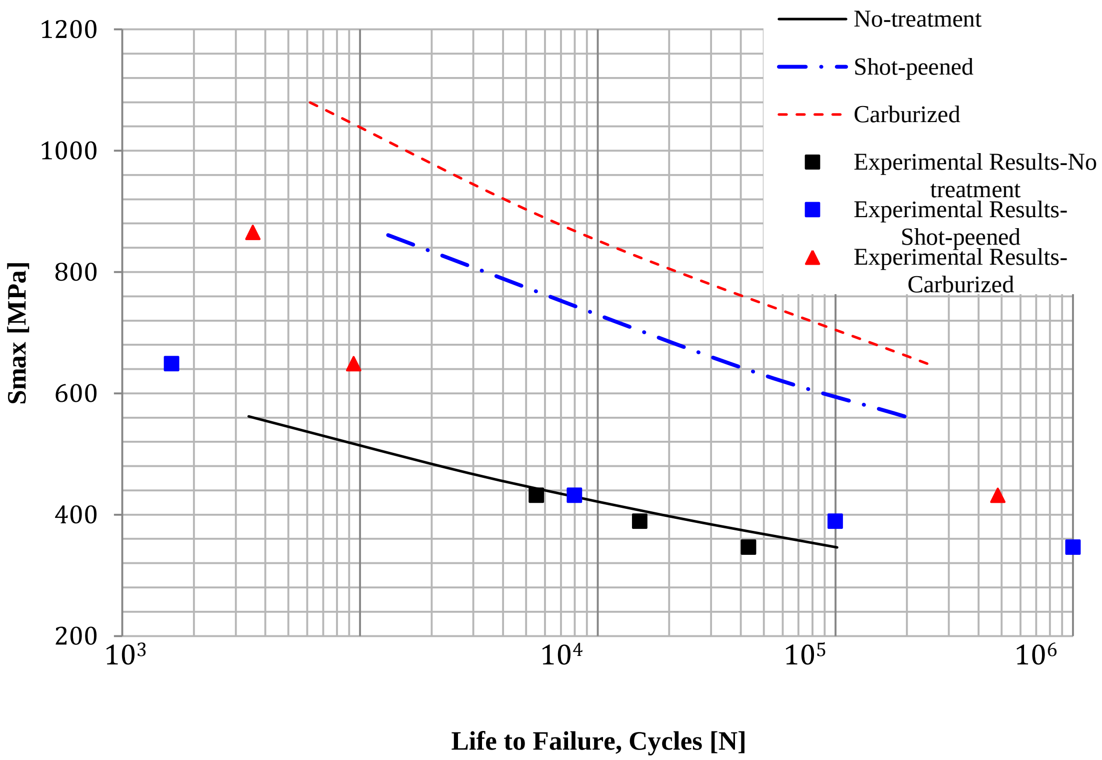

Figure 55: S-N Curves of AISI 4130 CF Steel from Power Law Relationships

The same pattern is observed in the case of the carburized component. Predictions of the carburized component's fatigue life, using the power law relationship, are much longer than those derived from the rotating bending tests. The hardness of the carburized component of 615 BHN exceeds the hardness limit of 400 BHN for calculation of a theoretical fatigue limit. As a result, a fatigue limit of 700 MPa is assigned in such cases, making predictions very general and consequently inaccurate.

On the other hand, experimental data of the non-treated specimen, and theoretically predicted S-N curve for the same component in Fig. 55 seem to be in better agreement than the rest of the results, especially at lives in the proximity of 10^5 cycles. At longer than 10^5 lives the power law relationship gives better results for the fatigue life of the non-treated component, while the opposite occurs at lives below the threshold of 10^5 cycles. To explain this difference in the fatigue lives due to experiments and due to predictions from the power law relationship, one should take into account that most of the parameters used to calculate the power law relationship are mere estimates based on the components hardness, and effects of machining or other parameters are not included.

At longer lives, longer than 10^5 cycles, the predicted fatigue life of the non-treated component is better when the power law relationship is used. The power law relationship assumes an “infinite life” at the fatigue limit (S_e), and as a result the predicted S-N curves are flatter in the vicinity of 10^6 cycles.

It can thus be concluded that the power law relationship is a valid way to estimate the fatigue life of a component, always depending on the degree of certainty required by these results. This empirical relationship does not give valid predictions for the fatigue lives of components that have been surface treated, as it does not take into account many important factors, as is stress relaxation, which affect the fatigue life of the component, or hardness above 400 BHN. Finally, this empirical relationship used to determine the S-N curve is conservative at lower lives, when the plastic strains due to higher loading affect the performance of the component. On the other hand, at longer lives the estimation of the S-N curve using the power law relationship gives a longer lives and a higher fatigue limit. However, the predictions agree with experimental data in the transition lives between LCF and HCF regions.

For the majority of steel components the exponent of N in Eq. 20 has a value of -0.085. Provided that the material in question is steel and the ratio of the fatigue limit to the ultimate strength is 0.5, Eq. 20 can be rewritten in terms of the ultimate strength as [21]

$$S = 1.62 S_u N^{-0.085} \quad for \;\; 10^3 < N < 10^6 \tag{30}$$

When the hardness of a steel component is not known, but its carbon concentration is, the graph of Fig. 26 can be used to estimate the hardness and microstructure of the steel. The microstructure of the steel may be martensite, tempered martensite or fine pearlite, based on the heat treatment the steel has been processed through. As a result, knowing the carbon concentration of the steel, three different levels of hardness may be read from the hardness as a function of carbon concentration graph (Fig. 26), based on the three microstructures.

Two different carbon concentrations are known for the AISI 4130 CF steel. The untreated components have a 0.3wt% carbon, while the carburized components have a 0.9wt% concentration on their surface layer at a case depth of 0.762 mm. For each of these two concentrations the hardness versus carbon concentration graph (Fig. 26) can supply information for an upper and lower limits of surface hardness. Table 8 gives the hardness for the lower limit, at pearlite microstructure, and the upper limit, martensite microstructure. These limits of hardness can be used in the power law relationship in order to empirically define an S-N curve for AISI 4130 CF steel in each of these microstructures and stress concentrations. Comparing the hardness values of Table 8 to those measured on the fatigue specimen surfaces, it can be concluded that the non-treated specimens of 210 BHN are somewhere between a fine pearlite and martensite microstructure, rather more close to fine pearlite, while the carburized specimens of 615 BHN are closer to a martensitic microstructure.

Table 8: BHN Hardness for Fine Pearlite and Martensite Steels at 0.3wt% and 0.9wt% C Concentrations

Concentration (wt% C)	**Fine Pearlite BHN Hardness**	**$S=10^{C}N^{b}$**	**Martensite BHN Hardness**	**$S=10^{C}N^{b}$**
0.3	150	$S=10^{2.92}N^{-0.085}$	570	$S=10^{3.22}N^{-0.085}$
0.9	295	$S=10^{3.36}N^{-0.085}$	697	$S=10^{3.22}N^{-0.085}$

The graph in Fig. 56 shows all S-N curves determined form the values of Table 8, and the curves for the non-treated and carburized specimens determined by the tests of the AISI 4130 CF specimens under fully reversed cyclic loading. The S-N curve based on experimental data of the untreated specimen falls between the S-N curves determined by the hardness for 0.3wt% C concentration. Experimental results are closer to the lower limit of hardness, that of fine pearlite microstructure at 150 BHN, agreeing thus with the above conclusion of a fine pearlite microstructure based on the hardness value. The values of the empirically determined curve coincide with experimental results close to lives of 1,000 cycles. The same pattern occurs when examining the empirical results for the 0.9wt% C concentration and the carburized experimental data curve. The curve of the experimental data falls in between the two curves constructed based on the fine pearlite and martensite hardness of 295 HBN and 697 HBN. At lower fatigue lives, at and below 10^4 cycles the experimental data curve tends to the martensite limit. At longer lives the experimental data curve approaches the fine pearlite curve, while it almost coincides with it at the vicinity of 10^6 cycles.

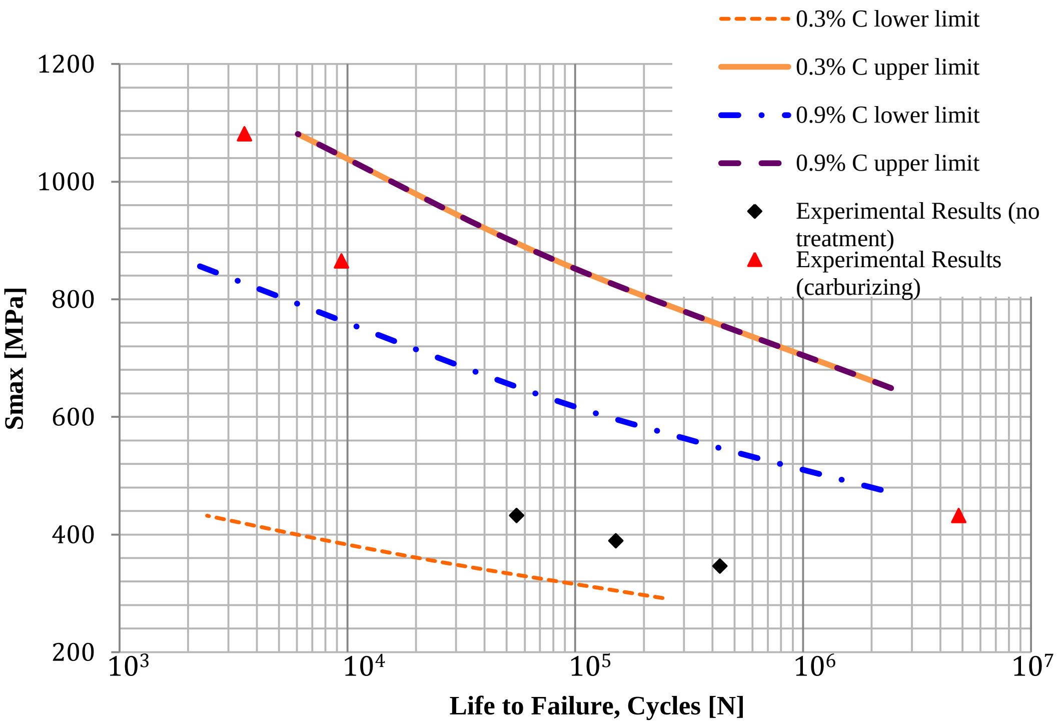

Figure 56: S-N curve of AISI 4130 CF Fatigue Specimens, based on surface Carbon content

The surface treatment of carburizing is a surface treatment requiring heat, to trigger the diffusive process that will enhance the steel surface with extra carbon. During this process, the steel was heated to a high temperature (920°C), which changes the microstructure of AISI 4130 CF steel to austenite, and then quenched quickly at a lower temperature of 220°C, where the formation of martensite is possible. As a result, not only the structure of the surface of the specimen has become martensitic, but compressive residual stresses have been induced on the surface of the steel due to differences in microstructure between the surface and the core, created due to the quenching process (section I.1.2). As mentioned in the case of the fatigue life of shot peened components these residual stresses relax as the stress level and revolutions of cycling increase. Taking this into consideration, the tendency of experimental data to the lower limit S-N curve, due to the 295 BHN hardness, can be explained.

A final observation on the graph in Fig. 56 is based on a comparison of the S-N curves empirically determined using the power law relationship at the higher limits of hardness, at martensitic microstructures. The S-N curve for 0.3wt% and 0.9wt% C are identical. The reason for this similarity of the two fatigue lives is based on the fact that the power law can be predicted up to a hardness of 400 BHN. Above this hardness only one fatigue limit is possible for the calculation of the S-N curve, of 700 MPa.

I.3.2.2 Prediction of Fatigue Life Using Damage Prediction Models

The discussion up to this point concerns the total fatigue of the component being cycled until it fails completely by fracture. However, while the component is being cycled it fatigues and damage accumulates slowly leading to failure of the component. Damage accumulation is very important when variable amplitude loading conditions are imposed on the component being cycled [28], but it is equally important in understanding how a component fatigues under constant amplitude cyclic stress.

In this section the three damage accumulation models (Eq. 22-24) presented earlier are examined for the case of AISI 4130 CF and AISI 6150 steel. Damage accumulation for the steel is estimated for each model, and the fatigue life of the component is then estimated using the damage accumulation data.

Damage is calculated for a range of maximum stress amplitudes between 75 MPa and 350 MPa for a load ratio of 0.5 for AISI 4130 CF, and 250 MPa to 560 MPa for a load ratio of 0.2, which is the average load ratio of the fatigue tests on leaf springs (section I.3.1.2), for AISI 6150. These stress amplitudes correspond to high cycle fatigue (HCF) loading at this load ratio. For each of the three damage models mentioned above, a two-parameter Weibull analysis (Eq. 31) [64,73-74] was performed in order to decide which of the three models gives more realistic results for damage and fatigue life, as compared to experimental data [75].

$$F(t) = 1 - exp\left[-\left(\frac{t}{\alpha}\right)^{\beta}\right] \; for\; t \geq 0 \tag{31}$$

The analysis on both the accumulated damage and fatigue life involves a scale parameter α and a shape parameter β for each damage model (Table 9). When the shape parameter β, which defines the shape of the cumulative damage curve, is larger than 1, then failure increases with time [64]. The scale parameter α gives the mean value of damage caused to the material after one loading cycle. Damage per cycle is thus, smaller as predicted by the Broutma-Sahu model in AISI 4130 CF and the Palmgren-Miner model in AISI 6150, and larger in the case of Hashin-Rotem predictions in both steels.

Table 9: Shape and Scale Parameters of AISI 4130 CF and AISI 6150 for all Damage Models

Damage Model	**β**		**α**	
	AISI 4130 CF	**AISI 6150**	**AISI 4130 CF**	**AISI 6150**
Palmgren-Miner	0.70	1.18	$1.04\text{x}10^{-6}$	$6.21\text{x}10^{-6}$
Broutman-Sahu	0.91	1.89	$6.95\text{x}10^{-7}$	$3.51\text{x}10^{-6}$
Hashin-Rotem	0.38	0.40	$1.63\text{x}10^{-4}$	$1.17\text{x}10^{-2}$

The cumulative distribution of damage is shown in Fig. 57. The two linear models coincide in the case of AISI 4130 CF (Fig. 57(a)). Broutman-Sahu and Palmgren-Miner models give almost identical results. Compared to the two linear models, Hashin-Rotem gives a lower probability of failure at stresses between 75 MPa and 150 MPa, and larger probability between 150 MPa to 240 MPa. However, it agrees with the other two models estimating approximately 80% probability of failure at 260 MPa (Table 10).

The cumulative distributions for damage for AISI 6150 (Fig. 57(b)), shows the two linear models to coincide at lower stresses. Broutman-Sahu and Palmgren-Miner models give almost identical results up to the mean stress of 360 MPa. Compared to the two linear models, Hashin-Rotem gives a higher probability of failure at stresses between 256 MPa and 350 MPa and, and lower probability between 360 MPa to 460 MPa and 462 MPa to 560 MPa. However, it agrees with Broutman-Sahu at 485 MPa. The Hashin-Rotem model estimates an approximately 95% probability of failure at 560 MPa, which is just 1% higher than that estimated at the same mean stress lever by the two linear models.

It can be observed from the graphs of Fig. 57 that the curve based on the Hashin-Rotem model, for both AISI 4130 CF and AISI 6150, is a smooth curve resembling a best-fit line for the other two linear model predictions. It is also worth mentioning that the maximum deviation of Hashin-Rotem from the other two models is at about 225 MPa, 25 % greater than Broutman-Sahu and Palmgren-Miner, in AISI 4130 CF, and at 360 MPa in the case of AISI 6150. Table 10 gives the average damage accumulated in both metals at different mean stress ranges.

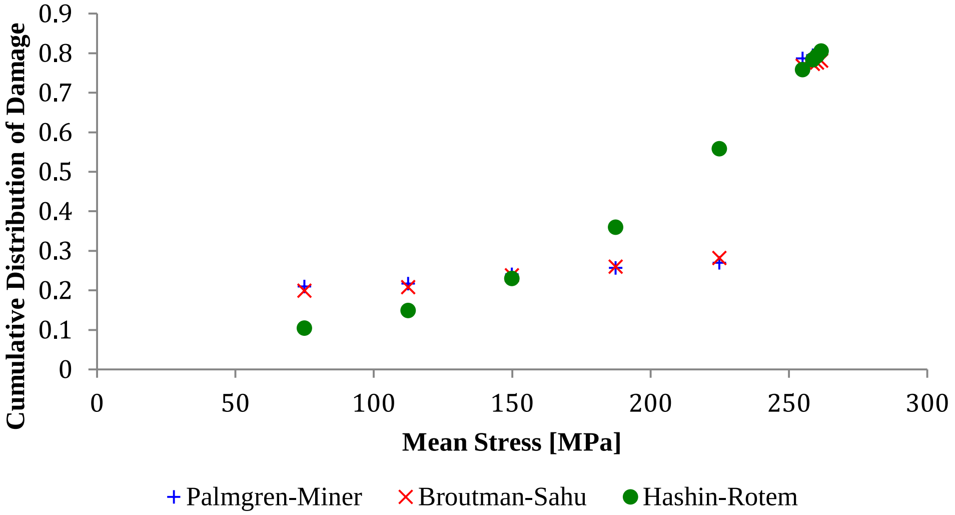

(a)

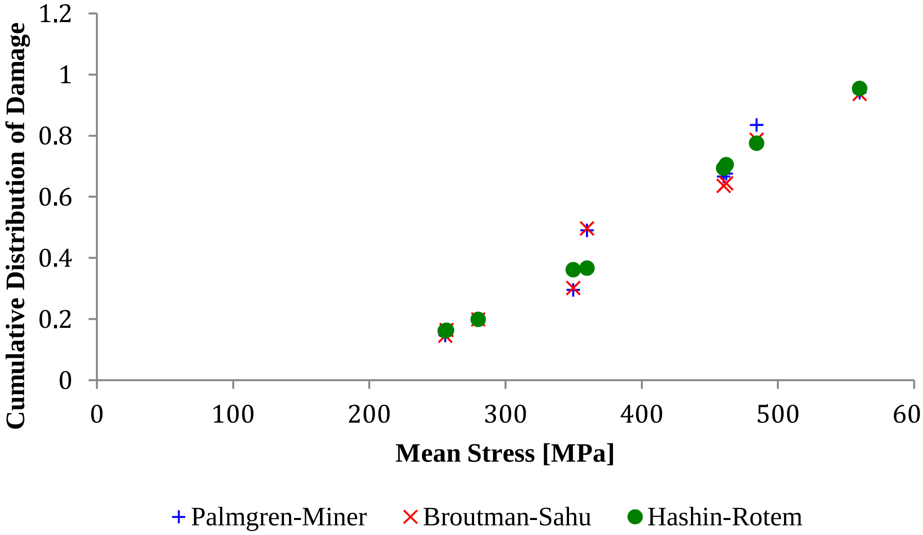

(b)

Figure 57: Cumulative Distribution of Damage for AISI 4130 CF (a), AISI 6150 (b)

Fig. 57 shows cumulative damage distribution for one cycle (K=1). The fatigue life of the material can be calculated by calculating the value K when each of the three models equals 1, at failure. Fig. 58 gives the cycles to failure versus mean stress. Experimental data presented in previous sections at load ratio of -1, is included as a means of comparison. A similar pattern to cumulative distribution of damage is observed when comparing the three models with respect to the fatigue life of the material.

Table 10: Average Cumulative Distribution of Damage for AISI 4130 CF and AISI 6150

Mean Stress [MPa]	Palmgren-Miner	Broutman-Sahu	Hashin-Rotem
AISI 4130 CF Steel			
75-150	0.22	0.21	0.17
150-240	0.26	0.26	0.40
240-262	0.80	0.80	0.80
AISI 6150 Steel			
250-300	0.17	0.16	0.16
330-360	0.50	0.50	0.45
460-560	0.83	0.79	0.78

The two linear models for AISI 4130 CF give similar results and are in agreement with experimental data up to 225 MPa. The Hashin-Rotem model greatly underestimates the fatigue life of steel by one order of magnitude at the low stress of 75 MPa, and more than three orders of magnitude at 250 MPa. A close look between the cumulative distribution of damage and S-N curves shows that the larger the probability of failure, the smaller the fatigue life of the material. In addition, the deviation of Hashin-Rotem from the two linear models in Fig. 57 is proportional to the amount of underestimation of the fatigue life in Fig. 58. Hashin-Rotem gives a lower fatigue life compared to Broutman-Sahu and Palmgren-Miner models. It does not account for the fact that the slope of the fatigue life curve of steel is minimum at and below the endurance limit of the material, which is 319 MPa. The two linear models also start deviating from experimental results above 225 MPa, the stress at which the probability of failure in cumulative distribution of damage curve stops being constant and rises again. Above this mean stress value, the two linear models also deviate from each other, as is the case in Fig. 57 but for a larger stress interval this time.

For AISI 6150, the plot of Fig. 58(b) shows the two linear models giving similar results at lower stresses up to 280 MPa, while at higher stresses they differ by one order of magnitude, with the Broutman-Sahu model giving better fatigue life. The experimental results give a lower fatigue life for the same stresses, with 48 % difference in life cycles at a mean stress level of 560 MPa when compared to Palmgren-Miner model results, and 79% difference when compared to results from the Broutman-Sahu model. The Hashin-Rotem model greatly underestimates the fatigue life of steel by two orders of magnitude at the mean stress of 256 MPa, and more than four orders of magnitude at 560 MPa, when compared to experimental data (Table 11). The experimental results fall between the linear and non-linear models. However, it should be reminded that the experimental results for steel are taken from fatigue tests carried out on steel leaf springs that have been surface treated by shot peening. The effect of this surface treatment cannot be accounted for when using the damage models examined in this study.

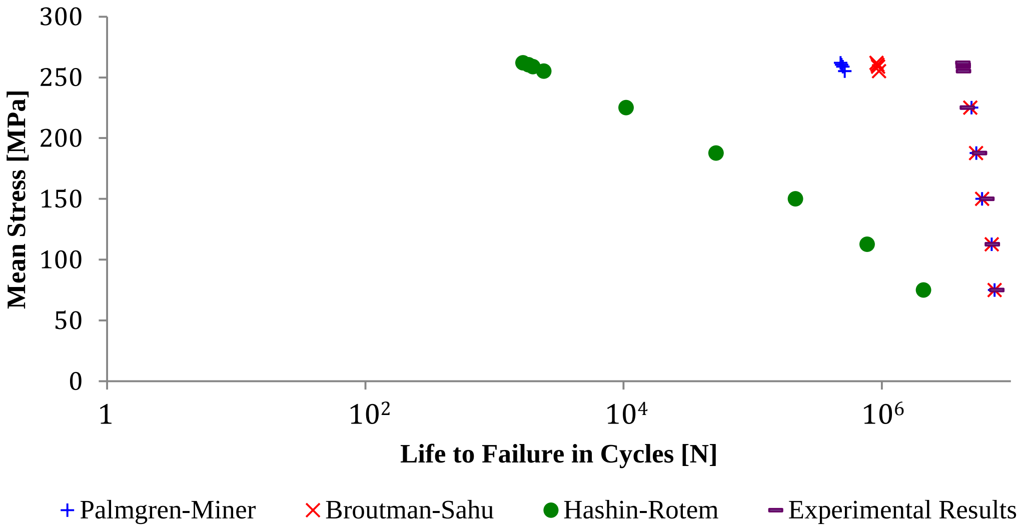

(a)

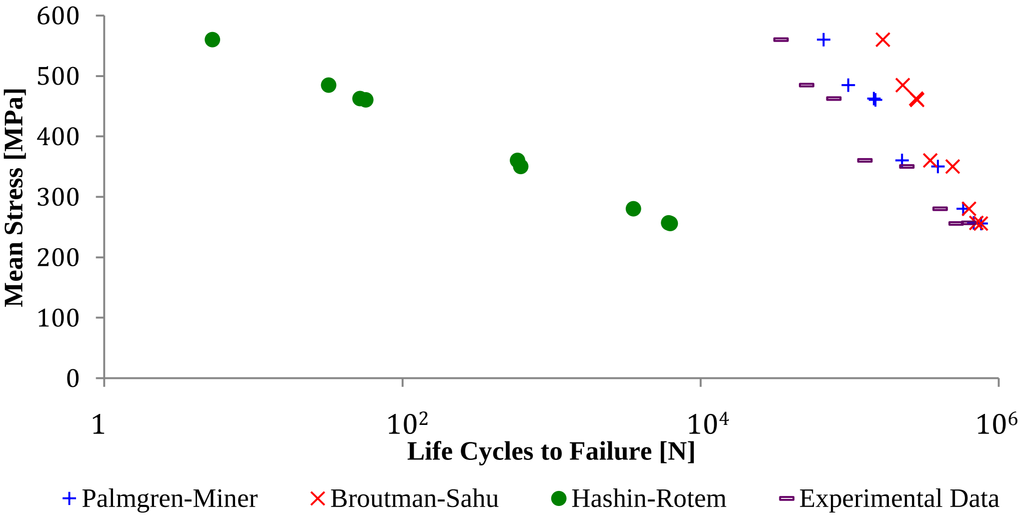

(b)

Figure 58: Mean Stress vs. Cycles to Failure for AISI 4130 CF (a) and AISI 6150 (b)

A general underestimation of the fatigue life is observed, if the effect of the load ratio on the fatigue life is taken into account. A larger load ratio means better fatigue life

(Fig. 22). The predicted results for the fatigue life of AISI 4130 CF loaded at R=0.5 should have been better than those of experimental data at R=-1, as in the latter case mean stress is higher [35]. Similar to the case of AISI 4130 CF, the deviation of Hashin-Rotem from the two linear models is proportional to the amount of underestimation of the fatigue life.

Table 11: Average Fatigue Life of AISI 4130 CF and AISI 6150

AISI 4130 CF

Mean Stress [MPa]	Palmgren-Miner	Broutman-Sahu	Hashin-Rotem
75-150	6.8×10^{6}	6.8×10^{6}	8.0×10^{5}
150-225	5.0×10^{6}	5.0×10^{6}	5.0×10^{4}
225-262	5.0×10^{5}	9.0×10^{5}	2.0×10^{3}
Compared to Experimental Data			
	Below	Below	Below

AISI 6150

Mean Stress [MPa]	Palmgren-Miner	Broutman-Sahu	Hashin-Rotem
255-350	6.0×10^{5}	6.5×10^{5}	4.0×10^{3}
350-480	2.7×10^{5}	3.9×10^{5}	300
480-560	8.3×10^{4}	2.0×10^{5}	20
Compared to Experimental Data			
	Above	Above	Below

Overestimation and underestimation of the fatigue life, is a reason to reconsider using the damage models as the sole mean of designing a component for cyclic application. The dependence of the model on stress information is important at lower stresses, where experimental data and both linear models are in agreement. However, the stress dependent, linear model is better in predicting the fatigue life of steel [28].

I.3.3 Finite Element Analysis

In the course of this study, of determining an optimum material for the manufacturing of leaf springs as suspension systems based on fatigue life analysis, both experimental and theoretical approaches have been followed. In the preceding discussion, the experimental fatigue tests completed were presented, as well as some theoretical calculations determining the damage accumulation, fatigue life and fatigue limits for AISI 4130 CF and AISI 6150.

In order to enhance the results of this research, two FE programs, ABAQUS/CAE and fe-safe^{TM}, were used. These programs help in determining the critical points in the component where failure might initiate and/or occur, as well as, in the case of fe-safe^{TM}, predict the life of the component. Comparison of the outcome of the simulations carried out using these FEA aids to experimental data, enables one to understand how faithful to reality these results are, and to what extend they can be trusted in situations were the possibility of multiple or any experiments is not possible.

The Simulia-Dessault System’s product ABAQUS/CAE (ABAQUS/CAE) has powerful capabilities in modeling and estimating the response of solid bodies or structures under loading. The user can begin the analysis from drawing a model of the solid or structure to be examined, input information on the material, forces and interactions, and the software utilizing the fundamentals of finite element analysis proceeds to an output file (*.odb*) that can be modified to give the desired response in graphical and/or visual representation.

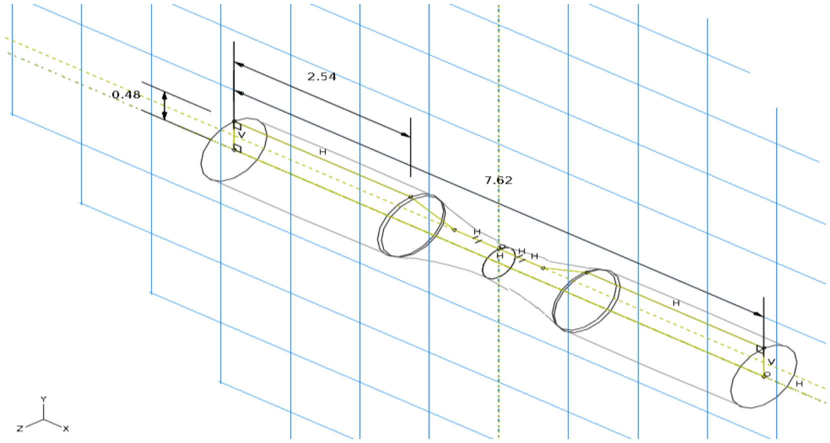

Figure 59: 3D Sketch of Fatigue Specimen for ABAQUS/CAE modeling (all dimensions are in cm)

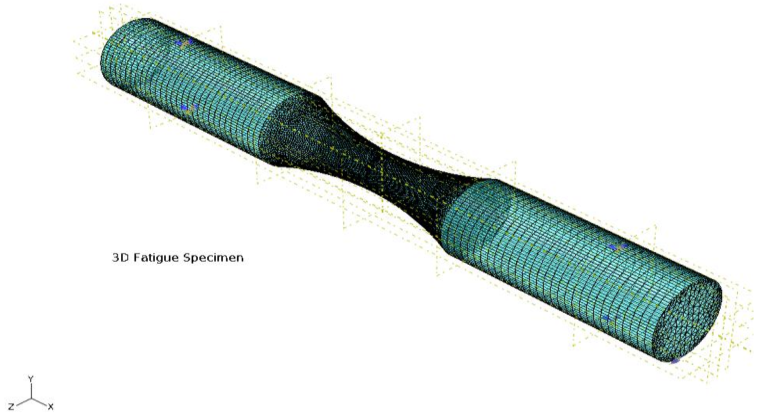

Figure 60: 3D meshed Fatigue Specimen for ABAQUS/CAE Modeling

A representation of the hourglass fatigue specimen (Fig. 59 and 60) was created with ABAQUS/CAE in order to simulate a full cycle of rotating bending, as the software does not provide for a finite element analysis under cyclic loading conditions. The dimensions of the model are identical to the specimens tested on the R.R. Moore Rotating Beam apparatus, and the boundary conditions were kept as true to the actual tests as possible. A bending moment, varying in magnitude between the tests completed, simulated the loading. The bending moment ranged between 100 Ncm to 500 Ncm, increasing at intervals of 100 Ncm. These values correspond to a maximum bending stress (S_{11}) as calculated by ABAQUS/CAE ranging between 96.22 MPa and 481.1 MPa. For all simulations of the rotating bending specimen model the surface finish was assumed to be that of a smooth specimen, and as a result no residual stresses were considered in the analysis.

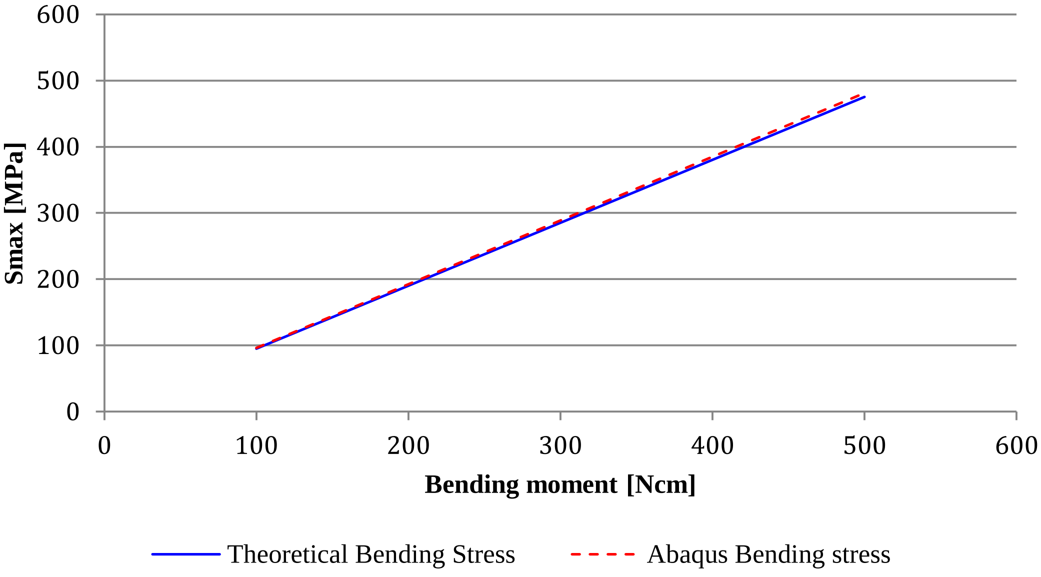

Figure 61: Maximum Bending Stress vs. Applied Bending Moment

The graph in Fig. 61 shows the relationship between maximum bending stress in the model (S_{11}) and applied bending moment in Ncm. The relationship is linear, as is the relationship of the second curve, the solid curve, estimated by using the maximum stress equation

$$\sigma_{max} = \frac{Mc}{I} \tag{32}$$

where M is the applied bending moment, c is the distance form the surface where the stress is measured to the neutral axis of the component, and I is the moment of inertia. Calculations of maximum stress were made at the surface of the center of the fatigue specimen, where all failures were demonstrated through fracture, during the fatigue tests under reversed loading. When the two curves of Fig. 61 are compared it can be observed that the error percentage of the ABAQUS/CAE simulations, when compared to the theoretical calculations, is only 1.2%.

Visualization of the simulation's outcome gives information regarding the motion of the specimen during one full revolution of its cyclic bending application, as well as information on the critical points of the component were stress concentrates the most and a crack initiation becomes a critical possibility. As Fig. 62 shows the middle of the component is most probably the point where a crack will initiate leading the component to failure. This prediction of the FEA comes in complete agreement with what actually occurred during failure through fracture of the fatigue specimens under rotating bending.

In order to detect the effects of the presence of defects on the fatigue life of AISI

4130 CF steel, 2D models of a cracked hourglass component (Fig. 63) were analyzed on ABAQUS/CAE and then tested on fe-safe^{TM}.

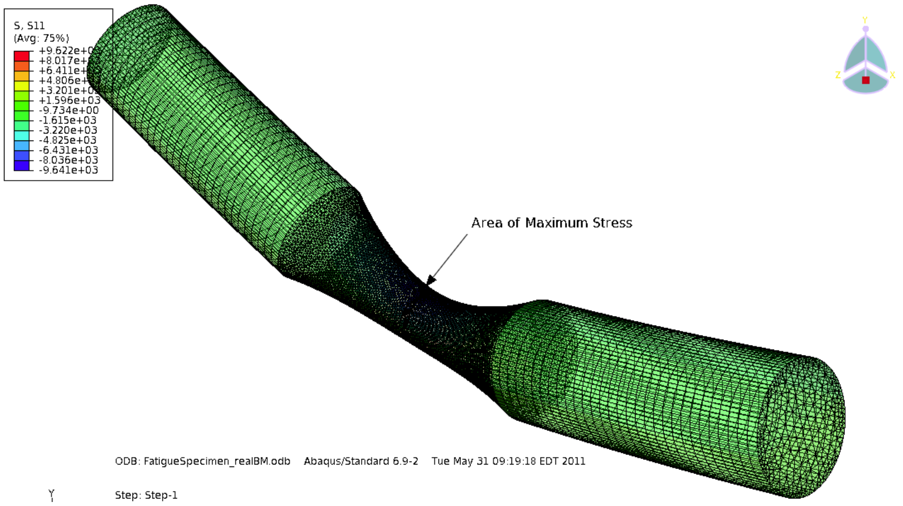
S, S11
(Avg: 75%)
+9.622e+0
+8.017e+
+6.411e+
+4.806e+
+3.201e+0
+1.596e+03
-9.734e+00
-1.615e+03
-3.220e+03
-4.825e+03
-6.431e+03
-8.036e+03
-9.641e+03
Area of Maximum Stress
ODB: FatigueSpecimen_realBM.odb Abaqus/Standard 6.9-2 Tue May 31 09:19:18 EDT 2011
Step: Step-1
Y
Z
X

Figure 62: 3D Fatigue Specimen, Visualization of Bending in ABAQUS/CAE

Fe-safe^{TM} is a new software developed by Safe Technology Ltd. offering the possibility of estimating the fatigue life of metal or composite components. One of the main uses of this powerful tool is as a postprocessor for ABAQUS. The user can get information on the fatigue life of a metal or composite component undergoing complex cyclic loading just by providing the software with an ABAQUS .odb file, and inputting a cyclic loading history to the fe-safe^{TM} interface. Fe-safe^{TM} estimates the fatigue life of a component in cycles up to the point that initiation of a crack may be possible. Although fe-safe^{TM} is a powerful finite element tool, the results of such analysis should be considered as mere indications and always verified with experimental data. Since fe-safe^{TM} gives the fatigue life of a component as the cycles required for a crack to be initiated on the surface of the component, analysis of defected components should be used just for the purposes of comparison to non-defected components.

Six types of cracks were tested. Four edge cracks with crack length to width ratio ranging from 0.1 to 0.4, a slanted edge crack, and a 45° interior crack. The crack length of the slanted edge and interior cracks is 0.9 and 9 mm, respectively (Fig. 64). The specimens were loaded under pure bending, and as a result the corresponding crack surface displacement was of Mode I (Fig. 65) [28].

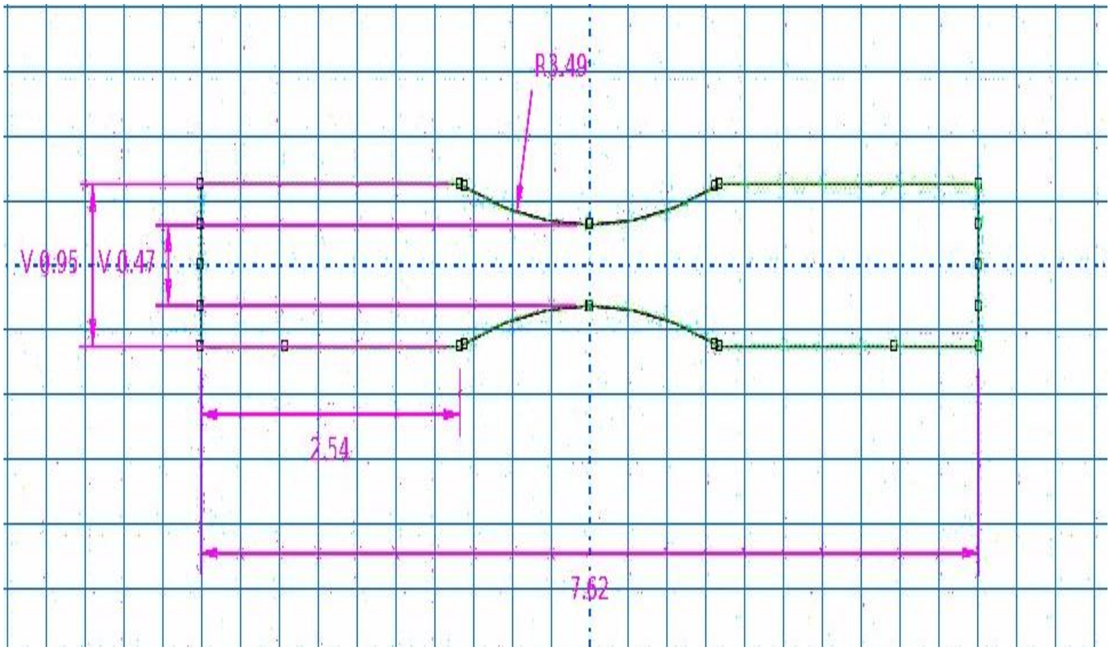

Figure 63: 2D sketch of Fatigue Specimen for ABAQUS/CAE modeling (Dimensions in cm)

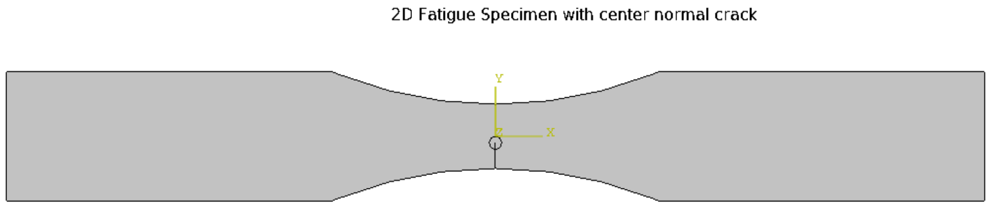
2D Fatigue Specimen with center normal crack
Y
Z
X

(a) Normal Crack at the center of the 2D Fatigue Specimen

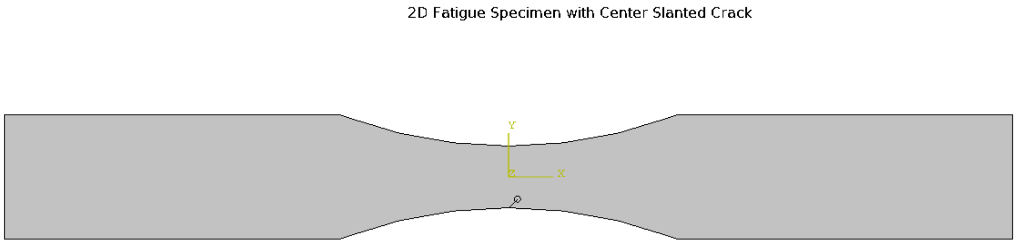
2D Fatigue Specimen with Center Slanted Crack
Y
Z
X

(b) Slanted Crack at the center of the 2D Fatigue Specimen

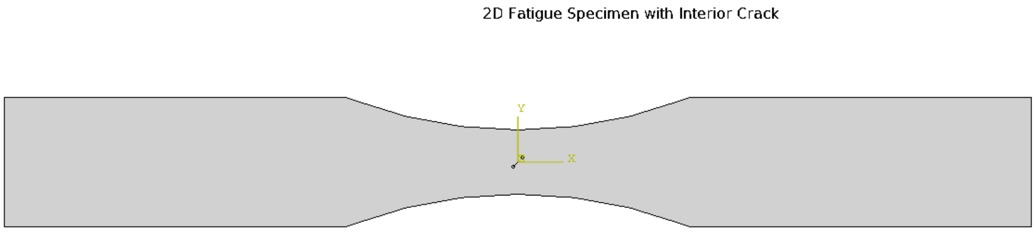
2D Fatigue Specimen with Interior Crack
Y
X

(c) Interior Crack at the center of the 2D Fatigue Specimen

Figure 64: 2D Fatigue Specimens with cracks

One of the most important parameters in fracture mechanics is the *stress-intensity factor* (K). The stress-intensity factor relates the *nominal stress level* (σ) in the component and the *crack length* (α), to characterize the stress field in front of a sharp crack in a component. Depending on the displacement mode, the position of the crack in the component and the loading, the stress-intensity factor will be calculated accordingly. For the bending conditions of this study the appropriate relationships for the stress-intensity factor are [32].

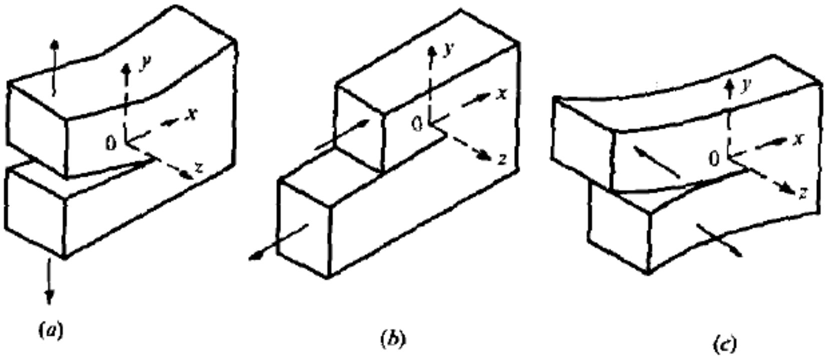

Figure 65: The three basic modes of fracture: (a) Mode I (tensile opening), (b) Mode II (in-plane sliding), (c) Mode III (anti-plane shear) [28]

$$\mathrm{K_I} = \frac{6M}{B(W-\alpha)^{3/2}} \times g\left(\frac{\alpha}{W}\right) \tag{33}$$

$$\mathrm{K_I} = \frac{6M}{W^2}\sqrt{\pi\alpha}F\left(\frac{\alpha}{W}\right) \tag{34}$$

$$F\left(\frac{\alpha}{W}\right) = 1.122 - 1.40\left(\frac{\alpha}{W}\right) + 7.33\left(\frac{\alpha}{W}\right)^2 - 13.08\left(\frac{\alpha}{W}\right)^3 + 14.0\left(\frac{\alpha}{W}\right)^4 \tag{35}$$

where M is the applied bending moment, B is the component's width, W its thickness, and α the crack length (Fig. 66). The function g$\left(\frac{\alpha}{W}\right)$ varies based on the crack length to width ratio and Table 12 gives values of the function for some such ratios [32].

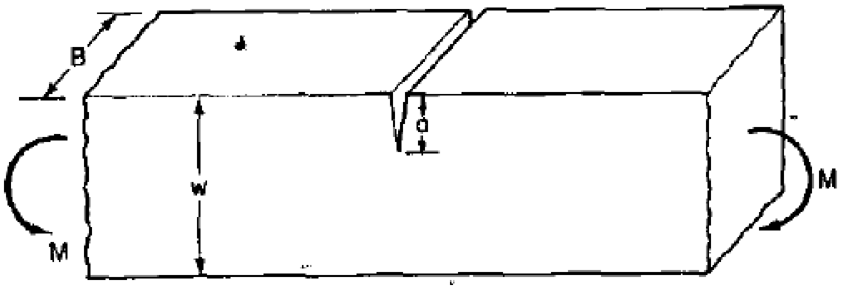

Figure 66: Edge-notched Beam under Bending [32]

Table 12: Stress Intensity Factor Coefficients [32]

$\boldsymbol{\frac{\alpha}{W}}$	0.05	0.1	0.2	0.3	0.4	0.5	0.6 and larger
$\mathbf{g}\left(\frac{\alpha}{W}\right)$	0.36	0.49	0.60	0.66	0.69	0.72	0.73

The stress-intensity factor is used primarily when the stress-strain response of the component is linear-elastic. When this response becomes elastic-plastic a second parameter becomes of importance. The *J-integral* characterizes the stress-strain field at the crack tip using an integral path that begins away from the crack tip, where the analysis is purely elastic, and then substitutes it with the inelastic region in the vicinity of the crack tip. When the behavior of the cracked component is linear-elastic, as is the case of this study, the J-integral is the same as the *energy release rate* per unit crack extension (G) and follows the relationship [32]

$$J_{\mathrm{I}} = G_{\mathrm{I}} = \frac{(1-\nu^2)\mathrm{K_I}^2}{E} \tag{36}$$

As seen from Eq. 36 the J-integral is proportional to the square of the stress-intensity factor, and as a result depends on the crack surface displacement mode. As mentioned earlier the mode concerning this study is the opening mode, mode I, and for this reason I is the subscript characterizing the stress-intensity (K_I) and J-integral parameters (J_I).

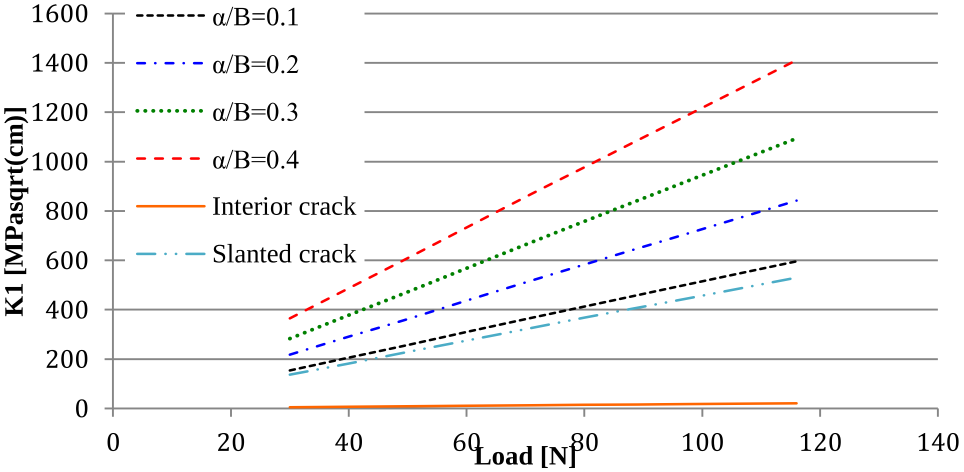

Figure 67: K_I vs. Applied Load

All models were tested under one full cycle of pure bending, for loads ranging between 30 and 120 N, and the K_I, J_I, and bending stress (S_{11}) were calculated using

ABAQUS/CAE. Fig. 67 and 68 show how K_I and J_I vary with varying load. As the load is increased, and the crack opens wider both parameters increase. The interior crack is the only case of crack not affected by loading having an almost constant and, approximately, zero K_I and J_I. Since the crack is interior, in the middle of the component and angled at 45° above and below the neutral axis, it will not grow but remain constant, during the flexural motion. As a result, not much changes in the stress field of the crack, nor much energy is released, as the crack does not grow very fast. The crack with the steepest slope, showing the greater values of K_I and J_I, is the crack having a crack length (α) to component width (B) ratio (α/B) of 0.4. In the 2D case this ratio becomes α/W. As the crack length gets smaller, and the ratio decreases, the values of the two parameters decrease, and increase more slowly with increasing load. The slanted crack model shows the lowest values, and its curve has the smoothest slope. It can be concluded that cracks perpendicular to the component's surface have larger stress-intensities and energy release rates.

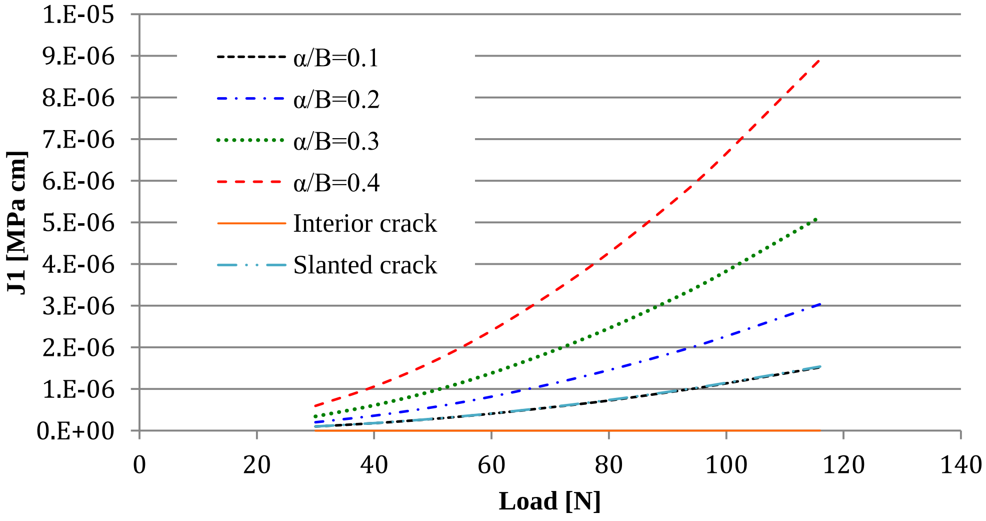

Figure 68: J_I vs. Applied Load

The bending stresses were measured along the length of the specimen and at the neutral axis of the specimen. Fig. 69 shows the bending stress distribution in each model along the length of the specimen, where the origin is taken at the center of the specimen, above/in between the crack tip. The larger crack model presents the greater fluctuation of stress among the models, while the stress distribution of the slanted and interior crack models are the least fluctuated. It can also be noticed that since the cracks are located in the middle of the components, the stress distribution on the right side of the component is a mirror image of the left side stress distribution. At the center of the component, above the crack, the bending stress is always at or below zero, except for the case of the interior crack where it fluctuates from 123 to -123 MPa. However, this symmetry does not hold for the case of the slanted crack.

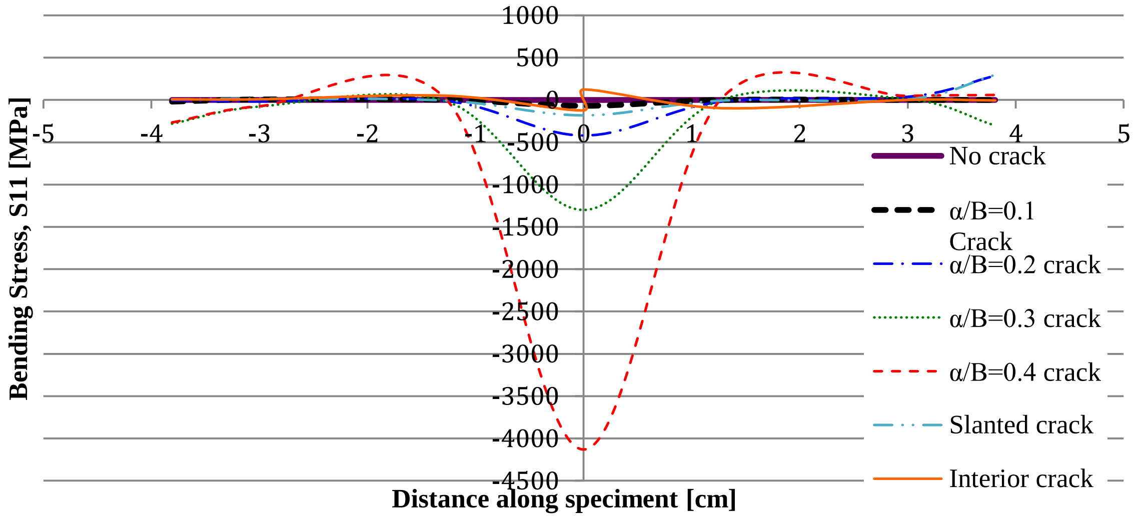

Figure 69: Bending Stress Profiles in the center of 2D cracked Specimens

It can thus be concluded that, as expected [32], cracks not only increase the stress intensity factors and strain energy release rates in the component as they grow, the crack angle and position has an effect on the magnitude of damage it causes in the component (Fig. 70). Bending stresses are higher for larger normal surface cracks, while interior or slanted cracks affect the components in a smaller degree.

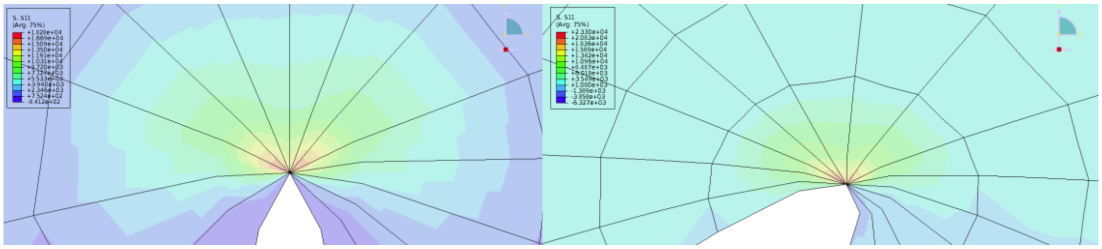

(a) Normal crack **(b) Slanted crack**

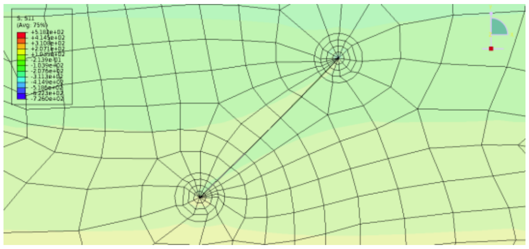

(c) Interior crack

Figure 70: Contour Plots of Stress Profiles at crack Region

Using fe-safe^{TM} the fatigue life of the components may be determined in two major different ways: either through receipt of strain information from strain gages positioned on the component in question, or using the software as a postprocessor to an FEA software as ABAQUS. For the purposes of this study the second procedure was used.

To determine the fatigue life based on an FEA output, fe-safe^{TM} imports the elastic stress data from the ABAQUS .*odb* file, the output file of the analysis. The software offers a wide variety of fatigue algorithms from which to choose in order to estimate the fatigue life of the model in question. An extended material library is also offered and classified based on the types of metal materials available in the library. Given that information on the properties of the material in question are known, new metal materials can be added in the fe-safe^{TM} materials library, or existing ones may be modified. Among the vast range of material's properties included under each metal in the material library, there is a listing of the suggested algorithm to be used during the fatigue life analysis.

As just mentioned above, there are a variety of fatigue life algorithms whether the stresses on the component are uniaxial or multi-axial. Uniaxial stresses are mostly considered in theory and very controlled experimental situations, and therefore, the suggested algorithms are mostly based on multi-axial stresses [76].

Before indulging in mentioning the available algorithms and explaining the one used for this study, the steps followed by the software to reach the desired result of the component's life should be outlined.

To estimate the fatigue life of a component fe-safe^{TM} detects a possible fatigue crack initiation point on the surface of the component examined. When the ABAQUS/CAE .*odb* file is imported and the appropriate material is chosen and modified, if necessary, the software recognizes the elastic surface stresses form the FEA output file. The software uses these stresses in order to calculate the appropriate stresses and/or strains to be used with the fatigue life algorithm. The FEA output stresses used are the in-plane principal stresses, and the corresponding stress tensor is multiplied by the user defined load history in order to calculate a time history for the stress tensor

$$S_{ij}(t) = \left(S_{ij}\right) \times P(t) \tag{37}$$

where S_{ij} is the stress tensor form the *.odb* ABAQUS/CAE file, and P(t) is the user defined load history. When the response is multi-axial, and stress-strains to be calculated are plastic-elastic, a multi-axial cyclic plastic-elastic correction is used for the calculation [76].

Neuber's rule (1961) (Eq. 37) is used for the above conversion of elastic to plastic-elastic strains/stresses. Neuber's rule was initially formulated for shear strained bodies, however it is used in determining a plastic strain and/or stress from a calculated elastic strain and/or stress, when the plastic deformation is involved in the components response [28,76]. Neuber's rule equates the product of elastic stress and strain, to the product of elastic-plastic stress and strains by multiplying the former with the appropriate stress concentration factor (K_t). Neuber's rule can be simplified to Eq. 39 when the nominal stresses and strains are elastic. The stresses and strains are calculated using elastic analysis as in the case of FEA [28].

$$\Delta\sigma\Delta\varepsilon = \mathrm{K}_t{}^2\Delta S\Delta e \tag{38}$$

$$\Delta\sigma\Delta\varepsilon = \mathrm{K}_t{}^2\frac{S^2}{E} \tag{39}$$

In the above equations Δσ and Δε are the local stress and strain ranges, respectively, ΔS and Δe are the nominal stress and strain ranges, and K_t is the stress concentration factor.

Once all stresses have been converted to the appropriate form, and a time history for the stress tensor has been evaluated, the chosen fatigue algorithm is used to estimate the fatigue life of the component. If necessary, mean stress correction algorithms are included in the analysis to account for the effect of mean stresses on the fatigue life of the component. The following equations present some of the available fatigue life algorithms provided by fe-safe^{TM}. Among these the one the software suggests for AISI 4130 CF steel is the Brown Miller strain-life algorithm (Eq. 43) [76].

Uniaxial stress life: $$\frac{\Delta\sigma}{2} = \sigma'_f\left(2N_f\right)^b \tag{40}$$

Maximum principal strain: $$\frac{\Delta\varepsilon}{2} = \frac{\sigma'_f}{E}\left(2N_f\right)^b + \varepsilon'_f\left(2N_f\right)^c \tag{41}$$

Maximum shear strain: $$\frac{\Delta\gamma_{max}}{2} = 1.3\frac{\sigma'_f}{E}\left(2N_f\right)^b + 1.5\varepsilon'_f\left(2N_f\right)^c \tag{42}$$

Brown Miller: $$\frac{\Delta\gamma_{max}}{2} + \frac{\Delta\varepsilon_n}{2} = 1.65\frac{\sigma'_f}{E}\left(2N_f\right)^b + 1.75\varepsilon'_f\left(2N_f\right)^c \qquad (43)$$

where $\Delta\gamma_{max}$ is the shear strain range and $\Delta\varepsilon_n$ is the normal strain.

The Brown Miller algorithm calculates fatigue life on a plane basis. It is based on the assumption that the maximum fatigue damage occurs on the plane where the maximum shear strain amplitude is developed. As a result, the fatigue damage in the material is a function of the plane's shear and normal strains (Fig. 71). This algorithm gives realistic fatigue life estimates for metals of ductile nature, and tends to be non-conservative when the metal is brittle [76].

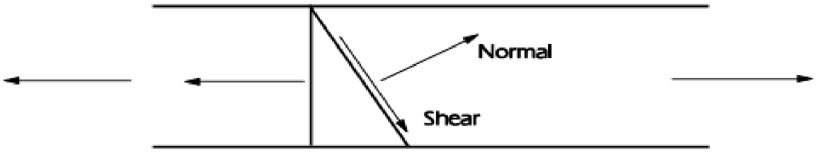

Figure 71: Normal and Shear Stresses along surface planes for Fatigue Life Estimation using the Brown Miller Algorithm [55]

For the fatigue estimation based on the Brown Miller algorithm, perpendicular and angled at 45° planes are assumed to divide the components surface. Three perpendicular planes are assumed on the surface of the component, and these are further separated to eighteen planes where the fatigue lives are calculated. On each plane, the time history of the shear and normal strains to the plane are calculated using the principal strains calculated form the in-plane principal stresses imported from then FEA output. If required, a mean stress analysis is performed to determine the effect of mean normal stresses on the fatigue of the component being examined, and the final fatigue life is calculated, as the shortest life among those calculated on all planes [76].

To account for mean stress effects, the user can choose among the following algorithms (Eq. 5-7 and 44) or define a new one. If the effect of mean stresses is to be considered negligible, the fatigue life algorithm may be used without the mean stress correction [21,28].

Smith-Watson-Topper: $$\frac{\Delta\varepsilon}{2}\sigma_{max} = \frac{(\sigma'_f)^2}{E}\left(2N_f\right)^{2b} + \sigma'_f\varepsilon'_f\left(2N_f\right)^{b+c} \qquad (44)$$

The suggested mean stress correction algorithm for AISI 4130 CF and AISI 6150 steel is the one attributed to Morrow (Eq. 16) [20,27], and the Brown-Miller–Morrow algorithm becomes

$$\frac{\Delta\gamma_{max}}{2} + \frac{\Delta\varepsilon_n}{2} = 1.65\frac{(\sigma'_f - \sigma_m)}{E}\left(2N_f\right)^{b} + 1.75\varepsilon'_f\left(2N_f\right)^{c} \qquad (45)$$

Fig. 72 shows the effect of Morrow mean stresses on the fatigue life of a smooth steel component of AISI 4130 CF, of no residual stresses. The difference in the estimated fatigue lives after the stress correction is very small. From the graph it can be concluded, that the mean stress correction gives better results, of longer lives, than the case were mean stresses are not considered. Consequently the stresses involved in the analysis of the rotating fatigue of the hourglass specimens should be compressive [33,35].

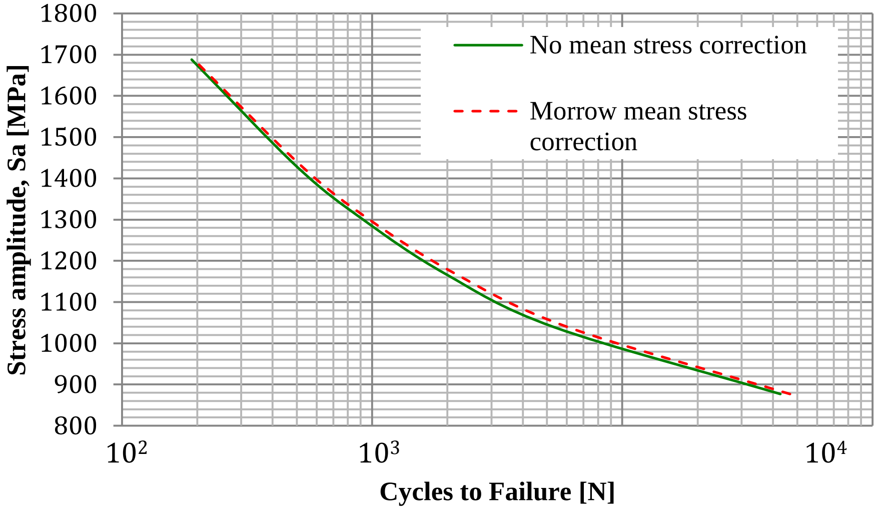

Figure 72: Effect of Morrow Mean Stress on the Fatigue Life of AISI 4130 CF steel, estimated using fe-safe^{TM}

Apart from the strain ranges calculated from the FEA output stresses, some additional material properties are necessary for the above algorithms to calculate the desired fatigue life estimate. These properties are summarized in the following table (Table 13).

The smooth AISI 4130 CF specimen ABAQUS/CAE output, were imported as input data in fe-safe^{TM} and their fatigue life was estimated at different loadings. The ABAQUS/CAE analysis was assumed for smooth components free of surface finishes or treatments that could have an effect on their fatigue. However, since no X-Ray diffraction, or other processes, were possible to examine the exact surface roughness of the specimens tested under the actual rotating bending conditions on the R.R. Moore apparatus nor the case depth of the compressive residual stress field due to machining or surface treating, a trial and error procedure was carried out to determine were exactly the experimental data of section I.3.1.1 rests. Fe-safe^{TM} offers a great variety of surface finish factors that the user can select from, and the software takes into consideration the effects of such finishing when estimating the fatigue life based on the FEA input data.

Table 13: Material Properties for Fatigue Life estimation[4]

Property	Definition
σ'_f	fatigue strength coefficient
ε'_f	fatigue ductility coefficient
n'	cyclic strain-hardening exponent
K'	cyclic strength coefficient
b	Basquin's exponent
c	Coffin-Manson exponent

Fe-safe^{TM} offers surface factor values between 1 and 2.5. In some literature, as in the graphs of Fig. 73 and 74, these values are given as the reciprocal of K_s[5]. The surface factors selected for estimating the fatigue life of the FEA rotating bending model, were between 1 and 2.5, and based on surface roughness for the value $1.6<Ra\leq4$ μm. In addition to these values of K_s, three types of finishing were also considered;

---

[4] All properties required in the calculations of this thesis are presented in Appendix A, for all materials of this research.

[5] On the fe-safe^{TM} interface the surface factor is given the symbol K_t and not K_s as in most texts.

precision forging, fine machined and machined. Fe-safe^{TM} offers the possibility of assigning residual stresses on the surface of the component to be accounted for in the estimation of its fatigue life. As a result, in the case of the current simulations, three different values of compressive residual stresses, 100 MPa, 550 MPa and 650 MPa, were chosen at K_S=1 and 1.5.

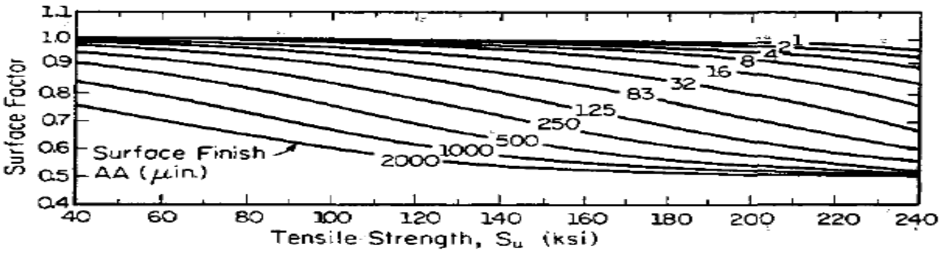

Figure 73: Surface Finish Factor vs., Surface Roughness and Strength for Steel Components [21]

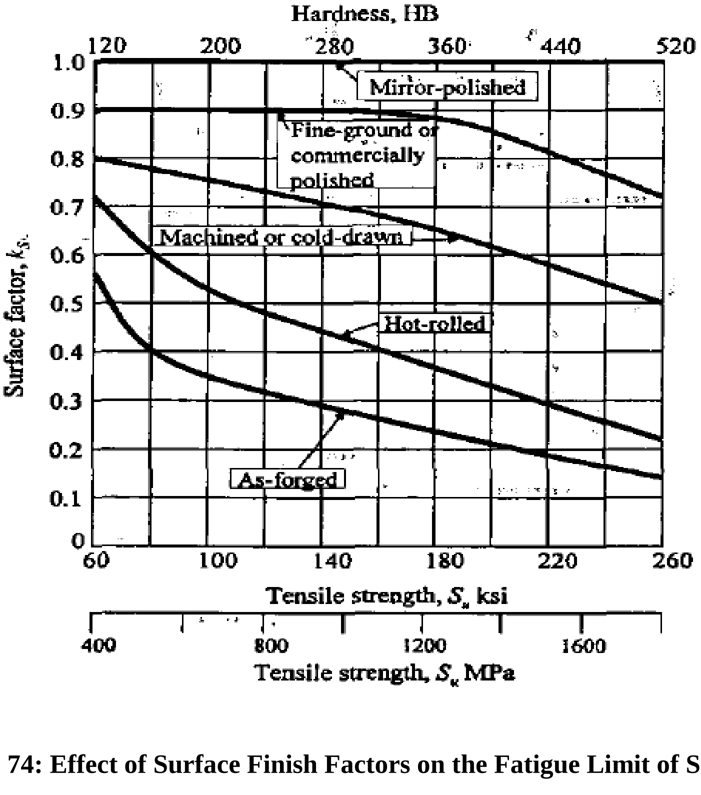

Figure 74: Effect of Surface Finish Factors on the Fatigue Limit of Steels [33]

Fig. 73-74 show different curves empirically determining the range of the surface factors depending on the finish process or roughness of the component [21,33]. The simulations were completed for nine different maximum stress levels; identical to those the specimens were subjected to under the rotating bending tests. Each simulation at each stress level was repeated for each different value of surface factors. Fig. 75 is a representation of the S-N curves formed based on the data from the simulations. Comparing these curves to each other, it can be concluded that the smallest the stress concentration factor, the greater the fatigue life of the component. As a result, mirror polished specimens, of K_s=1, show the longest life, and the worst lives are for components whose K_s=2.5. This is due to the fact that a mirror-polished, also referred to as smooth, component is considered to be free of dents, scratches or defects that increase the stress concentrations at their vicinity and may be possible crack initiation points [32]. As the K_s value increases, the surface of the component is more crudely prepared and the surface roughness increases, thus decreasing the ultimate tensile strength of the component (Fig. 74), and increasing the possibility of crack imitation [21,33]. The effect of surface finish is more important at HCF lives, where cracks do not dominate the fatigue lives of the components, as is the case in the LCF region [21]. As a result, the surface of a component should always be conditioned very carefully, when it is destined for long life applications. Among the surface finishes of Fig. 74, machined is especially dangerous, as it may induce tensile residual stresses on the surface of the component, which are deleterious to its fatigue life [20,68].

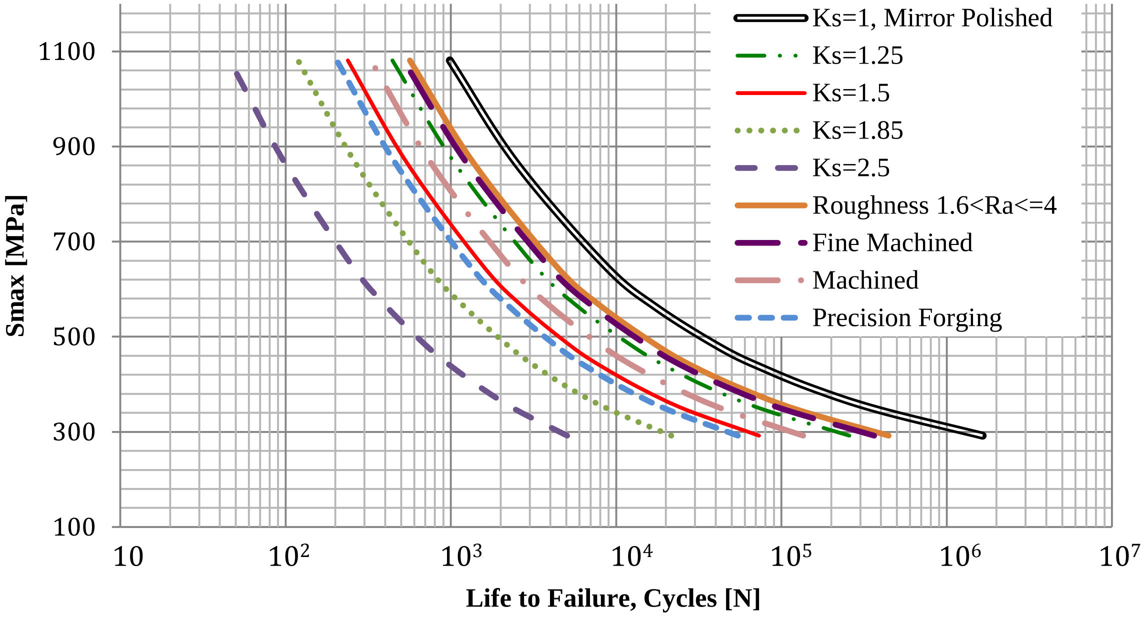

Figure 75: Effect of Surface Concentration Factor on Fatigue Life

From Fig. 75 it can be observed that the fatigue lives for fine machined and surface roughness of 1.6<Ra≤4 μm have minor differences. The same occurs when comparing the S-N curves for machined components and precision forging. Plotting the S-N curves for surface factors 1 to 2.5, and comparing the results to the experimental data for the non-treated material (Fig. 76), it can be observed that for the portion of the S-N curve between 10^5 and 10^6 cycles, experimental and theoretical (fe-safe^{TM}) data for K_s=1 (mirror polished), are in agreement. On the other hand, the fatigue limit, as stress level at lives longer than one million cycles, observed in these curves is larger in the case of experimental data. This observation does not give the actual fatigue limit of the material but the lowest stress value of testing and simulation at which the component in question survives a life greater than a million cycles. A first conclusion could therefore be drawn judging fe-safe^{TM} as conservative

at longer lives of the HCF region (above 10^3 cycles). At the LCF region, below 10^3 cycles, experimental data is below all lives estimated at the different surface factors. It can therefore, also be concluded that fe-safe™ gives overestimated predictions of the fatigue lives when plastic strains are an important part in the calculation of the fatigue life. It should be mentioned that in the FE analysis with ABAQUS/CAE, AISI 4130 CF was assumed to be perfectly elastic, and from the elastic stresses of the output file, fe-safe™ calculates elastic-plastic strains, and not perfectly plastic strains.

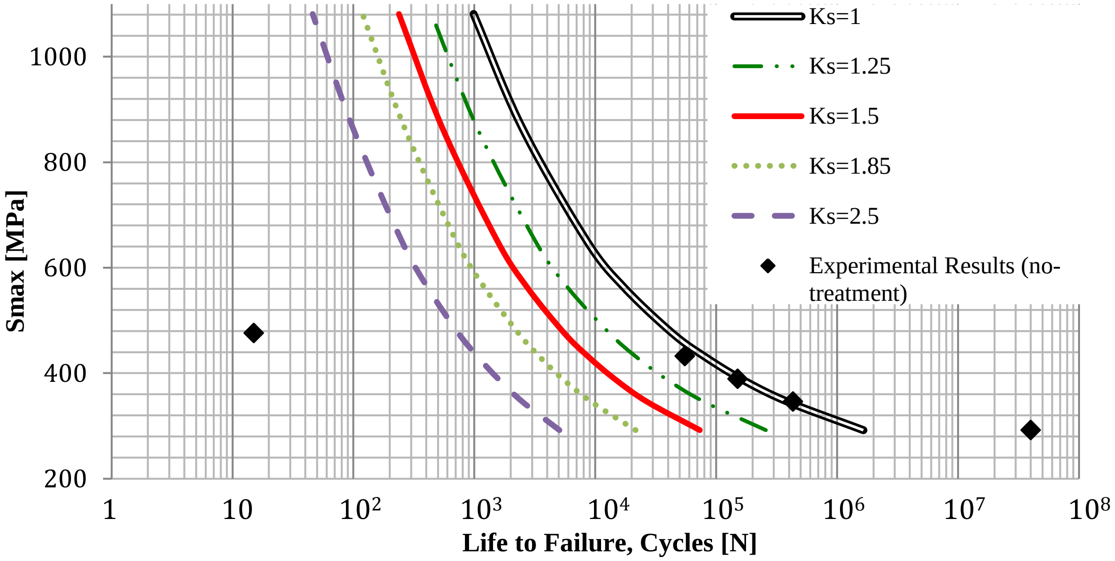

Figure 76: AISI 4130 CF Fatigue lives; Comparison of fe-safe™ estimates and experimental results

The simulations with the assigned compressive residual stresses are plotted in similar graphs (Fig. 77 and 78) to the ones discussed previously, and compared to experimental results of shot-peened, carburized and smooth specimens. A first observation from the graphs is the positive effect compressive residual stresses have on the fatigue life of a component. The greater the magnitude of these stresses the longer the estimated lives. However, fe-safe™ does not have the capacity of estimating relaxation of these stresses, and thus adjusting accordingly the fatigue life estimates. This can be seen by comparing the curve of the experimental data of shot-peened components to the fe-safe™ curves. In the case of K_s=1 (Fig. 77), experimental results of shot peened components lay between the curves for 100 and 550 MPa in compressive residual stress, and closer to the 550 MPa curve, in the region of HCF, above 10^5 cycles. Below this life, experimental results are below all estimated curves containing effects of compressive residual stresses.

In the case of K_s=1.5 (Fig. 78), experimental data of shot peened components shows longer lives than fe-safe™ data of 650 MPa in surface compressive residual stresses at lives above $7x10^4$. Looking at the LCF region of the graph, and with the effect of residual stress relaxation present, experimental data for the shot-peened component falls below the curve for 100 MPa of compressive residual stresses. The carburized components appear to have a very high level of compressive residual stresses, as their fatigue life is longer than the estimated fatigue life of smooth specimens with 650 MPa in compressive residual stresses.

The effect of compressive residual stresses, at HCF, can be also observed by a comparison of the position of the experimental results in each of the plots in Fig. 77 and 78. In the case of estimates based on K_s=1 (smooth specimens) (Fig. 77), experimental data shows smaller lives than the estimates with residual stresses. However, when the surface factor increases, K_s=1.5, and the surface of the component is more prone to cracks and defects, the experimental data of the smooth specimen approaches the fe-safe^{TM} life of 650 MPa of residual stresses, in the HCF region. This shows that compressive residual stresses indeed delay the propagation of cracks, thus improving fatigue life [28,32-33].

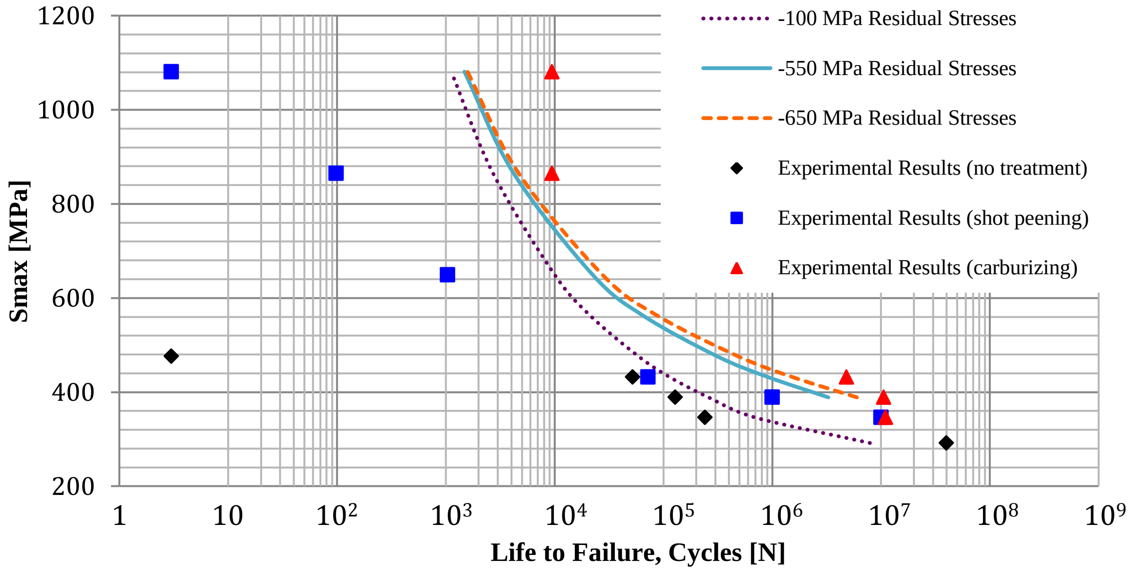

Figure 77: Fatigue Life estimates at K_s=1 and different compressive residual stress levels

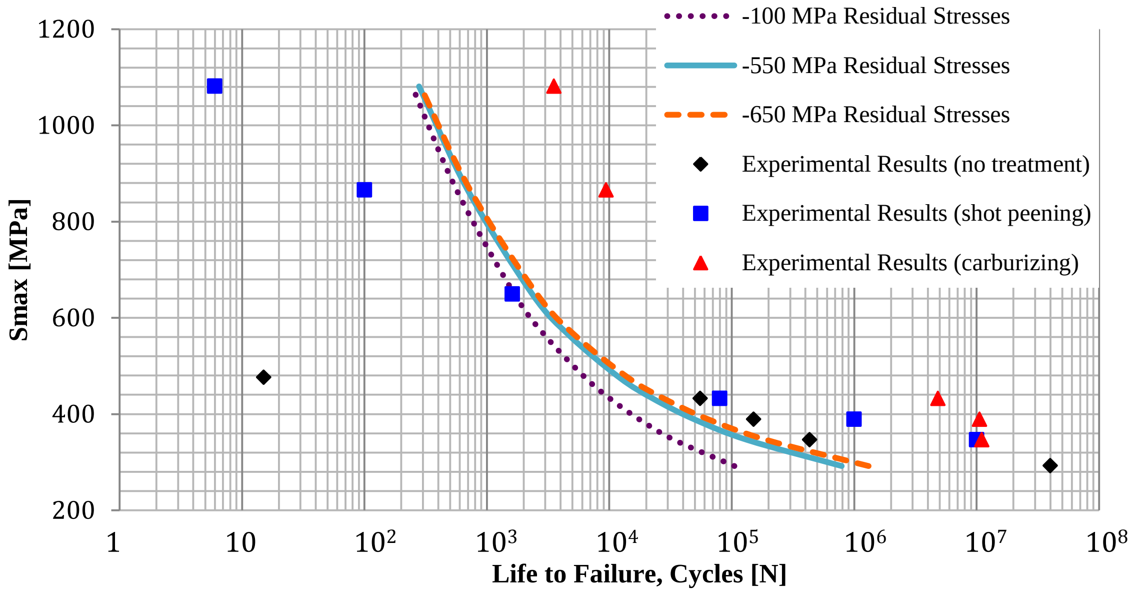

Figure 78: Fatigue Life estimates at K_s=1.5 and different compressive residual stress levels

The above analysis gave insight on the effects of surface factors on the fatigue life, as well as those of the magnitude of the residual compressive field of the shot peened AISI 4130 CF specimens. It also showed that fe-safe^{TM} has great capabilities in giving comparable fatigue life estimates to experimental data for HCF, and is conservative enough to be used as a design criterion for components that are destined for applications that require long lives. On the other hand, it overestimates the fatigue life at lives of LCF, and the simulations do not include the appropriate instruments to account for actual residual stress relaxation in the fatigue life estimates.

As just mentioned, fe-safe^{TM} estimates the fatigue life of a component to the point of a possible surface crack initiation and not to the point of total fracture, as is the case of the experimental tests carried on the R.R. Moore Rotating Beam apparatus. For this reason, fe-safe^{TM} is not the appropriate software to estimate the fatigue life of cracked components as the ones discussed before. However, the fatigue life of such components, may be estimated using the following relationship [76]

$$S_{e_{notched}} = \frac{S_{e_{smooth}}}{\mathrm{K}_t} \tag{46}$$

where

$$\mathrm{K}_t = \frac{Stress\ at\ notch}{Stress\ at\ nominal\ cross\ section} \tag{47}$$

As shown previously, the critical stresses in a cracked component occur at the crack tip and crack region (Fig. 70). It is these stresses that will determine the fatigue life of the component. Fe-safe^{TM} estimates the fatigue life of a component based on the assumption that there exists a point on its surface were a crack might be initiated and propagated. Using the Brown Miller algorithm the fatigue life of the defected components was estimated.

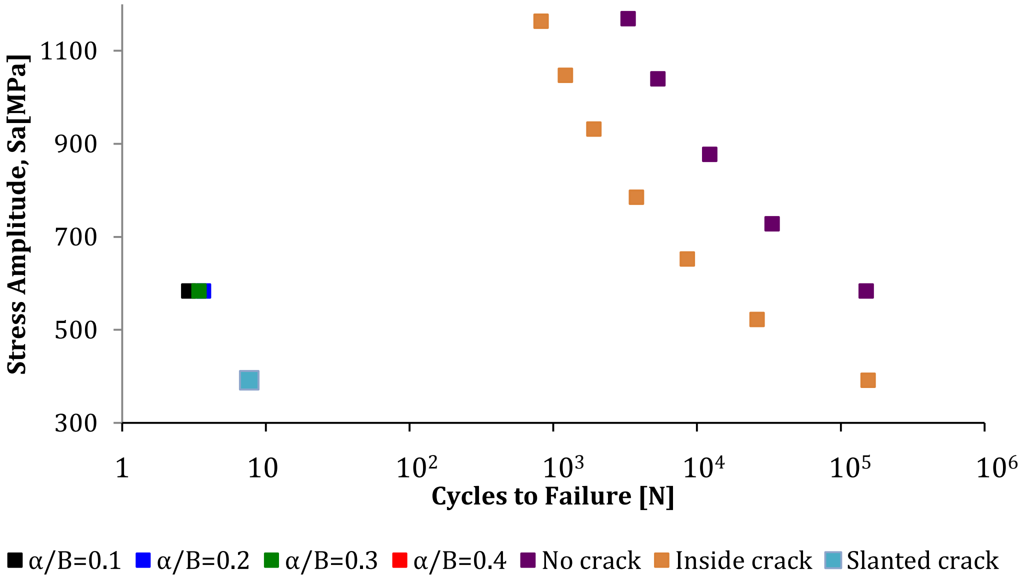

Figure 79: Estimated Fatigue Life of cracked AISI 4130 CF Specimens

As seen from the S-N curves of the cracked specimens (Fig. 79), fe-safe^{TM} estimates that the fatigue life of the surface cracked specimens is in the order of a few cycles. On the other hand, when the internally cracked specimen's fatigue life is compared to that of a smooth specimen, it can be concluded that under rotating bending interior cracks do not propagate in a very rapid rate, and specimens with this type of cracks may be expected to have a life a bit shorter than the smooth specimens. It should be noted however, that the interior crack is not normal but makes 45° angles with the bending axis, propagating thus in a slower way than the normal cracks.

Since the specimens with surface cracks, fail after a few cycles, 8 cycles to failure being the maximum recorded for the slanted crack, their fatigue limit is very low, and ranges between 3 and 5 MPa. However, the fatigue limit for the case of the interior crack, is estimated from the above simulations to approximately 129 MPa, for a K_t= 3.4 (Table 14).

Table 14: Stress Concentration Factor and Fatigue Limit for Cracked Specimens

	α/B=0.1	**α/B=0.2**	**α/B=0.3**	**α/B=0.4**	**Interior crack**	**Slanted crack**
K_t	115	115	122	134	3.4	93
S_e	3.8	3.8	3.58	3.26	128.5	4.75

A model of the leaf spring specimen was created true to dimensions, in ABAQUS/CAE. The loading and supports were designed similar to the tests conditions of the fatigue test rig. Since no information on the compressive residual stress field can be known without the performance of an X-ray diffraction measurement, the model was not assigned a residual stress field, and no input data was added to the model to account for the effects of the heat treatment. In addition to the above, it should be considered that the variable thickness and width of the leaf as well as the fact that the holes and fillet angles, are plausible regions of high stress concentration. As a result, in order to define a satisfactory mesh size for the analysis, a straight beam of similar length dimensions as the leaf, and of width and thickness equal to the maximum width and thickness of the leaf spring, and finally of zero camber was modeled. The appropriate mesh was determined after comparison of the results of maximum bending stress form the simulations on ABAQUS/CAE to the theoretical maximum bending stress at the center of the beam.

$$\sigma_{center} = -\frac{Mc}{4I} \tag{48}$$

The difference between FE results and theoretical calculations was less than 1%.

A straight beam with a hole of the same diameter (19 mm) (Fig. 80) as that in the center of the leaf spring was also modeled and tested for the maximum bending stress in order to determine the effects of stress concentrations due to the existence of a center hole. Comparison of the two ABAQUS/CAE simulations, of the straight beam with and without a center hole (Fig. 81), shows that as the applied load increases, the bending stress increases. The bending stress in the beam with the center hole is much larger, approximately 25% larger. Fig. 82 (a) and (b), shows visualization of these results. From the contour plots of Fig. 82, it can be observed that the straight beam without the hole shows greater stress concentration to the region where the beam is supported on the compression surface, and high stress concentration on the tension surface below the loading point. This is not the case in the beam with the center hole, as the area around the hole on the tension surface is the one with the highest stress concentration.

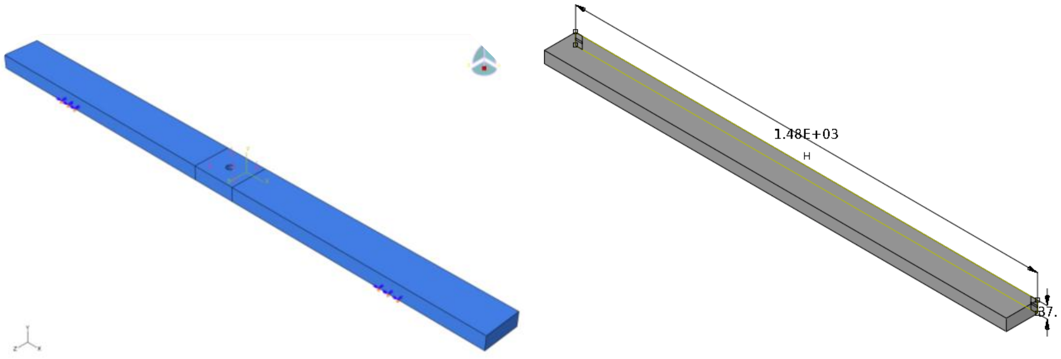

Figure 80: ABAQUS/CAE straight beam models with center hole (left) and without (right) (Dimensions in mm). Loading and supports are also shown (left)

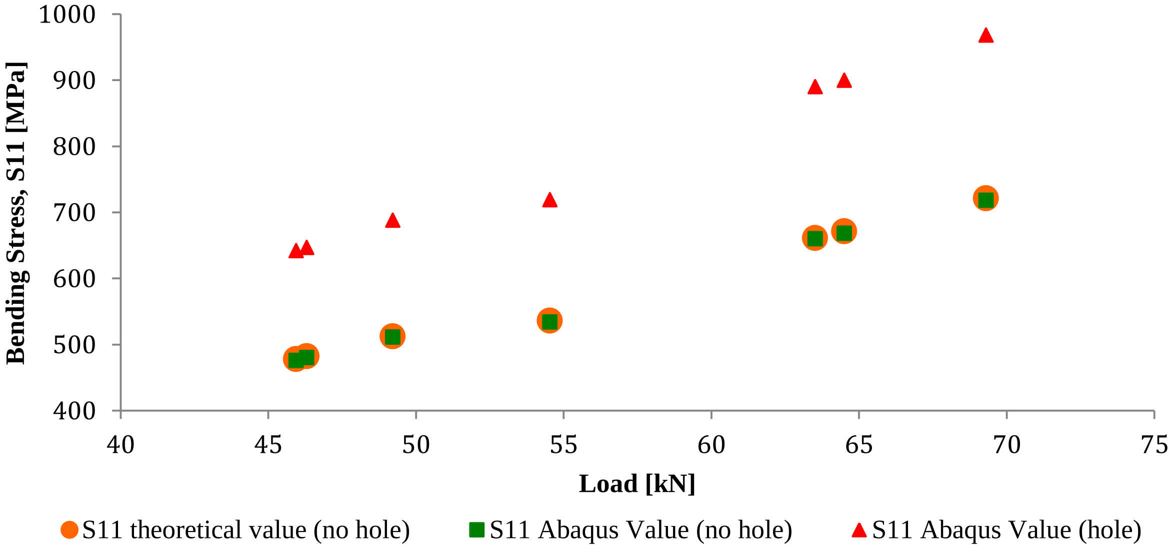

Figure 81: Bending Stress vs. Applied Load in AISI 6150 Beam ABAQUS/CAE models

Fig. 81 shows a comparison between a theoretical model (Eq. 48), and the two above beam models (Fig. 80), with and without a center hole, regarding the maximum bending stress in the models. In all three cases, as is expected, bending stress increases as the applied load increases. The theoretical calculations agree to those estimated form the ABAQUS/CAE simulation, within 1%. However, the model with the center hole presents a much larger bending stress, 200 MPa larger at smaller loads and approximately 250 MPa at larger loads.

The contour plots of the stress profile in Fig. 82 (c) show the areas where maximum stress develops in the leaf spring past 1,000 cycles. As in the case of the actual fatigue tests of the leaf springs, maximum stresses develop in the tension surface midway between the center of the leaf and the supports. Maximum stresses also develop on the compression surface above the supported area. These latter stresses are due to the way the supports are modeled. However, since this model predicts a maximum stress region on the tension surface, similar to the region where failure occurred in actual fatigue testing of the leaf spring, the ABAQUS/CAE model of Fig. 82(c) will be used as the input model for the fe-safe^{TM} estimation of fatigue life of the AISI 6150 steel.

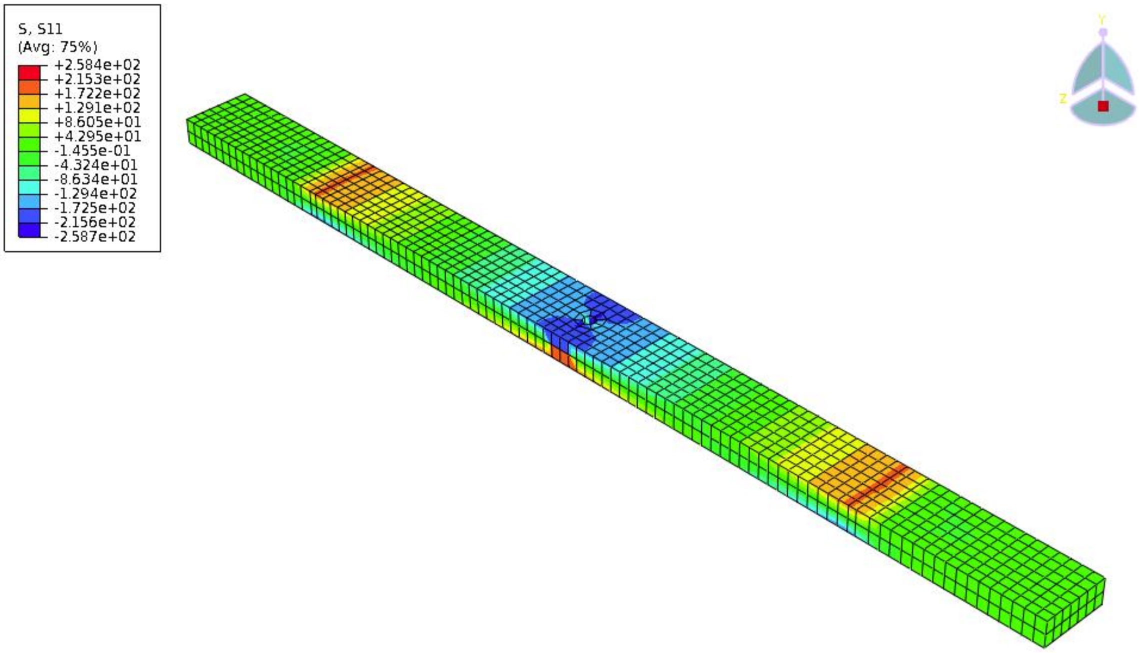
S, S11
(Avg: 75%)
+2.584e+02
+2.153e+02
+1.722e+02
+1.291e+02
+8.605e+01
+4.295e+01
-1.455e-01
-4.324e+01
-8.634e+01
-1.294e+02
-1.725e+02
-2.156e+02
-2.587e+02
Y
Z

(a)

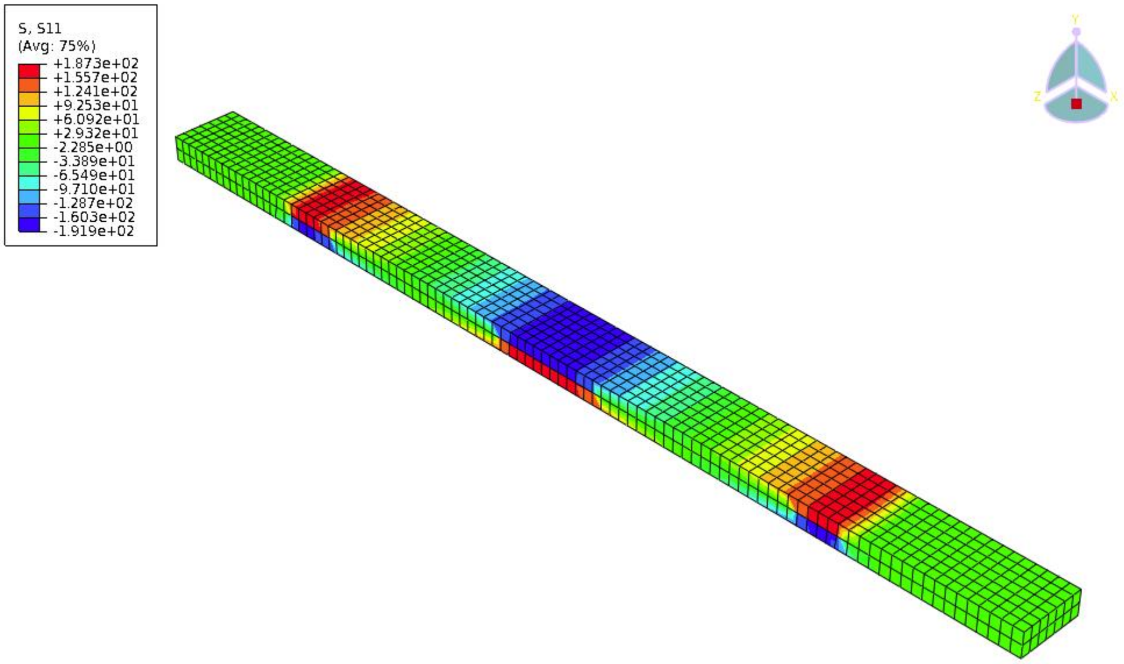
S, S11
(Avg: 75%)
+1.873e+02
+1.557e+02
+1.241e+02
+9.253e+01
+6.092e+01
+2.932e+01
-2.285e+00
-3.389e+01
-6.549e+01
-9.710e+01
-1.287e+02
-1.603e+02
-1.919e+02
Y
Z
X

(b)

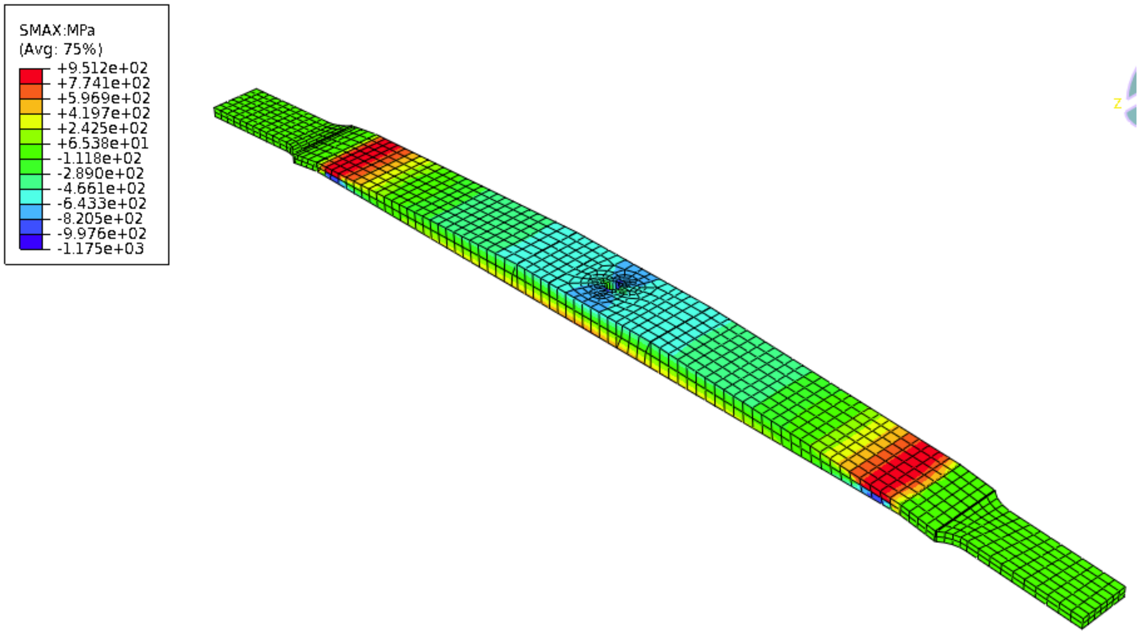
SMAX:MPa
(Avg: 75%)
+9.512e+02
+7.741e+02
+5.969e+02
+4.197e+02
+2.425e+02
+6.538e+01
-1.118e+02
-2.890e+02
-4.661e+02
-6.433e+02
-8.205e+02
-9.976e+02
-1.175e+03
Z

(c)

Figure 82: ABAQUS/CAE visualization of stresses in straight beam models with center hole (a) and without (b) and leaf spring (c)

As was the case for the AISI 4130 steel, the residual stress field is not known, nor is a fixed value of the ultimate tensile strength of the material. Both of these parameters are important data for the estimation of the fatigue life of the leaf spring using fe-safe^{TM}. Fe-safe^{TM} detects the cycle during which a possible crack may initiate on the surface of the input FE model, and as a result surface parameters are very important. Experimental results in section I.3 have shown that the tensile strength in the material varies between the surface and the core of the leaf spring, 995 and 1630 MPa. Estimates of the fatigue life of the leaf spring were calculated using fe-safe^{TM} for these two tensile strengths, as well as for four different surface factors

(K_s=1.5,1.7,1.8,2), and four different compressive residual stresses (-350 to -1000 MPa) at K_s=1.5. The surface factors are selected based on databases giving empirical surface factors for shot peened components to range between 1.5 and 2 [77], as shown for the case of AISI 4130 CF.

In order to choose the appropriate surface factor to represent the fatigue life estimates, four different estimates were completed at both the surface and core ultimate tensile strength levels. As seen on Fig. 83 all estimates based on the different surface factors show much lower lives than the experimental data when the fatigue life is estimated at the surface tensile strength of 995 MPa. Among the four surface factors used, experimental data only agrees with the K_s=1.5 life at longer lives above $5x10^5$ cycles. A similar analysis is shown in Fig. 84 for the case of estimates based on the 1630 MPa tensile strength of the core. In this case experimental data spans across the estimated results at the different surface factors. At longer lives experimental data lays closer to the estimated life at the larger surface factor, while the opposite occurs at shorter lives, when the experimental data curve is closer to the life estimate at K_s=1.5.

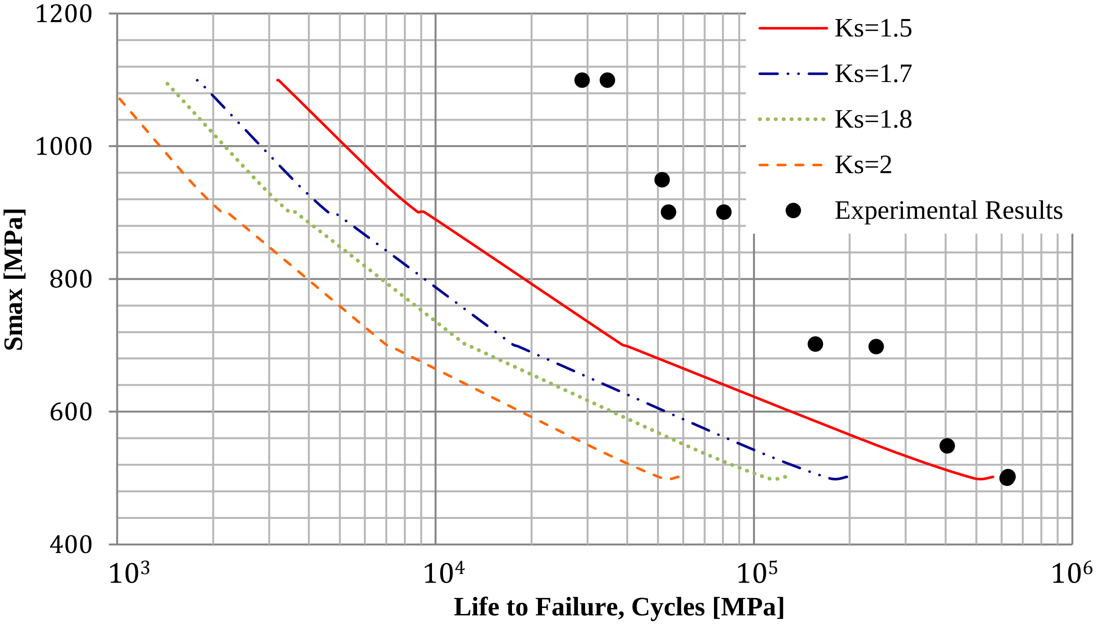

Figure 83: fe-safe^{TM} Fatigue Life estimates for 995 MPa Ultimate Strength

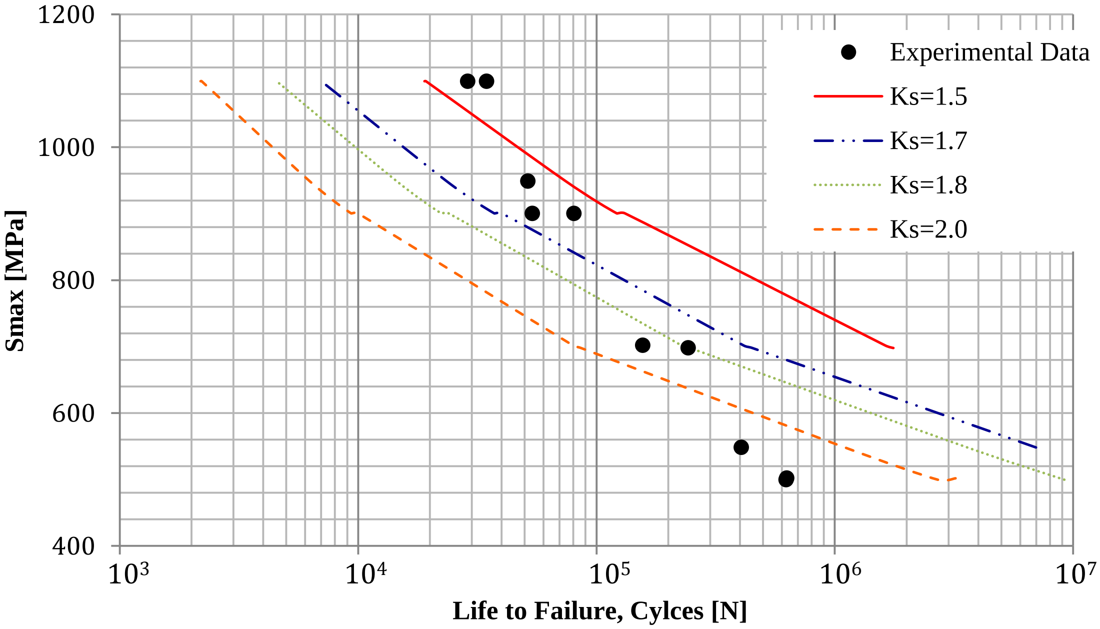

Figure 84: fe-safe^{TM} Fatigue Life estimates for 1630 MPa Ultimate Strength

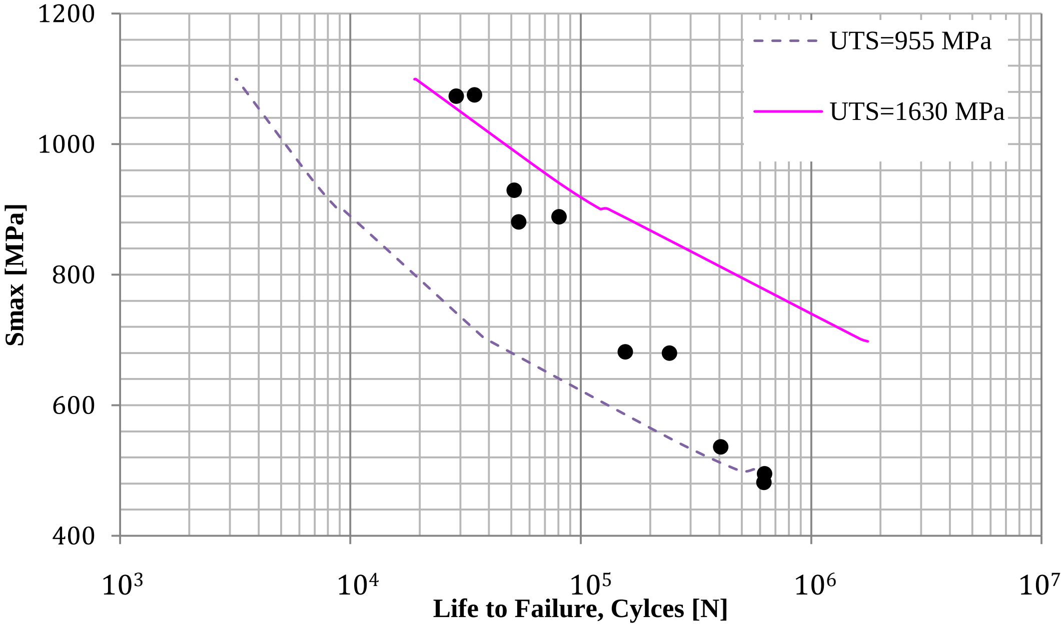

Figure 85: Effect of Ultimate Tensile Strength on Fatigue Life if AISI 6150 Steel

The fatigue life of the leaf spring is shown on an S-N graph in Fig. 85 estimated at K_s=1.5 and ultimate tensile strengths of 995 MPa and 1630 MPa. The expected positive effect on the fatigue life of an increasing ultimate tensile strength is obvious by comparison of the two estimated S-N curves. The S-N curve due to experimental data spans across the fe-safe^{TM} prediction curves. It should be taken into account, that the fatigue life curve due to the experimental data is influenced by a gradient of ultimate strengths between the surface and core of the leaf spring, existing due to the heat treating process, i.e. oil-quenching and tempering. The design of the leaf spring has also an influence on the fatigue life, and some aspects of this design may not have been covered during FEA modeling. An example of these aspects concerns the thickness variation along the leaf, for which not much information was known.

However, the experimental results lay between the upper and lower tensile strengths observed in the material of the leaf spring.

At longer lives, when the component enters the region of the endurance limit experimental results are closer to the S-N curve of 995 MPa in ultimate tensile strength. This is the surface tensile strength, and as discussed earlier HCF is the region where fatigue life is based on the applied stress, which is primarily elastic [20]. The HCF region is mostly concerned with the propagation of a crack that leads to failure of the material through fracture [21,28,32,35], and as a result it is only reasonable to find experimental data coinciding with the surface based ultimate tensile strength S-N curve, at longer lives.

When the fatigue life of experimental results rests below 10^5 cycles, the data points are in the region of the S-N curve of the higher ultimate tensile strength, of 1630 MPa, which belongs to the core of the leaf spring. This region of the fatigue curve is close to the LCF region, where the initiation of a crack is of greater importance as plastic strains and deformation become the reasons for fatigue failure [21,28,32,35].

Accounting for the effect of residual stresses, the same estimates as above are repeated at four different compressive residual stress levels. As expected based on theory the larger the magnitude of the compressive residual stress the greater the fatigue life [21,28].

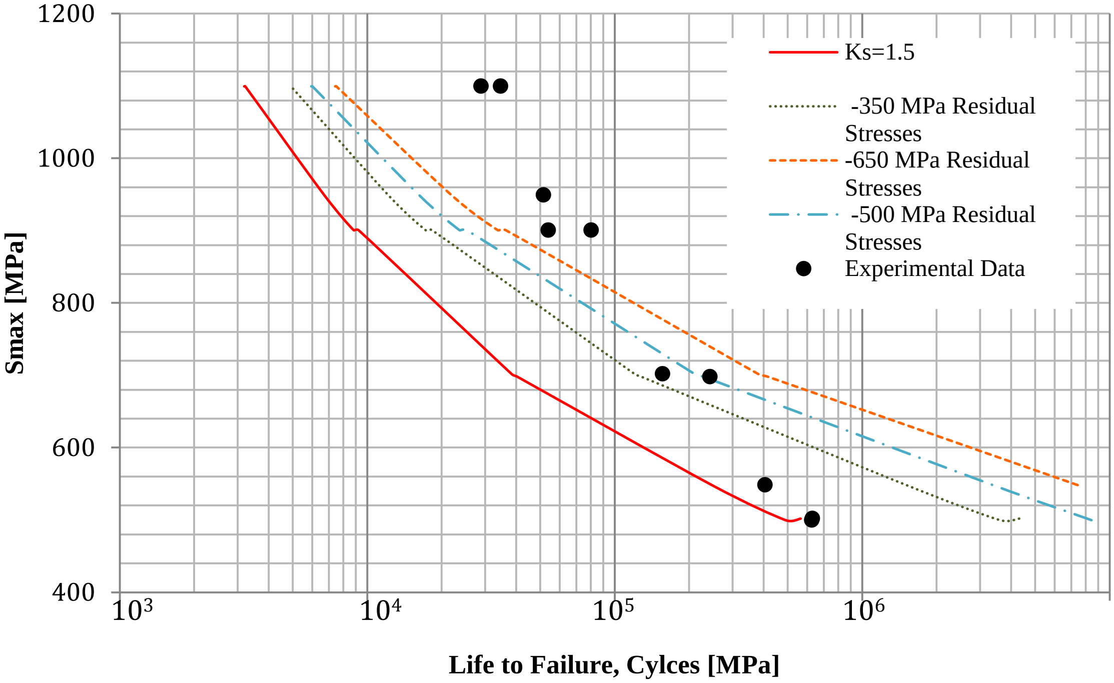

Figure 86: fe-safe^{TM} Fatigue Life estimates for 995 MPa Ultimate Strength with residual stresses at Ks=1.5

When repeating the above comparison at 1630 MPa (Fig. 87), the experimental data is much smaller than the estimates. This is reasonable enough, based on the fact that fatigue failure starts on the surface of the leaf spring where the tensile strength is estimated at 995 MPa.

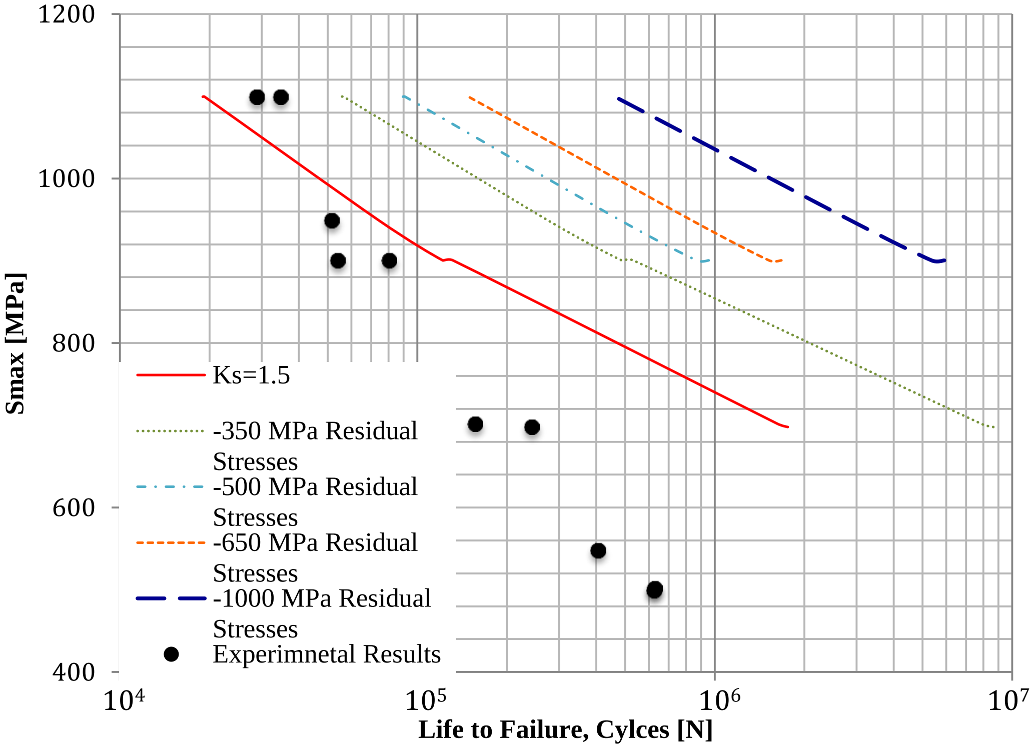

Figure 87: fe-safe^{TM} Fatigue Life estimates for 1630 MPa Ultimate Strength with residual stresses at Ks=1.5

I.4 Repairs of Steel Leaf Springs

Suspension systems are an important vehicle component assuring control of the vehicle as well as comfort and safety of the ride. Suspensions therefore, and consequently leaf springs, should be checked in a regular basis in order to assure they are working properly. Leaf springs may need readjustments and/or repositioning on the vehicle, however, when their life is approaching to its end, the only way to repair them is by replacing them.

When the fatigue life of a spring ends through fracture the results are catastrophic, and in most cases very dangerous for the passengers of the vehicle. If the suspension is a single leaf spring that has failed, a new leaf spring should be used as replacement, while if the leaf spring is part of a multi-leaf assembly, a single leaf can be replaced and the assembly will have to be preset and adjusted from the beginning. In this latter case, the leaf spring assembly will not operate as new, as the non-failed leaves will have already accumulated fatigue damage.

Repairing a metallic structure that has failed through fracture or cracking can be done through welding. Although welding of leaf springs is rising in demand among the car mechanics, as the leaf spring prices rise and world economy collapses, manufacturers reply to this demand should always be negative [15].

As seen in earlier sections discussing the fatigue life of AISI 6150 leaf springs, fatigue failures are demonstrated as cracks that propagate to fracture on the tension surfaces of the leaf. It was also shown that these fracture points occur at areas of maximum stress (section I.3). These areas of possible crack initiation points do not vary a lot among leaf springs of the same type as their application is very specific and the way they are loaded and cycled does not fluctuate a lot to cause redistribution of these stresses. It can therefore be concluded that if a leaf spring of a certain type demonstrated maximum bending stress in the area between the loading point and its support, as was the case of the leaf springs tested for this research, leaf springs of the same type will also demonstrate same maximum stress profiles. In the case that a leaf spring fails at one of these points and is repaired by welding, the welded area will be the area under maximum stress.

Similar to a hole or other geometric discontinuities, welding of a component will invoke changes in its geometry, thus affecting the stress-field flow lines and raising the stress concentration at the location of the weld (Fig. 88) [32]. This location of maximum stress concentration due to welding will also become the point of maximum stress under loading, in the case of a welded leaf spring, leading to the initiation and propagation of fatigue cracks in this area.

Fig. 89 shows various stress concentration regions for weldments. Depending on the way a leaf spring fails, through a crack or complete fracture, either a full or partial penetration butt weld should be used. Most of the fatigue cracks in weldments are initiated at weld toes or terminations, rather than internal regions, based on the fact that a surface discontinuity is the least tolerated discontinuity during the fatigue life of a component [32].

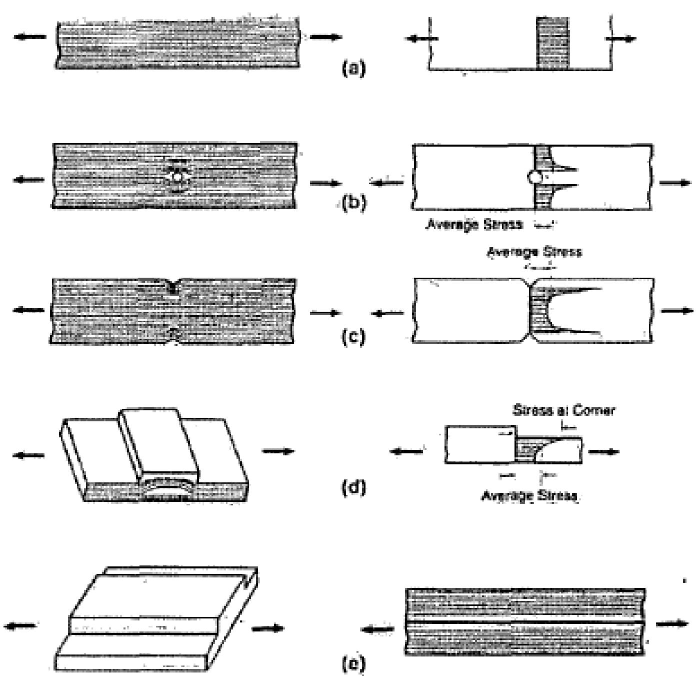

Figure 88: Flow Lines and Concentration of Stress [32]

There exist many design codes and standards for weldment fatigue. Based on the BS 7608 standard there are eight different classes of steel weldments (B, C, D, E, F, F2, G, W) for which S-N design curves independent of ultimate and mean stresses have been determined (Fig. 90). Based on these curves, the fatigue limit for the full (Class B) and partial (Class F2) butt welds for a steel weldment, are 100 and 35 MPa [33]. These fatigue limits are very low for applications similar to that of suspension leaf springs, however testing the fatigue life of welded leaf springs is not within the scope of this research.

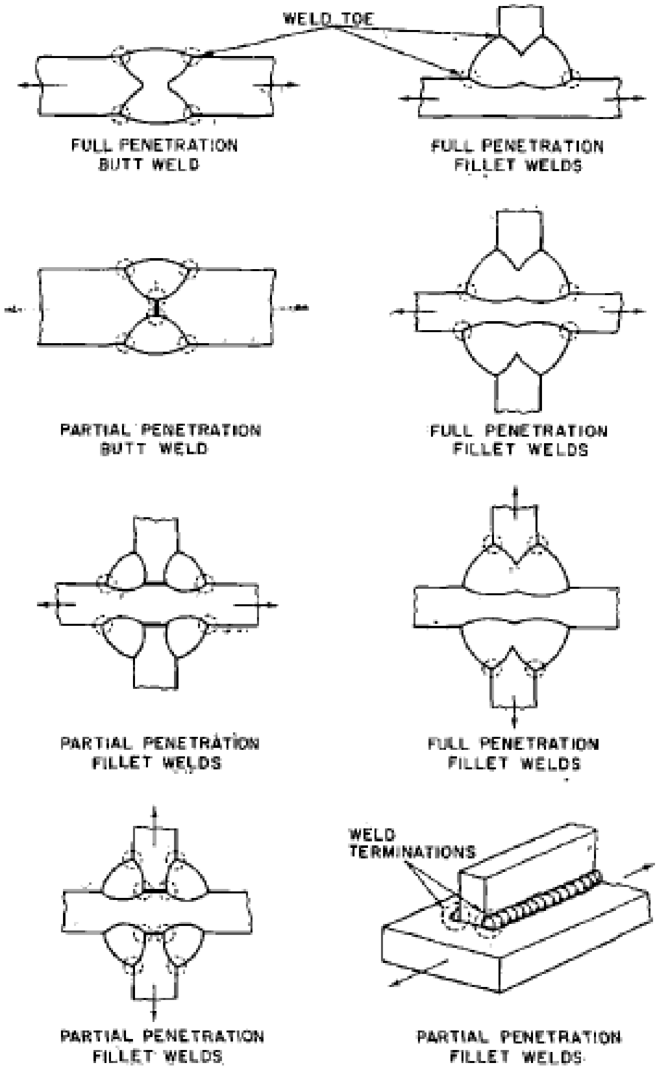
WELD TOE
FULL PENETRATION BUTT WELD
FULL PENETRATION FILLET WELDS
PARTIAL PENETRATION BUTT WELD
FULL PENETRATION FILLET WELDS
PARTIAL PENETRATION FILLET WELDS
FULL PENETRATION FILLET WELDS
WELD TERMINATIONS
PARTIAL PENETRATION FILLET WELDS
PARTIAL PENETRATION FILLET WELDS

Figure 89: Stress Concentration Regions (circled areas) for welds [32]

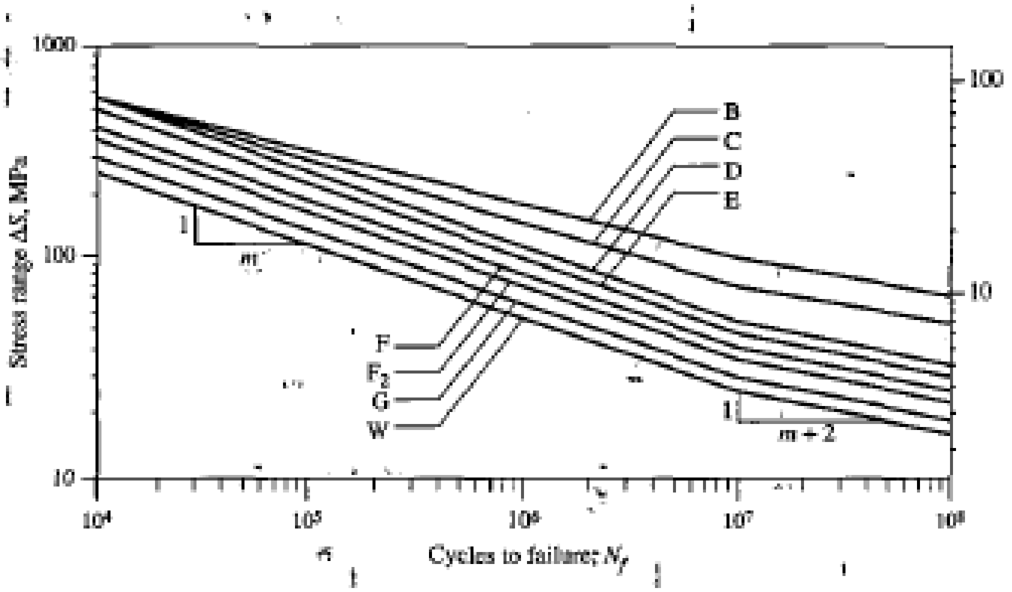

Figure 90: S-N curves for Weldment Fatigue Design (BS 7608 Standard) [32]

On another note, welding may affect the spring rate of the leaf, as it is going to affect the geometry and mass, and consequently deflection of the leaf under loading. Welding of a leaf spring, therefore, is not a repair solution. It will not prolong the fatigue life of the leaf spring effectively, but instead will become a possible cause of a new failure that can even lead to an accident.

I.5 Conclusions

Section I.3 of this part discussed the fatigue life of AISI 4130 CF and AISI 6150 steel based on experimental results, calculations and finite element analysis.

Experimental results on the fatigue life of AISI 4130 CF showed that the induction of compressive residual stresses on the surface of the steel, by means of a surface treatment, improves the fatigue life of the component and increases its fatigue limit and surface hardness. However, the effect of stress relaxation becomes a crucial parameter that needs to be taken into account when designing a component.

Heat treating a steel component, as in the case of the AISI 6150 leaf springs, will alter the microstructure of the material. Depending on the thickness of the component and the duration of the treatment, the component that has undergone quenching and tempering will end up with a martensitic microstructure, which is not uniform throughout its thickness. As a result, the ultimate strength of the material will differ between the core and the surface of the component. This difference in microstructure has an effect on the micro-hardness of the steel. The core micro-hardness is uniform and starts decreasing as measurements are taken towards the surface of the component. In the case of leaf springs, where a tension and a compression surface may be distinguished based on the way the leaf spring is mounted and operated as a suspension system, the micro-hardness on the compression surface is higher than on the tension surface.

Experiments are the most accurate technique to gather information on the fatigue life of components. However, experiments are time consuming and expensive to perform. Calculations based on models and relationships developed to estimate the fatigue life of a component may be good approximations to experimental data, with certain limitations.

The power relationship may give an estimate on the fatigue life of a component only for a certain interval of life cycles, while when used with information on steel hardness, there is an upper limit to the ultimate strength that the steel in question may have. Damage accumulation models on the other hand, may give some insight on the damage accumulation and fatigue life patterns of a material but depending on the model chosen the results may be overestimated of underestimated.

Surface and heat treatments, size of the component, environmental effects, as well as other factors that affect fatigue may be incorporated in some, not all, calculations without always accurately portraying reality. It can therefore be concluded, that estimating the fatigue life of a component using models should be done with caution as an indication of the life of the component, and always verified by experimental data.

Finite element analysis has developed a lot over the years and there exist today powerful tools that can give very good predictions of the fatigue life and failure of components. Despite the vast range of options that these tools offer to help define all the characteristics of the component, they still fail in giving results that perfectly agree with experimental data, as well as results on components with possible defects. However, finite element software may be used as a design tool to investigate the fatigue and failure response of a material especially in the HCF region.

Although both damage models and finite element analysis should be verified by experimental data, it can be used as a tool to compare the fatigue lives of two materials. From the discussion in section I.3 of this part it was shown that AISI 6150 is a stronger steel that can sustain longer lives than AISI 4130 CF.

Considering failure of steel leaf springs and their option of repair there is little that can be done. It is almost impossible to detect and prevent cracks and defects on the surface of a leaf spring while it is active on a vehicle. On the other hand, upon failure of the leaf spring the only repair option is welding which is not recommending for components undergoing fatigue loading. Therefore, leaf springs may only be replaced once they have failed. In the case of a multi-leaf assembly, there is no need to replace the whole assembly but only the leaf that has failed. However, re-assembly of the spring and presetting should be repeated, and the fact that the old leaves have accumulated damage should be considered.

II. COMPOSITES

II.1 Composite Materials

Composites are a very large category of materials whose main characteristic is that they are the combination of two or more distinct constituents. Concrete, bones and wood are examples of composite materials. However the present research will concentrate on a category of composites called Fiber-Reinforced Plastics (FRP). FRPs are synthetic composites of epoxy resin and fibrous high strength materials. FRPs are high in strength and stiffness while very low in weight, and are many times utilized as an alternative to metals in structures where high performance and low weight is a desirable combination. Another reason why composites are a very popular alternative to metals, regards applications requiring materials of high corrosion resistance [78].

This research will discuss unidirectional and bidirectional reinforced-plastics. The fibers in a FRP can exist in two major forms; as unidirectional reinforcement where the fibers are continuous along one direction of the composites, or bidirectional reinforcement, also referred to as woven, where the fibers are knit in a cloth form and fibers occupy two directions of the composite.

FRPs with glass fiber reinforcements, what is commonly known as fiberglass, are called Glass Fiber Reinforced Plastics (GFRPs) [79], and are the main material used in the production of composite leaf springs. Glass is a non-crystalline material with isotropic properties [8]. Glass fibers may be silica, oxynitride, phosphate and halide, and the fibers are named by a capital letter of the Latin alphabet. As a result, the most common glass fibers E-glass are named after abbreviating the word *Electrical* thus denoting the electrical conductivity properties of the fibers. The high strength S-glass fibers, used in the aerospace industry, also take their name from the abbreviation of the word *Strength*. There are also other types of glass fibers such as C-glass and R-glass, also having names describing their properties. S-glass fibers are divided in subcategories, one of which, S2-glass, will be discussed and compared to E-glass in this research.

Apart from the fibrous constituent, composite materials also have a matrix constituent. Generally in composites the matrix constituent may be any type of known material, however, polymeric matrices are the most commonly used in composites [8,63]. Polymer Matrix Composites (PMCs) may have a thermoplastic, thermoset or rubber matrix. However, thermosets are the most widely used as composite matrices in GFRPs due to the ease of manufacturing they can provide. The advantage of PMCs is the ease of production and the variability in means and processes they can accept during production. However, a main disadvantage during production is that they have a low maximum working temperature due to their high coefficient of thermal expansion, and care should be taken with their exposure to moisture [8].

Apart form the high stiffness and stress at a lower weight; composites provide a variety of ways to be formed. One of the advantages of composite materials is that there is no need to first create the composite and then the component to be manufactured, as both component and composite material are manufactured simultaneously, as will be shown later in the production of composite leaf springs.

The orientation of fiber reinforcement in FRPs can be chosen in the optimal combination for the structure to be manufactured, whether the reinforcement is unidirectional or woven. The fibers in a unidirectional composite are placed randomly in a matrix. The matrix and fiber volume fractions will determine the final properties of the composite, which may be expressed through the rule of mixtures (Appendix B) [8,63,80].

A composite material may have a laminar form, meaning that it is composed of a definite number of layers, also referred to as laminae or plies, each of which have a matrix and fiber constituent. The fiber orientation may vary among the laminae, as may vary the fiber and matrix fractions and materials. All laminae together compose the laminate or ply stack (Fig. 91), the composite material having a certain ply sequence defined by the different fiber orientations in the plies. The ply, or stacking, sequence, volume fractions of the constituents, and number of laminae in the laminate determine the ultimate properties of the composite structure. The number of plies can be even or odd, and will result in an anti-symmetric or symmetric laminates (Fig. 92), which will also affect the performance and properties of the composite structure [78,81].

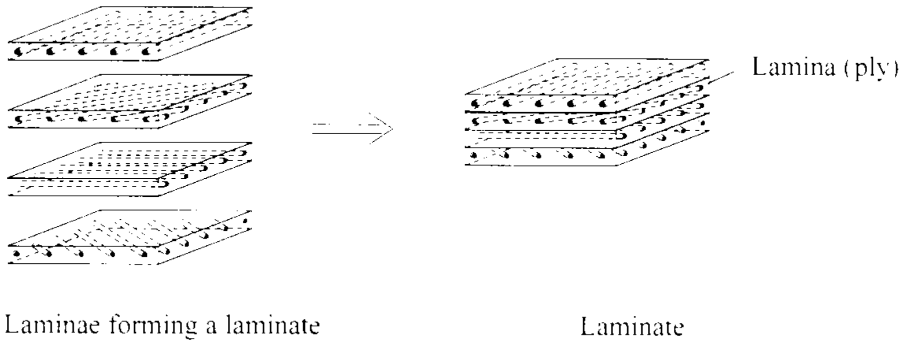
Lamina (ply)
Laminae forming a laminate
Laminate

Figure 91: Laminated Composite [82]

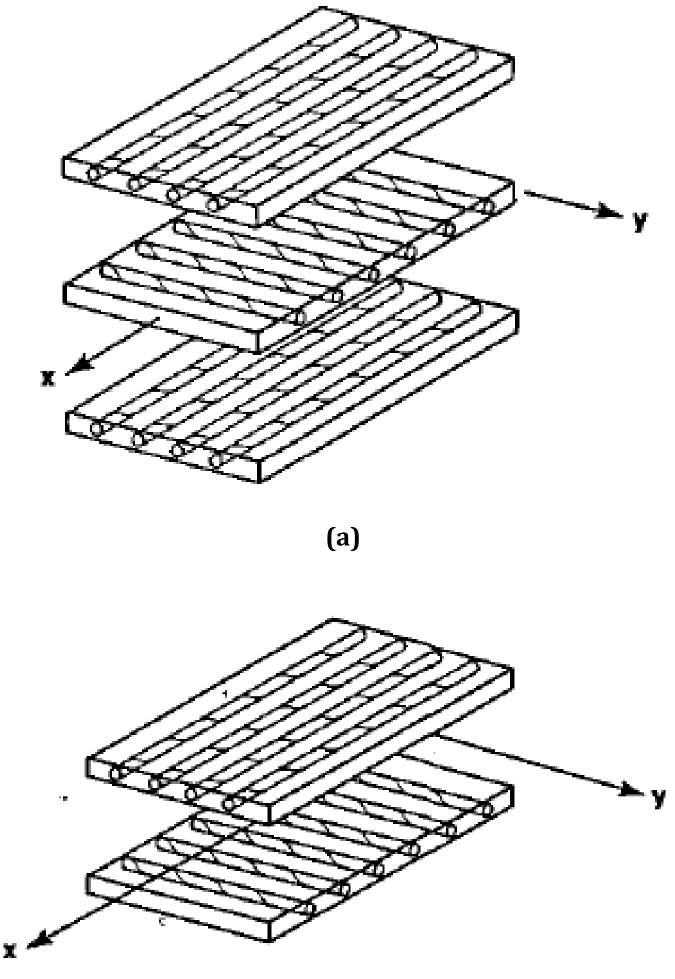

(a)

(b)

Figure 92: Unbonded views of anti-symmetric (a) and symmetric (b) cross-ply laminates [81]

To proceed with any type of analysis of a lamina it is important to define a coordinate system. The Cartesian coordinates are typically used. It is possible that the fibers of a unidirectional lamina do not have the same orientation as the axis of a Cartesian coordinate system, but instead they make an angle with one of the axis (Fig. 93). Such a lamina is called angle or off-axis lamina, and a set of principal axis should be defined where direction 1 will be along the direction of the fibers, and direction 2 transverse to the fibers. A lamina whose fibers are oriented along the x or y-axis is called an on-axis lamina.

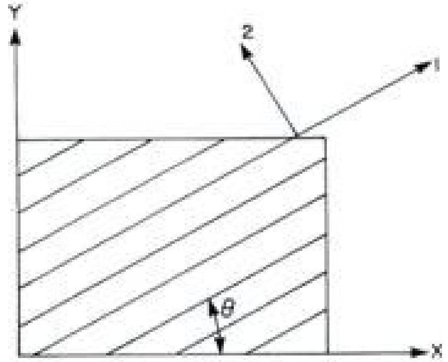

Figure 93: Representation of an angle lamina with the local and principal directions [83]

When an angle lamina is loaded longitudinal, or transversely, along the x or y directions, the loading is called off-axis. When the load direction coincides with the fibers' orientation the loading is termed on-axis loading [83].

Due to the very different mechanical properties of a GFRP's constituents (Appendix A), composite materials do not have an isotropic nature. The anisotropy of a laminate may be different for each layer, and therefore it is important to develop an analysis for the individual laminae, before considering the laminate as a whole. Apart from anisotropic, composites tend to be orthotropic or transversely isotropic. Most available theories and analysis however, are limited to orthotropic laminae.

A unidirectional composite is one that has all its reinforcing fibers positioned along one of its three directions (Fig. 94). Contrary to an isotropic material, such as a metal, the stiffness and strength of a composite varies depending on the direction of the material along which the properties are measured. When the composite in consideration is unidirectional, isotropic behavior can be assured in a cross-section of the material taken perpendicular to the fibers. A transversely isotropic material, as shown in Fig. 94, has identical properties along 2 and 3 directions. Transversely isotropic materials, therefore, have two sets of mechanical properties, along the transverse and longitudinal to the fibers directions, respectively [8].

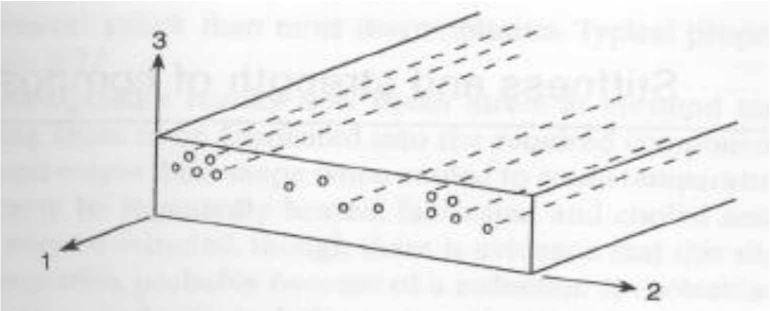

Figure 94: Orientation of the fibers of a unidirectional composite along x1 direction [8]

Apart from high stress and stiffness, composite materials fail differently than metals. Although, like metals composites are considered to have failed when they stop performing according to their design criteria [63], contrary to the case of homogeneous isotropic materials such as metals where fatigue failure is characterized by the initiation and propagation of a crack, fatigue failure in composites is the result of accumulated damage [8,84]. Although in metals the strength of materials changes little or not at all during fatigue cycling [58], and it is the crack propagation that defines fatigue damage, in composites the strength of the material starts decreasing slowly early in the fatigue life, and towards the end of it, close to failure, the rate of decreasing strength becomes very rapid [85].

The effect of the intensity of the stress applied also differs among metals and composites. While low stresses are critical in the design of a metal structure, it is higher stresses, defining low cycle fatigue, with which caution should be taken when designing a composite structure [59].

Due to the different constituents that combine to make composite materials, failure of the composite may be due to different mechanisms called the failure modes of the composite. In composites failure begins in a micromechanic level, the level at which the mechanical behavior of the constituents is examined [80,82-83], and may be demonstrated as fiber, matrix or interface dominated failure, which includes delamination and debonding. Matrix and fiber failures are the cracking and fracture of the matrix or fiber constituents, respectively. Interface dominated failure, is the failure that is demonstrated at the interface of composites constituents. Debonding is a microstructure interface-dominated failure mode, which involves the separation of the fibers from the matrix constituent. Delamination is also an interface-dominated failure during which adjacent laminae of the composite separate form each other, and is mainly initiated by interlaminar tension and shear caused by the existence of free edge effects, structural discontinuities, variations in temperature and moisture, as well as localized defects induced in the material during manufacturing (e.g. drilling) [63,86]. Among these failure modes, delamination is maybe the most usual failure mode in laminated composites, especially components that undergo cyclic loading as composite leaf springs.

As micromechanic failure becomes macromechanical (Fig. 96) the result is catastrophic failure. Depending on the loading that caused failure in the structure, failure modes can be characterized as tensile, compressive or shear.

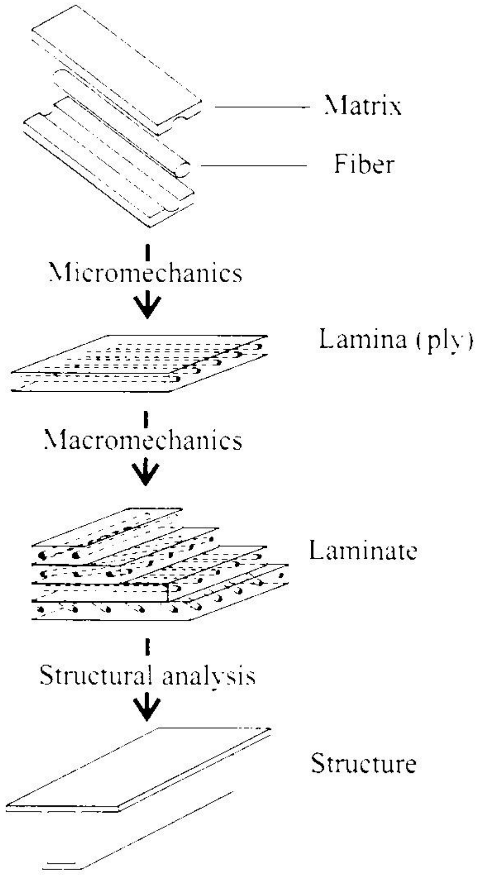
Matrix
Fiber
Micromechanics
Lamina (ply)
Macromechanics
Laminate
Structural analysis
Structure

Figure 95: Analysis Levels of Laminated Structures [82]

II.2 Manufacturing of Composite Leaf Springs

As mentioned in the previous section composite structures and metallic structures follow different manufacturing processes. As in most cases the composite material is formed of its constituents during the structure’s manufacturing process. The difference in the isotropy of metals and composites also affects the design of manufacturing process, and in the case of the composites, extra care should be taken in designing the process [9].

Composite materials may be manufactured in a variety of ways among which the more widely known include the lay up or ply lamination method, pultrusion, filament winding and compression molding.

Most composite leaf springs have unidirectional fibers oriented along the length of the leaf [9-10]. The matrix of the composite material is epoxy resin. The orientation of the fibers in the composite leaf spring is chosen to resist tension and compression developed due to the bending forces of the loading application. The role of the resin in the component is important as it supports the fibers while they are under compression and as a result helps prevent bucking, but also acts as the medium that transfers shear loading between adjacent layers of fibers. After the matrix has solidified during curing, which in the leaf spring manufacturing process requires heat and pressure applied to the product during molding, the leaf spring will demonstrate excellent strength in the direction of the fibers. In the direction perpendicular to the fibers the strength of the leaf spring will not be as high. Some manufacturers reinforce the perpendicular direction with fibers through use of alternating angles [9].

Filament winding and lamination followed by compression molding are the two dominant methods followed by the composite leaf spring industry. The major difference between them is the form of the raw materials. In filament winding the fibers and the resin are provided separately to the filament winding machine and the composite is formed as the leaf spring is formed. The lamination method utilizes sheets of pre-impregnated fibers in semi-cured resin that are called prepregs.

The filament winding process is the main process of composite leaf manufacturing used in the automotive industry [10]. The fibers and resin are combined by guiding the fibers into a resin bath and then over to a rotating mandrel, which rotates in such a way that enables the desired orientation of the fibers according to the leaf spring design. The shape of the mandrel will also vary depending on the end product of the filament winding process. Before the fibers reach the mandrel and after they have been immersed in the resin bath, they go through a set of rollers that squeeze out the excess resin. The process of the fibers being immersed in the resin bath is called wet impregnation and since the fibers are deposited in layers on the mandrel to create a composite layered shape, the whole process of filament winding becomes a wet lay-up process. Since leaf springs have a curved shape, the mandrel that would allow for the production of such geometry will have a shape that allows for the production of two leaf springs simultaneously.

The shape of the mandrel can vary to allow for a constant thickness or tapered thickness (parabolic) leaves (Fig. 96). However, for the leaf spring to have the desired fiber volume, material properties and dimensions, the composite leaf spring that gets out of the mandrel should be cured under pressure and heat. The curing process occurs in a die that matches the leaf spring design parameters, while the mandrel over which the leaf spring is wound becomes part of the mold for this curing process (Fig. 96). The temperature, pressure and curing time depends on the epoxy, dimensions and desired mechanical properties of the end product. When curing is completed the composite structure is taken out of the mold and is cut at the sides to form the two composite leaves [9,12].

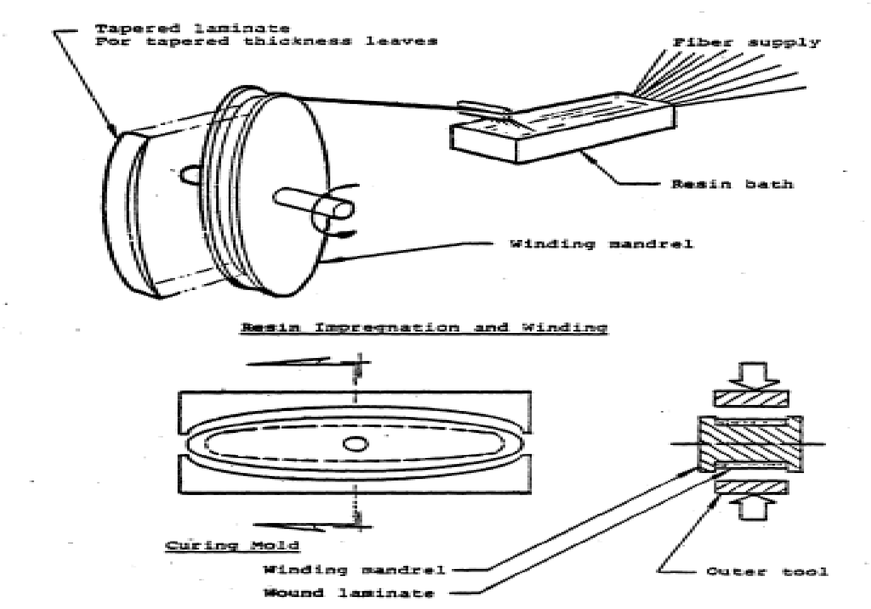
Tapered laminate
For tapered thickness leaves
Fiber supply
Resin bath
Winding mandrel
Resin Impregnation and Winding
Curing Mold
Winding mandrel
Wound laminate
Outer tool

Figure 96: Filament Winding Process [9]

When the raw materials to be utilized are in the form of prepregs, they will be shipped to the manufacturer in the form of rolls, tape or sheets depending on the desired dimensions and quantity of the end product. Care should be taken with prepreg handling, as the products should be stored in a room with the appropriate temperature and humidity specified by the prepreg manufacturer. The formation of a leaf spring from prepreg sheets is termed compression molding. The sheets are cut to the appropriate shape for the leaf spring model to be created and they are stacked in the appropriate sequence until the desired thickness of the leaf is reached. Prepreg materials for the manufacturing of composite leaf springs are unidirectional and the sheets can be oriented to the desired direction to achieve the fiber orientation of the leaf spring design. In order to produce a leaf spring of varying cross-section, different length prepregs can be stacked in the desired sequence. The stacked prepregs are placed in a metal mold and heated under pressure until the composite is cured (Fig. 97). Due to the narrow thickness of the leaf springs, it is often usual to create wider sections and then use a cutter to cut the leaves to the appropriate width (Fig. 98).

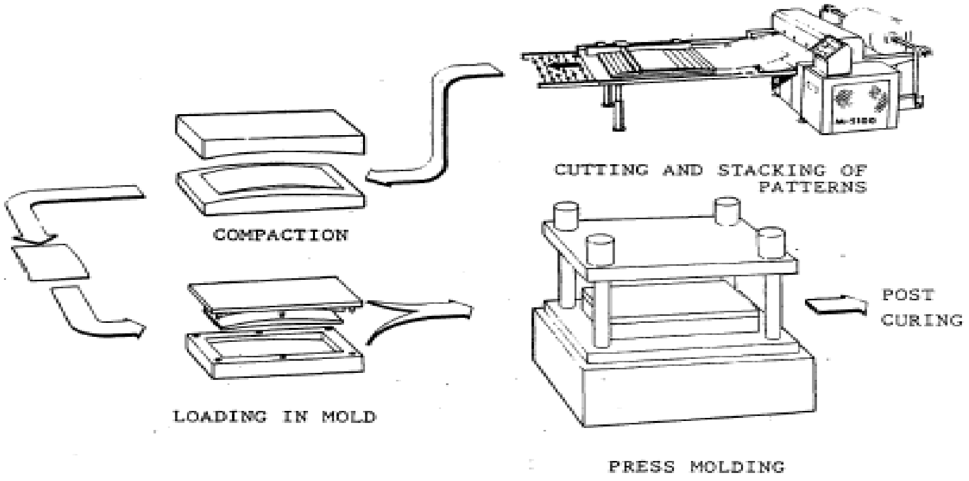

Figure 97: Compression Molding Process [9]

When a composite leaf spring is manufactured from either of the above processes the ends of the leaves will be processed. Using cutters appropriate for composite materials the ends of the composite leaves will be trimmed, tapered or rounded to reduce stress concentrations and provide the leaf with the appropriate end shape that its design requires. If round (eye) ends are dictated by the leaf spring design, the eyes will be attached to the end of the leaf. The eyes need to be metallic as it is still hard for the industry to manufacture durable composite rounds ends. As a result, metallic eyes are attached to the ends of the leaves [13].

Before the final assembly stage a polyurethane coating will cover the leaves to protect the composite from environmental effects. Although in many vehicles a single composite leaf spring will have the strength to replace a steel multi-leaf assembly [14], if an assembly of composite leaf springs is required the leaves will be assembled similar to a steel assembly and be prepared for the aftermarket [9].

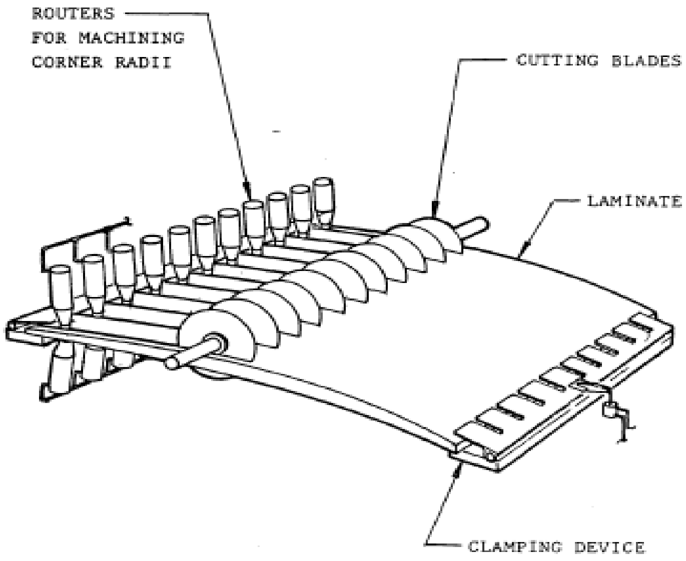

Figure 98: Cutting of Leaf Springs [9]

II.3 Classical Lamination Theory (CLT)

As mentioned earlier a laminate is the assembly of laminas (or plies) of the same or different materials. A laminate's plies may be stacked in the same sequence, meaning that the angles of each ply are oriented along the same direction to a reference axis, or the orientation of the fibers in each lamina may differ. Since composite materials are not isotropic as metals, one cannot apply the stress analysis results of a laminate to describe the stress response of each lamina composing the laminate. The Classical Lamination Theory (CLT), applicable only to orthotropic continuous laminated composite materials, is the set of equations that allows for the development of a constitutive relationship that will define a state of stress for each lamina of the laminate. The development of strain-displacement, stress-strain, laminate load-strain and moment-curvature relationships are all part of CLT [80-81].

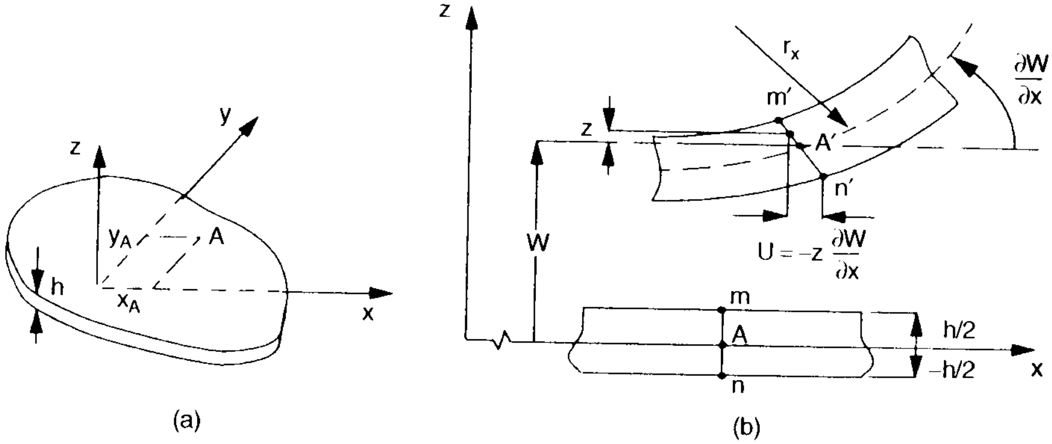
z
y
y_A
A
h
x_A
x
(a)
z
r_x
m′
$\frac{\partial W}{\partial x}$
z
A′
n′
W
$U = -z\frac{\partial W}{\partial x}$
m
A
n
h/2
−h/2
x
(b)

Figure 99: CLT Plate Geometry [80]

According to CLT the nonzero midsurface strains in a plate loaded in the lateral direction (Fig. 99) are

$$\{\varepsilon^0\} = \begin{Bmatrix} \varepsilon_x^0 \\ \varepsilon_y^0 \\ \gamma_{xy}^0 \end{Bmatrix} = \begin{Bmatrix} \dfrac{\partial U_0}{\partial x} \\ \dfrac{\partial V_0}{\partial y} \\ \dfrac{\partial U_0}{\partial y} + \dfrac{\partial V_0}{\partial x} \end{Bmatrix} \tag{49}$$

Under loading the mid-surface of the plate may suffer some curvatures which can be related to the radius of curvature of the mid-surface of the plate. In a laminate the strain variation is dependent both on the nonzero mid-surface strain and the curvature and can therefore be represented by the following relationship

$$\begin{Bmatrix} \varepsilon_x \\ \varepsilon_y \\ \gamma_{xy} \end{Bmatrix} = \begin{Bmatrix} \varepsilon_x^0 \\ \varepsilon_y^0 \\ \gamma_{xy}^0 \end{Bmatrix} + z \begin{Bmatrix} \kappa_x \\ \kappa_y \\ \kappa_{xy} \end{Bmatrix} \tag{50}$$

The stress-strain relationship for an off-axis configuration, where the principal and local axis do not coincide, relates stress to strain through the stiffnes matrix $[\bar{Q}]$. Although the strain varies continuously in the laminate, this should not necessarily be the case for stress, based on the possible varying fiber orientation of the laminas and consequetly of $[\bar{Q}]$ for each such lamina. As a result, the state of stress at different points in the lamina can be established, if the state of strain at those points is known. The state of stress can be specified for the different plies of the laminate following the equation below for the kth lamina

$$\begin{Bmatrix} \sigma_x \\ \sigma_y \\ \tau_{xy} \end{Bmatrix}_k = [\bar{Q}]_k \left(\begin{Bmatrix} \varepsilon_x^0 \\ \varepsilon_y^0 \\ \gamma_{xy}^0 \end{Bmatrix} + z \begin{Bmatrix} \kappa_x \\ \kappa_y \\ \kappa_{xy} \end{Bmatrix} \right) \tag{51}$$

In order to proceed with the above equation to determine the stress state in different individual plies, it is imperative that the ply in question is assigned a name. Usually, numbers determine plies and as a result k takes values form 1 to N, where N is the total number of plies. Ply counting begins from the bottom of the laminate (Fig. 100). A laminate has a certain thickness h, and the mid-plane of the laminate is at the middle of the laminate, dividing the thickness h in two. Each ply also has its own thickness, however it is also useful for calculations regarding laminate analysis that will be discussed later to know the thickness z that describes the portion of laminate thickness form the mid-surface to the top of the lamina under examination.

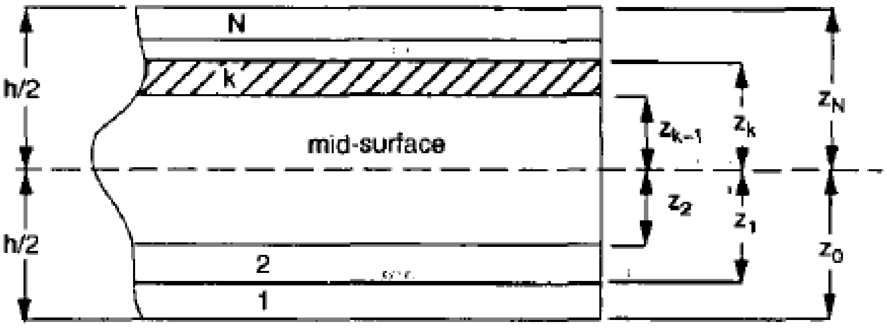

Figure 100: Nomenclature of Laminae Stacking [80]

The loads required for the development of load-displacement relationships are a set of resultant forces and moments in a representative section of the laminate. Forces (N) have units of force per unit length of the laminate (N/m) and the moments (M) have units of length times force per unit length of laminate (Nm/m). Both resultant forces and moments must satisfy equilibrium conditions in the laminate. For thin plate theory the effect of shear strains, γ_{xz} and γ_{yz}, may be neglected, but shear forces, Q_x and Q_y, should be accounted for. The forces and moments satisfying the equilibrium conditions are

$$\begin{Bmatrix} N_x \\ N_y \\ N_{xy} \end{Bmatrix} = \sum_{k=1}^{N} [\bar{Q}]_k \left(\int_{z_{k-1}}^{z_k} \begin{Bmatrix} \varepsilon_x^0 \\ \varepsilon_y^0 \\ \gamma_{xy}^0 \end{Bmatrix} dz + \int_{z_{k-1}}^{z_k} z \begin{Bmatrix} \kappa_x \\ \kappa_y \\ \kappa_{xy} \end{Bmatrix} dz \right) \tag{52}$$

$$\begin{Bmatrix} M_x \\ M_y \\ M_{xy} \end{Bmatrix} = \sum_{k=1}^{N} [\bar{Q}]_k \left(\int_{z_{k-1}}^{z_k} z \begin{Bmatrix} \varepsilon_x^0 \\ \varepsilon_y^0 \\ \gamma_{xy}^0 \end{Bmatrix} dz + \int_{z_{k-1}}^{z_k} z^2 \begin{Bmatrix} \kappa_x \\ \kappa_y \\ \kappa_{xy} \end{Bmatrix} dz \right) \tag{53}$$

Figures 101 (a) and (b) show the positive sign convention of forces (Eq. 52) and moments (Eq. 53) for laminate loads.

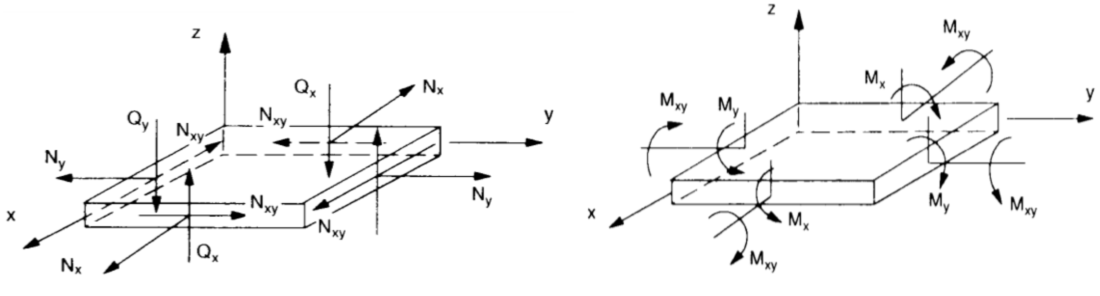

(a) **(b)**

Figure 101: Positive Sign Convention for CLT of Forces (a) and Moment (b) [80]

The load and moment can be expressed grouped in a matrix form as

$$\begin{Bmatrix} N \\ \cdots \\ M \end{Bmatrix} = \begin{pmatrix} A & \vdots & B \\ \cdots & \cdots & \cdots \\ B & \vdots & D \end{pmatrix} \begin{Bmatrix} \varepsilon^0 \\ \cdots \\ k \end{Bmatrix} - \begin{Bmatrix} N^T \\ \cdots \\ M^T \end{Bmatrix} \quad \rightarrow \quad \begin{Bmatrix} \widehat{N} \\ \cdots \\ \widehat{M} \end{Bmatrix} = \begin{pmatrix} A & \vdots & B \\ \cdots & \cdots & \cdots \\ B & \vdots & D \end{pmatrix} \begin{Bmatrix} \varepsilon^0 \\ \cdots \\ k \end{Bmatrix} \tag{54}$$

where

Extensional Stiffness Matrix: $$[A_{ij}] = \sum_{k=1}^{N} [\bar{Q}_{ij}]_k \, t_k \tag{55}$$

Extension-Bending Coupling Matrix: $$[B_{ij}] = \sum_{k=1}^{N} [\bar{Q}_{ij}]_k \, t_k \bar{z}_k \tag{56}$$

Bending Stiffness Matrix: $$[D_{ij}] = \sum_{k=1}^{N} [\bar{Q}_{ij}]_k \left(t_k {\bar{z}_k}^2 + \frac{{t_k}^3}{12} \right) \tag{57}$$

and $\{N\}^T$ and $\{M\}^T$ are thermal loads and thermal moments, respectively, created because of the existence of thermal gradients.

In the above equation t_k is the thickness of the kth lamina and $\bar{z}_k$ is the location of the centroid of the kth lamina, as measured from the mid-plane of the laminate. Since the mid-plane of the laminate separates the laminate in two, $\bar{z}_k$ can be either positive or negative.

When a laminate is being cured, the gradient temperature field of the laminate may result in residual strains and curvatures in the laminate. Due to the stacking arrangement of a laminate, where the fiber orientation among plies varies, the dilatational (changes in shape and dimensions) changes in each lamina are different.

As a result, since plies are constrained between adjacent plies and deform because of this constraint, the residual stresses in each ply will be different, but the final state of the laminate will be characterized by a uniform residual strain. Depending on the materials of the plies, the temperature difference, the stacking sequence, as well as other parameters, these residual strains and stresses may be either compressive or tensile. Residual curvatures are present in anti-symmetric matrices. Moisture absorption may have similar influences as thermal effects, but the current research will ignore hygral effects [80]. For that matter the relationships presented here do not include such parameters.

A simplification to the above equations occurs when the laminate is symmetric and in that case [B]=0. Also in the case that a laminate is a cross-ply laminate (where the laminae have fiber orientations of 0° and 90° degrees), the [B] matrix is symmetric with the off-diagonal elements equal to zero and B_{11}= -B_{22} and B_{33}= 0 [80].

II.4 Lamina Failure Prediction Using Failure Theories

Understanding how a structure fails is one of the key parameters to better design structures. As mentioned earlier composites fail in different ways than metals and there exist a few modes according to which failure may be demonstrated. However, similar to metals composites will fail when the stresses in the structure exceed the structure's strength. Failure will always begin in the micromechanic level, and when it becomes macromechanical will most often be catastrophic. To understand the mechanisms behind complete laminate failure, an examination of the individual lamina failure should be considered first, whether failure is due to fiber failure, matrix failure or failure at the fiber-matrix interface. Failure due to interlaminar stresses is not considered to fall under the in-plane failure theories categories, and for that matter when failure theories are discussed the bond between adjacent laminae is considered to be perfect [80-81].

Stiffness varies in a lamina due to the two constituents present. As a result stiffness is greater in the fiber direction, and smaller in the transverse direction to the fibers (Appendix A). The same holds for the strength of the lamina. Three maximum failure strengths characterize a lamina. The maximum failure strength in the longitudinal direction (X) taken along the fiber direction, which for convenience is coincided with direction 1, the maximum failure strength in the transverse direction 2 (Y), and a maximum shear failure strength (S) [80]. Due to this non-uniform maximum strength distribution in the lamina, the largest stress applied on the lamina may not always be the one that causes failure, as is the case in an isotropic material, but the stress that will cause failure should be examined both in its magnitude and direction in which it is applied. Consequently, failure in a lamina may occur in different directions, and there exist tensile and compressive maximum failure strength in both the longitudinal (along the fibers) and transverse directions. Compressive maximum failure strengths are distinguished by a prime sign (X’ and Y’). Compressive and tensile maximum failure strengths do not only differ in direction but also in magnitude. The sign of applied shear strength will not affect the maximum failure shear strength, but may affect the allowable failure load to be predicted by failure theories [80,83].

There exist many failure theories to compare the lamina state of stress to a failure criterion that helps hypothesize a failure theory. All failure theories are in-plane theories. Interlaminar failure is not considered in such analysis. Generally, failure theories are developed for unidirectional laminae and their analysis is based on the perpendicular and shear strength of the lamina. Failure theories for woven materials exist [87-88] but are still being developed. These are out of the scope of this research. Two major categories of failure theories remain. These categories distinguish between failure theories that do not couple the five failure modes, namely compressive or tensile along longitudinal direction, compressive or tensile along transverse direction, in-plane shear, and are called non-interactive failure modes, and the interactive failure modes that do include this coupling between the failure modes [83].

The following four failure theories are among the most widely used in lamina failure prediction. For the purpose of this research the Tsai-Hill failure theory, that takes into consideration the interaction between the three unidirectional lamina strength parameters, $(\sigma_1^T)_{ult}$, $(\sigma_2^T)_{ult}$, $(\tau_{12})_{ult}$, will be employed [83].

a) Non-Interactive Failure Theories

The Maximum Stress and Maximum Strain theories are employed by resolving the applied stresses or strains in the lamina, to stresses and strains in the local axis, and comparing the latter to the corresponding ultimate strengths or strains of the lamina. Following the above inequalities, when the applied resolved stresses or strains are equal or larger than the unidirectional lamina's ultimate strengths and strains failure occurs.

b) Interactive Failure Theories

Tsai-Hill failure theory is based on Von-Mises distortional energy yield criterion for isotropic materials, applied to anisotropic materials. Hill adopted the theory to a unidirectional lamina and Tsai, based on the distortion energy theory proposed that a lamina fails if the following relationship is violated

$$\frac{{\sigma_1}^2}{X^2} - \frac{\sigma_1 \sigma_2}{X^2} + \frac{{\sigma_2}^2}{Y^2} + \frac{{\tau_{12}}^2}{S^2} < 1 \tag{58}$$

The above relationship is modified for plane stress failure, and can be applied for both tensile and compressive strengths.

The Tsai-Wu failure theory is based on Beltrami's total strain energy theory, and is also a very popular interactive failure theory.

Due to the different stacking sequences of the laminae of a laminate, the fibers are not always aligned along the longitudinal direction (direction x_1). An angle ply is a lamina whose fibers make an angle θ with the global axis. To apply the failure theories to an angle lamina one should find the stresses and strains in the material axis (Appendix B).

Failure theories are not accurate enough to be used alone for predicting the failure in composites and they should always be verified against experimental results. Tsai compared the above theories to experimental results of an angle lamina under uniaxial loading in the x-direction (both compression and tension) (Fig. 102). The Maximum Stress and Maximum Strain Failure theories deviate significantly form the experimental results. On the other hand, Tsai-Hill and Tsai-Wu failure theories are in good agreement with the experimental results. Varying the strength as a function of the angle in the angle ply, creates smooth curves in the case of Tsai-Hill and Tsai-Wu theories, but ends up in cusps in the case of Maximum Stress and Maximum Strain failure theories. In the later two, the cusps explain a change in failure mode. Maximum Stress and Maximum Strain failure theories give a failure mode, unlike Tsai-Hill and Tsai-Wu failure Theories [83].

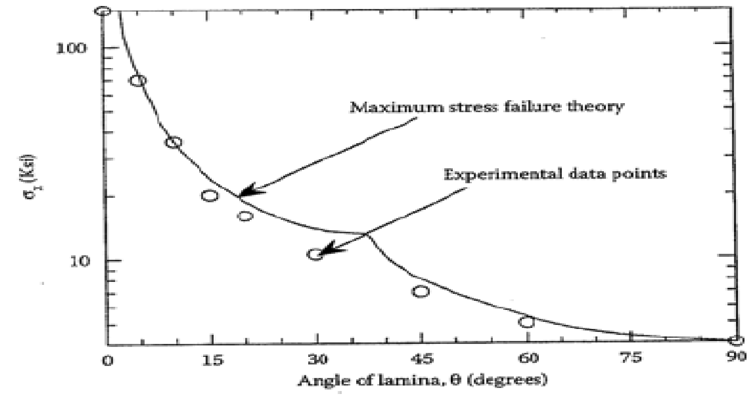
Maximum stress failure theory
Experimental data points
σ_1 (Ksi)
100
10
0
15
30
45
60
75
90
Angle of lamina, θ (degrees)

(a)

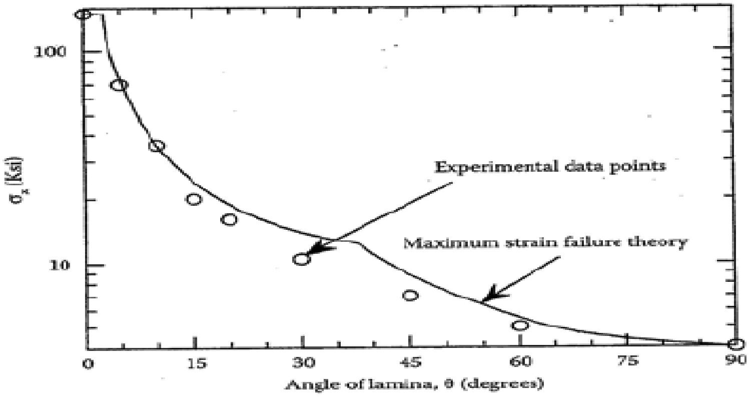
Experimental data points
Maximum strain failure theory
σ_x (Ksi)
100
10
0
15
30
45
60
75
90
Angle of lamina, θ (degrees)

(b)

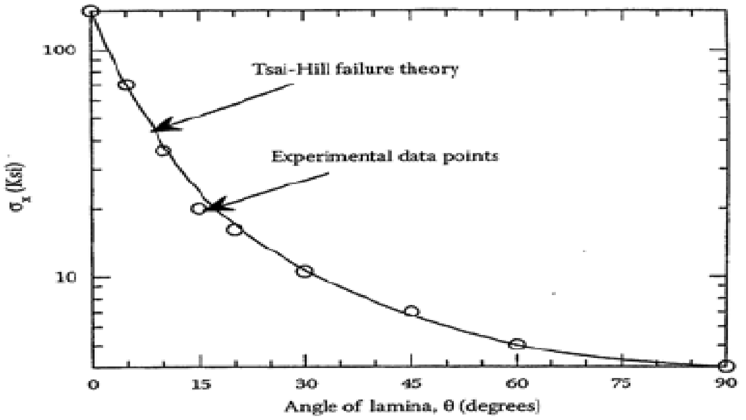
Tsai-Hill failure theory
Experimental data points
σ_x (Ksi)
100
10
0
15
30
45
60
75
90
Angle of lamina, θ (degrees)

(c)

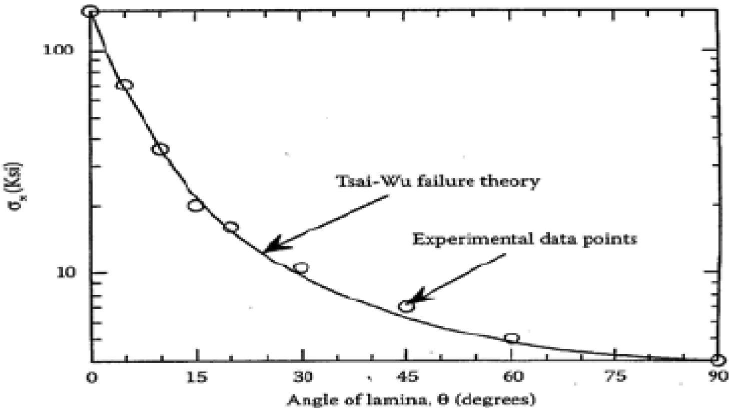

(d)

Figure 102: Maximum normal tensile stress in the x-direction as a function of lamina angle, θ, using maximum stress (a) and maximum strain (b), Tsai-Hill (c) and Tsai-Wu (d) failure theories [83].

Failure Theories are very useful in investigating the way the laminate will fail and therefore contributing to a more efficient design of the laminate. Since failure theories analyze each lamina separately, it is useful to apply such analysis in order to determine the lamina that will fail first in a laminate, as well as the maximum allowable load that can be sustained by the lamina. Once the first ply to fail has been determined, the failed ply can be degraded and the process continues to determine the lamina that will fail second. Fig. 103 shows how laminate failure is determined from the first-ply failure to the last-ply failure step, when the lamina is considered to have failed completely.

The following analysis uses just first-ply failure analysis for two different types of composite laminate materials, S2 glass fiber/epoxy and E glass fiber/epoxy, for three different stacking sequences. The first-ply failure analysis uses the Tsai-Hill failure theory and CLT to determine the material of greater strength, and the stacking sequence that strengthens the laminate the most.

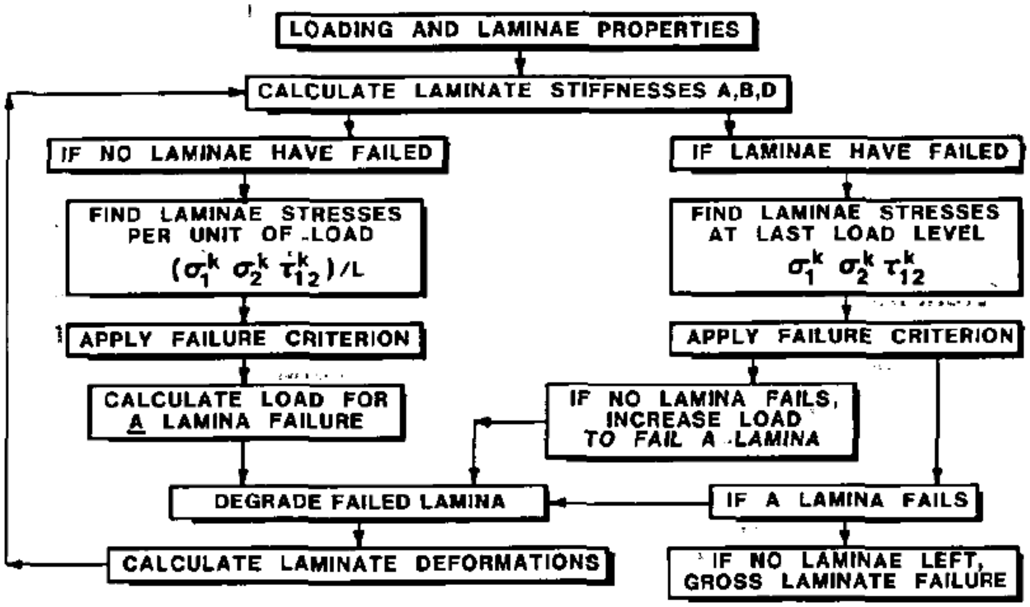
LOADING AND LAMINAE PROPERTIES
CALCULATE LAMINATE STIFFNESSES A,B,D
IF NO LAMINAE HAVE FAILED
IF LAMINAE HAVE FAILED
FIND LAMINAE STRESSES PER UNIT OF LOAD $(\sigma_1^k\ \sigma_2^k\ \tau_{12}^k)/L$
FIND LAMINAE STRESSES AT LAST LOAD LEVEL $\sigma_1^k\ \sigma_2^k\ \tau_{12}^k$
APPLY FAILURE CRITERION
APPLY FAILURE CRITERION
CALCULATE LOAD FOR A LAMINA FAILURE
IF NO LAMINA FAILS, INCREASE LOAD TO FAIL A LAMINA
DEGRADE FAILED LAMINA
IF A LAMINA FAILS
CALCULATE LAMINATE DEFORMATIONS
IF NO LAMINAE LEFT, GROSS LAMINATE FAILURE

Figure 103: Analysis of Laminate Strength [81]

II.5 Results and Discussion

The previous sections of this part gave a brief introduction on composite materials and the theory behind estimating the response to failure of a laminated composite. The Classic Lamination Theory (section II.3) gives the basic equations required to approach the laminate micromechanically, in order to investigate the failure response of each layer. The failure theories discussed in section II.4 set failure criteria, in order to determine the load conditions that may lead to ply failure.

In a composite, laminate failure initiates in a micromechanical level, through failure of one ply of the laminate. Failure theories can determine first ply failure, and together with Classical Lamination Theory subsequent ply failure can be identified.

CLT and the Tsai-Hill failure theory are used to investigate first ply failure in three laminates of different ply sequence. Calculations (section II.5.1) show which laminate and which fiber orientation is stronger. A comparison between S2 and E glass fiber/epoxy laminates shows which of the two materials is more appropriate as a composite leaf spring material.

Finite element analysis is used to analyze composite laminates and examine the difference between a macromechanical and micromechanical approach to failure (section II.5.2). Fe-safe^{TM} for composite materials is used to predict the fatigue life of

S2 and E glass fiber/epoxy laminates thus adding to the comparison of the two materials.

Another way to predict of the fatigue life of composites, and their accumulation of damage is though the Damage Models, presented in Part I. The three models discussed earlier are applied in section II.5.3 to predict damage accumulation and fatigue life of the two glass fiber/epoxy materials.

As mentioned earlier, the most accurate way to investigate the fatigue of a material is through real life experiments. Three point bending fatigue tests have been performed on E glass fiber/epoxy laminated beams, and are discussed in section II.5.4.

II.5.1 First Ply Failure of GFRP laminates

The stacking sequence followed in the manufacturing of composite leaf spring is in most cases a general stacking sequence of [$0^o/45^o/0^o/45^o$], and the leaf springs are made either by 4 or 8 laminae depending on the thickness of the leaf spring and the desired design [10]. To show the effect of stacking sequence in the failure of a laminate, three stacking sequences were considered. The three different stacking sequences were applied to thin plates of 6 mm thickness (Fig. 104) composed of 22 layers of approximately 0.3 mm laminae. The three stacking sequences examined using the Tsai-Hill failure theory, are:

Cross-Ply Laminate: $[90^o/0^o]_{11}$

Angle-Ply Laminate: $[-45^o/+45^o]_{11}$

General Stacking Laminate: $[0^o/45^o]_{11}$

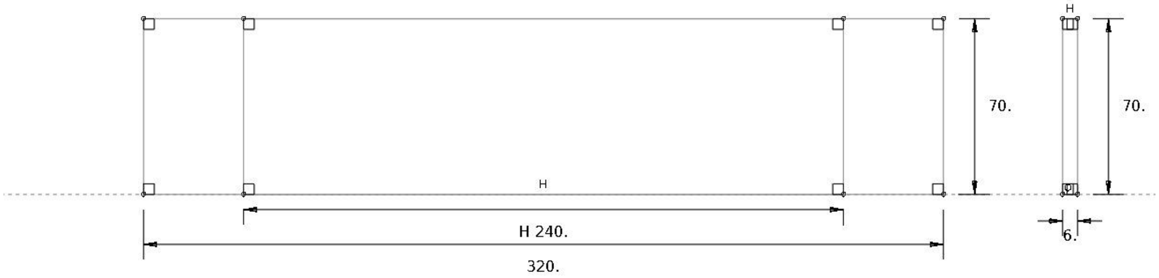

Figure 104: Dimensioned Sketch of Composite Laminate with Span Length Markings, Dimensions in mm

The analysis assumed that the laminated beams are loaded laterally along the fiber direction, and the analysis was performed in such a way so as to determine the maximum allowable moment that each lamina can sustain in that direction. The analysis took into consideration thermal effects for a temperature difference of -2.2^{o}C, while hygral effects were neglected. The interlaminar bonds were considered perfect and no failure in the lamina interface was considered.

It was mentioned earlier that the stresses in each lamina may be different, while the strain state is uniform in the laminate. Table 15 gives the non-zero mid-surface strains and curvatures for the six different laminates considered, when loading is due to a bending moment of 1000 Nm/m.

Table 15: Mid-surface Strains and Curvatures

Laminate Type: fiber direction	**E glass fiber/epoxy Strain**	**S2 glass fiber/epoxy epoxy Strain**
Cross-Ply Laminate: strains	$\begin{Bmatrix} 3.1x10^{-3} \\ -2.1x10^{-5} \\ 0 \end{Bmatrix}$	$\begin{Bmatrix} 2.9x10^{-3} \\ -1.9x10^{-4} \\ 0 \end{Bmatrix}$
Cross-Ply Laminate: curvatures	$\begin{Bmatrix} 36 \\ -3.6 \\ 0 \end{Bmatrix}$	$\begin{Bmatrix} 33 \\ -3.0 \\ 0 \end{Bmatrix}$
Angle-Ply Laminate: strains	$\begin{Bmatrix} -2.1x10^{-5} \\ -2.1x10^{-5} \\ 3.1x10^{-3} \end{Bmatrix}$	$\begin{Bmatrix} -1.9x10^{-5} \\ -1.9x10^{-5} \\ 2.9x10^{-3} \end{Bmatrix}$
Angle-Ply Laminate: curvatures	$\begin{Bmatrix} 70 \\ -38 \\ 3.1x10^{-2} \end{Bmatrix}$	$\begin{Bmatrix} 60 \\ -31 \\ 2.3x10^{-2} \end{Bmatrix}$
General Stacking Laminate: strains	$\begin{Bmatrix} -2.7x10^{-3} \\ 9.6x10^{-4} \\ 1.7x10^{-3} \end{Bmatrix}$	$\begin{Bmatrix} -2.4x10^{-3} \\ 6.6x10^{-4} \\ 1.7x10^{-3} \end{Bmatrix}$
General Stacking Laminate: curvatures	$\begin{Bmatrix} 34 \\ -12 \\ -12 \end{Bmatrix}$	$\begin{Bmatrix} 31 \\ -10 \\ -11 \end{Bmatrix}$

From the above table it can be observed that the strain and curvature values for S2 glass fiber/epoxy beams are equal or smaller to the same values for the E glass fiber epoxy beams. However, each fiber orientation sequence presents the same order of magnitude of these values irrespective of the fiber material chosen. As a result, general stacking sequence has the smallest curvatures in all directions, while the angle ply laminates have the smallest strains in the x and y directions. Cross-ply laminates experience no shear strains.

After defining the stresses and strains using CLT, the principal stresses are evaluated and the maximum allowable moment for each lamina is calculated. Due to the quadratic nature of the failure theory both a clockwise and a counterclockwise moment are evaluated, whose magnitudes are almost identical. Fig. 105 (a) to (f) show how the absolute values of these moments vary among the different plies in each laminate examined.

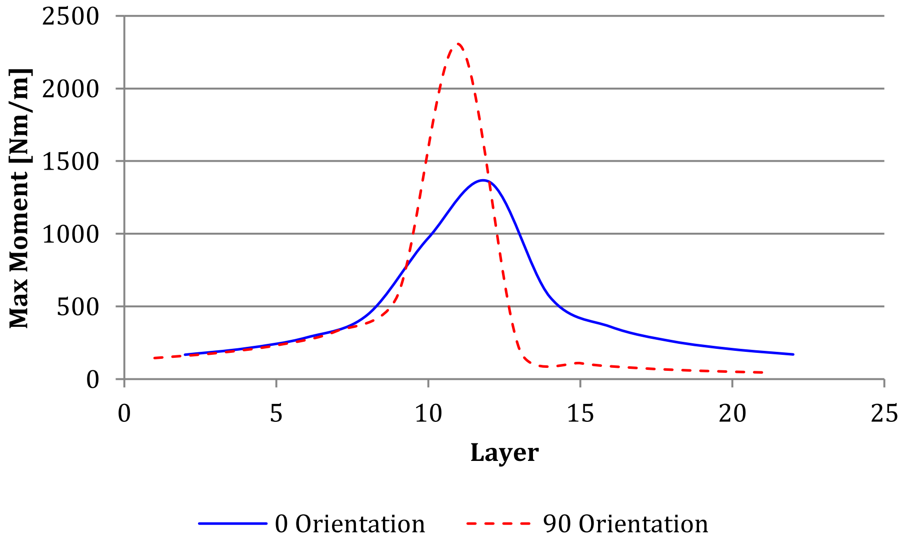

(a) Cross-Ply Laminate of E glass fiber/epoxy

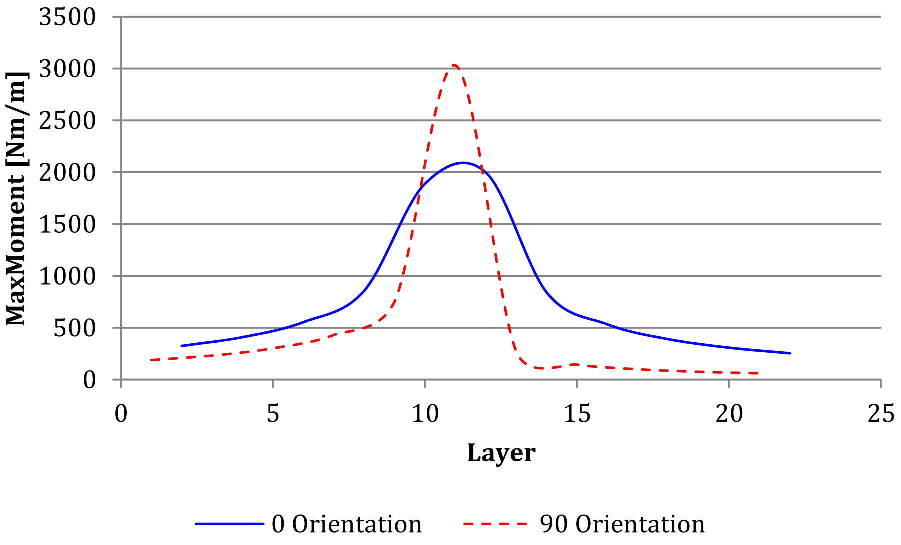

(b) Cross-Ply Laminate of S2 glass fiber/epoxy

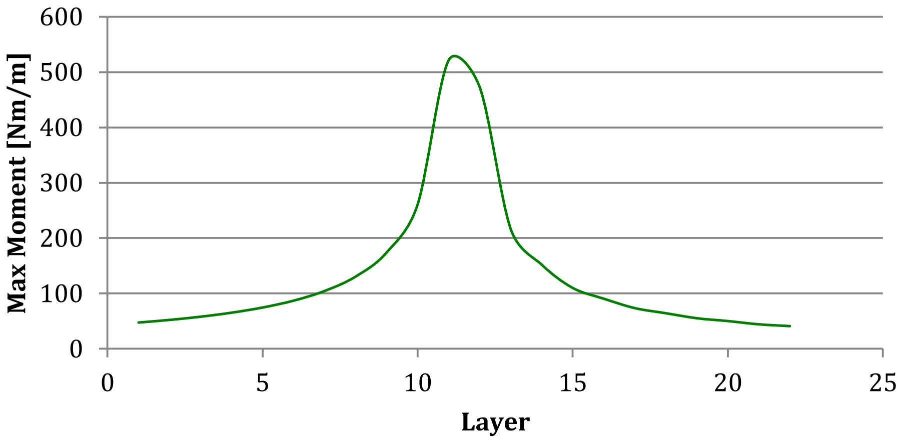

(c) Angle-Ply Laminate of E glass fiber/epoxy

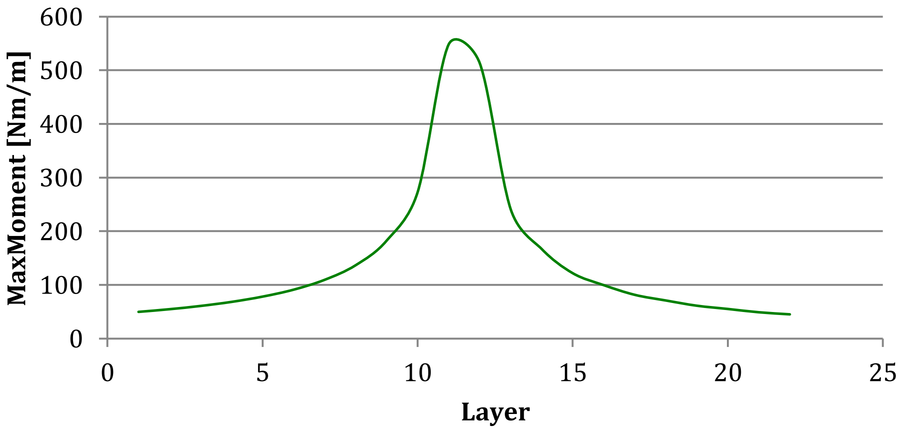

(d) **Angle-Ply Laminate of S2 glass fiber/epoxy**

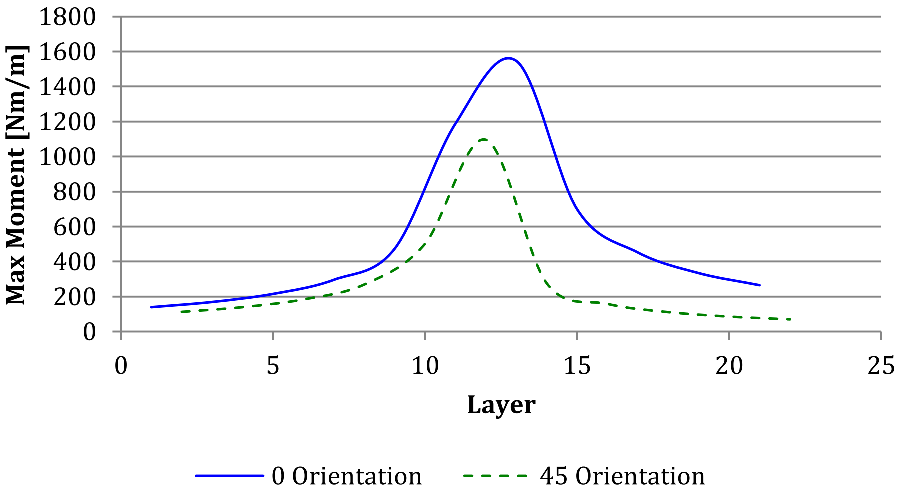

(e) General Stacking Laminate of E glass fiber/epoxy

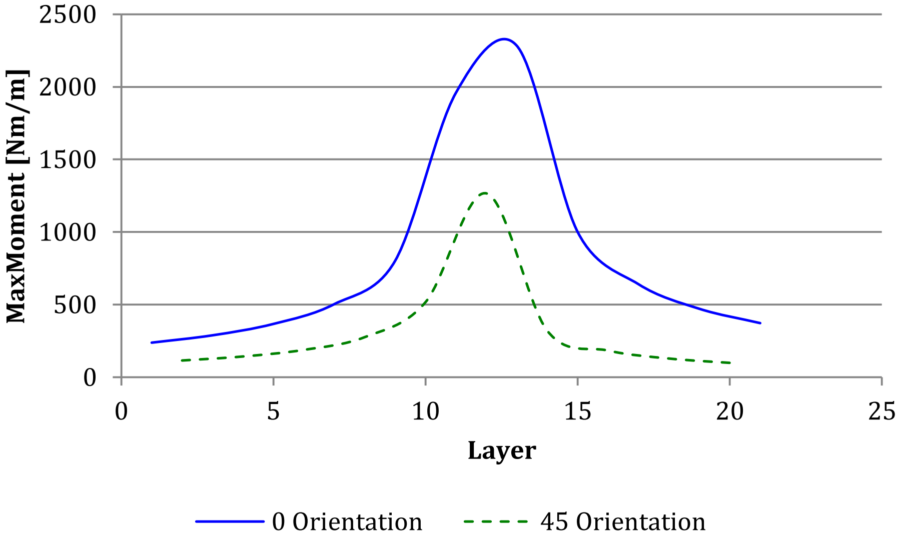

(f) General Stacking Laminate of S2 glass fiber/epoxy

Figure 105: Maximum Applied Moment per layer that will cause Failure, for the different stacking sequences and materials examined

The above figures show that the maximum allowable moment sustained in the bottom and top plies is small and approximately equal, and that the middle ply can support the largest moment. As a result, it can be concluded that the first ply to fail will be either of the top or bottom ones. From the above figures, one can understand the importance of knowledge of the fiber orientation in a lamina. Different, fiber orientations can sustain different amounts of load. When the fibers are oriented longitudinally in the lamina, parallel to the x direction, the amount of load sustained is the greatest. In the case of the angle ply laminates, where the fibers are oriented in opposite directions, only one curve is shown in the graphs. The reason for that is the fact that the moment increases and decreases through the thickness of the lamina in equal increments, due to the fibers of the adjacent laminae making equal but opposite angles with the x direction.

In a laminate, the ply with the smallest load carrying capacity will fail first. Table 16 presents the smallest possible moment for each laminate and the layer, as well as orientation that these moments occur.

Table 16: Minimum Moment to Cause First-ply failure in Laminates

Minimum Moment in Lamina [Nm/m]	**Laminate**	**Lamina Number**	**Lamina Fiber Orientation**
45	Cross-Ply E glass fiber/epoxy	21	90°
60	Cross-Ply S2 glass fiber/epoxy	21	90°
41	Angle-Ply E glass fiber/epoxy	22	45°
45	Angle-Ply S2 glass fiber/epoxy	22	45°
69	General Stacking E glass fiber/epoxy	22	45°
81	General Stacking S2 glass fiber/epoxy	22	45°

From the table above it is clear that the S2 glass fiber/epoxy is a stronger material than E glass fiber/epoxy, as the maximum load its laminae can sustain is always larger than the corresponding laminae in the E glass fiber/epoxy laminate. It is also obvious form Table 16 that the stacking orientation is also an aspect that determines the strength of the material apart form the material itself. Among the sequences examined the general stacking appears to be the strongest sequence, and the angle-ply the least strong. In all laminates, failure occurs at the top layers of the laminate, while the 0° orientation of fibers is always the strongest and never seems to fail first. When all off-axis laminae fail in the above laminates, it will be the 0° orientation of fibers that will be carrying all applied load in the laminate.

It can thus be concluded that S2 glass fiber/epoxy is a stronger material to be considered for cyclic loading applications as in the case of composite leaf springs, and that the general stacking sequence followed in the composite leaf spring manufacturing process is a good laminate sequence for such applications requiring strength of the material.

The laminates considered above are anti-symmetric laminates of 22 layers each. As a result, the orientation of fibers in the top and bottom of the laminate are not the same, and care should be taken of positioning the laminate in the appropriate way depending on the application, so that failure will not be initiated in an undesirable position. However, the number of laminae in a composite structure may also be odd, and such laminates are called symmetric. For the case of the angle-ply stacking sequence a symmetric with 21 layers, E glass-fiber epoxy beam of similar lateral and transverse dimensions, was examined, under the same loading and thermal conditions.

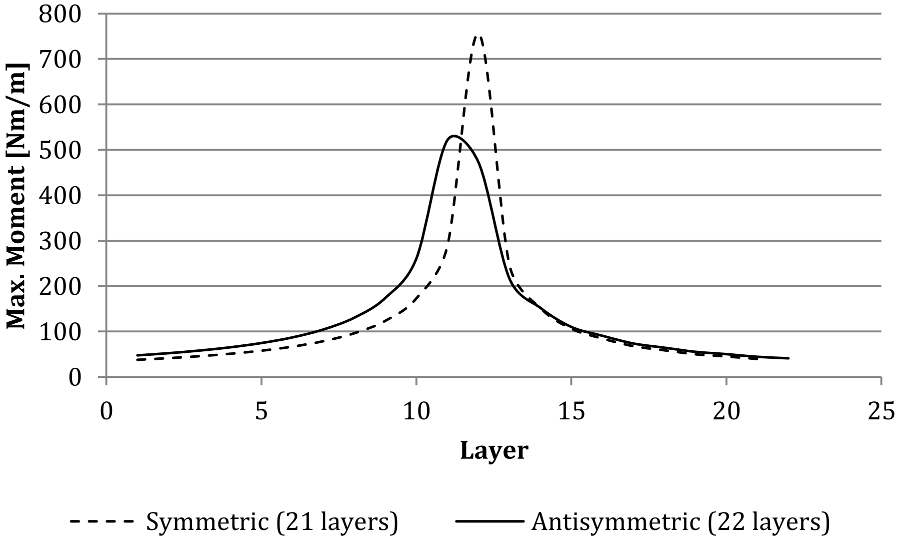

Figure 106: Maximum Applied Moment per layer that will cause Failure, for symmetric and anti-symmetric angle-ply, E glass fiber/epoxy laminates

From the above figure, it can be seen that the bottom layers of the anti-symmetric laminates are stronger than those of the symmetric one, while the symmetric laminate is stronger in its midsection. The top layers have very similar strengths although the anti-symmetric lamina, will sustain a larger moment at those layers. The symmetric laminate will fail before the anti-symmetric, under application of similar loads at ply 1 of -45° fiber orientation under a moment of 38 Nm/m. This explains, the choice of the automotive industry to manufacture composite leaf springs with an even number of layers.

II.5.2 Finite Element Analysis

Failure in a composite begins in the micromechanic level of the composite's constituents and their interaction with each other, and manifests its effects on the performance of the structure macromechanically. Therefore, composites can be examined both macromechanically, as a whole solid structure where no attention is paid to what happens in the individual lamina that compose the structure, as well as micromechanically where each lamina is examined separately.

This section will examine the differences between a macromechanic analysis approach and a micromechanic analysis approach of general stacking composite beams of smaller and the same dimensions as the ones considered in the previous section (Fig. 104). Both S2 glass fiber/epoxy and E glass/fiber epoxy will be considered, as well as a comparison of a symmetric (3 laminae) to an anti-symmetric (2 laminae) beams will be shown. Finally, the effects of geometric discontinuities, which interrupt the continuous flow of unidirectional fibers, such as holes (Fig. 107), will be shown through an analysis of bending stresses. All beams are examined under bending, while supported by simple supports at both sides of the beam, creating a span length to thickness ration of 60:1 [89]. Macromechanic measurements are taken through the thickness at the center of the beam at intervals close to the center of each lamina. Micromechanic measurements are taken at the middle of each lamina.

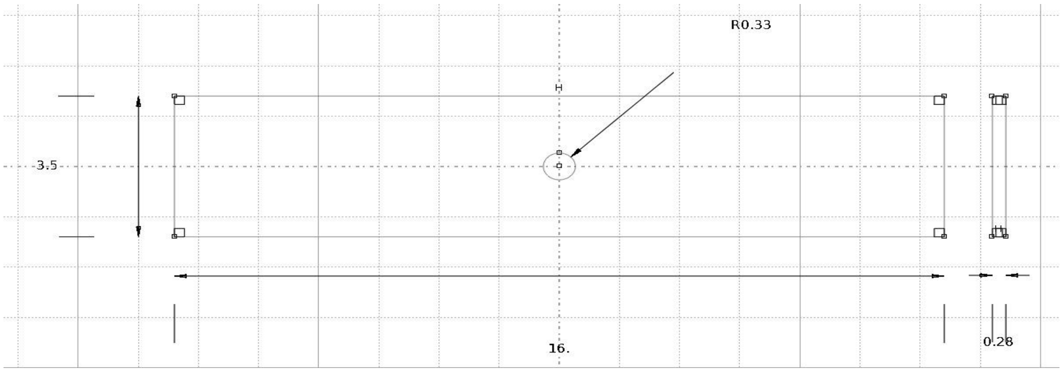

Figure 107: Sketch of Composite Lamina Plate with Hole, Dimensions in mm

As shown in the previous section, the effect of the materials of the composite structure is as important as the staking sequence chosen for the structure. Choosing a different angle orientation for each ply will greatly affect and determine the behavior of the structure. In the previous section four different orientations were chosen for the fibers of each layer in the composite beams. The fibers were oriented 0°, 45°, -45° or 90° form the x-direction. In each case of different orientation, the load applied to the beam will be carried differently by the fibers, and as a result the behavior of the beams will vary. Earlier in this research, the spring rate was discussed as an important parameter in leaf spring design. The spring rate, which is related to the amount the beam deflects under a given load, characterizes the stiffness of the leaf spring and helps classify it for a specific vehicle application. In composite materials, where the load capacity of the structure changes depending on the orientation of the fibers, different orientations will result in different deflections and therefore different spring rates, under the same loading conditions.

Table 17: Beam Deflections for Different Materials and Different Fiber Orientations

Materials	Theoretical Deflection	ABAQUS deflection
AISI 6150 steel	0.04 mm	0.04 mm
S2 glass [6]	0.09 mm	0.09 mm
Epoxy [7]	2.26 mm	2.26 mm
S2 glass fiber/epoxy	0.18 mm	0.18 mm
E glass fiber/epoxy	0.19 mm	0.19 mm

Orientation of S2 fibers	ABAQUS Deflection
0°	0.23 mm
45°	0.74 mm
-45°	0.74 mm
90°	-1.1 mm
0° with center hole of 0.7 mm diameter	0.23 mm

The deflection of a single layer of S2 glass fiber/epoxy for the four different orientations, mentioned above, were examined in ABAQUS. The beams had a span length to thickness ratio of 60:1, and loaded under three point bending at 50 MPa. The above deflections were compared to the deflection of a steel beam loaded under the same conditions, and to those of an S2 glass fiber/epoxy beam, were the beam was considered to have isotropic behavior.

The more flexible materials are the composites, as is expected from their modulus of elasticity (Appendix A). The S2 glass fiber/epoxy deflection estimate lies within the range of the fiber and epoxy deflections. These estimates show that the most flexible constituent in the composite is the matrix, and that steel is twice as stiff as the S2 glass fibers. As a result, the volume fraction of the constituents of a composite may be chosen to accommodate the stiffness required by a composite component's design. Steel is the stiffest material, followed by S2 glass fiber/epoxy, while E glass fiber/epoxy will be the most flexible one. The orientation of the fibers, will also affect deflection, and as a result when the fibers are oriented parallel to the x-direction the beam will deflect the least. An angle ply will have about 30% higher deflection than the plies with 0° orientation of their fibers. When the fibers are perpendicular to the x–direction, the ply will deflect towards the opposite direction. In this latter case the load is transverse to the direction of the fibers, and the fibers carry the minimum load possible. As a result, a bending stress along the length of the beam is minimum, almost zero, while the expected bending stress of 50 MPa will be along the direction of the beams width. It can be concluded that a 0° orientation is the strongest and stiffer orientation for a beam under bending, and 90° orientation should definitely not be the only orientation chosen for a beam under bending applications.

---

[6] Macroscopic calculation of deflection, for the case where the fiber volume fraction is 100%.

[7] Macroscopic calculation of deflection, for the case where the matrix volume fraction is 100%.

Design of composite structures generally avoids geometric discontinuities such as holes. The reason for this design precaution lies on the fact that fibers are the composite constituent to carry most of the load in the composite, and any interruption in the flow of this constituent will have an effect in the load carrying capacity of the structure. Similar to metals a geometric discontinuity becomes a stress concentration raiser area. However, since such discontinuities may be unavoidable in composite structures new failure theories such as the Waddoups-Eisenmann-Kaminski criterion have been developed to examine failure in such composite components, but examination of this criterion is outside the scope of this thesis [96]. Examining a beam of the same dimensions and loading condition as the above, having a center hole of 0.3 mm radius (Fig. 107), and fibers oriented parallel to the x-direction, the same deflection as the beam with 0° orientation of fibers is observed, but instead of a 50 MPa bending stress will have a bending stress of 70 MPa around the region of the hole (Fig. 108). During drilling of a center hole, as is required from many steel leaf spring designs, the fibers and matrix would be damaged, and the structures load carrying ability would be transferred to a smaller fraction of the fibers and matrix.

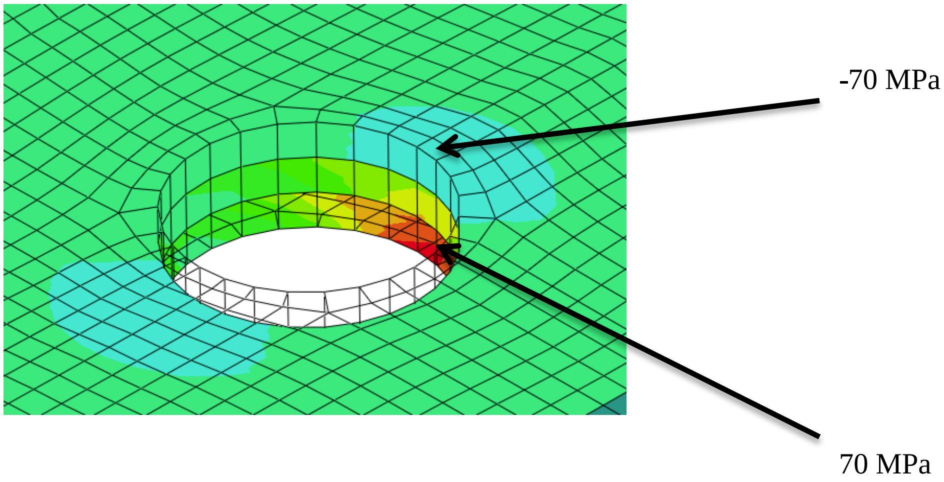

Figure 108: Detail of Bending Stress Contour Plot around Hole Area

Depending on the number of the plies that make up a composite structure the thickness of the structure can be decided, as well as whether the structure will be symmetric or not. In the previous section, symmetric and anti-symmetric composite structures differed both in dimensions but also in the way that CLT calculations are carried out. Keeping the span length to thickness ratio to 60:1, two general stacking S2 glass fiber/epoxy beams were examined in ABAQUS, under three point bending conditions at 50 MPa. The anti-symmetric beam composed of two layers, had an approximate thickness of 0.6 mm and a stacking sequence of [0°, 45°]. The symmetric beam of three layers, and approximate thickness 0.8 mm, had a top and bottom layer with fiber orientation at 0° (stacking sequence [0°, 45°, 0°]). Table 18 gives the displacements of each structure, and compares them to a steel beam of the same dimensions, and a beam considered to be made of an isotropic material having the S2 glass fiber/epoxy properties.

Table 18: Symmetric and Anti-symmetric Beam Deflections

	Deflections
Symmetric (3 layers)	
S2 glass fiber/epoxy	0.70 mm
Steel	0.08 mm
S2 glass fiber/epoxy isotropic	0.39 mm
Anti-Symmetric (2 layers)	
S2 glass fiber/epoxy	0.75 mm
Steel	0.12 mm
S2 glass fiber/epoxy isotropic	0.59 mm

It is only reasonable that the steel beam remains as the stiffest among those examined, due to its high modulus of elasticity. In both the anti-symmetric and symmetric cases when the S2 glass fiber/epoxy is treated as an isotropic material the deflections calculated are smaller than those estimated for a lay up structure where the material is treated as transversely isotropic. This shows why it is important to understand what are the properties in each direction of the composite, and what are the orientations of the fibers in each lamina. A comparison between the anti-symmetric and symmetric composite structures, where the symmetric has one extra layer and as a result, is thicker, shows that the anti-symmetric beam is more flexible and will deflect an extra

0.05 mm than the symmetric beam. Together with the results on first ply failure of symmetric and anti-symmetric general stacking sequence composites, it can be concluded that symmetric structures tend to be stiffer and less strong, and will fail under application of smaller loads, than anti-symmetric structures. The composite leaf spring industry chooses anti-symmetric designs of four or eight layers [10], depending on the application for the leaves.

Due to the different orientations of the fibers in the above structures, the maximum stresses in each lamina may vary. Fig. 109 shows how the maximum bending stress varies in each lamina. In the anti-symmetric beam the top and bottom layers do not have the same maximum bending stress due to the different fiber orientation in each layer. The same happens in the layers of the symmetric beam. The outer layers at 0° fiber orientation have a mush greater stress than the middle layer at 45°.

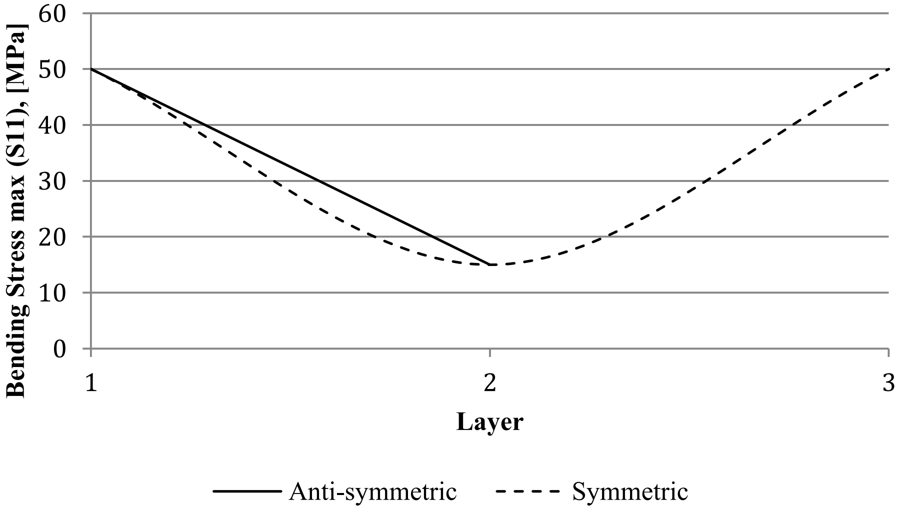

Figure 109: Maximum Bending Stress per Ply of Symmetric and Anti-symmetric Composite Beams

Moving to a larger structure of 22 layers, and general stacking sequence (Fig. 110), the differences between viewing the structure micromechanically and macromechanically may be more obvious. The span length to thickness ratio of this structure is kept at 60:1. The beam is still loaded under three-point bending but the stress is raised to 500 MPa, and the deflection for the composite beam and a steel beam of the same dimensions are shown in the table below.

Table 19: Deflection of 22 Layer Beams

Materials	Deflection
AISI 6150 steel	3.8 mm
S2 glass fiber/epoxy	31 mm

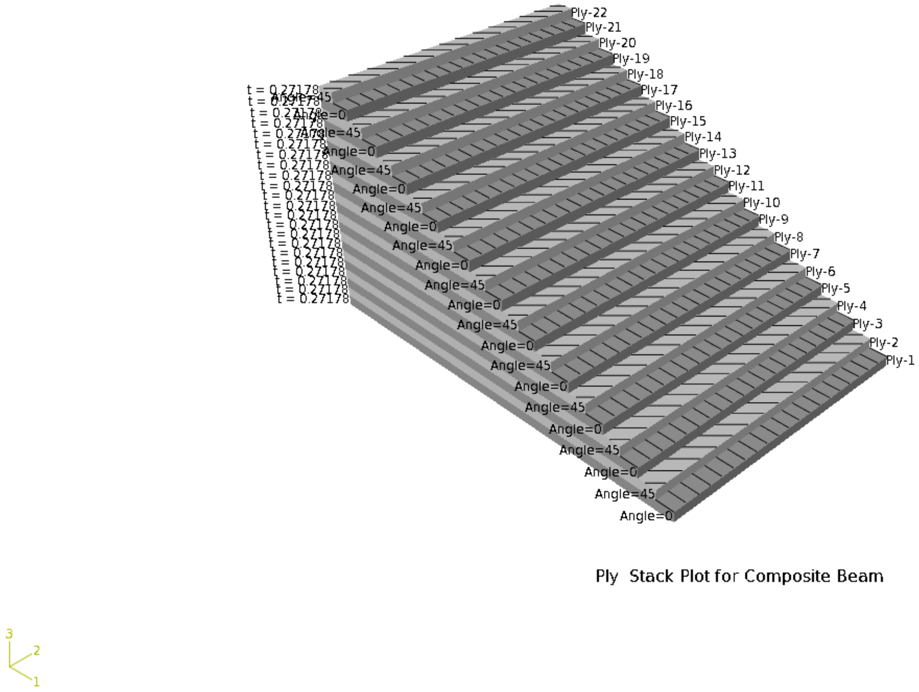
Ply-22
Ply-21
Ply-20
Ply-19
Ply-18
Ply-17
Ply-16
Ply-15
Ply-14
Ply-13
Ply-12
Ply-11
Ply-10
Ply-9
Ply-8
Ply-7
Ply-6
Ply-5
Ply-4
Ply-3
Ply-2
Ply-1
t = 0.27178
Angle=45
Angle=0
Angle=45
Angle=0
Angle=45
Angle=0
Angle=45
Angle=0
Angle=45
Angle=0
Angle=45
Angle=0
Angle=45
Angle=0
Angle=45
Angle=0
Angle=45
Angle=0
Angle=45
Angle=0
Angle=45
Angle=0
Ply Stack Plot for Composite Beam
3
2
1

Figure 110: General Stacking Sequence: Ply Stack Plot with Ply Fiber Orientation

Fig. 111 shows how the stresses vary between adjacent laminae in the composite beam. The stress measurements are taken at the middle if each ply for all 22 plies. The figure shows that the top part of the beam is under compression, while the bottom is under tension, as is expected for the particular loading conditions. However, the values of stress at each layer are not at 500 MPa. On the contrary they vary between absolute values of 900 to 970 MPa in the plies of 0° fiber orientation, and 330 to 380 MPa in the 45° fiber orientation laminae. The majority of the load is indeed being carried by the fibers parallel to the x-direction, as discussed previously, and the variation between the stresses in adjacent lminae is constant throughout the composite.

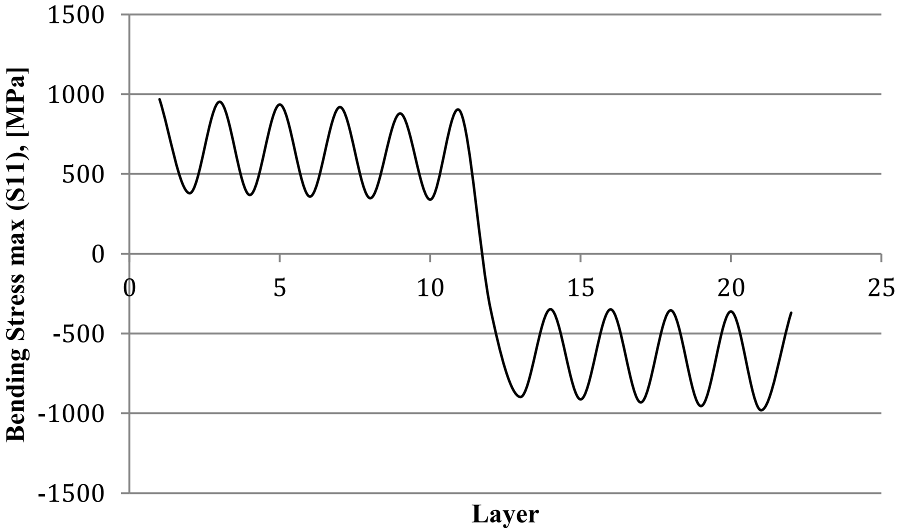

Figure 111: Maximum Bending Stress per Lamina of Anti-symmetric 22 Layer General Stacking S2 glass fiber/epoxy Beam

This same behavior of the stress fluctuation between adjacent laminae, can be observed if the principal stresses calculated using the CLT in section II.4 are plotted versus the number of layers of the composite. Fig. 112 (a) to (c) show the stresses in the longitudinal direction for the different ply sequence S2 glass fiber/epoxy structures examined under a bending moment of 1000 Nm/m in the previous section. The fluctuation in the angle ply sequence is smaller due to the fact that the fibers are oriented at opposite directions. In the case of cross ply where the first layer has its fibers oriented transversely to the x-direction, the stresses in the first layer are smaller that those in the second one, and the magnitude of the stresses of the last layer (at 0° orientation of fibers) are larger than those of the second to last layer. The opposite holds for the general stacking sequence where the first layer fibers are at 0° orientation, and the last layer fibers at 45° orientation. In all cases presented up to now the mid-surface of the beams is at zero stress, as expected for the neutral axis of a beam.

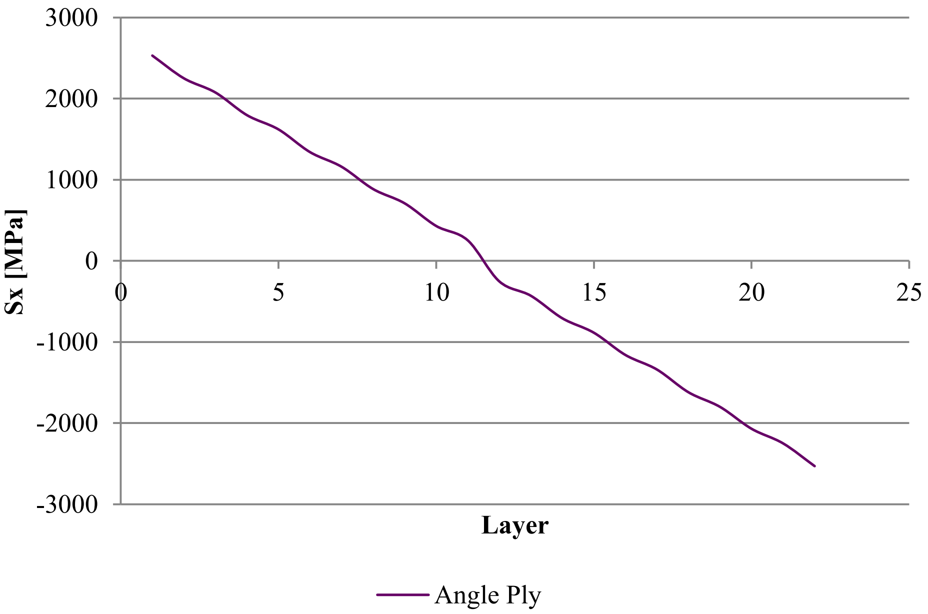

(a)

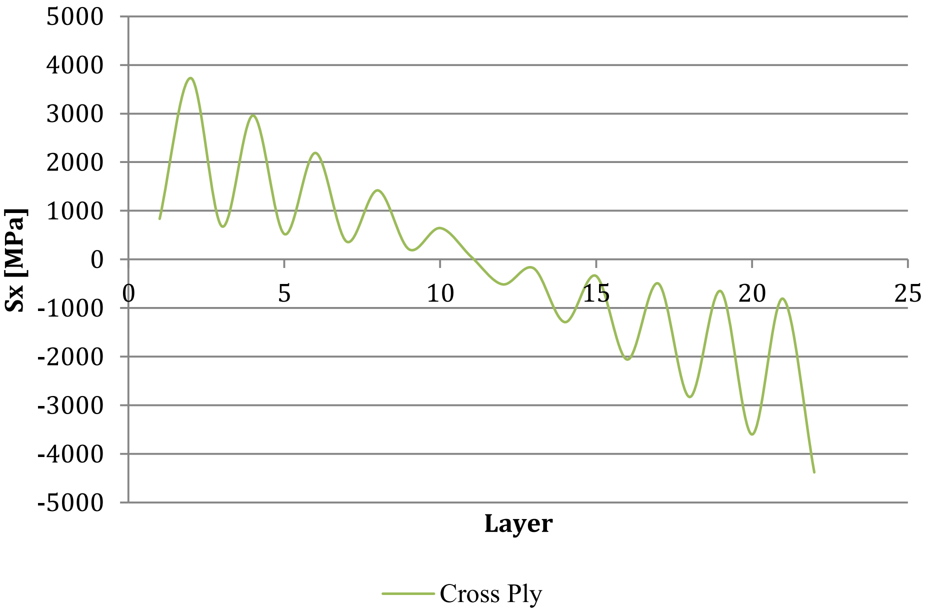

(b)

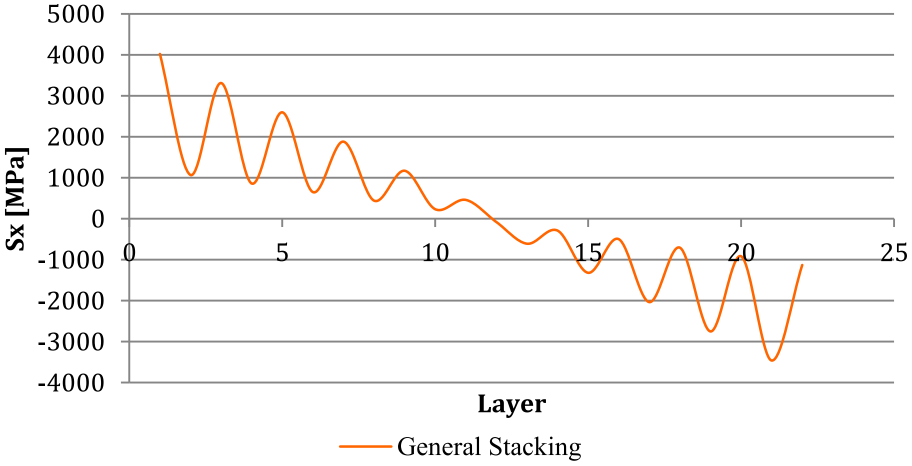

(c)

Figure 112: Principal Stress per Lamina of Anti-symmetric 22 Layer Angle Ply (a), Cross Ply (b), and General Stacking (c) S2 glass fiber/epoxy Beam

The bending stress profile of the composite, is also evaluated macromechanically through the thickness at the center of the structure. As seen in Fig. 113 the macromechanical stress profile of the composite structure does not show the fluctuation of the stresses in the individual plies. The profile may not be completely linear as in the case of the isotropic steel beam, but clearly gives the stresses of the beam as a whole, rather of each plies.

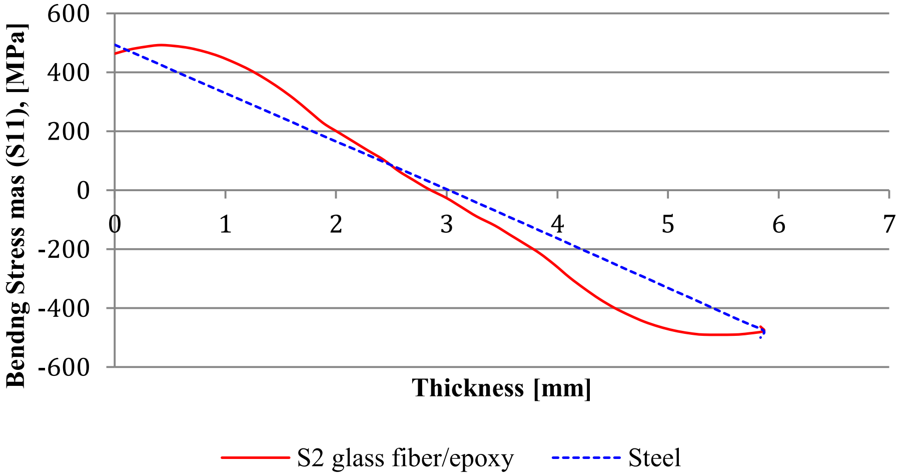

Figure 113: Bending stress profile of AISI 6150 steel and S2 glass fiber/epoxy Beams

Comparing the two stress profiles it is obvious that a micromechanics approach of the stresses gives more detail of how the stresses alternate between layers, while the macromechanic approach shows the bending stress profile of the beam as the stress decreases from the bottom to the top layers. The macromechanic bending stresses are the same in each lamina of same fiber orientation, explaining that the fluctuation of the stresses is due to the fact that adjacent laminae have different fiber orientations.

In Part I of this thesis the finite element post processor software was used to estimate the life of both AISI 4130 and AISI 6150 steel components. Comparing the results from fe-safe^{TM} to experimental data, it seems that, especially in the case of AISI 4130 steel, fe-safe^{TM} gives realistic estimates of fatigue life for the HCF regions, specifically between 10^3 and 10^6 cycles. In general, fe-safeTM is a very recent software and even more recent is fe-safe^{TM}/composites, which includes a module to help the user build a composite material database and estimate the fatigue life of composites.

The composites module for fe-safe^{TM} was first launched in 2010 by Helius: Fatigue of Firehole Technologies, Inc. Helius: Fatigue operates as an add-on to fe-safe^{TM} through a composite material database and a fatigue analysis plugin tool. The composite material database is very limited, but Helius: Fatigue allows for the creation of new materials through the use of an interactive interface, provided that the materials in question are carbon/epoxy, glass/epoxy or Kevlar/epoxy. The user can input the mechanical properties of the lamina, fiber and matrix, as well as the ultimate strengths of the material in different directions. Due to the lack of properties that define material fatigue in metals such as those presented in Table 13, the user must provide longitudinal and transverse S-N data of the material that will be used in the analysis. Fe-safe^{TM}/composites assumes that longitudinal S-N data is measured for loads applied in the direction of the fibers for a load ratio and frequency supplied by the user. On the other hand, the user can choose the loading angle of the transverse S-N data. In the case of a metal component fe-safe^{TM} estimates fatigue based on the detection of a possible crack point on the surface of the component. In a similar matter fe-safe^{TM}/composites estimates fatigue when there is a possibility of matrix cracking, as the matrix in a composite is the most vulnerable constituent of the structure.

Depending on whether the material is a fiber reinforced plastic or a metal, fe-safe^{TM} will follow a different method in fatigue life estimation. The reason of the different approach depends on the difference between the way failure is initiated and propagated in a metal and a composite. In general, and as mentioned earlier, the total number of cycles that lead to failure (N_f) can be decomposed to the cycles required to initiate damage (N_i) and to those required for damage to propagate (N_p) [90].

$$N_i + N_p = N_f \tag{59}$$

However, the time of damage initiation and propagation is different for each of the two types of materials. Many defects that are present in a metal, such as dislocations and grain boundaries, can initiate damage in the material by creating new defects. As a result, the initiation life if often neglected and the number of cycles that lead to failure is assumed to equal the number of cycles required to propagate damage. Propagation time is longer, because during damage propagation the metal undergoes strain hardening, due to the plasticity at the crack tip. Strain hardening and crack propagation may last for thousands of cycles [90].

Strain hardening is negligible in a composite, such as in unidirectional glass fiber/epoxy laminate. If a defect of critical size is nucleated in such a composite laminate, the life of the laminate becomes very short and damage leading to failure propagates very fast. The initiation life therefore, becomes longer compared to the propagation one, in the case of a composite, so the assumption of the number initiation cycles being equal to the number of cycles to failure can be made [90].

Failure in a composite is due to damage accumulation. As microcracks in the matrix constituent accumulate they may reach a critical volume that leads to the formation of a macroccrack that results in failure of the component. The kinetic theory of fracture can be used to model this type of fatigue. The stresses that will cause damage in the matrix constituent are not the same as those developed in the composite, imported in the *.odb* files. As a result, a methodology that will translate these stresses to those of the matrix is required, before the KFT can be applied. In a similar manner as Neuber's rule is utilized in the fatigue life analysis of metals, Helius: Fatigue uses the multicontinuum theory (MCT) to extract the stresses of the matrix constituent form the calculated composite stresses at every integration point of the FE model, and afterwards applies the KTF to predict the fatigue life in the matrix constituent of the composite [90].

As mentioned earlier there are various ways in which a composite may fail. Helius: Fatigue approaches the fatigue life estimation as a matrix phenomenon and for that fact it seeks to calculate the stresses in the matrix. Figure 114 form the Helius: Fatigue Theory Manual describes the process followed in predicting the fatigue life of a composite structure when fe-safe^{TM}/composites is used in conjunction with Helius: Fatigue.

The theory of continuum mechanics lies on the premises of representing and evaluating the physical quantity in question at a sole material point. This is achieved by averaging the quantity over a representative volume element (RVE) surrounding the material point of interest. RVE may be small compared to the dimensions of the body, whose microstructure is partly composed by the quantity in question, but has the appropriate size to represent this quantity in an accurate statistical manner in the body. Based on the fact that two or more constituents exist in composite materials the RVE must be large enough to provide an accurate representation of the material with all its constituents. The fact that fibers in a unidirectional FRP are randomly spaced, make it hard to find a small enough RVE that will not result in high computational time and difficulty, and lead to a common assumption that fibers in unidirectional FRP are uniformly distributed over the composite, allowing for the dimensions and choice of RVE to be represented by a single unit cell [90].

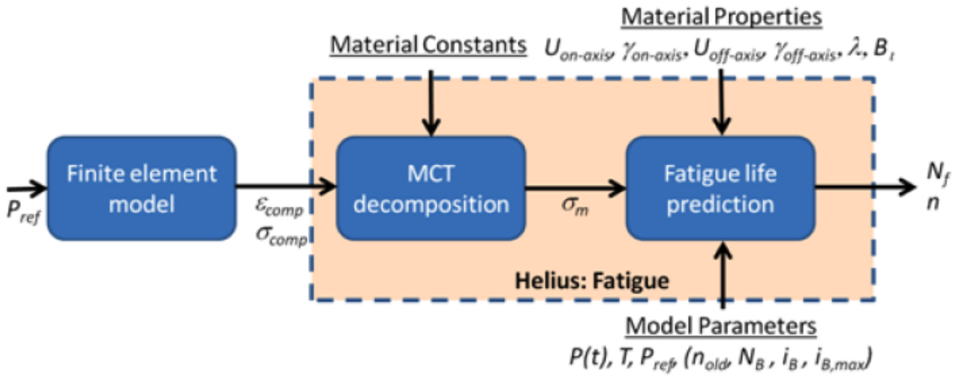
Material Properties
Material Constants
$U_{on-axis}, \gamma_{on-axis}, U_{off-axis}, \gamma_{off-axis}, \lambda, B_i$
Finite element model
P_{ref}
ε_{comp}
σ_{comp}
MCT decomposition
σ_m
Fatigue life prediction
N_f
n
Helius: Fatigue
Model Parameters
$P(t), T, P_{ref}, (n_{old}, N_B, i_B, i_{B,max})$

Figure 114: Fatigue Failure Prediction Process Helius: Fatigue and fe-safe^{TM}/composites [90]

In a GFRP there exist two constituents: the matrix and the fibers. These constituents will be represented by a RVE element characterizing a material point in the composite. Multicontinuum therefore applies the fundamentals of continuum mechanics to the different materials that exist in the RVE. As a result, the unidirectional FRP material can be considered as two continua, the fiber continuum and the matrix continuum, that interact and coexist within the RVE of the composite material. Consequently the representation of the unidirectional FRP material in a multicontinuum manner can be perceived as three different volume averages; physical quantities of interest averaged over the fiber continuum (fiber average quantities), the matrix continuum (matrix average quantities) and over the entire RVE, representing the whole composite material, (homogenized or composite average quantities). Table 20 shows the three superscripts used to distinguish between variables for each type of average quantities.

Table 20: MCT average quantities symbols

Superscript Symbol	Type of average quantities
c	composite
f	fiber
m	matrix

The MCT apart from the classic continuum mechanics development of relationships between the various composite average quantities such as stress and strain, also enables the development of such relationships between the various constituent average quantities, as well as relationships that link the composite average quantities to the fiber and/or matrix average quantities [91].

As in classic continuum mechanics a domain of the RVE should be defined, in order to characterize the composite material's response at a point. This domain is represented by letter D, and $\boldsymbol{\sigma}(x,y,z)$ is the stress tensor field with respect to position, within each of the two constituents (fiber or matrix) of the composite microstructure. A composite average (or homogenized) stress state, $\boldsymbol{\sigma}^c$, fiber average stress state, $\boldsymbol{\sigma}^f$, and matrix average stress state, $\boldsymbol{\sigma}^m$, can also be defined within the RVE. This homogenized stress state can be expressed in relation to the domain (D, D_f, D_m), stress tensor field **σ**(x,y,z), and RVE total volume (V, V_f, V_m) as

$$\boldsymbol{\sigma}^i = \frac{1}{V^i}\int_{D^i} \boldsymbol{\sigma}(x,y,z)\, dV \tag{60}$$

where i represents c, f or m. Strains can be expressed in a similar manner as

$$\boldsymbol{\varepsilon}^i = \frac{1}{V^i}\int_{D} \boldsymbol{\varepsilon}(x,y,z)\, dV \tag{61}$$

As mentioned earlier damage in a composite laminate begins through microstructural damage, i.e. damage in either the fiber or matrix constituents. Only when the damage evolves to a critical stage does it demonstrate itself as damage/failure of the composite. As a result, average constituent stress and strain states are of greater importance in predicting damage evolutions and failure of the composite material, since it is the stress and strains in each constituent that affect damage evolution in the constituent itself.

In order to proceed with the MCT decomposition of the composite average stress and strain states to the respective fiber and matrix average states, constitutive relationships expressing average stress measurements in terms of the corresponding average strain measurements are needed. It is preferred that these relationships are kept linear[8] in order to achieve a unique MCT decomposition that in the mean time is mathematically tractable. Considering the letter **C** to represent a 6x6 constitutive matrix, θ a uniform temperature change in the material in respect to a reference temperature at which various material properties are measured, and **α** a 6x1 vector representing the thermal coefficient of expansion, the various volume-average linearized constitutive relationships become

---

[8] Linear constitutive relationships do not limit MCT decomposition to just linear problems, but allows for its use in nonlinear problems as well [90].

$$\boldsymbol{\sigma}^i = \boldsymbol{C}^i\left(\boldsymbol{\varepsilon}^i - \boldsymbol{\varepsilon}_o{}^i\right) = \boldsymbol{C}^i\left(\boldsymbol{\varepsilon}^i - \theta\boldsymbol{\alpha}^i\right) \tag{62}$$

In the case of the constitutive relationships being linear, **C** and **α** are constants.

The constitutive equations (Eq. 62) together with the matrix and fiber average strain states help compute the corresponding stress states.

The kinetic theory of fracture gives a description of the bond breaking process by processes that are activated by heat. KTF is used by Helius: Fatigue in order to predict the matrix fatigue failure, which can be translated to composite failure using MCT. Zhurkov [92-93], Coleman [94-95], and Regel [96-101] have done extensive research in the way KTF for polymers, and Helius: Fatigue approach has been developed based on such research.

The bond-breaking rate can be expressed as

$$K_b = \frac{kT}{h} exp\left(-\frac{U}{kT}\right) \tag{63}$$

where $exp\left(-\frac{U}{kT}\right)$ expresses possibility of that any given oscillation will overcome U. In terms of fracture and fatigue there exist two equilibrium states. State 1 represents the unbroken state, and state 2 the broken state (Fig. 115).

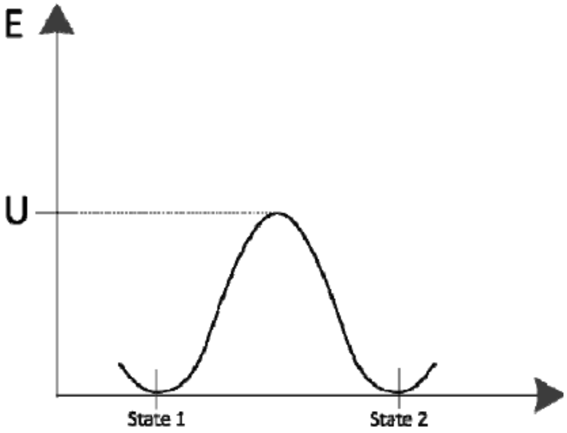

Figure 115: Energy barrier and activation energy required to move from State 1 to State 2 [90]

If a stress is considered, it will have an effect on the bond-breaking rate K_b (Eq. 63). Assuming that stress is in terms of energy per unit volume rather than in terms of force per unit area, the stress may reduce the required energy barrier to bond-breaking. Depending on the volume of the material where the processes occur, the amount of the energy barrier reduction will be the product of stress and activation volume ($\gamma\sigma$). The effects of the applied stress will modify the bond-breaking rate as

$$K_b = \frac{kT}{h} exp\left(-\frac{U-\gamma\sigma}{kT}\right) \tag{64}$$

MCT will translate the applied composite stress to the appropriate average matrix stress.

Helius: Fatigue distinguishes between two modes of fatigue failure: a) off-axis where failure is demonstrating via cracking parallel to the fibers in a unidirectional composite, and b) on-axis where failure is the result of matrix cracks at the fiber/matrix interface. In the off-axis mode it is tensile forces perpendicular to the fiber direction that play a crucial role in fatigue prediction, while for on-axis mode normal stresses in the axial direction will cause the crack creation in the matrix. Each mode will have different activation energy and volume, as well as a different effective stress.

As discussed in Part I, fe-safe^{TM} allows the user to consider the effects of mean stresses in the fatigue life prediction of a metal component. The mean stress effect in the fatigue analysis of composite materials is related to oscillating stress. The load ratio and mean stress describe sinusoidal loading that vary between a maximum and a minimum applied stress value, and as a result stress becomes a quantity dependent on time. Contrary to the case of constant load, an oscillating load in a unidirectional composite may affect the fatigue life of the composite.

Another physical parameter that affects fracture of a polymer under cycling is temperature. Research has shown that an increase in the frequency of cyclic loading [102], or the oscillatory stress [101,103], will show significant increase in heating of the polymer. This temperature increase is imperative to be accounted for, in order for the proper prediction of the fatigue life.

The last step in the fe-safe^{TM}/composites analysis using Helius: Fatigue is to link the bond-breaking rate to the macroscopic failure of the composite. Helius: Fatigue will only distinguish between a transverse (off-axis or mode 2) or longitudinal (on-axis or mode 1), mode of failure. If failure is due to delamination, the concept of the detachment of laminate layers should be addressed during the FE analysis. For the analysis of this thesis, all composite components failed by the longitudinal mode.

Fe-safe^{TM}/Composites was used to predict the fatigue life of two different composite materials, S2 glass fiber/epoxy and E glass fiber/epoxy. The composites were modeled in Abaqus as unidirectional with a stacking sequence of [0°/45°]. The laminates were anti-symmetric and composed of only two laminae in order to save computational time. The decision of the stacking sequence was made based on the failure theories analysis results of section II.5.1, and the fact that it is the sequence followed in the manufacturing of composite leaf springs. The dimensions of the Abaqus models are the same as those presented in section II.5.1 and Fig. 104, with the exception that in the case of the fe-safe^{TM} analysis the thickness of each lamina of the anti-symmetric laminate is 3 mm. The beams were modeled as loaded under three point bending with simple supports, and a span length of 24 cm.

The life predictions were completed for an applied maximum strength ranging between 461 MPa and 1075 MPa, and analysis was done for three different load ratios, R=-1, 0.1 and 0.2. Fig. 116 shows the fatigue life for the anti-symmetric S2 glass fiber/epoxy for lives between one and one million cycles. The life of the laminate exceeds 6x10^{10} cycles when the applied maximum stress is below 680 MPa, and for this reason the S-N curve is given for maximum stress values larger than 600 MPa and for lives up to 10^6 cycles.

A closer look at the S-N curve of the anti-symmetric S2 glass fiber/epoxy shows that similar to the case of steel changing the loading ratio affects the fatigue life of the composite. In a similar manner to steel cyclic applications under larger load ratios will have longer lives.

As mentioned earlier the stiffness in a lamina, and consequently a laminate, is not constant at all points as is the case of isotropic materials such as metals. The regions occupied by fibers are stiffer, having also greater ultimate strength, than the regions occupied by the matrix constituent. The amount of fibers occupying a composite will therefore have an effect on the fatigue life of the composite. As a result, the fatigue life of a symmetric laminate of the same material, of three layers with stacking sequence [0°/45°/0°], was also estimated for the same applied maximum stress and load ratios.

The three layered symmetric lamina, having exactly the same dimensions as the anti-symmetric one differing only in the thickness of its laminae being 2 mm each, presents the same pattern as far as the effect of the load ration on the fatigue life is concerned, meaning that the smaller R has a negative influence in the fatigue life of the composite. Comparing the results of the symmetric and anti-symmetric lamina, it is obvious that the fatigue life of the lamina with more layers is greater. At the applied maximum stress of 1075 MPa the lamina survives lives in the order of 10^5 cycles (Fig. 117).

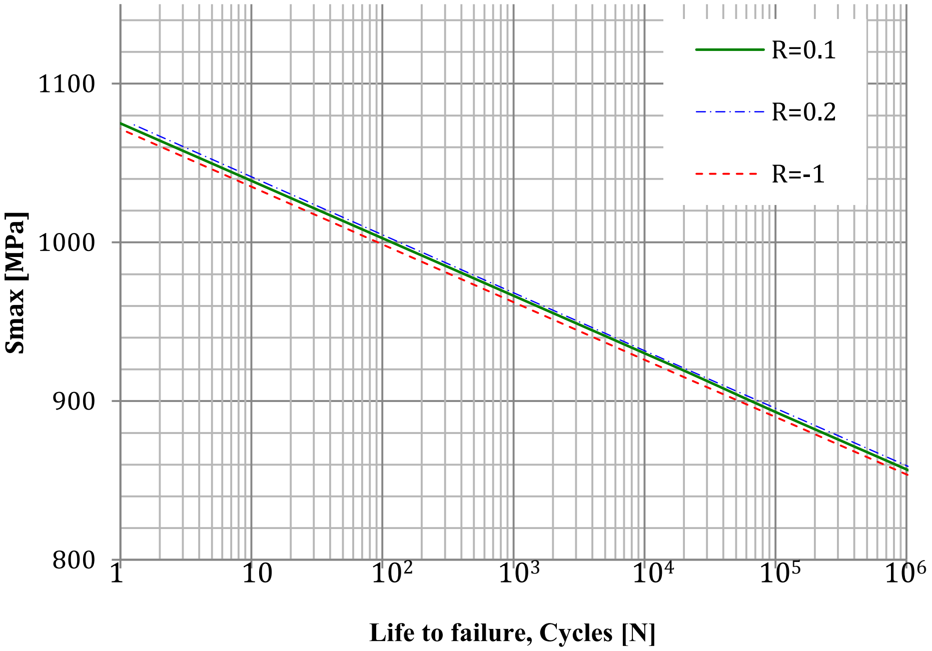

Figure 116: fe-safe™/Composites life estimate for S2 glass fiber/epoxy anti-symmetric 2-layerd laminate

As mentioned earlier, two of the major composite materials used in the manufacturing of composite leaf springs are S2 glass fiber/epoxy and E glass fiber/epoxy. The properties of the two composites (Appendix A) show that the S2 glass fiber/epoxy is stiffer along the fiber direction and has higher ultimate strengths in all directions and especially along the fibers. Comparison of these properties lead to speculation that the fatigue life of E glass fiber/epoxy will be shorter than the composite reinforced with S2 fibers. An analysis of an anti-symmetric unidirectional E glass fiber/epoxy laminate with a stacking sequence of [0°/45°], was performed on fe-safe^{TM}/Composites to predict the fatigue life of the laminate and compare it to that of the same laminate reinforced with S2 glass fibers.

Figure

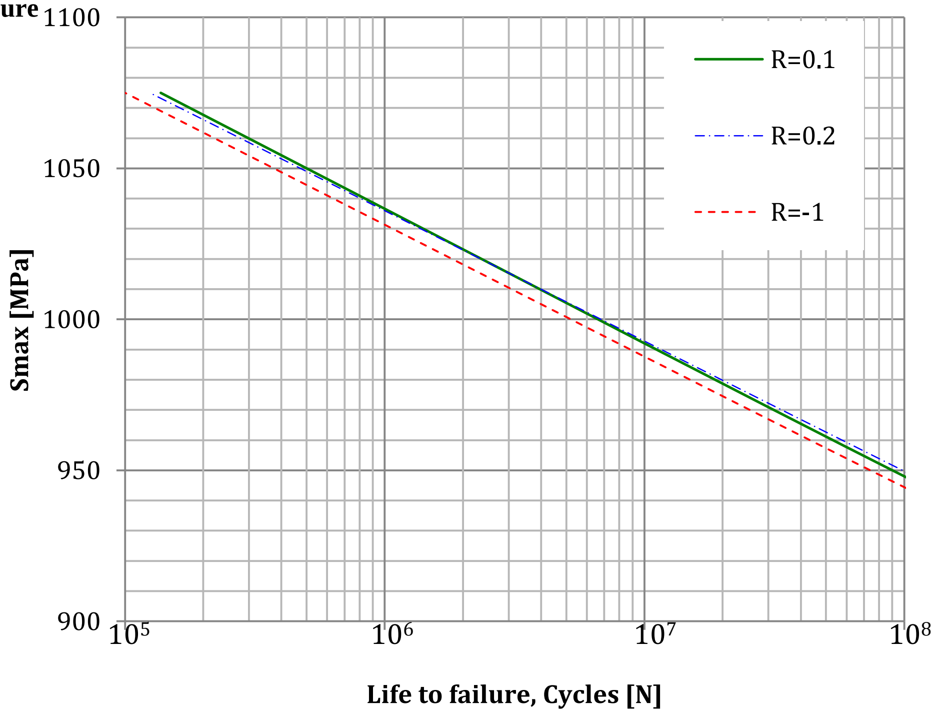

117: fe-safe^{TM}/Composites life estimate for S2 glass fiber/epoxy symmetric 3-layerd laminate

Fig. 118 is the S-N curve for the fatigue life of E glass fiber/epoxy for the three load ratios. As is the case in S2 glass fiber/epoxy the effect of load ratio on the fatigue life is positive as load ratio increases. The effect of load ratio is especially distinguished above 680 MPa, where the S-N curve for the fully reversed loading case separates form the other two curves. The fatigue life of the E glass fiber reinforced composite is much shorter than that of the S2 glass fiber reinforced one. Above a maximum applied stress of 680 MPa the fatigue life of the composite is below 50 cycles, and complete failure occurs at 918 MPa.

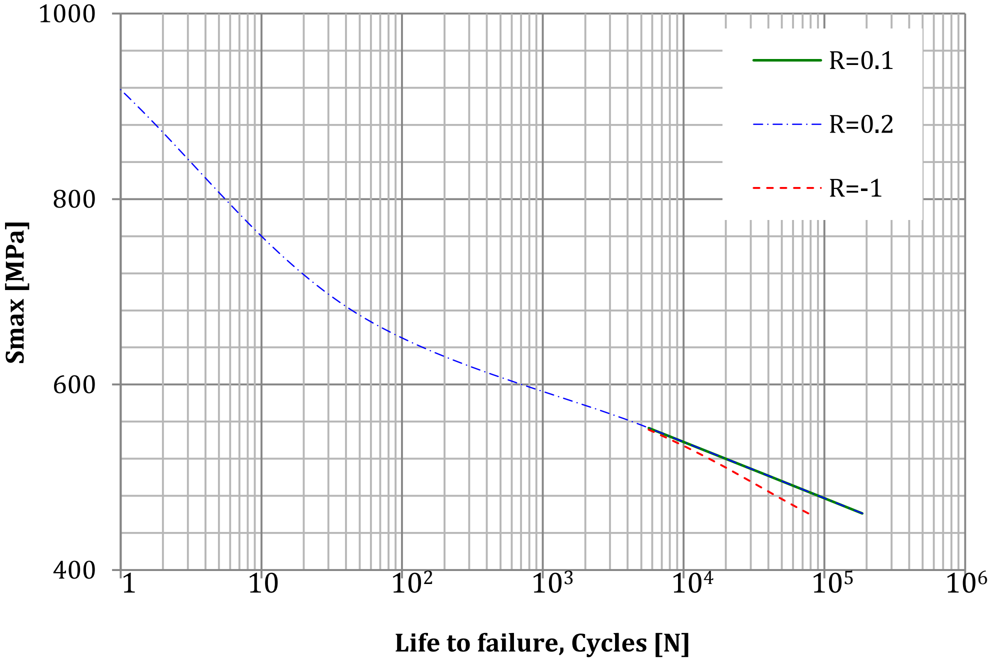

Figure 118: fe-safe^{TM}/Composites life estimate for E glass fiber/epoxy anti-symmetric 2-layerd laminate

In all three cases examined and discussed above the mode of failure was 1, meaning that the composites failed in the longitudinal direction.

II.5.3 Prediction of Fatigue Life Using Damage Prediction Models

Similar to section I.3.2.2 for steel, the damage models (Eq. 22-24) was used to determine the cumulative distribution of damage in the two fiber reinforced plastics discussed in this part of this thesis, as well as predict their fatigue life.

Damage was calculated for a range of maximum stresses from 500 MPa to 1100 MPa (corresponding to a range of mean stresses from 256 MPa to 560 MPa), and for a loading ratio of approximately 0.2. These stress amplitudes correspond to both low cycle (LCF) and high cycle (HCF) fatigue loading in both materials. A two-parameter Weibull analysis (Eq. 31) was performed for each of the three damage models mentioned above [64,74,104-105], in order to decide which model gives more realistic results for damage and fatigue life, when compared to experimental data [27,66].

A scale parameter α and a shape parameter β for each damage model were calculated through the analysis of the accumulated damage and fatigue life (Table 21). When the shape parameter β is larger than 1, failure increases with time [64]. The models for the composites accumulate damage independently of time. In these cases damage is purely dependent on the loading, and the shape parameter β is less than 1. The scale parameter α gives the mean value of damage caused in the material after one loading cycle. From Table 21 it can be concluded that for the case of the two linear models, damage per cycle is larger for E glass fiber/epoxy. In the case of the non-linear model, Hashin-Rotem, damage caused per cycle is also higher in E glass fiber/epoxy.

Table 21: Shape and Scale Parameters of Composites for all Damage Models

Damage Model	**β**		**α**	
	E glass fiber/epoxy	**S2 glass fiber/epoxy**	**E glass fiber/epoxy**	**S2 glass fiber/epoxy**
Palmgren-Miner	0.22	0.28	$1.29\text{x}10^{-3}$	$5.06\text{x}10^{-5}$
Broutman-Sahu	0.28	0.37	$2.68\text{x}10^{-4}$	$2.08\text{x}10^{-5}$
Hashin-Rotem	0.38	0.42	0.41	$8.49\text{x}10^{-3}$

The scale (α) and shape (β) parameters were calculated for each composite (Table 21). The mean value of damage caused in the material after one loading cycle is given by the scale parameter, and damage per cycle is larger for E glass fiber/epoxy, by at least one order of magnitude, for all damage models.

The cumulative distribution of damage predicted by the two linear models is similar at almost all mean stresses for S2 glass fiber/epoxy (Fig. 119(a)). Hashin-Rotem gives a lower probability of failure than Broutman-Sahu and Palmgren-Miner, for mean stresses between 256 MPa and 350 MPa. For stresses from 350 MPa to 485 MPa the probability of failure, from the Hashin-Rotem model, is higher, but at 485 MPa the failure probability is very close to that of the other two models. The Hashin-Rotem failure probability at 560 MPa, for S2 glass fiber/epoxy composite, is approximately 95%, 2% lower than that estimated by the two linear models at the same mean stress.

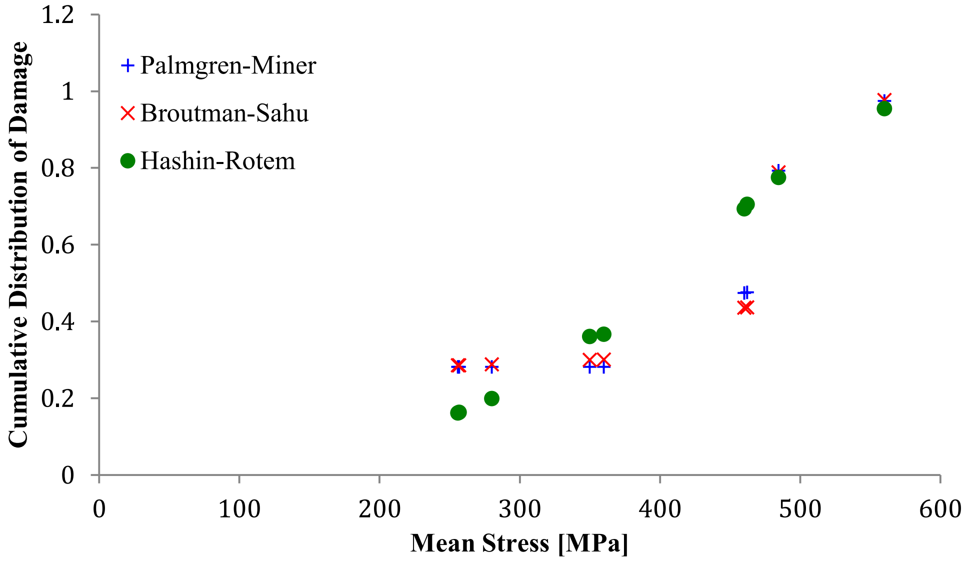

(a)

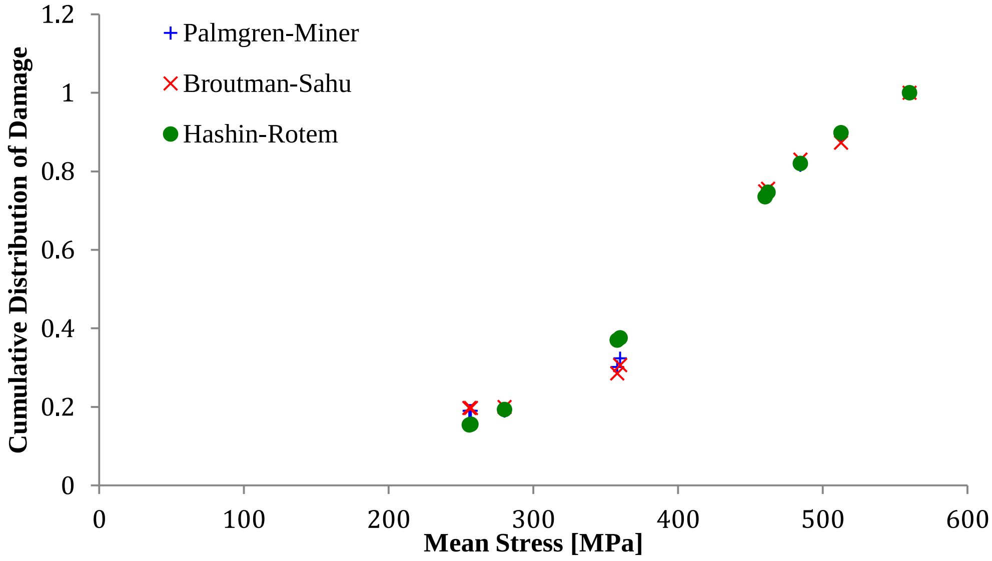

(b)

Figure 119: Cumulative Distribution of Damage vs. Mean Stress in S2 glass fiber/epoxy (a) and E glass fiber/epoxy (b)

For E glass fiber/epoxy composite the cumulative distribution of damage predicted by the Palmgren-Miner model is almost identical to that predicted by the Broutman-Sahu model (Fig. 119(b)). Both linear models show a constant probability of failure at low mean stresses up to 280 MPa. In both cases of the linear models, failure probability at these mean stress levels is approximately 19%. At mean stresses between 350 MPa and 400 MPa, the Broutman-Sahu model gives a bit lower probability of failure, and higher values at 460 MPa to 485 MPa. When these values of failure probability are compared to the results of the Palmgren-Miner model, they differ by at most 1%. 560 MPa is the mean stress level where all three models give a prediction of total failure, a cumulative damage of 1. The reason all models coincide at this point, is due to the fact that this mean stress level, for a loading ratio of 0.2, corresponds to a maximum stress of 1.1 GPa, which is higher than the ultimate tensile strength of the material. The non-linear model starts with lower probability of failure, than the other models, but the cumulative damage increases between 280 MPa and 360 MPa, giving a probability 5% higher than the Palmgren-Miner model. Above 460 MPa it agrees with the two linear models within less than 1%.

For both composites, but especially for the E glass fiber/epoxy, the curve of the Hashin-Rotem predictions is a smooth curve resembling a best-fit line for the two curves of the linear damage models. Hashin-Rotem deviates the most from the other two models in the case of the S2 glass fiber/epoxy composite. Hashin-Rotem deviates the most from the two linear models between 462 MPa to 480 MPa. At

462 MPa the non-linear model calculates a failure probability approximately 31% more than Palmgren-Miner and Broutman-Sahu models. The highest deviation of the Hashin-Rotem model from the two linear ones, in E glass fiber/epoxy, is 7% at 358 MPa.

An average of the cumulative distribution of damage predicted by all three models, at various mean stress ranges, is given for both composites in Table 22.

Table 22: Average Cumulative Distribution of Damage for S2 glass fiber/epoxy composite and for E glass fiber/epoxy composite

Mean Stress [MPa]	Palmgren-Miner	Broutman-Sahu	Hashin-Rotem
S2 glass fiber/epoxy			
265-350	0.28	0.29	0.26
360-485	0.54	0.54	0.57
560	0.97	0.98	0.95
E glass fiber/epoxy			
256-358	0.25	0.24	0.26
360-485	0.57	0.57	0.60
560	1.00	1.00	1.00

Although it may not be clear at a low mean stress range, as the stress level increases E glass fiber/epoxy suffers more damage than S2 glass fiber/epoxy. The reason E glass fiber/epoxy composite shows less cumulative damage at low mean stresses is due to the shape parameter (β), of the Weibul analysis that defines the shape of the cumulative distribution curve. When the shape parameter is small the distribution starts at lower values than those for larger parameters, but has a more rapid ascend.

Cumulative damage distribution for one cycle (K=1) is shown in Fig. 119, and discussed above. To calculate the fatigue life of the materials, the value K when each of the three models equals 1, i.e. at failure, needs to be determined. Fig. 120 gives the mean stress versus cycles to failure, where the short dashed line in each graph is experimental data from the literature [9].

For S2 glass fiber/epoxy composite up to 360 MPa Broutman-Sahu and Palmgren-Miner give similar results, and differ at 560 MPa by 89%. The Hashin-Rotem model underestimates the composite's life by two orders of magnitude at low mean stresses, when compared to experimental data.

The stress dependent linear model, Broutman-Sahu, compared to Palmgren-Miner, predicts lower fatigue life at lower stresses and higher life at higher stresses. This is explained by the fact that the Palmgren-Miner model is not sensitive to changes in stress, since it is a stress independent model. These changes in stress may be small but are important in a material that fails by accumulating damage under cyclic loading. Comparison of the predictions of the damage models to experimental data, shows that the two linear model predictions are higher by at most one order of magnitude, at very low mean stresses, while this is the case of experimental data compared to the non-linear model predictions at high mean stresses, above 400 MPa.

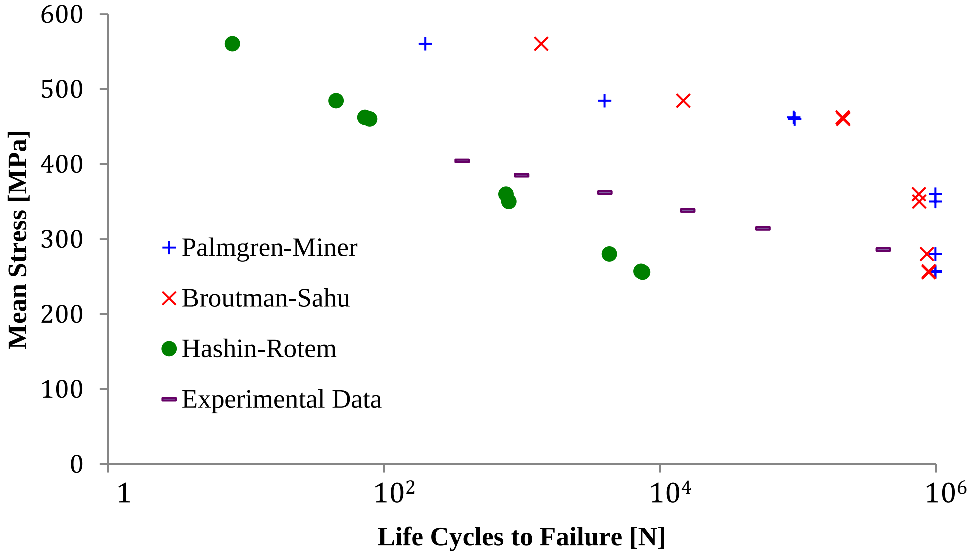

(a)

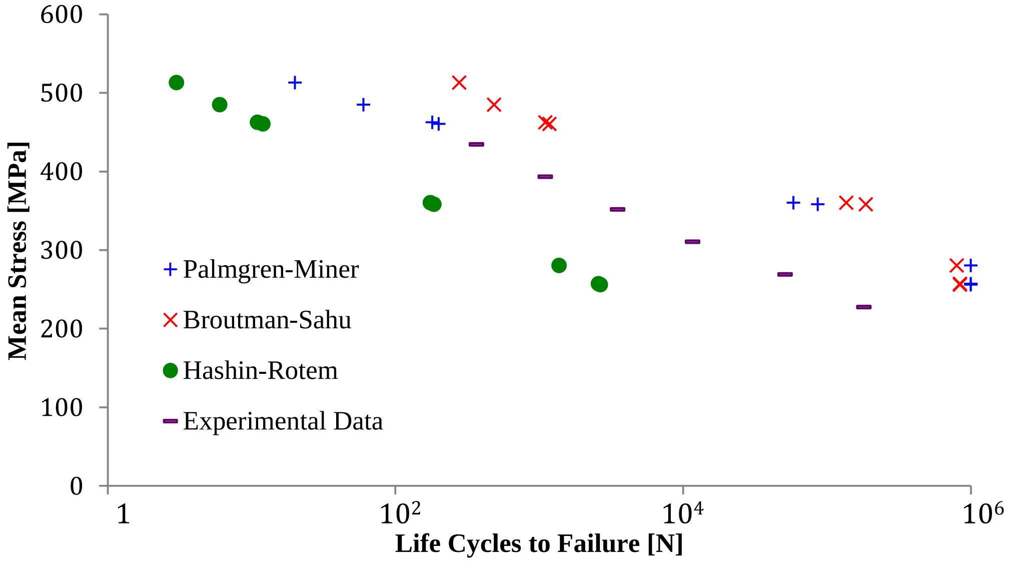

(b)

Figure 120: Mean Stress vs. Life to Failure for S2 glass fiber/epoxy (a), E glass fiber/epoxy (b)

In the case of the fatigue life predictions for E glass fiber/epoxy, not much difference can be observed from that of S2 glass fiber/epoxy, as far as comparison among the three damage models is concerned. The two linear models give a fatigue life differing from each other by less than one order of magnitude at low mean stresses up to 280 MPa (Palmgren-Miner gives a fatigue life 15% higher than Broutman-Sahu). Broutman-Sahu shows better results at higher stresses, 92% higher than Palmgren-Miner at 512 MPa. As is the case of this model in the previous composite, the fatigue life of the composite is underestimated by the Hashin-Rotem model.

The fatigue life predicted by the non-linear model is two orders of magnitude smaller than that predicted by the Palmgren-Miner model at low mean stresses, while at 560 MPa these predictions are one order of magnitude smaller than the Palmgren-Miner predictions, and two orders of magnitude less than the fatigue life given by the Broutman-Sahu model. A similar pattern for S2 glass fiber/epoxy composite can be observed when comparing the predictions of the damage models to experimental data at low mean stresses. At higher mean stresses, however, it is the Palmgren-Miner model that is closer to experimental data of E glass fiber/epoxy, while the Hashin-Rotem model remains within one order of magnitude below experimental data, at all mean stresses.

Experimental results for both composites fall between the linear and non-linear models. It is also worth observing that the predicted fatigue life is higher at the HCF region. The effect of damage accumulation in composite materials can be seen if close attention is paid to what happens when, as is the case of this study, the mean stress rises above 460 MPa. At this stress level the fatigue life drops by 72%, in S2 glass fiber/epoxy and 99% in E glass fiber/epoxy.

An average fatigue life at different mean stress ranges for all examined models and experimental data is presented for both materials in Tables 26. The fatigue life of E glass fiber/epoxy is lower than that of S2 glass fiber/epoxy by at least one order of magnitude at most mean stress ranges. Comparison of the predicted fatigue life to experimental data is also shown in the tables.

Table 23: Average Fatigue Life for S2 glass fiber/epoxy composite and E glass fiber/epoxy composite

S2 glass fiber/epoxy

Mean Stress [MPa]	Palmgren-Miner	Broutman-Sahu	Hashin-Rotem	Experimental Data
256-350	10^6	8.3×10^5	4.2×10^5	2.2×10^5
360-485	5.0×10^5	3.9×10^5	408	2.2×10^3
560	200	1.4×10^3	30	No Data
Compared to Experimental Data				
	Above	Above	Below	

E glass fiber/epoxy

Mean Stress [MPa]	Palmgren-Miner	Broutman-Sahu	Hashin-Rotem	Experimental Data
256-358	5.4×10^5	5.1×10^5	1.4×10^3	1.5×10^4
360-485	2.9×10^4	6.9×10^4	93	1.3×10^3
560	20	278	3	No Data
Compared to Experimental Data				
	Above	Above	Below	

II.5.4 Experimental Results

Three composite beams of dimensions shown in Fig. 115 were tested under three point bending at 350, 500 and 650 MPa. The tests were performed using an MTS closed-loop servohydraulic test system at the testing facilities of Massachusetts Materials Research, Inc. in West Boylston, Massachusetts. For the purpose of these tests, the support span to thickness ratio was adjusted to 20:1 [89] and the load ratio to -1. The deflection of the beam is calculated as

$$D = \frac{rL^2}{6d} \tag{65}$$

where D is the midspan deflection in mm, r the strain in mm/mm, L the support span in mm, and d the depth of the beam in mm. A strain rate of 0.1 was chosen for the case of these experiments. A set up of the tests on the composite beams is shown in Fig. 121.

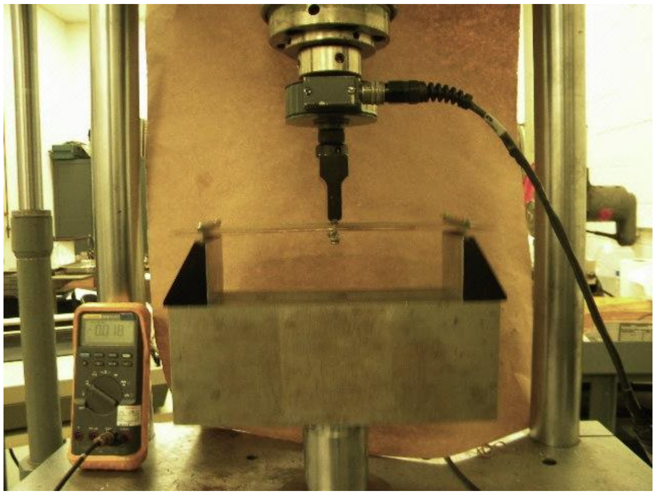

Figure 121: Experimental Fatigue Test Set-up of Composite Tests Beams

The beams were constructed using the hand lay-up method and cured in vacuum, through a vacuum bagging process. The fiber material was a plain weave 71/2oz E Glass, at thickness of 0.27178 mm, and the epoxy used was West System 105 Epoxy Resin mixed with West System 205 Hardener at 1:1: content ratio. The beams contained 22 layers of the fiber cloth, and their final average weight was at 174 g.

No failure of the composites was observed at 100,000 cycles for any of three loading conditions tested. This life is longer than what was predicted using fe-safe^{TM} for the 2 layer, unidirectional E glass fiber/epoxy beam of Fig. 118. Although both the simulated beam and real structure had the same dimensions, the fiber fraction in the two cases was different for the two constituents, fiber and matrix. The real life structures had more composite layers, and the fiber material was woven and not unidirectional.

In general, according to Naik and Shembekar's research [87-88], woven fabric composites have more balanced properties in the plane of the fabric, presenting higher resistance to impact and toughness when compared to unidirectional composites. In addition to this, the woven structure of the woven fabric composites enhances the out-of-plane strength of the composite, thus making the composite able to carry secondary loads that may result form load path eccentricities or buckling [87]. Woven fabrics are easier to work with than unidirectional prepregs or tapes, when constructing thick laminates, but the macromechanical lamina is heterogeneous rather than homogeneous as is the case of a lamina constructed with unidirectional material. As a result, the elastic behavior of a thin woven fabric laminate and a woven fabric lamina may not be the same, as is the case in unidirectional composites [88]. Similar to unidirectional composites, the choice of fiber orientation and thickness of the composite will affect the end properties of the laminate [88]. However, the advantages of woven fabrics come with the cost of a reduced in-plane stiffness and strength properties, and the reason lies in the undulation of the fiber yarns that help create the woven nature of the composite [87].

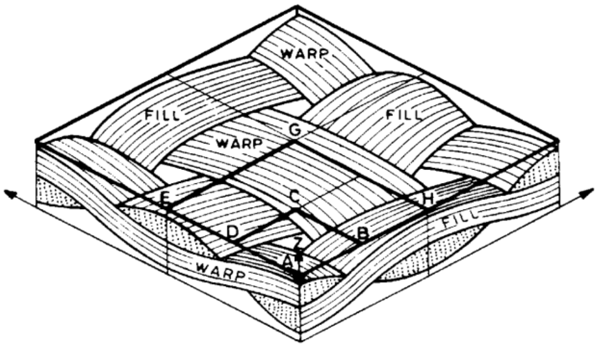

Figure 122: Plain Weave Representation [106]

It was shown that unidirectional composites fail through damage accumulation, and that failure may be demonstrated in different forms such as debonding, matrix or fiber cracking, as well as delamination. Woven fabric composites follow the same procedure of damage accumulation. As shown in Fig. 122 the interlacing fibers in a woven fabric are distinguished as fill and wrap. The wrap is the longitudinal fiber, and the fill the transverse. When failure of the composite is due to fiber cracking, under for example a quasi-static tensile loading, the fill strand will fail under transverse tension, while the wrap under longitudinal tension or shear. Failure in the wrap strand will initiate at the tip of the strand (Fig. 123 (b)) and under increasing tension loading will propagate to its mid-section at the interlacing region, the region where the fill and yarn are adjacent and the role of the matrix is insignificant. At this point, the load capacity will be passed onto the wrap strand. In tensile loading, the catastrophic failure of the woven composite is indicated through failure of the wrap strand, while shear failure in the wrap strand or transverse failure in the fill strand, matrix cracking and delamination are characterized as secondary and will result in a loss of stiffness of the woven fiber composite [106]. The role of the pure matrix in the gap region, where no interlacing is present but the matrix and wrap strand, is to suppress bending or extension effects. Failure can also be initiated in the matrix region. Once the matrix has failed, the wrap and fill strands will be affected next, but again catastrophic failure will be denoted through failure of the wrap strand (Fig. 123 (c)) [106]. As a result woven fiber composites have an extra direction than unidirectional composites for load carrying capacity.

Curtis and Moore in their study of the woven fiber composites’ fatigue life showed that under reversed axial loading the fatigue behavior of the composite depends on the stacking sequence [106-107], as shown earlier in section II.4. Their comparison was between satin-weave carbon/epoxy composites and the equivalent unidirectional ones. They studied three different stacking sequences that affected the isotropy of the laminates. Their results (Fig. 124) showed that woven fabric composites accumulated damage faster than unidirectional composites when having a square symmetric lay up sequence ($[0^\circ/90^\circ_2/0^\circ]_s$), and at the same rate as unidirectional composites when the stacking sequence is quasi-isotropic (($[\pm45^\circ/0^\circ/90^\circ]_s$ or $[0^\circ/09^\circ/\pm45^\circ]_s$) [107].

Similar to unidirectional composites the fiber and matrix volume, and fiber orientation will affect the fatigue life of the composite. In addition to the above, the interlacing of the fiber strands in the woven fiber composite will also have an effect on composite's life. For the purpose of the fatigue experiments completed for this section, the plain-weave fiber layers were not position in a general stacking sequence. Every layer had the same fiber orientation parallel to the longitudinal and transverse directions.

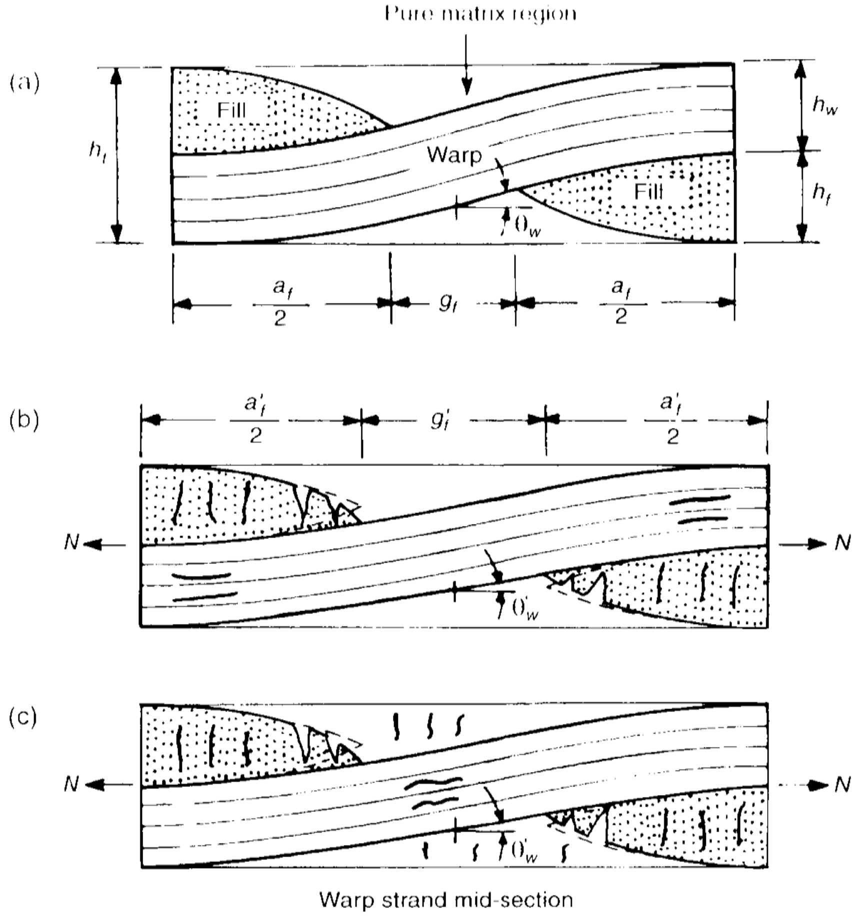
Pure matrix region
(a)
h_t
Fill
Warp
Fill
h_w
h_f
θ_w
$\frac{a_f}{2}$
g_f
$\frac{a_f}{2}$
(b)
$\frac{a'_f}{2}$
g'_f
$\frac{a'_f}{2}$
N
N
θ'_w
(c)
N
N
θ'_w
Warp strand mid-section

Figure 123: Development of Damage in Woven Fabric Composites, when Loaded under Quasi-static Tension: (a) Before Loading and (b and c) After Loading [106]

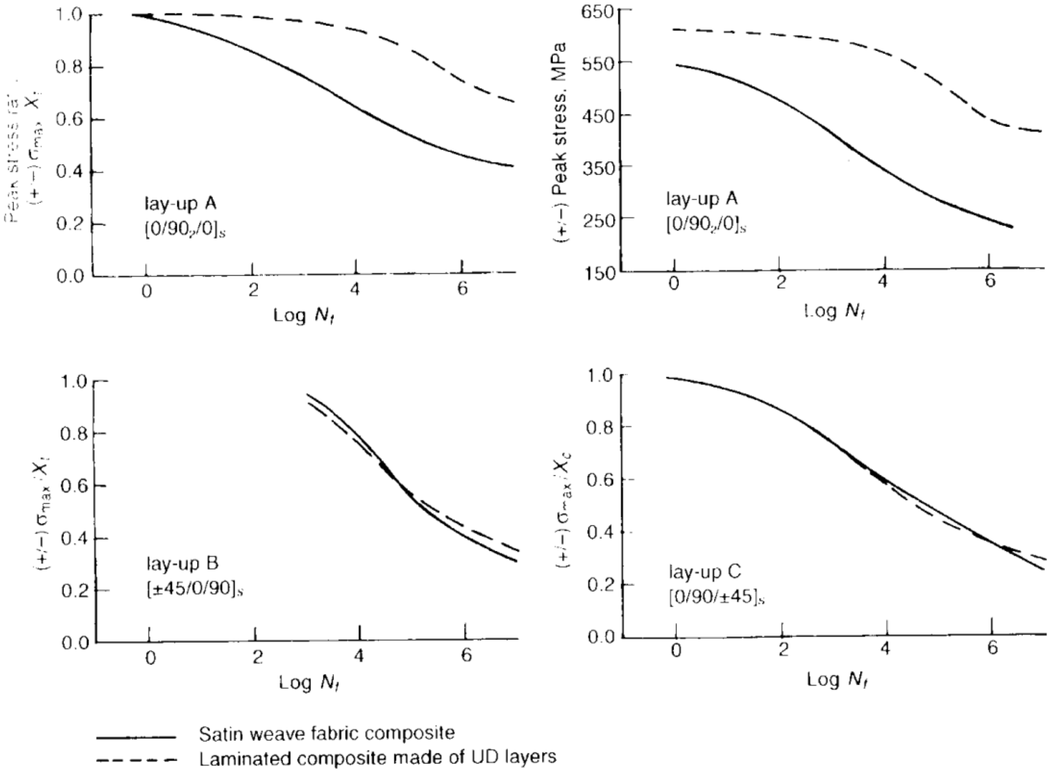

Figure 124:Carbon/epoxy Composite Fatigue Life Curves for Tension-Compression Loading [106-107]

II.6 Repairs of Composite Leaf Springs

Composites leaf springs are made of two constituents: an epoxy and fibers. Contrary to steel leaf springs, failure prevention of a composite leaf spring is possible when failure is initiated due to the delamination or debonding mode. When the leaf spring starts being affected by a separation of its laminae, there is a possibility that this mode of failure is demonstrating itself macromechanically before the component fails catastrophically or ceases to perform with adequacy. In such a case, and only if failure is constrained to the matrix constituent, the leaf spring may be repaired in the compression mold chamber. If the appropriate amount of heat is supplied to the leaf spring to return the matrix to a semi-cured condition and rebond its broken bonds, then the leaf spring may be cured again and placed back on the vehicle [10].

As a result, composite leaf springs apart from strength and good performance, also offer the opportunity of failure prevention and repair, when failure does not occur in the fiber constituent. Additionally, repairing of the composite leaf spring does not require extra machinery form what the composite leaf spring production line holds.

II.7 Conclusions

Composite materials have become a common alternative to metals in many industries. The automotive industry, and specifically leaf spring manufacturing, examined as a case study of this thesis, has turned to GFRPs as an alternative to steel in order to achieve lighter, more durable structures that provide the passenger with a safe comfortable ride while reducing fuel emissions.

Composites fail differently from steel, by accumulating damage, and failure may be demonstrated in different modes. Failure of a laminated composite starts in a micromechanical level at one single ply of the laminate, while catastrophic failure is demonstrated macroscopically. Classical Lamination Theory and failure theories help define the first and subsequent plies to fail under certain loading conditions.

Unidirectional composite laminates may be constructed in various ways by alternating the direction of the fibers in each ply, and selecting the number of layers to construct a symmetric or anti-symmetric laminate. Among the three ply sequences examined in this thesis the general stacking sequence was shown to be the stronger one, having layers that can withstand higher magnitudes of load than cross-ply and angle-ply laminates. Through the examination of the different ply sequences, it was also shown that the plies with fibers oriented along their longitudinal direction have the capability of withstanding higher loads while being stiffer than angle plies. The symmetry of the laminate will also affect the load magnitude each ply may sustain, as well as the flexibility of the laminate.

Comparing a macromechanical and micromechanical finite element analysis of the stresses in a laminated composite, the importance of considering each ply separately was underlined. The stresses developed in adjacent plies are different, thus giving a non-uniform stress profile in the component. FEA also showed that composite laminates are more flexible than steel components.

Estimating the fatigue life of a composite laminate may be done in many ways, one of which is finite element software fe-safe^{TM}. Specifically modified for unidirectional composite materials fe-safe^{TM} identifies the number of life cycles required to initiate a defect in a perfect laminated composite and provides the failure direction. Results of simulations on laminated beams showed that the load ratio affects the fatigue life of a composite in the same way it does in the case of metals. Cycling under higher loading ratios results in longer lives of the components. The type of fiber of the GFRP will also affect the fatigue life of the component. FEA justified the results of the previous failure analysis that S2 glass fiber/epoxy is a material that can undergo cycling before failure longer than E glass fiber/epoxy.

The damage accumulation models in the case of the two composite materials also helped distinguish the superiority of S2 glass fiber/epoxy in terms of its strength and durability. However, as in the case of steel (section I.3.2.2) when compared to experimental data damage models give an overestimated damage accumulation and fatigue life in the case of the linear models, and underestimated predictions in the case of the non-linear model.

To examine the case of woven fabric laminated composite, experimental results were performed on beams cycled under three point bending. Results showed that these composites could sustain long lives in all stress levels tested.

The above analysis gave great insight in the response of GFRPs to failure, and helped determine the optimum glass fiber/epoxy composite material among the two most common ones used in the composite leaf spring industry. However, the above models and software do not provide enough information on the type of failure mode or modes in the components. Interlaminar elamination is one of the most common failure modes, which may be the result of poor bonding of adjecent laminae that occurs at the manufacturing stage of a component. Trapped air bubbles at the interface of two layers in a laminated composite become the origin of separation of the adjacent layers. Treating a component as flawless will not give such information on the mechanism that leads to failure. The majority of these failure mechanisms may be detected and repaired as was discussed in Section II.6.

III. HYBRIDS

III.1 Hybrid Laminates

One of the most common words in the world of technology, hybrid, describes an object made from the combination of two different elements. The notion of hybrids in the materials world means the combination of a composite material with another material such as metal, wood or other composites. In the case of hybrids discussed in this part of this thesis, the metal does not take the place of one of the constituents of a composite, although there exist composites with one of their constituents being a metal, as for example metal matrix composites, rather it becomes an extra element of the structure apart from the two constituents that compose the composite material.

There are two ways that the two materials can coexist in a hybrid laminate. Each material can occupy a different lamina, and as a result compose a laminar hybrid laminate, or the second material can exist as a reinforcement of the composite, for example in the form of fibers, creating a interlaminar or intraply hybrid laminate. Fig. 125 shows the two types of hybrid laminates. Between the two types, laminar hybrid laminates are common in the leaf spring manufacturing world.

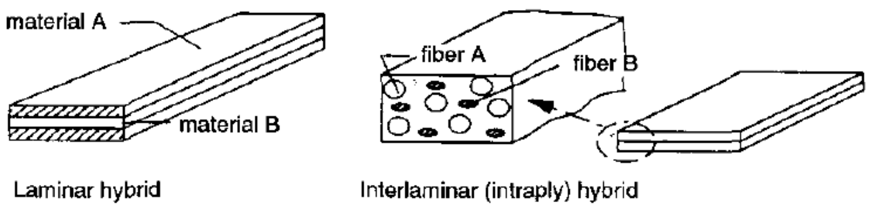

Figure 125: Laminar and Interlaminar Hybrid Laminates [80]

The main reason that the industry turns to hybrid laminates is economics. Composite materials tend to be very expensive as raw materials, and some fiber reinforcements such as graphite, tend to be much more expensive than others. A good example to describe this difference in expenses is a mixture of a intraply hybrid with 20% by volume graphite fibers mixed with glass fibers that produce a composite having 75% the strength and stiffness and 30% the cost of a composite reinforced only with graphite fibers [80]. In the automotive world, laminar hybrid leaf springs, made of laminae of fiber reinforced composite material and a lamina of steel, is a more affordable solution to a composite leaf spring, while minimizing the weight of the suspension without increasing the cost very much.

In general hybrid materials can be analyzed as composite materials. However as Hayashi first noticed, the behavior of intraply hybrid laminates is especially difficult due to what he calls hybrid effects [108]. Hybrid effects include the inability to define and accurately model the various mechanical properties of the hybrids, especially when using the rule-of-mixture approach (Appendix B) [109-111]. One serious difficulty is the scattering in the ultimate strength data of this type of hybrid laminates. On the other hand, CLT and failure theories can be applied to hybrid laminates, and especially laminar hybrid laminates, provided that the required material properties and constitutive relationships of the two materials are known or can be defined through experimentation [80]. The methodology followed is treating each lamina separately, as it is done in a composite laminate with varying lamina fiber orientations.

III.2 Hybrid Leaf Springs

Apart from economics another reason why hybrid leaf springs hold some popularity in the automotive world depends on the ease of formation of the leaf ends. Due to the nature of fiber reinforced composites the creation of curved ends (eyes) on the composite leaf is a difficult and not always successful task. As a result, these ends are separately manufactured from steel and are attached at the ends of the cured composite leaf spring during the assembly stage of the manufacturing process [89]. Geometrical discontinuities in the composites that interrupt the fibers create high stress concentration areas, and leaf spring manufacturers have been seeking an alternative to metallic eye attachment on composite leaf springs, which may also reduce the assembly time. Hybrid leaf springs are created with steel and composite leaves assembled in a leaf spring structure. The leaf spring end problem is thus solved, as it is the steel leaf of the hybrid assembly that is manufactured to have the appropriate end formation of the leaf spring.

There exist two types of hybrid leaf springs that can be distinguished from one another based on the way the leaves attach to each other. In one type the composite and steel leaves are attached to each other as in the case of a conventional steel leaf assembly through fasteners [112] (Fig. 126). Consequently, the leaves may touch each other but are not restrained by one another. As a result, interlaminar failure mode is not a concern, but friction between the leaves that may lead to fretting fatigue is an issue not to be overlooked. On the other hand, there is another hybrid type where the leaf spring operates as a laminate whose plies, in the case of the leaf spring leaves, are bonded to each other. Therefore, delamination between the plies may be a possible mode of failure, but for the means of this study the bonds between the leaves will be considered perfect.

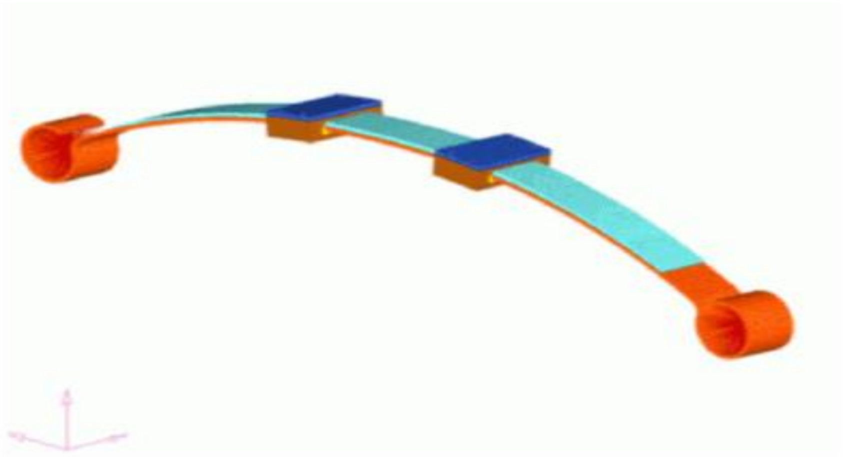

Figure 126: Hybrid Leaf Spring with two separate leaves [112]

Although in the first hybrid leaf spring type, the leaves are manufactured individually by the corresponding manufacturing process, in the second type the manufacturing process is different and requires that the end product is manufactured as one. US patent 6,461,455 B1 [113] suggests that the metal leaf is manufactured as usual in a steel leaf spring manufacturing process, but the hybrid leaf spring is manufactured in a compression mold as shown in Fig. 127.

A composite leaf spring may replace a multi-leaf suspension [14]. In the case of the hybrid leaf spring of Fig. 127, the number of steel and composite leaves depends on the type of suspensions in question, meaning the required stiffness and spring ratio of the suspension. On the other hand the hybrid leaf spring of Fig. 128 acts as a mono-leaf laminate whose laminae are individual leaf springs, one that is steel and two that are themselves composite laminates. The thickness of each laminae in the whole structure depends again on the type of the composite. However, a parabolic design can be successfully created using this method of hybrid leaf spring manufacturing. This design of the leaf spring therefore, resembles a sandwich structure where the steel layer is in-between two composite ones. Due to the requirement of the round (eye) ends of the leaf spring, the middle steel layer is not surrounded by composite material at its ends. On the other hand, the mid section of the leaf spring has the most amount of composite material, due to the parabolic shape of the leaf that requires the middle of the leaf spring having the greater thickness of the leaf structure.

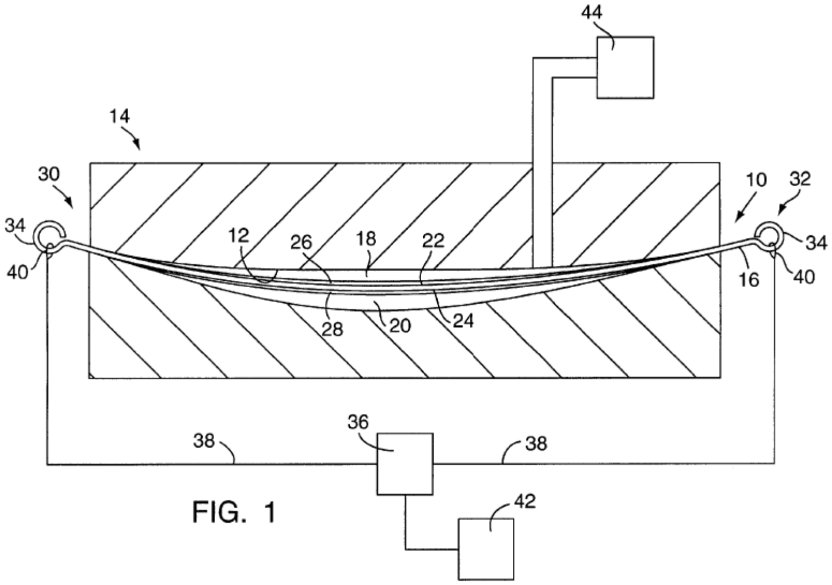

FIG. 1

Figure 127: Manufacturing of hybrid leaf spring in compression mold [113]

III.3 Results and Discussion

III.3.1 Finite Element Analysis

For the purposes of this thesis that seeks to determine the fatigue life of materials, two more simple hybrid beam structures were introduced, based on the concept of the hybrid design of Fig 128. Both beams were straight, with the steel layer in the middle of the beam, and constant cross section in the area of the span length. As shown in Fig. 129 the two beams differ in their end sides. One has straight ends where all three materials are visible (Fig. 129 (a)), while the other design has longer end sections where the composite layers nest the shorter steel layer in the structure (Fig. 129 (b)).

Both structures were studied using FE in ABAQUS to determine how stresses, and maximum deflection vary between the two different designs, when the beams are subjected to three point bending at 500 MPa. Table 24 shows the difference in the beams' deflection, in the y (vertical) direction, as well as their volumes.

Table 24: Maximum Displacement and Volume of Hybrid Beams

Structure	Displacement	Volume [mm^3]
Bent Edges	28 mm	134,018
Straight Edges	23 mm	134,400

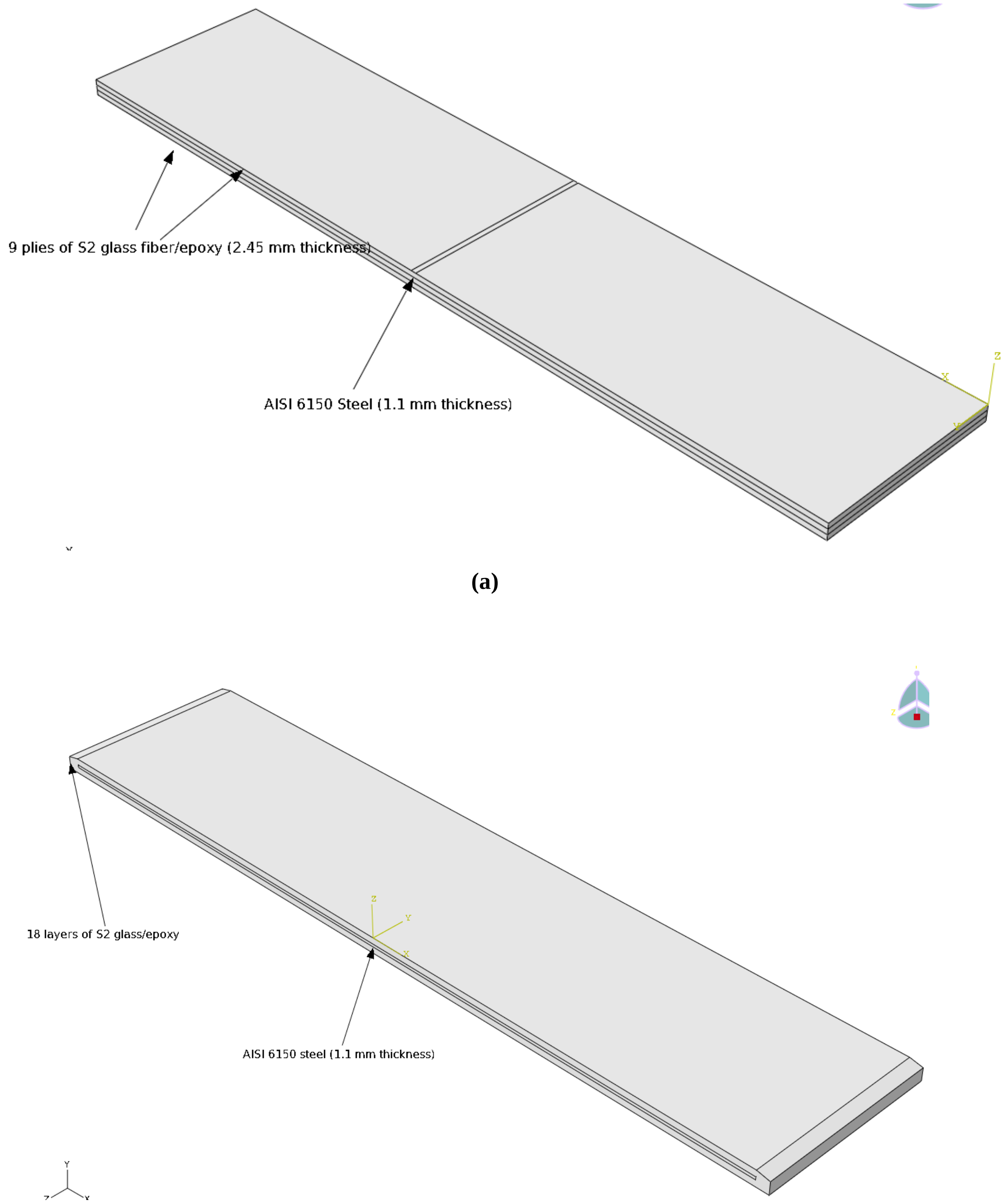
9 plies of S2 glass fiber/epoxy (2.45 mm thickness)
AISI 6150 Steel (1.1 mm thickness)
Z
X
Y
18 layers of S2 glass/epoxy
AISI 6150 steel (1.1 mm thickness)

(a)

(b)

Figure 128: ABAQUS Hybrid Beam: Straight Beam (a) Straight Beam with Bent Edges (b)

From Table 24, it can be concluded that the displacement for the structure with bent edges is smaller, and as a result the structure is stiffer with a larger spring rate. A small difference in the volume of the structures, resulting in weight difference, makes the bent edges hybrid beam lighter. However, the mass difference between the two different hybrid beam structures is very small to affect spring rate. Bent edges require less composite material, while the dimensions and mass of the steel layer remain the same as in the case of the straight edged structure. As a result, bent edges may economize weight, but not from the steel portion of the beam.

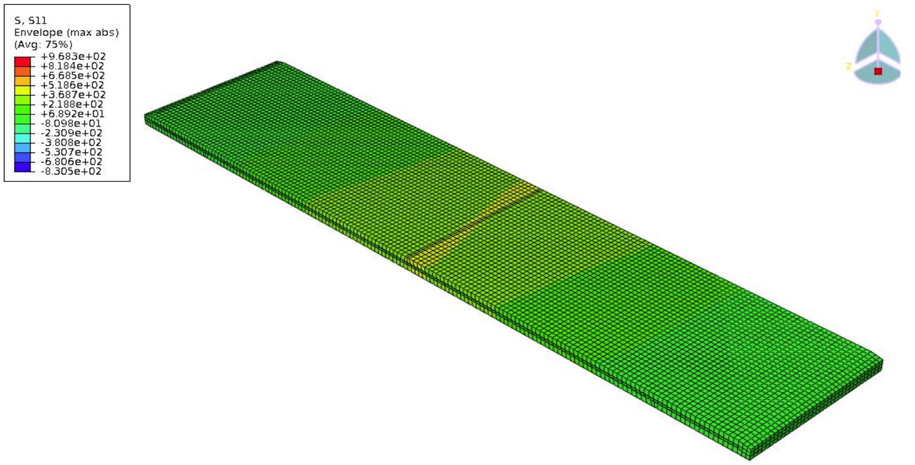
S, S11
Envelope (max abs)
(Avg: 75%)
+9.683e+02
+8.184e+02
+6.685e+02
+5.186e+02
+3.687e+02
+2.188e+02
+6.892e+01
-8.098e+01
-2.309e+02
-3.808e+02
-5.307e+02
-6.806e+02
-8.305e+02
Y
Z
X

Figure 129: Contour Plot of Bending Stress in Hybrid Beam with Bent Edges

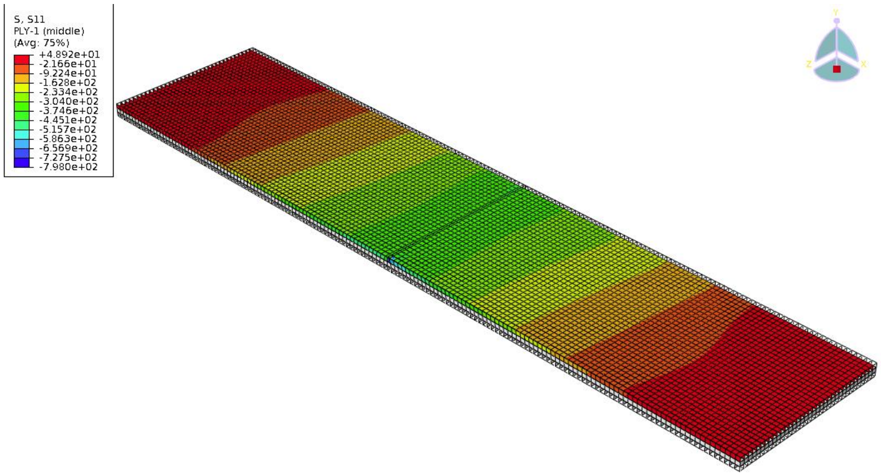
S, S11
PLY-1 (middle)
(Avg: 75%)
+4.892e+01
-2.166e+01
-9.224e+01
-1.628e+02
-2.334e+02
-3.040e+02
-3.746e+02
-4.451e+02
-5.157e+02
-5.863e+02
-6.569e+02
-7.275e+02
-7.980e+02
Y
Z
X

Figure 130: Contour Plot of Bending Stress in Ply 22 of Hybrid Beam with Straight Edges

Each hybrid beam was considered by two different approaches. A macromechanic approach, where the composite was viewed as a whole solid structure, and a micromechanic approach, where the stresses in each lamina were determined separately. For these approaches, profiles of the measured parameters were taken through the thickness and in the middle of the beam, respectively. In the first approach, where the composite is considered macromechanically, measurements are taken at a point close to the top surface of each lamina. In the micromechanic approach, measurements of the parameters are taken at the center of each layer. Fig. 129 and 130 show how ABAQUS treats visually these two approaches. In the macromechanic case, Fig. 129, the beam is considered as a solid while in the micromechanic approach, Fig. 130, contour plots of each layer can be viewed and examined separately, and measurements can be taken at different points in the layer. Fig. 129 shows the contour plot of the bending stress in the hybrid beam with bent edges as a solid, and Fig. 130 shows the bending stress contour plot of ply 1 in the straight edge hybrid beam.

The macromechanic bending stress of the two hybrid beams, loaded under three point bending at 500 MPa while keeping the 60:1 span length to thickness ration, are shown in Fig. 131. In both beams the steel layer's stress profile is linear, having its bottom surface under tension and its top surface under compression, while the mid-surface of the structures is at zero stress. The bottom composite layers, where plies 1 to 9 are located, are under tension, and the top plies, containing plies 11 to 19, under compression, as expected due to the loading type, and as discussed in PART II for the composite beams. The major difference between the two structures lies in the area where the composite connects with the steel layer. At these transition points there exists an increase in the bending stress magnitude, which is larger and more obvious in the case of the structure with straight ends. The reason for this spike in the curves of Fig. 131 is due to the fact that the stresses in the steel layer of the hybrid beams are larger in magnitude to those of the composite. The steel layer's stress profile in both structures is linear, and the stress profiles of the composite layers are almost constant in both top and bottom sections of both beams, with the straight edge beam having a bending stress 20 MPa smaller in magnitude than that of the bent edged beam.

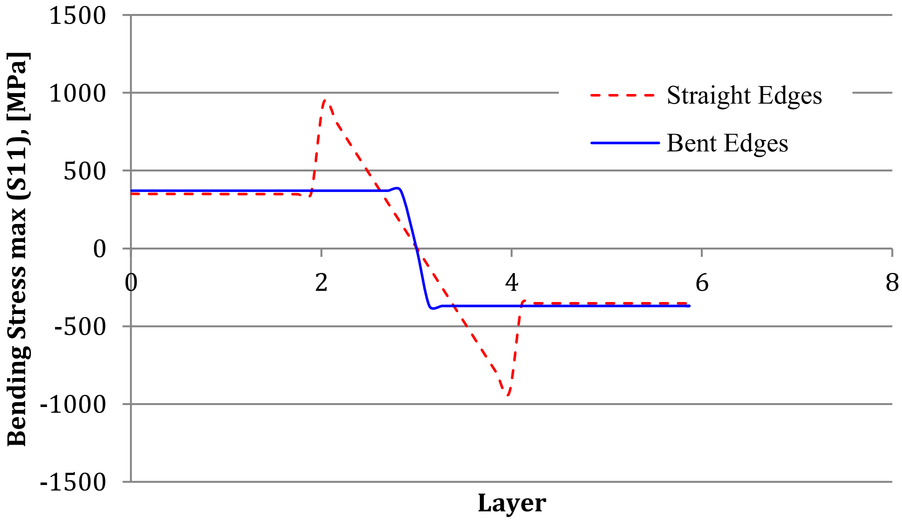

Figure 131: Macromechanic Bending Stress in Hybrid Beams

Studying the same parameter micromechanically allows understanding of how the stress varies between the different laminae of the composite material portions. The bending stresses are shown in Fig. 132 for both cases of hybrid beams. Contrary to the macromechanic curves of bending stress, where the laminar structure of the composite layers is not accounted for resulting in the curves being straight at each layer, the curves of Fig. 132 show the stress at the center of each of the nine laminae of the composite portion of the hybrid beans, and as a result those two parts of the curves are not straight but of sinusoidal shape. The sinusoidal nature of the curves at the composite layers is due to the fact that the laminae of these layers have alternating fiber orientations due to their general stacking sequence.

The bending stresses shown in the above figures follow similar trends due to the fact that in both hybrid beams the angle sequence and order of angle is the same. The difference between the two beams is that the bending stress in the middle of the laminae of the hybrid with bend edges has a constant amplitude in its curve when compared to that of the beam with straight ends where the stress between lamina of the same fiber orientation fluctuates by a stress between 2 to 4 MPa approximately, and larger stresses are observed at laminae closer to the mid-surface of the beam. In addition to this observation, the bending stress difference between adjacent layers is smaller in the case of the hybrid with bent edges. The steel layer in both cases shows the same stress profile of maximum bending stress magnitude at 400 MPa.

The geometry of the ends of a beam therefore, does affect the stress profile of the structure, and its stiffness. This is due to the fact that the fibers carrying the majority of the applied load follow the geometry of the structure, and on the premises of the composites' anisotropic behavior. Therefore, when designing a composite leaf spring of parabolic shape, and ends with complicated geometries, these effects should always be considered.

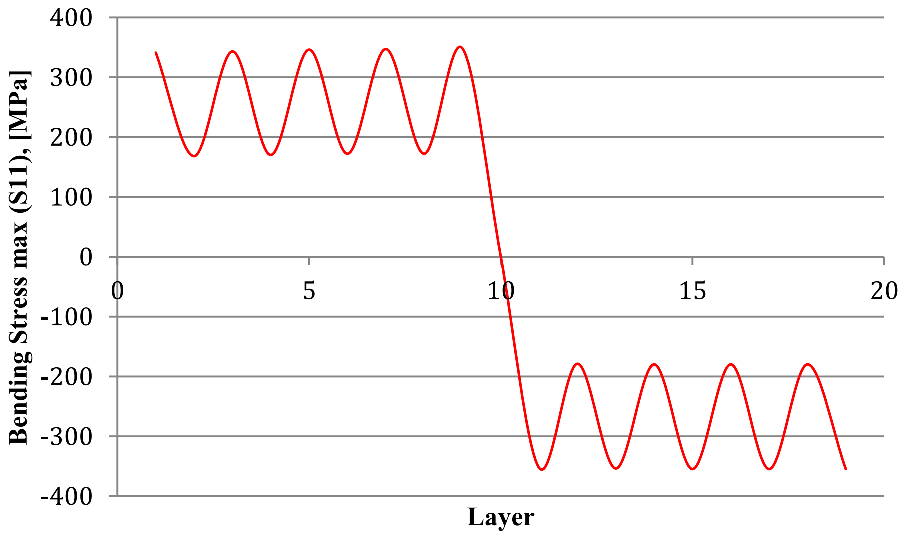

(a)

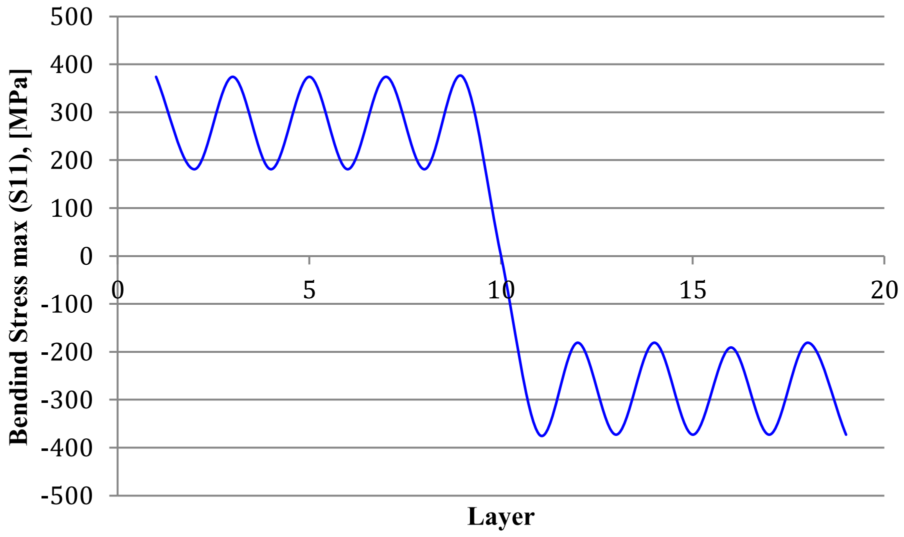

(b)

Figure 132: Micromechanic Bending Stress in Hybrid Beams; Straight edges (a), Bent Edges (b)

The above analysis shows, once more, how much different results may be evaluated by considering different approaches of composite structures. It is hard to judge which approach more accurately predicts reality when lacking experimental data, but it can go without argument that the micromechanic approach can give valuable insight in the behavior and response of each single layer of the composite.

Choosing an optimum hybrid structure between the two presented above, should depend on the needs of the application and based on comparable experimental fatigue data for each structure. However, since the stiffness of structures for suspension systems is very important, as well as weight concerns, depending on the stiffness and weight requirements of the destined application, the hybrid beam with bent edges will provide a slightly lighter, more flexible solution than the beam with straight edges.

III.3.2 Hybrid Laminate Failure Using Failure Theories

It was noticed earlier that due to the nature of the hybrid laminates, and especially of the multiple materials in the structure, it is hard to accurately model and understand the mechanical behavior of such structures. Fe-safe^{TM}/Composites cannot analyze hybrid or sandwich structures as the system can only handle analysis of one-material structures, of unidirectional nature, not woven, composites. For this reason, the current analysis was limited to a first-ply failure prediction using the Tsai-Hill failure theory, and fatigue experimental data.

Apart form the general dimensions of the beam analyzed, the failure theories discussed in this study will not distinguish between beams of different geometries, or geometric discontinuities. The analysis however, will depend on the type of materials of the composite, fiber angle orientation, thickness and number of plies, applied loads and/or moments, as well as temperature gradients. Along the same lines of the analysis followed for the S2 glass fiber/epoxy and E glass fiber/epoxy composites in section II.5.1, the hybrid beam of Fig. 128 (a) was analyzed using CLT and the Tsai-Hill failure theory, in order to determine the first ply to fail and the load that will initiate the hybrid laminate failure. The analysis was performed for both ultimate strengths of the AISI 6150 steel evaluated in section I.3.1.4, namely 1630 MPa and 995 MPa. Using the failure theories one cannot account for the ultimate strength gradient of the material, nor the existence of residual stresses or surface finish factors. Therefore two analyses, one for a hybrid laminate having a center lamina of AISI

6150 steel of ultimate strength of 1630 MPa, and one for a laminate of the same grade steel with ultimate strength 995 MPa, were performed.

The analysis for each hybrid was under the same moment and temperature conditions as for the composite beams, and the stacking sequence for the composite layers was chosen to be general stacking. The composite layers were symmetric laminates composed of nine lamina each having stacking sequence $[(0^o/45)_4/0^o]$. The two composite material layers, of nine laminae each, were approximately 2.5 mm in thickness, and the steel middle layer was 1 mm in thickness.

Table 25 gives the uniform strains, and curvatures developed under a bending moment of 100 Nm/m and a temperature gradient of -2.2^oC.

Table 25: Mid-surface Strains and Curvatures

Mid-surface strains	Curvatures
$\begin{Bmatrix} -2.0x10^{-5} \\ -2.9x10^{-5} \\ -1.0x10^{-5} \end{Bmatrix}$	$\begin{Bmatrix} 57 \\ -17 \\ -0.1 \end{Bmatrix}$

Similar to the case of the composite beams, the mid-surface strains are uniform in the composite, as are the curvatures. However, the stress in each layer of the structures is very different, and as a result the hybrid beam does not have a uniform stress profile. Fig. 133 show how σ_x varies in the composites, as calculated using CLT. Measurements of the longitudinal stress component are taken when the structure is loaded by a moment of 1000 Nm/m.

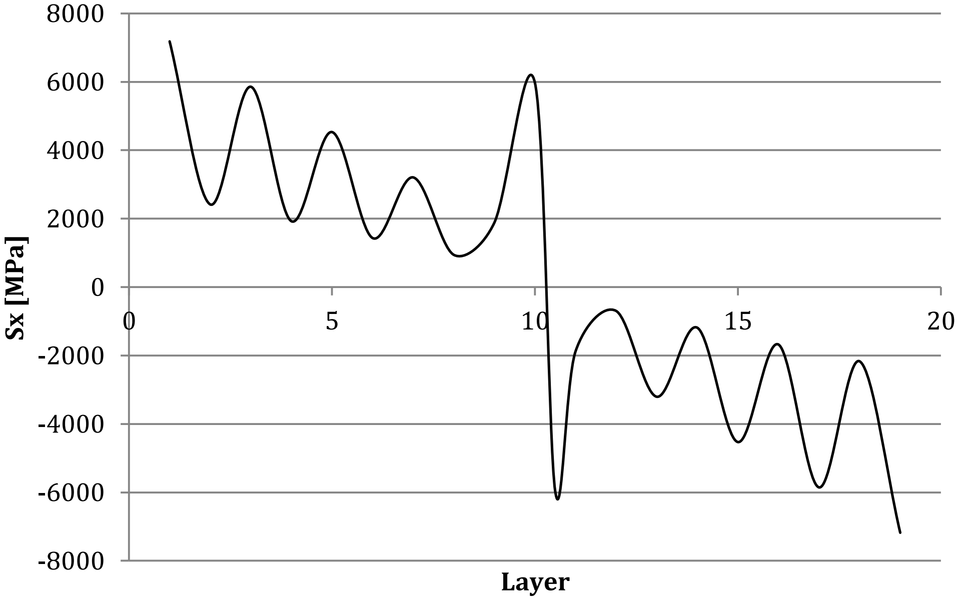

Figure 133: Longitudinal Stress Profiles in Hybrid Beam

In the above figure the isotropic central ply, has the expected linear stress distribution. On the contrary the two composite laminates, of nine plies each, present nonlinear profiles that also vary with the position of the laminates in the hybrid beam. It is lamina 1 that is stressed the most, and lamina 19 the least. An alternating pattern in the stresses can also be observed from Fig. 133, which is due to the varying fiber orientation in the two composite layers of the hybrid beam. Similar to the macromechanic stresses of Fig. 131 the stresses in the lamina adjacent to the steel ply present elevated stresses.

Following the stress calculations is the calculation of principal stresses and strains in order to move in the local coordinates of the fiber directions, and calculate the minimum moment required to begin failure of the structure. Following the Tsai-Hill failure theory, the first ply in the laminate to fail can be determined. In both cases of AISI 6150 ultimate strength, failure will begin in the second ply of the hybrid beam, whose fibers have a 45° orientation. Steel will be the second component to fail in the case of steel with ultimate strength of 995 MPa, but not in the case of the steel with ultimate strength of 1630 MPa, since the moment required to cause failure in the layer is higher than that required to cause failure of the first ply of the hybrid beam, at 0° fiber orientation. Fig. 134 shows the minimum moment that will cause failure in each layer of the hybrid beam.

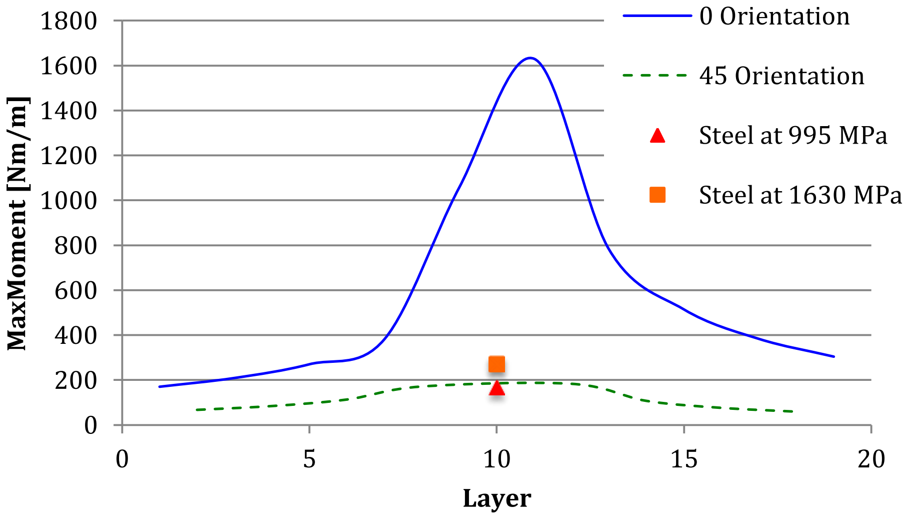

Figure 134: Minimum Applied Moment per layer that will cause Failure

The figure above shows a similar pattern as observed in the S2 glass fiber/epoxy laminate in section II.5.1 (Fig. 105 (f)) of general stacking sequence, regarding how the magnitude of the moment to cause failure varies according to the fiber orientation of the lamina. As a result, the laminae whose fibers are at 0° orientation with respect to the longitudinal direction require a larger moment in order to fail than do the laminae with fibers at 45° orientation. The moment magnitude of the 45° orientation laminae in the area of the beam around the middle steel layer is between the moment magnitudes of the two different steel strengths.

III.3.3 Experimental Results

Fatigue life experiments on hybrid beams with bent edges were completed under the same loading condition and with the same apparatus as those on composite beams in section II.5.4. The dimensions of the beams were same as those of Fig. 104, and the average weight of the beams was at 231 g. Due to the metal core of AISI 4130 steel these laminates are 57 g heavier than those of section II.8. The hybrid structures were manufactured using the hand lay-up and vacuum bagging methods, and have 18 composite laminae divided into two layers of 9 laminae by a 1 mm thick AISI 4130 steel layer. The testing set up is shown in the following figure.

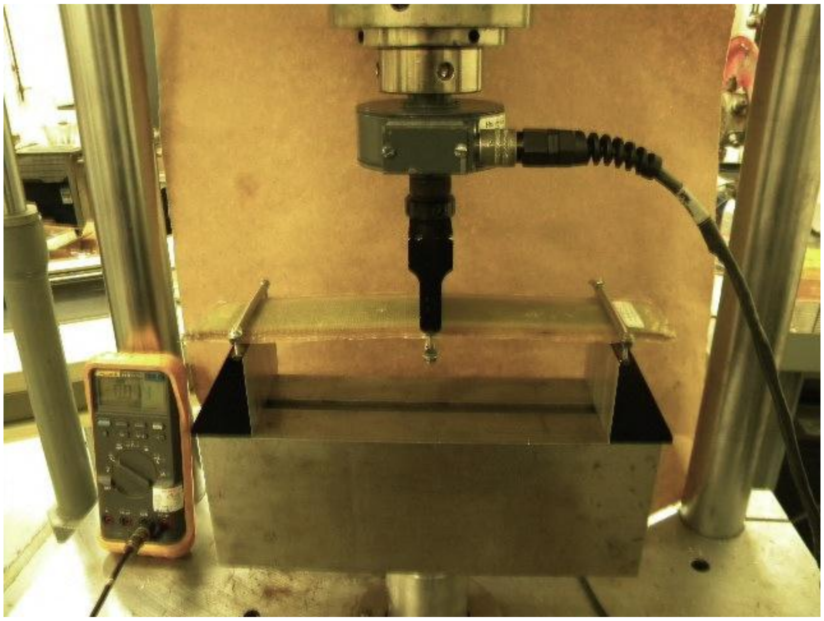

Figure 135: Experimental Fatigue Test Set-up of Hybrid Tests Beams

Similar to the composites of section II.5.4, the hybrid beams did not fail after 100,000 cycles.

III.4 Conclusions

Hybrid laminates are an alternative to both metals and composite materials. They are lighter than metals and cheaper than composite materials. Because of their laminated structure the Classical Lamination and failure theories may be applied in the same way as in laminated composites to distinguish between the micromechanical and macromechanical stresses, and define which ply of the laminate will fail under certain loading conditions. In the present analysis hybrid beams were considered to be composed of S2 glass fiber/epoxy general stacking laminates and an AISI 6150 core. The micromechanical stress profile in the beams was uniform only through the thickness of the steel core, and similar to the case of the composite beams, was non-uniform through the composite laminate layer thickness.

Failure theories showed that the plies with zero degree fiber orientation sustain the higher loads in the laminate, while the steel core is the first to fail if its ultimate strength is 995 MPa. In the case of an AISI 6150 core with ultimate strength of 1630 MPa, a lamina with 45° fiber orientation will fail first. One drawback of the failure theories, in the case of hybrid laminates, is that they do account for any surface treatment the steel core may undergo. As a result, it is hard to get accurate results in the case of a laminate with a steel core induced with compressive residual stresses due to a surface or treatment process. In addition to the above, as in the case of composite laminates failure mode may not be determined using CLT and failure theories.

Finite element analysis has not advanced to the point of predicting the fatigue life of laminates made of two different materials. As a result, finite element analysis is restricted to determine the stress and stiffness of the hybrids. Through such an analysis the effect of geometry and weight may also be investigated. On the other hand, damage accumulation models may not be used for structures composed of more than one materials.

Experimental results on the hybrid laminates were performed under the same conditions as those for glass fiber/epoxy laminates in section II.5.4. Experiments showed no failure of the hybrids at any of the stress levels tested.

As leaf spring structures hybrids will be manufactured using both manufacturing process for steel and GFRP materials. Failure may be detected and repaired depending on the layer of the composite that has failed. Failure in the composite layer or the interface of the glass fiber/epoxy and the steel core may be repaired unless the failure mechanism is debonding, while fracture of the steel core will not allow for repair of a hybrid leaf spring. Interlaminar delamination still remains an important failure mechanism for a hybrid laminate, as it may be demonstrated between two adjacent fiber/epoxy layers, or at the interface of a composite layer and the steel core. Future work through experimentation would be worth looking at delamination and its effects on the fatigue life of a hybrid component, especially at this latter interface between the steel core and the composite layer.

IV. ECONOMIC ANALYSIS

IV.1 Introduction

In the previous parts of this thesis it was shown that composite materials have better strength and fatigue life than steel, and are therefore more suitable to be used as car suspension. It was also mentioned earlier that some automotive industries have taken the step to replace the steel leaf springs of some sports cars, such as those in Corvette cars, with composite ones, thus improving the ride and performance of the vehicle, while minimizing its weight. The question thus arose why composite leaf springs are not that popular in heavy-duty vehicles. Since the above discussion has shown the superiority of composite leaf springs from a performance point of view, an economic analysis comparing the costs involved in the production of the two types of leaf springs will be used to help answer this question.

The economic analysis presented below will concentrate on the comparison of the following three aspects of the two production lines of leaf springs, the one for the steel one and that for the composite ones:

1. The *initial production costs*, involving all aspects required for the set up of a manufacturing facility.
2. The *manufacturing cots*, involving all costs toward the operating of the production line. Emphasis will be given to *prime costs*, which are the sum of *direct labor* and *direct materials costs*.
3. The special characteristics of each production line, such as the use of quenching oil in the production of steel leaves, the amount of leaves that may comprise a multi-leaf spring, as well as the weight difference between the steel and composite leaf springs.

Consequently, this analysis will not take into account other types of costs, such as research and development (R&D) costs, marketing and selling, or administrative costs. In general all non-manufacturing costs will not be considered. The costs considered for in this analysis can be distinguished in *non-recurring* and *manufacturing costs*, which will be defined in more detail later.

For the purpose of this analysis one unit of product will be taken to be one single leaf spring. Because the dimensions of a leaf spring will vary based on its application and the vehicle it is going to be mounted on, the average weight of a steel leaf is taken to be approximately 17 kg, and that of a composite leaf 7.3 kg.

From an economics point of view, the basis of the comparison of the two production lines is that their production capacity is the same. The production line of the steel springs requires 2 hours and 55 minutes [15] to produce an average number of 5 to 7 leaves, while that of the composite leaf springs requires 2 hours to produce 4 to 6 leaves [10]. It should be noticed that the production lines discussed in this analysis are composed of classic machinery operated mostly by physical personnel, and do not depend on any automated sections.

To better assist with any computations required for the comparison that follows, it is assumed that the production line of the steel leaf springs produces 6 leaves in 2 hours and 55 minutes or 2.92 hours, and the line of the composite leaf springs 5 leaves in two hours. This means that in one hour the steel leaf spring production line produces approximately two leaves, while the composite one 2.5 leaves.

Each production is considered to operate within one shift of eight hours, in a working week of five working days.

The amounts of the various costs presented below are in US dollars ($) of 2011. For the amounts collected in euros, an average currency exchange rate of 1.4 was used. The estimation of the various forms of costs presented, represent an average reality in the Eurozone.

The approach followed in this analysis is very similar to that used in the US army research of 1984 entitled "Manufacturing Process for Production of Composite Leaf Springs for 5 ton truck" [9].

IV.2 Non-recurring Costs

The non-recurring costs category consists of all the costs needed to complete the facilities required for the production, such as tooling, equipment and plant facilities. As the name of these costs imply, once they have been accounted for and realized they will not appear again unless one of the components they refer to fails. In the case of the two lines discussed here, the non-recurring costs refer to the costs of the plant facilities and machinery of the lines.

IV.2.1 Tooling and Equipment

Tables 26 and 27 presents all the non-recurring costs involved in the production of steel and composite leaf spings, respectively.

It followes from the tables that the cost for the installation of the production line of steel leaf springs is approximately \$3.75 million, and for composite ones \$0.43 millions.

Table 26: Non-recurring costs for steel material leaf springs

Machine title	Machine Description	$
Crane Bridge	Carrying raw material plates to 1st machine	9,800
Saw	Cuts raw material plates to desired length	16,800
Punching Press	Creates center hole in leaf spring, required for the assembly stage	35,000
Drill	Creates holes on leaf required for the assembly stage	11,200
Eye rolling machine	Gives required curvature to 1st leaf ends	56,000
Cover rolling machine	Gives required curvature to 2nd leaf end	16,100
Steel cutting machine (end shaping)	Cuts leaf ends in required share (diamond/tapered)	23,100
Annealing Furnace	Heats leaf to red hot color appropriate for end forging and cambering	739,200
Leaf Transfer Unit	Transfers hot leaves from annealing furnace to cambering station	107,800
Thickness sizing machine	Gives leaf its varying cross sectional shape	189,000
8 Station Cambering Machine	Gives leaf the desired camber	949,200
45 ton Oil Tank	Hosts Quenching Oil	22,960
Oil Cooling System	Cools oil in oil tank when oil temperature exceeds prescribed maximum	85,400
2 plastic tanks for oil circulation	Contains Oil during oil tank cleaning process	4,200
Oil filter	Filter that collects metal precipitates or pieces form the oil bath	64,400
Conveyor belt and drain rack	Carries and drains quenched leaves out of oil tank	49,000
Tempering Furnace	Tempers quenched leaves	961,800
Shot peening machine	Surface treats leaf spring before the reach the assembly stage	392,000
9000L Natural gas tank	Hosts natural gas for furnace powering	21,000
Portable Hardness testing equipment	Measures the surface hardness of leaf springs	3,920
	Total	**3,757,880**

Table 27: Non-recurring costs for composite material leaf springs

Machine title	Machine Description	$
Filament Winding Machine	Transfers fiber material through resin bath and winds them to the desired shape	181,102
Wet Wind Fiber Delivery Tooling	Tool to make machine operate in wet winding mode	1,578
Prepreg Fiber Delivery Tooling	Tool required in prepreg formation	7,144
Programmable-Digital Electronic Fiber Tensioning System	Dispensing of tensed fibers, also logging tension data	54,013
Roller-Type Fiber Redirect Board Assembly	Redirects fiber in 90 degrees angle from tensioning system to central machine	4,988
Bookshelf Fiber Dispensing Creel	Stationary fiber dispensing creel	2,623
1-Frictiona Type Tensioning	Add on to tensioning system	2,287
Traveling Festooning System	Guides the fiber Bookshelf fiber dispensing creels to minimize fiber damage	1,676
Mylar/Veil Dispenser	Dispenser for mylar and veil	1,988
Fiber Dip type Resin Bath	Resin bath assembly	4,318
Drum Type Resin Bath	Different type of bath, where fibers touch a drum during dipping	4,270
Digital-Programmable Doctor Blade	Controls resin properties in drum type resin bath	2,961
Digitally Controlled Re-circulation Liquid Type Resin Bath Heater	Recirculates resin to assure appropriate temperature	2,657
Resin Drip Tray	Collects resin that has dripped off the fibers	589
Machine Control AC	Prevents overheating of electronics	1,738
IR Curing Panel	Allows part to cure during filament winding	9,555
Uninterruptible Power Supply	Assures an 30 min of power in the event of power failure	2,475
Digital Auxiliary Outputs	Program generation to assist in output triggering during filament winding execution	1,025
Safety Edge	Emergency stop in the event that the machine carriage encounters a foreign object	1,418
Cable Pull-Switch	Emergency stopping of the machine in the event of stepping over or pulling the cable	971
Horizontal Carriage Whisker Switches	Another emergency stop mechanism	3,140
Compression Mold Press	Molds/cure composite structure	20,000
Prepreg Storage Fridge	Stores prepregs to appropriate temperature and humidity	2,000
Cutting Equipment	Cuts composite structures to desired size	100,000
	Total	**432,516**

IV.2.2 Plant Facilities

Concerning the plant facilities of each line, research showed that for the installation of the steel leaf spring production line a space of approximately 2000 m^2 is required, while the same space for the composite leaf spring line is only 700 m^2. This means that the cost of the primary investment is very different between the two lines. The above plant facilities estimations do not include other spacial needs apart from those of the production line equipment, such as personnel locker rooms, office spaces, storage and stock spaces, raw material stock spaces etc. Assuming that the cost of infrastructure of an industrial building is approximately $1,100 per square meter, assumption based on the Greek reality, we can arrive to the conclusion presented in Table 28.

Table 28: Plant Facilities Costs

	Plant facilities	
	Steel leaf springs	**Composite leaf springs**
Square meters	**2,000**	**700**
$/m²	**1,100**	**1,100**
Total cost ($)	**2,200,000**	**770,000**

The table above shows that the facilities construction costs to host the steel leaf spring production line is $1.4 millions higher than the same cost for the facilities hosting the steel leaf spring production line. Although, the results of this research do not give very detailed information regarding the plant facilities, the fact that research has shown that a four leaf steel leaf spring can be replaced by a mono-leaf composite spring [14], can lead to the conclusion that the need for storage space in the composite leaf spring plant will be smaller than for the steel leaf spring plant.

IV.2.3 Conclusions on Non-recurring Costs

Table 29 shows a comprehensive picture of the non-recurring costs involved in each of the two production lines compared.

Table 29: Non-recurring Costs for the two Production Lines

		Steel leaf springs	Composite leaf springs
Non-recurring costs	**Tooling and equipment**	**3.75**	**0.43**
	Plant facilities	**2.2**	**0.77**
Total ($ million)		**5.95**	**1.2**

From the table it can be concluded, that the cost of creating a steel leaf spring production line is significantly higher than the same cost for a similar capacity production line for composite leaf spring. The difference of the two is approximately $4.75 millions, and the main reasons for this difference lies in the fact that the equipment required for the production line of steel leaf springs is greater in number and requires more space, as most of the machines are very large.

IV.3 Manufacturing Costs

The manufacturing costs category involves all forms of costs that are directly connected to the manufacturing process of a product. They include the *direct labor*, *direct materials* and *manufacturing overhead costs*. The definitions of each of these costs will be presented in the following sections.

Direct labor costs concern the work that is directly and substantially related to the production of a product. They refer to all these costs that can be traced in each product unit (e.g. engineering work). Another name for this type of costs is *touch labor costs*, which actually refers to the personnel "touching" the product during its manufacturing process.

The study of the two production lines leads to the conclusion that for the proper functioning of the lines the following two amounts of direct labor, as the number of personnel, are required:

Table 30: Direct Labor Costs

	Steel leaf springs	**Composite leaf springs**
Direct labor units	**12**	**5**

The mean hourly cost is estimated at $11, without considering taxes or insurance withholdings. This means that for the steel leaf spring production the total hourly cost of labor is $132 (for 12 workers), while for the composite leaf spring production it is $55 (for 5 workers). Consequently, the average hourly cost, without considering taxes or insurance withholdings, for the steel leaf spring production is significantly higher than that for the composite leaf spring line. This is due to the fact that a smaller amount of personnel is required to operate the production line of composite leaf springs.

Direct material costs involves all the costs of the raw materials required for the manufacturing of the final product. It should be mentioned that in this cost category correspond all the materials that can be directly detected in the final product. As a result, secondary materials, of lower cost and small importance, which either cannot be traced or is not worth to be traced in the final product, are not included in this cost category. Such materials are presented in sections I.1, I.2, II.1 and II.2, where the production lines of each leaf spring type are discussed. According to the research realized for this analysis, the unit cost for the required raw material for the production of steel leaf springs is

Table 31: Unit Cost for Steel Leaf Spring Raw Materials

Material	Unit	Unit cost ($)
Steel	kg	0.9

Respectively, the same cost for the raw materials required in the production of composite leaf springs is

Table 32: Unit Cost for Composite Leaf Spring Raw Materials

Material	Unit	Unit cost ($)
E glass fibers	kg	0.4
S2 glass fibers	kg	2.7
Resin	kg	0.3

It is worth mentioning again, that the materials E glass fiber and S2 glass fibers can be used alternatively depending on the production needs, or the properties of the end product. However, the cost of both materials is presented for a more comprehensive comparative analysis. It should also be mentioned, that the average content of the fiber and epoxy materials in composite leaf spring is typically 55% and 45%, respectively. These percentages are reflected both in these materials' content in the final product but also in the production costs.

In all manufacturing processes there exist some materials that are wasted and do not end up in the final products. Such materials are called "scrap", but for the purposes of this analysis no scrap cost is considered. All the costs of raw materials correspond to material physically included in the final product.

Manufacturing overhead costs are all costs related to the production line, excluding direct labor and direct materials costs. They are two elements of costs that relate indirectly to the production line. Basic elements of this form of costs are indirect labor and indirect materials costs, maintenance and repairs on production line equipment, heat, light and other utilities, property taxes, depreciation, insurance on manufacturing facilities, and others. Costs that involve other functions of the manufacturing process except the actual production, such as sales or administrative functions, are not included in the manufacturing overhead costs. Studies have shown that manufacturing overhead costs are 16% of the sales income.

However, the purpose of the present analysis is not the complete economic analysis of a potential investment in one of the two production lines, but the comparison of the two lines themselves from a cost perspective. Unfortunately, the collection of information on the composite leaf spring manufacturing costs was very limited due to the availability of such information, much of which was restricted due to secrecy as the research and development of such products is very current. The goal of this analysis is to arrive to conclusions that will point to the different aspects of the composite leaf spring production line that will show whether it is superior to that of steel leaf springs or not. The approach followed involves primarily prime costs as the sum of direct labor and direct materials costs.

For the above reasons, and within the frame of manufacturing overhead costs, the quenching oil will be examined. The quenching oil is only used in the steel leaf spring production, and costs approximately $2,330 per ton. Only 5 tons of quenching oil are evaporated after a 125 ton leaf spring production. The quenching oil needs not total replacement, other than the amount evaporated, but needs conditioning every six months [15]. Therefore, it is not a direct material cost but a manufacturing overhead cost.

Maintenance costs will vary depending on the reasons for which maintenance is required and the type of equipment to be maintained. Due to the various conditions applying to maintenance, and the variation of equipment involved in each production line, it is not possible to compare maintenance costs between the two production lines in a comprehensive and reasonable manner. It goes without doubt to argue that the maintenance cost in the steel leaf spring production line will be higher due to the greater number of machines compared to the equipment required for the production of composite leaf springs. However, as far as maintenance is concerned the production line of steel leaf springs has a certain advantage over that of composite leaf springs as the majority of its equipment can be used independently and the production, although delayed, may continue in part without the simultaneous operation of all its equipment. In the case of composite leaf springs, only cutting and surface treating equipment may be used independently from the rest of the production line.

IV.4 Economic Analysis

For the production of steel leaf springs the cost of direct labor per hour is estimated at $132. The direct materials cost is estimated at $0.9 per kilogram. One unit of end product weighs 17 kg and the production line produces 2 leaves per hour. As a result, the production line may give 16 leaves per shift with

- direct labor cost = $132 x 8 hrs = $1,056
- direct material cost = 16 leaves x 17 kg of steel per leaf x $0.9/kg of steel = $245 approximately
- **Prime Cost per shift = $1,056 + $245 = $1,301**

The direct labor costs for the production of composite leaf springs is estimated at $55. The direct material cost is estimated for both cases of fiber materials, E-glass and S2-glass. It is also taken into consideration that the contents of resin and fiber material in the leaf springs, 55% and 45% respectively, do not only correspond to the leaves' weight but also to the cost of each material. The weight of the composite leaf is taken to be 7.3 kg and the production line can give 2.5 leaves per hour. If the fiber material used is E-glass, then for a production of 20 leaves per shift the production costs per shift are

- Direct labor cost = $55 x 8 hrs = $440
- Direct material cost = 20 leaves x 7.3 kg x [(55% x $0.4/kg) + (45% x $0.3/kg)] = $52
- **Prime cost per shift = $440 + $52 = $492**

Similarly for the case of S2-glass fibers

- Direct labor cost = \$55 x 8 hrs = \$440
- Direct material cost = 20 leaves x 7.3 kg x [(55% x \$2.7/kg) + (45% x \$0.3/kg)] = \$237
- **Prime cost per shift = \$440 + \$237 = \$677**

IV.5 Conclusions

If all the above results are represented collectively in Tables 33 and 34, it can be seen that within the time of a week the productvity and the operational cost of each prodction line is

Table 33: Total Prime Costs for Each Production Line in One Week

		Composite leaf	
	Steel leaf	**E-glass fiber**	**S2-glass fiber**
Number of leaves	**80**	**100**	
Direct labor cost ($)	5,280	2,200	2,200
Direct materials cost ($)	1,225	260	1185
Prime cost ($)	**6,505**	**2,460**	**3,385**

Similarly for the non-recurring costs

Table 34: Total Non-recurring Costs for Each Production Line in One Week

Amounts in millions US$		**Steel leaf springs**	**Composite leaf springs**
Non-recurring costs	**Tooling and equipment**	**3.75**	**0.43**
	Plant facilities	**2.2**	**0.77**
Total		**5.95**	**1.2**

The above tables show clearly that under the assumptions made for this analysis, the production and aftermarket availability of composite leaf springs, may be a successful one economically compared to the production and current aftermarket availability of the steel leaf springs. If in the above analysis the cost of quenching oil is taken into account, the difference between the costs of the two lines will be greater.

Research has shown that composite leaf springs have stronger properties at lower weight than steel leaf springs. Rajendran and Vijayarangan [14] showed in their research that a composite mono-leaf spring may replace a steel multi-leaf spring of seven leaves, while preserving all the required suspenison properties at 85% less weight. If such studies are taken into account and less composite than steel leaves are required for the suspension of a vehicle, then the production of composite leaf springs will be more beneficial and more profitable.

Currently composite leaf springs are priced approximately 3 to 4 times higher than steel ones. One of the main reasons of this price selection are the research and development costs which have not been discussed up to this point and will not preoccupy further this analysis. The reason of the high research and development costs is due to the fact that composite leaf springs are a new product, which is still under development. Steel leaf springs are products that have existed for years, and most of the development on these is completed. There exist hundreds of models of steel leaf springs, parabolic or conventional, for the various types of vehicles that exist. On the contrary, the design and development of composite leaf springs is a new one and the materials' involved properties and behavior are still being examined and researched. As a result, the cost of R&D for the production line of composite leaf springs will continue to be a high one, but is an investment worth making, as this product is part of a very competitive market, especially in the present day when the cost of gasoline is constantly increasing, and vehicle carriage weight is a major solution to less gasoline consumption.

V. COMPARISON OF MATERIALS

In the first three parts of this thesis the strength and fatigue life of three different types of materials was examined and discussed, in connection to applications of cyclic loading and for the case study of leaf springs as vehicle suspension systems.

Part I presented the failure mechanisms in metals through the initiation of cracks and their propagation to failure, as well as the effects of residual stresses on the fatigue life and strength of a steel structure such as a leaf spring. Part II presented the way composite structures fail through damage accumulation, the failure modes, and how failure in composites differs from failure in metals. The failure propagation in composites from the micromechanic to the macromechanic level was also discussed, as well as the failure initiation lamina. Finally, a composite structure, which is a combination of the above two materials, was presented in Part III and evaluated for its strength based on different geometries and fatigue life. The cost of leaf spring production was discussed in Part IV, for the case of three different materials, AISI 6150 steel, S2 and E glass fiber/epoxy.

Two different steel materials were examined in Part I; AISI 4130 and AISI 6150, which is utilized as the main material in the manufacturing of leaf springs. Between the two steels, AISI 6150 presented longer lives explaining the reason for which it is an appropriate material for leaf spring manufacturing. Similarly in Part II, two different composite materials were examined, having different types of glass fiber constituents. Through the damage models, failure theories, and life prediction through finite element methods, it was shown that S2 glass fiber/epoxy is a composite of greater durability than E glass fiber/epoxy. However, there still remains to complete a comparison among the two materials, AISI 6150 and S2 glass fiber/epoxy, and three structures, steel, composite and hybrid beams, to decide upon an optimum solution that will combine high strength, performance, stiffness and low weight all at a reasonable manufacturing cost.

V.1 Comparison of Materials Based on Damage Prediction Models

It was previously mentioned in this thesis that the main ingredient in failure of composite materials is accumulation of damage, while for metals initiation and propagation of a crack is the main characteristic of metal failure.

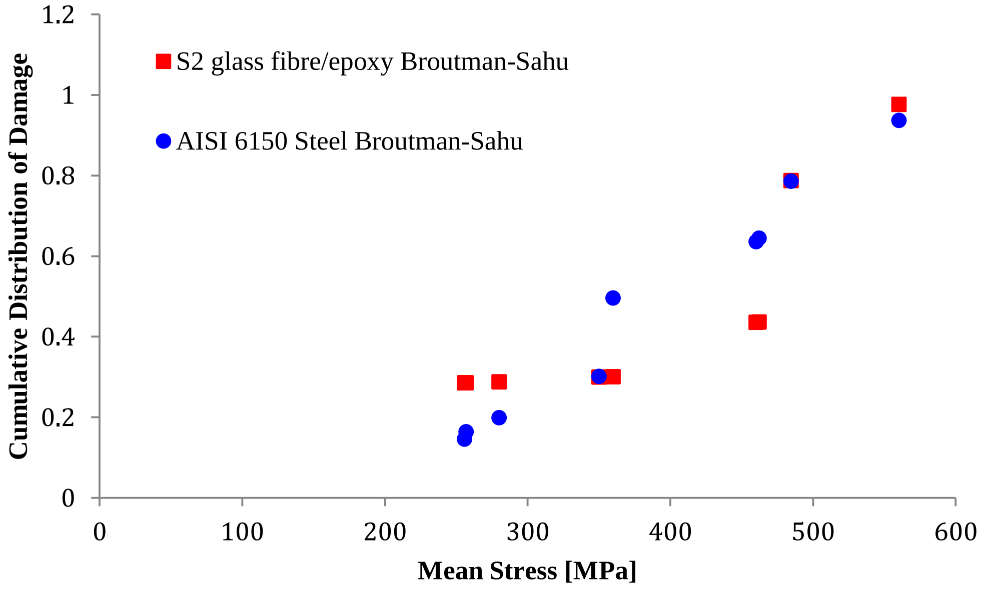

Figure 136: Cumulative Distribution of Damage of AISI 6150 Steel and S2 glass fiber/epoxy

The above figure shows the cumulative damage for the two materials for the Broutman-Sahu model. The Broutman-Sahu model is chosen for this comparison as the model that gives longer lives at HCF region, among the three models tested, and because it was originally developed as a modification of Palmgren-Miner for GFRPs. Both materials were examined under the same range of mean stresses, and failure for both is estimated when cumulative damage in the material is at 100%. At mean stresses below 360 MPa the damage accumulation of steel is lower than that of the

GFRP (28% failure probability estimated for S2 glass fiber/epoxy, and 15% for steel). However, the cumulative distribution of damage for the composite is constant between 250 and 360 MPa, while it is rising in the case of steel, coinciding with that of the composite at approximately 360 MPa. Between 360 and 485 MPa, the damage accumulation in the composite is 30%, and it is lower by approximately 20% compared to steel. At failure the composite has a slightly higher damage accumulation, by 3%. This can be explained by the inhomogeneous nature of composites that fail due to damage accumulation, and the fact that in steel failure is based on crack initiation and propagation. From the above comparison it can be concluded that the composite accumulates damage from the beginning of loading when a crack in steel is most probably not even initiated yet. However, at the point where the failure probability for steel is higher than that of the composite, it can be suspected that a crack in the steel material has formed and is being propagated.

Plotting the mean stress to life cycles curve of the two materials (Fig. 137), At low stresses up to approximately 400 MPa the composite has a longer life than steel. Past 400 MPa, the fatigue life of the steel does not change significantly, while the life of the composite drops very rapidly as the stress increases. This fatigue life pattern can be explained based on the way S2 glass fiber/epoxy accumulates damage compared to steel. The difference in the materials' lives is larger at stresses in the LCF region where damage accumulation in the composite is larger, and crack initiation dominates the fatigue life of the metal. On the contrary, this difference is smaller at HCF stresses.

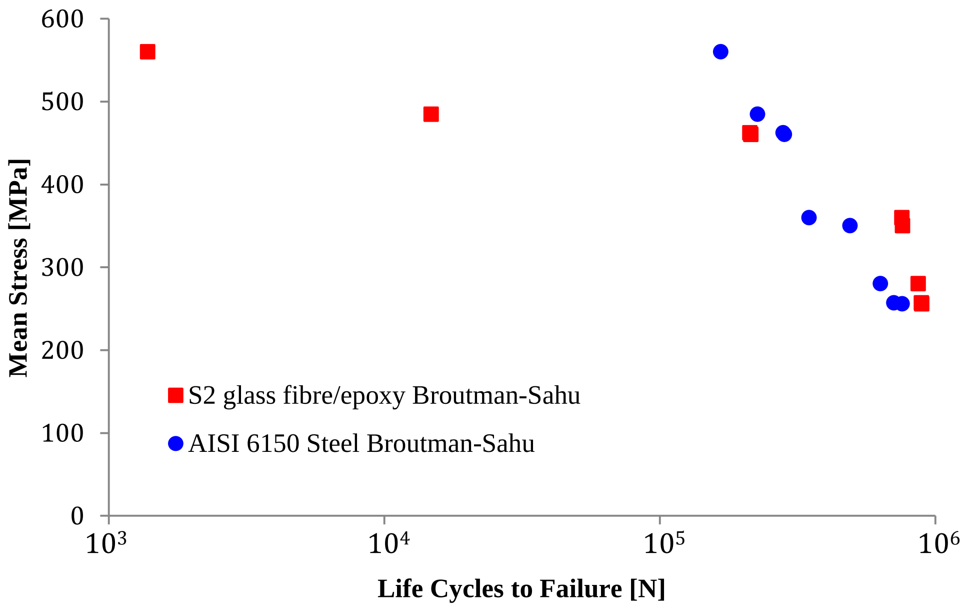

Figure 137: Mean Stress vs. Cycles to Failure of AISI 6150 Steel and S2 glass fiber/epoxy

V.2 Comparison of Materials Based on Fatigue Life

Studies have shown that composite materials can replace steel in application of cyclic loading such as in the case of leaf springs [9,12-14, 113-115]. In all these cases the fatigue life of the composite was longer than that of steel. In the current thesis apart from damage models and experimental results, finite element methods were also used to estimate the fatigue life of the two materials.

V.2.1 Life Estimation Using fe-safe^{TM}

The fatigue life of composite beams using fe-safe^{TM} was presented in section II.5.2, and showed how the fatigue life of the two composites varied based on the different loading ratios examined. It was also shown that the fatigue life of a symmetric thicker beam was slightly larger than the anti-symmetric thinner beam, and that S2 glass fiber/epoxy had a longer life than a similar composite with E glass fibers. In Part I similar simulations showed that a good approximation to experimental results of leaf springs was a loading ratio of 0.1, and a surface factor of 1.5 with 500 MPa compressive residual stresses. The fatigue life of an AISI 6150 beam of UTS at 1630 MPa, of same dimensions as the composite beam of 2 layers tested with fe-safe^{TM}, and at the above loading ratio, surface factor and residual stresses was also estimated using fe-safe^{TM}, for means of comparison. The results of this comparison are shown in Fig. 138, for a life between 10^3 and 10^6 cycles. From the S-N curve of the figure below it can be observed that the fatigue life of the composite is longer than that of the steel below 950 MPa and above $3x10^4$ cycles. Above this stress level the fatigue life of steel is longer, and at 1075 MPa steel has a life of approximately $59x10^3$

cycles, while the composite fails. Another observation that can be made from Fig. 138 is that the S-N curve of the composite has a more constant slope than that of steel.

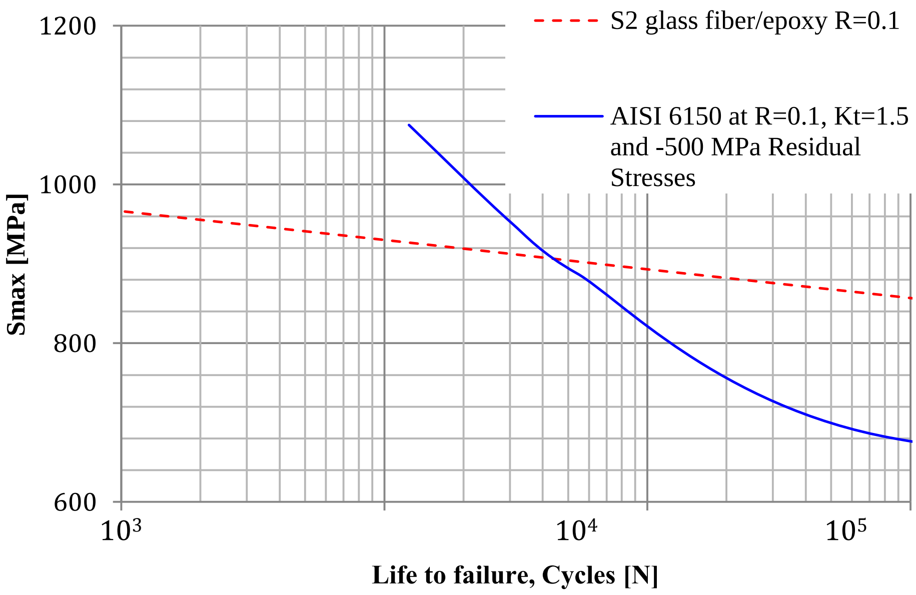

Figure 138: Fatigue Life of AISI 6150 Steel and S2 glass fiber/epoxy using fe-safe^{TM}

From the above figure it can be seen that S2 glass fiber epoxy has longer lives at lower stresses, but as the stresses increase, above 950 MPa, steel performs better. As a result, it can be concluded that for cyclic applications at lives in the LCF region steel is a better choice of material.

V.2.2 Life Estimation from Experimental Results

In Part I of this thesis it was discussed that due to the manufacturing process of leaf springs the core and surface of the leaf spring ends up with different ultimate strengths. The fatigue of the core portion of the leaf spring was tested under reversed loading. Under reversed loading were also tested three composite and three hybrid beams at 350, 500 and 650 MPa. Table 35 gives a comparison of the results of the three structures and two materials.

Table 35: Fatigue Life of Structures

Approximate Stress Level	**Fatigue Life**		
	AISI 6150	**S2 glass fiber/epoxy** (Woven fabric)	**S2 glass fiber/epoxy-AISI 4130 Hybrid Beam** (Woven fabric)
350 MPa	> $3x10^6$ cycles	No failure up to 10^5 cycles	No failure up to 10^5 cycles
500 MPa	$8.1x10^4$ cycles	No failure up to 10^5 cycles	No failure up to 10^5 cycles
650 MPa	$5x10^4$ cycles	No failure up to 10^5 cycles	No failure up to 10^5 cycles

From the above table it is obvious that the S2 glass fiber/epoxy and hybrid beams have a higher fatigue life than the steel leaf spring core.

V.3 Material Selection

The above two sections show that composite and hybrid materials are in general, more appropriate for loading applications when compared to steel. However, apart form fatigue life performance, the flexibility and weight of a structure is also important in applications such as leaf springs for suspension systems.

Finite element analysis of a beam with dimensions as those of Fig. 104, show that steel is generally stiffer and heavier than composite and hybrid beams. Table 36 gives the maximum deflection of steel, S2 glass fiber/epoxy, and the hybrid beams, as well as an average weight for these structures, when loaded under 3 point bending at 500 MPa.

Table 36: Deflection and Weight of Structures

Structure	Deflection [mm]	Weight [g]
AISI 6150	4	1052
S2 glass fiber/epoxy	31	174
Hybrid with Straight Edges	23	412
Hybrid with Bent Edges	28	411

The lightest structure is the composite one, followed by the hybrid structure with bent edges. The stiffest and heaviest among the structures is the AISI 6150 steel one. As a result, composite and hybrid structures are a good strong light alternative to metals. As shown in section II.5.2, the flexibility of the composite and hybrid structures, may be altered by adding laminae or changing the stacking sequence and/or composite constituents volume fraction. However, these options will have an effect on the fatigue life of the composite.

Another comparison that can be made is based on the first ply failure of the hybrid beam and the composite one. The moment required to initiate first ply failure in S2 glass fiber/epoxy composite of 22 laminae and general stacking sequence (section II.5.1) is larger than that required to initiate first ply failure of the hybrid composite (section III.3.2). As a result, according to failure theories the composite beam is stronger than the hybrid one.

Apart form the above there exist two more aspects that are important to be taken into consideration in order to complete the material selection process for a leaf spring. The first aspect relates to the fact that composite leaf springs may be repaired when the mode of failure relates to matrix cracking, delamination, or debonding. The only failure mode that will lead to catastrophic irreparable failure is fiber cracking. On the contrary, a steel leaf spring may not be repaired as discussed in section I.4. Related to repairs is also the issue of failure detection which may be obvious in composite leaf springs when the failure mode is interlaminar delamination. In the case of steel leaf springs, the detection of cracks is nearly impossible, while the propagation of a crack is very rapid to allow for detection of an initiated crack.

Finally, cost becomes the last but not the least aspect of a material selection process for the industry. In Part IV it was shown that the manufacturing process of composite leaf springs is more cost effective and can be proven more profitable, once the technology progresses, than that of steel leaf springs. According to this economic analysis hybrid leaf springs become the least cost effective solution, as they require both production lines, for their manufacturing.

VI. CONCLUSIONS

Four materials, two steels and two composites, were presented in the above study. AISI 4130, AISI 6150, E glass fiber/epoxy and S2 glass fiber/epoxy were all examined to determine their fatigue life and failure behavior in respect to cyclic loading applications, and in particular, their appropriateness as a raw material for leaf spring manufacturing.

Surface treatments of the two steels showed that changing the residual stress field of steel, either through the induction of a residual field through shot peening, or a diffusion process such as carburizing, would enhance the fatigue life of the material and its performance. It was also shown that the heat treatment the steel undergoes during manufacturing of a leaf spring alters the microstructure of the outside layer generating another aspect to affect the fatigue life of steel components. In a similar manner in the second part of this research, and related to the failure theory models, it was shown that the number of plies and especially the fiber orientation in each lamina may be chosen in such a manner to design a product with the appropriate fiber orientation sequence and dimensions for the destined application. The fiber and matrix volume fractions may also be chosen in the manufacturing of composite structures, to accommodate the structures' desired properties.

A comparison of the fatigue lives of the two stronger materials of the two material groups, steels and composites, showed the superiority of S2 glass fiber/epoxy to AISI 6150 steel in cyclic bending applications at HCF lives. This comparison was completed using both experimental results and finite element methods, among which was the newly launched software: fe-safe^{TM}. The fatigue analysis of the materials was accompanied by a study on the different ways steel and composites fail, which lead to the conclusion that composites have a better fatigue life than metals under stresses related to HCF, while metals perform better than composite under stresses related to LCF.

The manufacturing process of a component is very crucial as it involves all the design parameters, and property modifications that will produce an appropriate component for aftermarket applications. In the case of leaf springs as suspension systems, the manufacturing approach differs for each material. From the research completed on the manufacturing processes of composite and steel leaf springs, it was obvious that composites are easier and less costly to manufacture. In addition to their less complicated and expensive production, the different failure modes of composites, and their failure through damage accumulation make composites a material that allows for repairs, as well as failure prediction in leaf springs, which are not feasible when the leaf springs are manufactured from steel.

Leaf springs have a typical life of 100,000 cycles, which lies in the HCF region. From the findings of this research, it can be concluded that S2 glass fiber/epoxy is an appropriate material for the manufacturing of leaf springs. Adding to the equation its low density, S2 glass fiber/epoxy will not only give high performance components but also light components that will help minimize the total vehicle weight which may have a positive effect in fuel emission reduction, rendering all type of vehicles with composite leaf springs more environmentally friendly, and a less expensive commodity for their drivers.

The spring ratio is a determining parameter in leaf spring design. It connects suspension performance to load carrying capacity of the suspension, and therefore the vehicle. The capacity of a composite material to have different volume fractions of the two constituents and direct the orientation of the major load carrying constituents, the fibers, to affect the flexibility of the component, makes S2 glass fiber/epoxy even more efficient as a material for leaf spring manufacturing. Strength and stiffness of the composite may also be further combined to create leaf spring assemblies of fewer leaves than those of the existent steel assemblies [14]. As a result, the suspension weight may decrease even more.

This research has shown that S2 glass fiber/epoxy is an appropriate material for leaf spring manufacturing with superior properties to steel, and the possibility of entering the aftermarket with a competitive price. At present composites have not conquered the aftermarket mainly due to their high prices. Market research reveals that a typical steel leaf spring of $88 will have a price of $295 if made from a composite material. The reason why composite leaf springs tend to be much more expensive than steel ones, does not depend on the actual manufacturing process but on the lack of developed technology and designs. Steel leaf spring designs and technology has been available to the industry for many decades and there is no further need for these industries to invest on a research and development sector for their product. On the contrary, GFRPs are still a new product, constantly under investigation and development, offering a vast range of alternatives to optimize the design of structures. In the leaf spring industry design of suspension with composite materials is still under development, especially when there are still parts of the spring that are not made of composite material but of steel. As a result, investment in a research and development department for the composite leaf spring industry, together with a strong advertising campaign that will persuade car mechanics of the advantages of a GFRP suspension, made from a material which in layman terms is referred to as “plastic” and consequently is explained as a material of less strength than metals, are among the reasons due to which composite springs are expensive.

Composites have already replaced metals in many areas of the industry and medicine, and there is constant research for their development. Whenever a light structure, a structure that will not fail because of corrosion, or a structure that may be repaired if needed, is in question, a composite material is involved and replaces a metal. FRPs, whether their fibers are carbon, Kevlar or glass, are very popular in many application that involve transportation means on land, air or water. Modern bicycles, boats, racing cars and aerospace or aviation vessels, all contain at least one FRP component. With the introduction of polymers in air springs, and GFRP leaf springs in sports cars, such as the Corvette, the time has arrived for the heavy-duty suspension industry to take the step and dynamically introduce composites to the heavy-vehicle leaf spring market.

However, further experimental research could help this step forward giving answers to many questions. Interlaminar delamination, as a major cause of failure in composite laminates should be investigating through experimental non-destructive techniques to determine how it is caused, at which fatigue lives it is more obvious and dangerous, as well as possible means to prevent it. In a similar manner, damage accumulation in composite laminates may be further investigated to define a critical number of life cycles where damage accumulation increases rapidly, the regions of the composite damage more intensely demonstrates itself, as well as a comparison of experimental analysis to damage accumulation models. In addition to the above, fatigue tests of GFRPs at lives greater than 100,000 cycles may give insight in the performance of these materials and their appropriateness for applications other than suspension systems. Finally on the subject of composite leaf springs, research on the design of a leaf, based on the shape, number of cycles, stacking sequence and leaf count may open new doors in the composite leaf spring industry.

REFERENCES

[1] Erjavec, J. Automotive technology. A Systems Approach. Fourth. New York: Thomson Delmar Learning, 2005.

[2] Gillespie, T. D. Fundamentals of vehicle dynamics. Warrendale: Society of Automotive Engineers, Inc., 1992.

[3] Jain, K. K. and Asthana, R. B. Automobile engineering. New Delhi: Tata McGraw-Hill, 2002.

[4] Sanders, T. Laminated Springs: Leaf Spring Design. Wexford College Press, 2007.

[5] "SAE Manual on Design and Application of Leaf Springs." Warrendale: Society of Automotive Engineers, Inc, 1982.

[6] Lorenz, A. GKN: The making of a Business 1759-2009. 1st. Wiley & Sons, Inc, 2010.

[7] Strong, A. B. Fundamentals of composite manufacturing: materials, methods and applications. 2nd. Michigan: SME, 2008.

[8] Matthews, F. L., et al. Finite Element Modelling of Composite Materials and Structures. Cambridge: Woodhead Plublishing Ltd., 2000.

[9] Anderson, R. N. Manufacturing Process for Production of Composite Leaf Spring for 5-ton Truck. No. 12999. Ciba-Geigy Coorporation. Fountain Valley, 1984.

[10] Arslan, N., Professor of Mechanical Engineering at Balikesir University, R&D Department Yaysan S.A. Roselita Fragoudakis. September 2010.

[11] Owen, M. J. "Fatigue Damage in Glass-Fiber-Reinforced Plastics." Krock. Composite Materials (Volume 5: Fracture and Fatigue). Ed. Broutman, L.J. New York: Academic Press, 1974. 313-340.

[12] Al-Qureshi, H. A. "Automobile leaf springs from composite materials." Journal of Materials Processing Technology 118 (2001): 56-61.

[13] Shokrieh, M. M. and Rezaei, D. "Analysis and Optimizaion of a composite Leaf Spring." Composite Structures 60 (2003): 317-325.

[14] Rajendran, I. and Vijayarangan, S. "Optimal Design of a Composite Leaf Spring Using Geneticc Algorithms." Computers and Structures 79 (2001): 1121-1129.

[15] Papadopoulos, C. Leaf Spring Production Technician at AUTOKINITISTIKI S.A. Roselita Fragoudakis. July 2010.

[16] Bringas, J. E., ed. CASTI Metals Black Book. Edmonton: CASTI Publishing Inc., 2000.

[17] AUTOKINITISTIKI.gr. <www.autokinitistiki.gr>.

[18] Tekeli, S. "Enhancement of Fatigue Strength of SAE 9245 Steel by Shot Peening." Materials Letters 57 (2002): 604-608.

[19] Wick, A., et al. "Effect of Shot Peening Parameters on the Surface Characteristics of Differently Heat Treated AISI 4140." 7th International Coference on Shot Peening (ICSP 7). Warsaw, 1999. 42-53.

[20] Shaw, B. A., et al. "The role of residual stress on the fatigue strength of high performance gearing." International Journal of Fatigue 25 (2003): 1279-1283.

[21] Bannantine, J. A., et al. Fundamentals of Metal Fatigue Analysis. New Jersey: Prentice-Hall, Inc, 1990.

[22] Bringas, J. E., ed.The Metals Black Book: Ferrous Metals. Ed. Bringas, J. E. Second. CASTI Publishing, Inc., 1995.

[23] Porter, D. A. and Easterling, K. E. Phase Transformations in Metals and Alloys. Second. Chapman & Hall, 1992

[24] Barett, C. and Massalski, T. B. Structure of Metals: Cruystaloographic Methods, Principles, and Data. Third revised. New York: Pergamon Press, 1980.

[25] Heat Treater's Guide: Practices and Procedures for Iron and Steels. 2nd. ASM International, 1995.

[26] Fragoudakis, R., et al. "Fatigue Assessment and Failure Analysis of Shot Peened Leaf Springs." 2nd International Conference of Engineering Against Fracture (ICEAF II). Mykonos, 2011.

[27] Todinov, M. T. "Residual stresses at the surface of automotive suspension springs." Journal of Materials Science 35 (2000): 3313-3320.

[28] Suresh, S. Fatigue of Metals. Ed. Cahn, R. W., Davis, E. A. and Ward, I. M. Cambridge: Cambridge University Press, 1991.

[29] Verhoeven, J. D. Fundamental sof physical metallurgy. New York: John Wiley & Sons, Inc., 1975.

[30] Verhoeven, J. D. Steel Metallurgy for the non-Metallurgist. Ohio: ASN International, 2007.

[31] Vander Voort, G. F. "Macroscopic Examination Procedures." Metallography in Failure Analysis. Houston: McCall French, 1977. 33-63.

[32] Barson, J.M. and Rolfe, S. T. Fracture and Fatigue Control in Structures: Applications of Fracture Mechanics. 3rd. Philadelphia: ASTM International, 1999.

[33] Stephens, R. I., et al. Metal Fatigue in Engineering. New York: Wiley & Sons, Inc, 2001.

[34] Fatemi, A. and Yang, L. "Cumulative fatigue damage and life prediction theories: a survey of the state of the art for homogeneous materials." International Journal of Fatigue 20.1 (1998): 9-34.

[35] Osgood, C. C. Fatigue Design. New York: Wiley-Interscience, 1970.

[36] Farrahi, G. H., Lebrun, J. L. and Couratin, D. "Effect of Shot Peening on Residual Stress and Fatigue Life of a Spring Steel." Fatigue Fracture of Engineering Materials and Structures 18.2 (1995): 211-220.

[37] Menig, Rainer, et al. "Residual Stress Relaxation and Fatigue Strength of AISI 4140 under Torsional Loading after Conventional Shot Peening, Stress Peening and Warm Peening." 8th International Conference on Shot Peening (ICSP-8). Weinheim: WILEY-VCH Verlag GmbH & Co. KGaA, 2003. 311-316.

[38] Capello, E., et al. "Relaxation of resiual stresses induced by turning and shot peening on steels." J. Strain Analysis 39.3 (2004): 285-290. Carlson, Harold. Spring Designer's Handbook. Vol. 1. New York: M. Dekker, 1978.

[39] Torres, M. A. S. and Voorwald, H. J. C. "An evaluation of shot peening, residual stress and stress relaxation on the fatigue life of AISI 4340 steel." International Journal of Fatigue 24 (2002): 877-886.

[40] Iwata, N., et al. "Effect of shot peening on fatigue fracture for an as quenched martensitic steel." Materials Science and Technology 18 (2002): 629-632.

[41] Bergström, J. and Torsten E. "Relaxation of Shot Peening Induced Compressive Stress During Fatigue of Notched Steel Samples." Second International Conference on Shot Peening . Chicago: American Shot Peening Society, 1984. 241-248.

[42] Aggarwal, M. L., et al. "A stress approach model for predictions of fatigue life

by shot peening of EN45A spring steel." International Journal of Fatigue 28 (2006): 1845-1853.

[43] Rustem, S. L., et al. "Increasing the Durability of Automobile Springs." Institute of Technology of the Moscow Automobile Factory 3, 1972.

[44] Farfran, S., et al. "High cycle fatigue, low cycle fatigue and failure modes of a carburized steel." International Journal of Fatigue 26 (2004): 673-678.

[45] Asi, O., et al. "The relationship between case depth and bending fatigue strength of gas carburized SAE 8620 steel." Surface & Coatings Technology 201 (2007): 5979-5987.

[46] Asi, O., et al. "The effect of high temperature gas carburizing on bending fatigue strength of SAE 8620 steel." Materials and Design 30 (2009): 1792-1797.

[47] Cammett, J. T., et al. "The Effect of Shot Peening Coverage on Residual Stress, Cold Work, and Fatigue in a Nickel-base Superalloy." 9th International Conference on Shot Peening (ICSH9). Paris: IITT-International, 2005. 267-272.

[48] "SAE J443: (R) Proceedures for Using Standard Shot Peening Almen Strip." 2010.

[49] Fathallah, R., et al. "High cycle fatigue behavior prediction of shot-peened parts." International Journal of Fatigue 26 (2004): 1053-1067.

[50] Al-Obaid, Y. F. "Shot peening mechanics: experimental and theoretical analysis." Mechanics of Materials 19 (1995): 251-260.

[51] Guagliano, M. "Relating Almen intensity to residual stresses induced by shot peening: a numerical approach." Journal of Materials Processing Technology 110 (2001): 277-286.

[52] Guagliano, M. and Verhani, L. "An approach for prediction of fatigue strength of shot peened components." Engineering Fracure Mechanics 71 (2004): 501-512.

[53] Diepart, C. P. "Moddeling of Shot Peening Residual Stresses - Practical Applications." Materials Science Forum 163-165 (1994): 457-464.

[54] Boyer, H. E., ed. Atlas of Fatigue Curves. Ohio: American Society for Metals, 1986.

[55] Callister, W. D., Jr. Materials Science and Engineering: An Introduction. 5th.

New York: Wiley & Sons, Inc., 2000.

[56] Hashin, Z. and Rotem, A. "A Cumulative Damage Theory of Fatigue Failure." Materials Science and Engineering 34 (1978): 147-160.

[57] Christensen, R. M. "falurecriteria.com." 18 October 2008. falurecriteria.com. 18 March 2010 <www.falurecriteria.com>.

[58] Kaechele, L. E. "Review and Analysis of Cumulative Damage Theories." The Rand Coorporation, 1963.

[59] Salkind, M. J. "Fatigue of Composites." Composite Materials: Testing and Design (Second Conference) STP 497. Philadelphia: American Society for Testing and Materials, 1972. 143-169.

[60] Miner, M. A. "Cumulative Damage in Fatigue." Journal of Applied Mechanics 12.3 (1945): A159-164.

[61] Epaarachchi, J. A. "A study on estimation of damage accumulation of glass fiber reinforced plastic (GFRP) composites under a block loading situation." Composite Structures 75 (2006): 88-92.

[62] Broutman, L. J. and Sahu, S. "A New theory to Predict Cumulative Fatigue Damage in Fiberglass Reinforced Plastics." Composite Materials: Testing and Design (Conference), ASTM STP 497. American Society for Testing and Materials, 1972. 170-188.

[63] Agarwal, B. D., et al. Anaysis and Performance of Fiber Composites. New Jersey: John Wiley &Sons, 2006.

[64] Wang, A. S. D., et al. "Effects of Proof Tests on the Strength and Fatigue Life of a Unidirectional Composite." Fatigue of Fibrous Composite Materials, ASTM STP 723. Ed. J. B. Wheeler. American Society for Testing and Materials, 1981. 116-132.

[65] Christensen, R. M. "A physically based cumulative damage formalism." Internatioal Journal of Fatigue 30 (2008): 595-602.

[66] "R.R Moore: Rotating Beam Fatigue Testing System." 2004. <www.instron.com>.

[67] "ISO 1143." Metallic materials -- Rotating bar bending fatigue testing. 2010.

[68] Mogul, J. "Metallographic Characterization of Fatigue Failure Origin Areas." Metallography in Failure Analysis. Houston: McCall French, 1977. 97-120.

[69] Matlock, D. K., et al. " Surface Processing to Improve the Fatigue Resistance of Advanced Bar Steels for Automotive Applications." Materiasl Research 8.4 (2005): 453-459.

[70] Hull, D. Fractography: observing, measuring, and interpreting fracture surface topography. Cambridge: Cambridge University Press, 1999.

[71] Tisza, M. Physical Metallurgy for Engineers. Ohio: ASM International, 2001.

[72] "ISO/CD 88265." Metallic Materials-conversion of hardness values, ISO standard. 2003

[73] Murthy, et al. Weibull Models. New Jersey: Wiley & Sons, Inc., 2004.

[74] Kelly, A. Concise Encyclopedia of Composite Materials: Revised Edition. Elsevier Science, Ltd., 1994.

[75] Fragoudakis, R. and Saigal, A. The effect of carburizing on the fatigue life of 4130 steel. Proceedings of 2010 TMS Annual Meeting, EPD Congress 2010, Seattle, WA 2010, pp. 463-70.

[76] “fe-safe User Manual.” Vol. 2. Safe Technologies. UK, 2009.

[77] Understanding Fatigue Analysis. <www.eng.cam.ac.uk/DesignOffice/cad/proewild3/usascii/proe/promec/online/fatigue>.

[78] Eckold, G. Deasign and Manufacture of Composite Structures. Cambridge: Woodhead Publishing Ltd., 1994.

[79] Nawy, E. G. Fundamentals of high-performance concrete. Second. Canada: John Wiley & Sons, 2001.

[80] Staab, G. H. Laminar Composites. Boston: Butterworth-Heinemann, 1999.

[81] Jones, R. M. Mechanics of Composite Materials. Second Edition. Philadelphia: Taylor & Francis, Inc., 1999.

[82] Kollar, L. P. and Springer, G.S. Mechanics of Composite Structures. Cambridge: Cambridge University Press, 2003.

[83] Kaw, A. K. Mechanics of Composite Materials. Florida: CRC Press LLC, 1997.

[84] Owen, M. J. "Fatigue Damage in Glass-Fiber-Reinforced Plastics." Krock. Composite Materials (Volume 5: Fracture and Fatigue). Ed. Broutman, L. J. New York: Academic Press, 1974. 313-340.

[85] Broutman, L. J. and Sahu, S.A. "Progressive Damage of a Glass Reinforced Plastic During Fatigue." 24th Annual Technical Conference, Reinforce Plastics/Composites Div. SPI, 1969.

[86] Sridharan, S. Delamination Behavior of Composites. Cambridge: Woodhead Publishing Ltd., 2008.

[87] Naik, N. K. and. Shembekar, P. S. "Elastic Behavior of Woven Fabric Composites: I-Lamina Analysis." Journal of Composite Materials 26.15 (1992): 2196-2225.

[88] Shembekar, P. S. and Naik, N. K. "Elastic Behavior of Woven Fabric Composites:II-Laminate Analysis." Journal of Composite Materials 26.15 (1992): 2226-2246.

[89] ASTM Standard D790-10, 2010, "Flexural Properties of Unreinforced and Reinforced Plastics and Electrical Insulating Materials", ASTM International, West Conshohocken, PA, 2010, DOI:10.1520/D0790-10.

[90] Firehole Technologies, Inc. "Helius: Fatigue, Theory Manual." Helius: Fatigue for fe-safe^{TM}. Firehole Technologies, Inc., September 2010.

[91] Hashin, Z. and Rotem, A."A fatigue failure criterion for fiber reinforced materials." Journal of Composite Materials 7 (1973): 448-464.

[92] Zhurkov, S. "Kinetic Concept of the Strength of Solids." Internaional Journal of Fracture (1965): 311-323.

[93] Zhurkov, S. and Kuksenko, V. "The micromechanics of polymer fracture." International Journal fo Fracture 11 (1975): 629-639.

[94] Coleman, B. and Marquardt, D. "Time Dependence of Mechanical Breakdown in Bundles of Fibers. II. The infinite ideal bundle under linearly increasing loads." Journal of Applied Physics 28 (1957): 1065-1067.

[95] Cleman, B. "Time Dependence of Mechanical Breakdown in Bundles of Fibers. I. Constant Total Load." Journal of Applied Physics 28 (1957): 1058-1064.

[96] Regel, V.R. and Tamuzh, V.P. "Fracture and Fatigue of Polymers and Composites (survey)." Mechanics of Composite Materials 13 (1977): 392-408.

[97] Tomashevskii, E.E., et al. "Kinetic Micromehanics of Polymer Fracture." International Journal of Fracture 11 (1975): 803-815.

[98] Kireenko, O.F., et al. "Polymer Fractography and Fracture Kinetics 2. The

Relationship between Fracture Surface Relief ad the Dependence of Strength on Time and Temperature." Mechanics of Composite Materials 7 (1971): 193-198.

[99] Regel, V.R., et al. "Investigation of the Processes of Thermal and Mechanical Degradation of Polymers using Mass Spectrometers. Review." Mechanics of Composite MAterials 11 (1975): 13-26.

[100] Regel, V. "Kinetic Theory of Strength as a Scientific Basis for predicting the lifetime of Polymers under Load." Mechanis of Composite Materials 7 (1971): 82-93.

[101] Kireenko, O.F. , et al. "Polymer Fractography and Fracture Kinetics 3.Fractographic Method of Estimaing the Local Heating at the Ends of Cracks in Cyclically Loaded Polymers." Mechanics of Composite Materials 7 (1971): 776-780.

[102] Sauer, J., et al. "Influence of Molecular Weight on Fatigue Behavior of Polyethelene and Polyestyrene." Polymer Engineering & Science 17 (1977): 246-250.

[103] Sauer, J. and Richardson, G. "Fatigue of Polymers." International Journal of Fracture 16 (1980): 499-532.

[104] Argon, A. S. "Statistical Aspects of Fracture." Composite MAterials, Vol. 5, Fracture and Fatigue. Ed. Broutman, L. J. New York: Acaemic Press, 1974. 154-189.

[105] Wheeler, J. B., ed. Fatigue of Fibrous Composite Materials. Vol. STP 723. Baltimore: American Society for Testing Materias, 1981.

[106] Naik, N. K. "Woven-fiber thermoset composites." Fatigue in Composites. Ed. Harris, B. Cambridge: Woodhead Publishing Ltd., 2003. 296-313.

[107] Curtis, P. T. and Moore, B.B. "A comparison of the Fatigue Performance of Woven and Non-Woven CFRP in Reversed Axial Loading." International Journal of Fatigue 9.2 (1987): 67-78.

[108] Hayashi, T. "Development on New Material Properties by Hybrid Composition." Fukugu Zairyo (Composite Materials) 1 (1972): 18-26.

[109] Phillips, L. N. "The Hybrid Effect - Does it Exist?" Composites 7 (1976): 7-14.

[110] Zwben, C. "Tensile Strength of Hybrid Composites." Journal of Materials Science 12 (1977): 1325-1333.

[111] Marom, G., et al. "Hybrid effects in Composites: Conditions for Positive or Negative Effects versus Rule of Mixures Behavior." Journal of MAterials Science 13 (1978): 1419-1425.

[112] Leevy, G. and Cao, K. Evaluation of a Multi-Leaf Hybrid Springs for Automotive Suspensions. Technical Paper. Visteon Corporation. Detroit: SAE International, 2004.

[113] Meatto, F., et al. Method of Producing a Hybrid Leaf Spring. US: Patent 6,461,455 B1. 8 Oct. 2002.

[114] Mouleeswaran, S.K. and Sabapathy V. "Analytical and experimental studies on fatigue life predictions of steel and composite multi-leaf spring for light passenger vehicles using life data analysis". Materials Science, 2007, 13.

[115] Mahdi, E., et al. "Light Composite Elliptic Springs for Vehicle Suspension." Comosite Structures 75 (2006): 24-28.

APPENDIX A

MATERIAL PROPERTIES

STEEL

AISI 4130 CF

Chemical Composition in wt%

C	Si	Mn	P	S	Cr	Mo	Fe
0.28-0.33	**0.15-0.30**	**0.4-0.6**	**0.035**	**0.04**	**0.9-1.1**	**0.15-1.25**	**97-98**

Properties

Density	7.85 g/cm^3
Modulus of Elasticity	205 GPa
Poisson's Ratio	0.290
Ultimate Tensile Strength	676 MPa
Fatigue Strength Coefficient (σ_f')	1695 MPa
Fatigue Ductility Coefficient (ε_f')	0.890
Cyclic Strain Hardening Exponent (n')	0.149
Cyclic Strain Hardening Coefficient (K)	1428
Fatigue Strength Exponent (b)	-0.081
Fatigue Ductility Exponent (c)	-0.690
Coefficient of Thermal Expansion (α)	11x10^{-6} C^{o-1}

AISI 6150

Chemical Composition in wt%

C	Si	Mn	P	S	Cr	Mo	Fe
0.56-0.64	**2**	**0**	**0.035**	**0.04**	**-**	**-**	**96**

Properties

Density	7.85 g/cm^3
Modulus of Elasticity	210 GPa
Poisson's Ratio	0.290
Ultimate Tensile Strength	1240 MPa
Fatigue Strength Coefficient (σ_f')	1860 MPa
Fatigue Ductility Coefficient (ε_f')	0.370
Cyclic Strain Hardening Exponent (n')	0.150
Cyclic Strain Hardening Coefficient (K)	2046
Fatigue Strength Exponent (b)	-0.087
Fatigue Ductility Exponent (c)	-0.580
Coefficient of Thermal Expansion (α)	12x10^{-6} C^{o-1}

COMPOSITES

FIBERS

E-glass

Chemical Composition in wt%

SiO_2	Al_2O_3	CaO	BaO	MgO	NaO_2
54.3	**15.2**	**17.2**	**8**	**4.70**	**0.60**

Properties

Density	2.55 g/cm^3
Modulus of Elasticity	72.4 GPa
Poisson's Ratio	0.220
Modulus of Rigidity	30.3 GPa
Coefficient of Thermal Expansion (α)	5.1x10^{-6} C^{o-1}

S2-glass

Chemical Composition in wt%

SiO_2	**Al_2O_3**	**CaO**	**BaO**	**MgO**	**NaO_2**	**B_2O_3**	**FeO**	**Other**
64.2	**24.8**	**0.01**	**0.20**	**10.27**	**0.27**	**0.01**	**0.210**	**0.03**

Properties

Density	2.00 g/cm^3
Modulus of Elasticity	80 GPa
Poisson's Ratio	0.200
Modulus of Rigidity	33.3 GPa
Coefficient of Thermal Expansion (α)	4.9x10^{-6} C^{o-1}

MATRIX

Properties

Modulus of Elasticity	3.15 GPa
Poisson's Ratio	0.350
Modulus of Rigidity	1.30 GPa
Coefficient of Thermal Expansion (α)	53x10^{-6} C^{o-1}

E GLASS FIBER/EPOXY

Properties

Density	2.10 g/cm^3
Volume Fraction of fiber	0.55
Modulus of Elasticity (E_{11})	39 GPa
Modulus of Elasticity (E_{22})	8.60 GPa
Modulus of Elasticity (E_{33})	8.60 GPa
Poisson's Ratio (ν_{12})	0.28
Poisson's Ratio (ν_{13})	0.28
Poisson's Ratio (ν_{23})	0.45
Modulus of Rigidity (G_{12})	3.80 GPa
Modulus of Rigidity (G_{13})	3.80 GPa
Modulus of Rigidity (G_{23})	2.97 GPa
Coefficient of Thermal Expansion (α_{11})	7.0×10^{-6} C^{o-1}
Coefficient of Thermal Expansion (α_{22})	21×10^{-6} C^{o-1}
Coefficient of Thermal Expansion (α_{33})	21×10^{-6} C^{o-1}
Longitudinal Tensile Strength	1080 MPa
Transverse Tensile Strength	39 MPa
Longitudinal Compressive Strength	620 MPa
Transverse Compressive Strength	128 Mpa
Shear Strength	60 MPa

S2 GLASS FIBER/EPOXY

Properties

Density	2.00 g/cm^3
Volume Fraction of Fibers	0.55
Modulus of Elasticity (E_{11})	43 GPa
Modulus of Elasticity (E_{22})	8.90 GPa
Modulus of Elasticity (E_{33})	8.90 GPa
Poisson's Ratio (ν_{12})	0.27
Poisson's Ratio (ν_{13})	0.27
Poisson's Ratio (ν_{23})	0.45
Modulus of Rigidity (G_{12})	4.50 GPa
Modulus of Rigidity (G_{13})	4.50 GPa
Modulus of Rigidity (G_{23})	3.07 GPa
Coefficient of Thermal Expansion (α_{11})	$5.0\text{x}10^{-6}$ C^{o-1}
Coefficient of Thermal Expansion (α_{22})	$26\text{x}10^{-6}$ C^{o-1}
Coefficient of Thermal Expansion (α_{33})	$26\text{x}10^{-6}$ C^{o-1}
Longitudinal Tensile Strength	2000 MPa
Transverse Tensile Strength	49 MPa
Longitudinal Compressive Strength	1240 MPa
Transverse Compressive Strength	158 Mpa
Shear Strength	62 MPa

APPENDIX B

EQUATIONS FOR COMPOSITE MATERIALS

$$\begin{Bmatrix} \sigma'_x \\ \sigma'_y \\ \tau'_{xy} \end{Bmatrix} = [T_\sigma] \begin{Bmatrix} \sigma_x \\ \sigma_y \\ \tau_{xy} \end{Bmatrix} \tag{B1}$$

$$\begin{Bmatrix} \varepsilon'_x \\ \varepsilon'_y \\ \gamma'_{xy} \end{Bmatrix} = [T_\varepsilon] \begin{Bmatrix} \varepsilon_x \\ \varepsilon_y \\ \gamma_{xy} \end{Bmatrix} \tag{B2}$$

where

$$[T_\sigma] = \begin{pmatrix} m^2 & n^2 & 2mn \\ n^2 & m^2 & -2mn \\ -mn & mn & m^2 - n^2 \end{pmatrix} \tag{B3}$$

$$[T_\varepsilon] = \begin{pmatrix} m^2 & n^2 & mn \\ n^2 & m^2 & -mn \\ -2mn & 2mn & m^2 - n^2 \end{pmatrix} \tag{B4}$$

where $m = \cos\theta$ and $n = \sin\theta$.

RULE OF MIXTURES

$$E_{11} = E_f \upsilon_f + E_m \upsilon_m \tag{B5}$$

$$E_{22} = \frac{E_f E_m}{E_m \upsilon_f + E_f \upsilon_m} \tag{B6}$$

$$G_{12} = \frac{G_f G_m}{\upsilon_f G_m + \upsilon_m G_f} \tag{B7}$$

$$v_{12} = \upsilon_f v_f + \upsilon_m v_m \tag{B8}$$

where the subscript *f* denotes fiber properties, *m* matrix properties, and υ is the volume fraction of each constituent

CLASSICAL LAMINATION THEORY (CLT)

Strains in plate loaded laterally

$$\varepsilon_x = \frac{\partial U}{\partial x} = \frac{\partial U_0}{\partial x} + z \tag{B9}$$

$$\varepsilon_y = \frac{\partial V}{\partial y} = \frac{\partial V_0}{\partial y} + z\frac{\partial \Psi}{\partial y} \tag{B10}$$

$$\varepsilon_z = \frac{\partial W}{\partial z} = 0 \tag{B11}$$

$$\gamma_{xz} = \frac{\partial U}{\partial z} + \frac{\partial W}{\partial x} = \left(\frac{\partial W_0}{\partial x} + \Phi\right) = 0 \tag{B12}$$

$$\gamma_{yz} = \frac{\partial V}{\partial z} + \frac{\partial W}{\partial y} = \left(\frac{\partial W_0}{\partial y} + \Psi\right) = 0$$

(B13)

$$\gamma_{xy} = \frac{\partial U}{\partial y} + \frac{\partial V}{\partial x} = \left(\frac{\partial U_0}{\partial y} + \frac{\partial V_0}{\partial x}\right) + z\left(\frac{\partial \Phi}{\partial y} + \frac{\partial \Psi}{\partial x}\right) = 0 \tag{B14}$$

$$U = U_0(x, y) + z\Phi(x, y) \tag{B15}$$

$$V = V_0(x, y) + z\Psi(x, y) \tag{B16}$$

$$W = W_0(x, y) \tag{B17}$$

Mid-surface Strains and curvatures

$$\{\varepsilon^0\} = \begin{Bmatrix} \varepsilon_x^0 \\ \varepsilon_y^0 \\ \gamma_{xy}^0 \end{Bmatrix} = \begin{Bmatrix} \dfrac{\partial U_0}{\partial x} \\ \dfrac{\partial V_0}{\partial y} \\ \dfrac{\partial U_0}{\partial y} + \dfrac{\partial V_0}{\partial x} \end{Bmatrix} \tag{B18}$$

$$\begin{Bmatrix} \kappa_x \\ \kappa_y \\ \kappa_{xy} \end{Bmatrix} = \begin{Bmatrix} \dfrac{\partial \Phi}{\partial x} \\ \dfrac{\partial \Psi}{\partial y} \\ \dfrac{\partial \Phi}{\partial y} + \dfrac{\partial \Psi}{\partial x} \end{Bmatrix} \tag{B19}$$

$$\begin{Bmatrix} \varepsilon_x \\ \varepsilon_y \\ \gamma_{xy} \end{Bmatrix} = \begin{Bmatrix} \varepsilon_x^0 \\ \varepsilon_y^0 \\ \gamma_{xy}^0 \end{Bmatrix} + z \begin{Bmatrix} \kappa_x \\ \kappa_y \\ \kappa_{xy} \end{Bmatrix} \tag{B20}$$

Constitutive Relationship

$$\begin{Bmatrix} \sigma_x \\ \sigma_y \\ \tau_{xy} \end{Bmatrix}_k = [\bar{Q}]_k \left(\begin{Bmatrix} \varepsilon_x^0 \\ \varepsilon_y^0 \\ \gamma_{xy}^0 \end{Bmatrix} + z \begin{Bmatrix} \kappa_x \\ \kappa_y \\ \kappa_{xy} \end{Bmatrix} \right) \tag{B21}$$

$$[\bar{Q}]_k = \begin{bmatrix} \bar{Q}_{11} & \bar{Q}_{12} & \bar{Q}_{13} \\ \bar{Q}_{21} & \bar{Q}_{22} & \bar{Q}_{23} \\ \bar{Q}_{31} & \bar{Q}_{32} & \bar{Q}_{33} \end{bmatrix} \tag{B22}$$

Forces and Moments

$$\begin{Bmatrix} N_x \\ N_y \\ N_{xy} \end{Bmatrix} = \sum_{k=1}^{N} \int_{z_{k-1}}^{z_k} \begin{Bmatrix} \sigma_x \\ \sigma_y \\ \tau_{xy} \end{Bmatrix}_k dz \qquad \text{(B23)}$$

$$\begin{Bmatrix} Q_x \\ Q_y \end{Bmatrix} = \sum_{k=1}^{N} \int_{z_{k-1}}^{z_k} \begin{Bmatrix} \tau_{xz} \\ \tau_{yz} \end{Bmatrix}_k dz \qquad \text{(B24)}$$

$$\begin{Bmatrix} M_x \\ M_y \\ M_{xy} \end{Bmatrix} = \sum_{k=1}^{N} \int_{z_{k-1}}^{z_k} \begin{Bmatrix} \sigma_x \\ \sigma_y \\ \tau_{xy} \end{Bmatrix}_k dz \qquad \text{(B25)}$$

$$\begin{Bmatrix} N_x \\ N_y \\ N_{xy} \end{Bmatrix} = \sum_{k=1}^{N} [\bar{Q}]_k \left(\int_{z_{k-1}}^{z_k} \begin{Bmatrix} \varepsilon_x^0 \\ \varepsilon_y^0 \\ \gamma_{xy}^0 \end{Bmatrix} dz + \int_{z_{k-1}}^{z_k} z \begin{Bmatrix} \kappa_x \\ \kappa_y \\ \kappa_{xy} \end{Bmatrix} dz \right) \qquad \text{(B26)}$$

$$\begin{Bmatrix} M_x \\ M_y \\ M_{xy} \end{Bmatrix} = \sum_{k=1}^{N} [\bar{Q}]_k \left(\int_{z_{k-1}}^{z_k} z \begin{Bmatrix} \varepsilon_x^0 \\ \varepsilon_y^0 \\ \gamma_{xy}^0 \end{Bmatrix} dz + \int_{z_{k-1}}^{z_k} z^2 \begin{Bmatrix} \kappa_x \\ \kappa_y \\ \kappa_{xy} \end{Bmatrix} dz \right) \qquad \text{(B27)}$$

$$\begin{Bmatrix} N \\ \cdots \\ M \end{Bmatrix} = \begin{pmatrix} A & \vdots & B \\ \cdots & \cdots & \cdots \\ B & \vdots & D \end{pmatrix} \begin{Bmatrix} \varepsilon^0 \\ \cdots \\ k \end{Bmatrix} \qquad \text{(B28)}$$

Extensional Stiffness Matrix

$$\left[A_{ij}\right] = \sum_{k=1}^{N}\left[\bar{Q}_{ij}\right]_k t_k \tag{B29}$$

Extension-Bending Coupling Matrix

$$\left[B_{ij}\right] = \sum_{k=1}^{N}\left[\bar{Q}_{ij}\right]_k t_k \bar{z}_k \tag{B30}$$

Bending Stiffness Matrix

$$\left[D_{ij}\right] = \sum_{k=1}^{N}\left[\bar{Q}_{ij}\right]_k \left(t_k {\bar{z}_k}^2 + \frac{{t_k}^3}{12}\right) \tag{B31}$$

Thermal Effects

$$\begin{Bmatrix} \sigma_x \\ \sigma_y \\ \tau_{xy} \end{Bmatrix}_k = [\bar{Q}]_k \left(\begin{Bmatrix} \varepsilon_x^0 \\ \varepsilon_y^0 \\ \gamma_{xy}^0 \end{Bmatrix} + z \begin{Bmatrix} \kappa_x \\ \kappa_y \\ \kappa_{xy} \end{Bmatrix} - \begin{Bmatrix} \alpha_x \\ \alpha_y \\ \alpha_{xy} \end{Bmatrix}_k \Delta\mathrm{T} \right) \tag{B32}$$

$$\begin{Bmatrix} \sigma_x \\ \sigma_y \\ \tau_{xy} \end{Bmatrix}_k^T = [\bar{Q}]_k \begin{Bmatrix} \alpha_x \\ \alpha_y \\ \alpha_{xy} \end{Bmatrix}_k \Delta\mathrm{T} \tag{B33}$$

$$\begin{Bmatrix} N \\ \cdots \\ M \end{Bmatrix} = \begin{pmatrix} A & \vdots & B \\ \cdots & \cdots & \cdots \\ B & \vdots & D \end{pmatrix} \begin{Bmatrix} \varepsilon^0 \\ \cdots \\ k \end{Bmatrix} - \begin{Bmatrix} N^T \\ \cdots \\ M^T \end{Bmatrix} \quad \rightarrow \quad \begin{Bmatrix} \widehat{N} \\ \cdots \\ \widehat{M} \end{Bmatrix} = \begin{pmatrix} A & \vdots & B \\ \cdots & \cdots & \cdots \\ B & \vdots & D \end{pmatrix} \begin{Bmatrix} \varepsilon^0 \\ \cdots \\ k \end{Bmatrix} \tag{B34}$$

FAILURE CRITERIA

Maximum Stress Criterion

$$-(\sigma_1^C)_{ult} < \sigma_1 < (\sigma_1^T)_{ult} \quad \text{or}$$

$$-(\sigma_2^C)_{ult} < \sigma_2 < (\sigma_2^T)_{ult} \quad \text{or}$$

$$-(\tau_{12})_{ult} < \tau_{12} < (\tau_{12})_{ult} \tag{B35}$$

Maximum Strain Criterion

$$-(\varepsilon_1^C)_{ult} < \varepsilon_1 < (\varepsilon_1^T)_{ult} \quad \text{or}$$

$$-(\varepsilon_2^C)_{ult} < \varepsilon_2 < (\varepsilon_2^T)_{ult} \quad \text{or}$$

$$-(\gamma_{12})_{ult} < \gamma_{12} < (\gamma_{12})_{ult} \tag{B36}$$

Tsai-Hill failure Criterion

$$\frac{{\sigma_1}^2}{X^2} - \frac{\sigma_1\sigma_2}{X^2} + \frac{{\sigma_2}^2}{Y^2} + \frac{{\tau_{12}}^2}{S^2} < 1 \tag{B37}$$

Tsai-Wu failure Criterion

$$F_{11}{\sigma_1}^2 + 2F_{12}\sigma_1\sigma_2 + F_{22}{\sigma_2}^2 + F_{66}{\sigma_6}^2 + F_1\sigma_1 + F_2\sigma_2 < 1 \tag{B38}$$

where σ_6 is the shear stress τ_{12}. There exist different definitions for the anisotropic parameters F_{ij}, F_1 and F_2. The following table shows some of the most common ones.

Table B1: Summary of Anisotropic Parameters for the Tsai-Wu Failure Theory [80]

Theory	F_1	F_2	F_{11}	F_{22}	F_{12}	F_{66}
Cowin [16]	$\frac{1}{X}-\frac{1}{X'}$	$\frac{1}{Y}-\frac{1}{Y'}$	$\frac{1}{XX'}$	$\frac{1}{YY'}$	$\frac{2S^2\sqrt{F_{11}F_{22}}-1}{2S^2}$	$\frac{1}{S^2}$
Hoffman [17]	$\frac{1}{X}-\frac{1}{X'}$	$\frac{1}{Y}-\frac{1}{Y'}$	$\frac{1}{XX'}$	$\frac{1}{YY'}$	$-\frac{1}{2XX'}$	$\frac{1}{S^2}$
Malmeister [18]	$\frac{1}{X}-\frac{1}{X'}$	$\frac{1}{Y}-\frac{1}{Y'}$	$\frac{1}{XX'}$	$\frac{1}{YY'}$	$\frac{S'_{45}\left[(F_1-F_2)+(S'_{45})(F_{11}+F_{22})\right]-1}{2(S'_{25})^2}$	$\frac{1}{S^2}$
Marin [19]	$\frac{1}{X}-\frac{1}{X'}$	$\frac{1}{Y}-\frac{1}{XX'}$	$\frac{1}{XX'}$	$\frac{1}{YY'}$	$\frac{1}{XX'}-\frac{XX'-S[X'-X-X'(X/Y)+Y]}{2S^2XX'}$	—
Tsai–Wu [20]	$\frac{1}{X}-\frac{1}{X'}$	$\frac{1}{Y}-\frac{1}{Y'}$	$\frac{1}{XX'}$	$\frac{1}{YY'}$	$\leq \pm\sqrt{F_{11}F_{22}}$ and is determined under biaxial stress	$\frac{1}{S^2}$
Gol'denblat–Kopnov [21]*	$\frac{1}{2}\left(\frac{1}{X}-\frac{1}{X'}\right)$	$\frac{1}{2}\left(\frac{1}{Y}-\frac{1}{Y'}\right)$	$\frac{1}{4}\left(\frac{1}{X}-\frac{1}{X'}\right)^2$	$\frac{1}{4}\left(\frac{1}{Y}-\frac{1}{Y'}\right)^2$	$\frac{1}{8}\left[\left(\frac{1}{X}+\frac{1}{X'}\right)^2+\left(\frac{1}{Y}+\frac{1}{Y'}\right)^2-\left(\frac{1}{S_{45}}+\frac{1}{S'_{45}}\right)^2\right]$	$\frac{1}{S^2}$

*S_{45} and S'_{45} are the shear strength of the 45° coupon subjected to positive and negative shear.